UVSOR ACTIVITY REPORT 2010

UVSOR II since 2003

Beam Transport & Injection Point were Moved.

Full Time Top-Up Operation Starts!

300 mA & 60 hours / week

Beam Current (mA) — 400, 300, 200, 100, 0

Day — Tuesday, Wednesday, Thursday, Friday
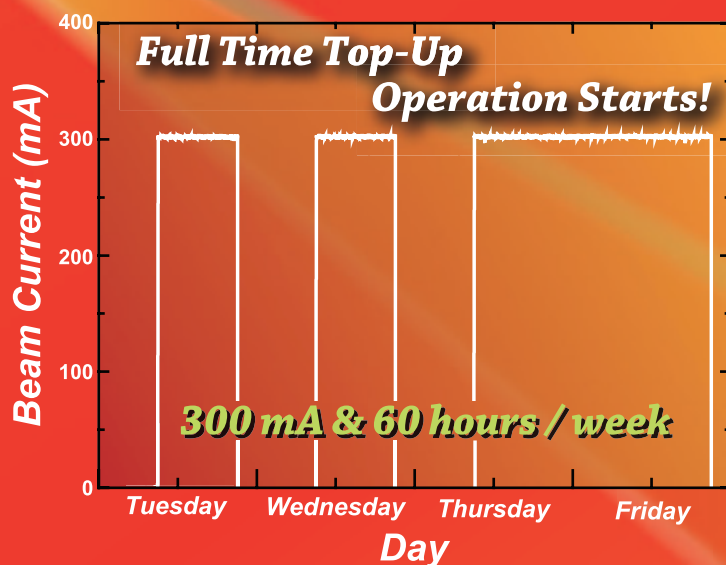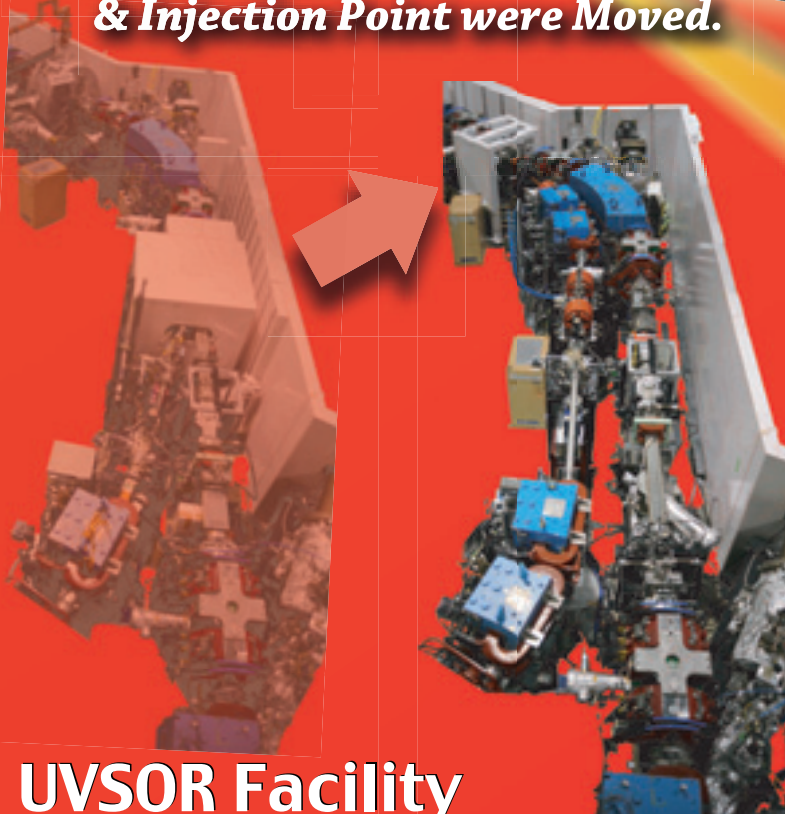
**UVSOR Facility
Institute for Molecular Science
National Institutes of Natural Sciences**

Preface

All of us at the UVSOR facility would like to send our deepest sympathy to the many people who lost their families, friends, and homes as a result of the earthquake in the northeast of Japan in March. Okazaki is located more than 500 km away from the most severely affected area. We felt the quake but it was not strong. At the UVSOR facility, there was no damage.

This Activity Report covers the research activities carried out at the UVSOR facility in FY2010 (April 2010-March 2011). This is the eighth volume in the new series for the third decade of UVSOR.

After the major upgrade in 2002–2003, we renamed the machine UVSOR-II. This is the only low-energy third-generation light source in Japan. UVSOR-II has been operated with a small emittance of 27 nm-rad and four undulators. Over the past four years, we have been preparing for the top-up operation and, this year, we started operating the ring fully in the top-up mode with a beam current of 300 mA.

The fifth undulator beam-line BL1U is currently under construction—it will be dedicated for coherent synchrotron radiation under the Quantum Beam Technology Program of the Ministry of Education, Culture, Sports, Science and Technology (MEXT). For this construction, two beam-lines, BL1A and BL1B, are currently being moved to vacant dipole ports.

Another upgrade program has been funded that includes replacement of the dipoles with combined function ones to reduce the emittance, installation of an undulator and construction of a microspectroscopy beam line. The reconstruction works will be carried out in spring 2012. After this upgrade, we shall call the machine UVSOR-III. Then, our efforts regarding the future plan will shift to design a completely new machine.

In UVSOR, we have four research positions for accelerator physics (1 full professor, 1 associate professor, and 2 assistant professors) and four research positions for photophysics and photochemistry (2 associate professors and 2 assistant professors). In April 2010, two young researchers, Drs. Masaharu Matsunami and Hiroshi Iwayama, joined the photophysics and photochemistry divisions as assistant professors.

We look forward to more exciting achievements in the coming years of UVSOR-II.

April 2011

Masaharu Katoh
Director of UVSOR

The JSSRR Scientific Award Given to Dr. Masaharu MATSUNAMI

In 2011, Dr. Masaharu MATSUNAMI, Assistant Professor working with Associate Professor Shin-ichi KIMURA, won the "Scientific Award" from the Japanese Society for Synchrotron Radiation Research (JSSRR) for his outstanding achievements on the "Combination of Photoemission and Optical Spectroscopies for the Study of Strongly Correlated Electronic Structure." Congratulations!

Dr. Masaharu MATSUNAMI

The Best Presentation Award at the Annual Symposium of the Japan Society for Molecular Science 2010 Given to Dr. Masanari NAGASAKA

Dr. Masanari NAGASAKA, Assistant Professor working with Professor Nobuhiro KOSUGI, won the "Best Presentation Award at the Annual Symposium of the Japan Society for Molecular Science 2010" from the Japanese Society for Molecular Science in 2010 for his oral presentation on "Hydration Structures of Alkali Metal Cations in Aqueous Salt Solutions Studied by Soft X-ray Absorption Spectroscopy." Congratulations!

The Nagoya University Outstanding Graduate Student Award Given to Mr. Yoshitaka TAIRA

Mr. Yoshitaka TAIRA, a PhD candidate of Nagoya University working with Professor Masahiro KATOH, won the "Nagoya University Outstanding Graduate Student Award" from Nagoya University in 2011 for his outstanding study on "Generation of Ultra-Short Gamma Ray Pulses and its Application." Congratulations!

The JSR10 Scientific Award for Students
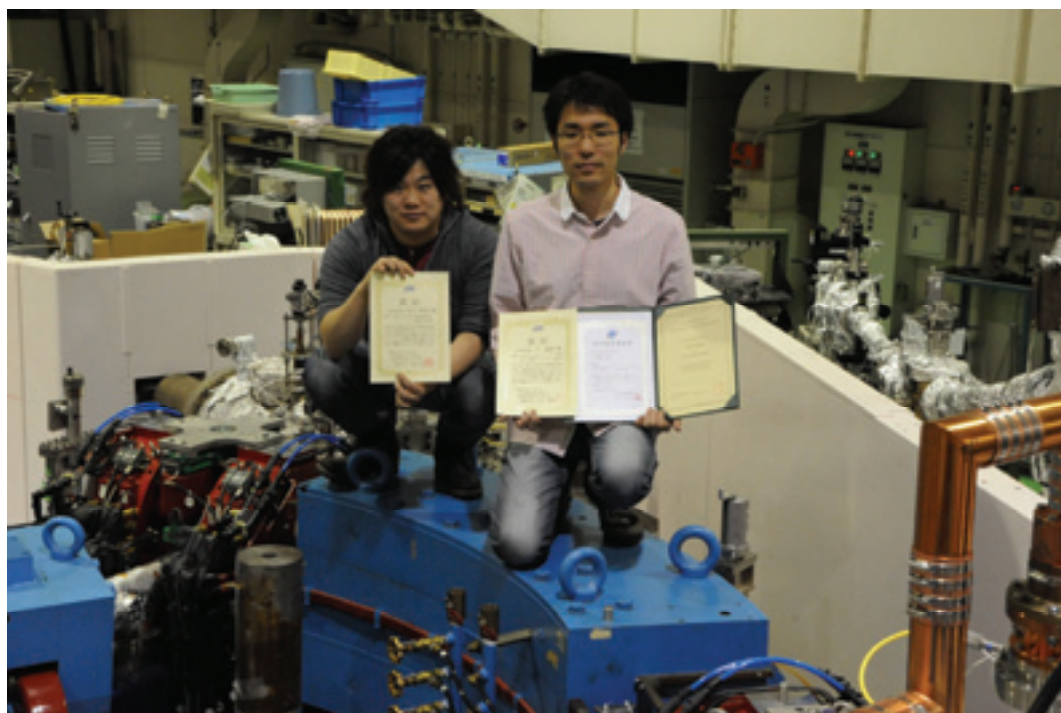## Given to Mr. Yoshitaka TAIRA

In 2010, Mr. Yoshitaka TAIRA, a PhD candidate of Nagoya University working with Professor Masahiro KATOH, won the "JSR10 Scientific Award for Students" from the Japanese Society for Synchrotron Radiation Research (JSSRR) for his poster presentation on "Generation of Ultra-Short Gamma Ray Pulses via Laser Compton Scattering in UVSOR-II." Congratulations!

The Young Best Presenter Award of the 53rd Symposium
on Radiation Chemistry Given to Mr. Yoshitaka TAIRA

In 2010, Mr. Yoshitaka TAIRA, a PhD candidate of Nagoya University working with Professor Masahiro KATOH, won the "Young Best Presenter Award of the 53rd Symposium on Radiation Chemistry" from the Japanese Society of Radiation Chemistry, for his poster presentation on "Development of Ultra-Short Gamma Ray Pulse Sources Using Laser Compton Scattering in UVSOR-II." Congratulations!

The JSR11 Scientific Award for Students
Given to Mr. Takanori TANIKAWA

In 2011, Mr. Takanori TANIKAWA, a PhD candidate of the Graduate University for Advanced Studies (SOKENDAI) working with Professor Masahiro KATOH, won the "JSR11 Scientific Award for Students" from JSSRR for his poster presentation on "Observation of Coherent Harmonics in Saturated Regime at UVSOR-II." Congratulations!

Mr. Takanori TANIKAWA (left) and Mr. Yoshitaka TAIRA (right)

UVSOR Organization

IMS OHMINE, Iwao (Director General)
IMS KOSUGI, Nobuhiro (Deputy Director General)

UVSOR Facility: KATOH, Masahiro (Director)

Accelerator Physics: KATOH, Masahiro (Prof.)

Photophysics: KIMURA, Shin-ichi (Assoc. Prof.)

Photochemistry: SHIGEMASA, Eiji (Assoc. Prof.)

Users in IMS

UVSOR Users Association

UVSOR Steering Commitee

UVSOR Staff

Director

KATOH, Masahiro	Professor	mkatoh@ims.ac.jp

Light Source Division (Accelerator Physics)

KATOH, Masahiro	Professor	mkatoh@ims.ac.jp	
ADACHI, Masahiro	Assistant Professor	adachi@ims.ac.jp	
ZEN, Heishun	Assistant Professor	zen@ims.ac.jp	
YAMAZAKI, Jun-ichiro	Unit Chief Engineer	yamazaki@ims.ac.jp	
HAYASHI, Kenji	Engineer	h-kenji@ims.ac.jp	
TANIKAWA, Takanori	Researcher	tanikawa@ims.ac.jp	(since Apr. 2011)
TOKUSHI, Tetsuzyo	Supporting Engineer	tetsuzyo@ims.ac.jp	

Beamline Division (Photophysics)

KIMURA, Shin-ichi	Associate Professor	kimura@ims.ac.jp	
MATSUNAMI, Masaharu	Assistant Professor	matunami@ims.ac.jp	
HASUMOTO, Masami	Unit Chief Engineer	hasumoto@ims.ac.jp	
SAKAI, Masahiro	Engineer	sakai@ims.ac.jp	
MIYAZAKI, Hidetoshi	IMS Fellow (PD)	hmiyazak@ims.ac.jp	(until Mar. 2011)
MORI, Tatsuya	Post-Doctoral Fellow	mori@ims.ac.jp	(until Feb. 2011)
IMURA, Keiichiro	Post-Doctoral Fellow	imura@ims.ac.jp	(since Apr. 2011)
TAKAHASHI, Toshiharu	Adjunct Associate Professor		
NISHI, Tatsuhiko	Guest Researcher	tnishi@ims.ac.jp	
OZKENDIR, Osman Murat	Guest Researcher	ozkendir@ims.ac.jp	(since Dec. 2010)

Beamline Division (Photochemistry)

SHIGEMASA, Eiji	Associate Professor	sigemasa@ims.ac.jp	
IWAYAMA, Hiroshi	Assistant Professor	iwayama@ims.ac.jp	
HORIGOME, Toshio	Facility Chief Engineer	horigome@ims.ac.jp	
NAKAMURA, Eiken	Unit Chief Engineer	eiken@ims.ac.jp	
KONDO, Naonori	Engineer	nkondo@ims.ac.jp	
ISHIKAWA, Lisa	Post-Doctoral Fellow	ishikawa@ims.ac.jp	(since Apr. 2011)

Secretary

HAGIWARA, Hisayo   hagiwara@ims.ac.jp
KAWAI, Shigeko   kawai@ims.ac.jp

UVSOR Steering Committee

KATOH, Masahiro	UVSOR, IMS	Chair
KIMURA, Shin-ichi	UVSOR, IMS	
SHIGEMASA, Eiji	UVSOR, IMS	
TAKAHASHI, Toshiharu	Kyoto Univ. (Adj. Assoc. Prof., IMS)	
YOKOYAMA, Toshihiko	IMS	
MITSUKE, Koichiro	IMS	
OHSHIMA, Yasuhiro	IMS	
TADA, Mizuki	IMS	
FUKUI, Kazutoshi	Fukui Univ.	
MATSUDA, Iwao	Univ. of Tokyo	
YOSHIDA, Tomoko	Nagoya Univ.	
KINOSHITA, Toyohiko	JASRI	
KOBAYASHI, Yukinori	KEK-PF	
KONDOH, Hiroshi	Keio Univ.	
SHIMADA, Kenya	Hiroshima Univ.	

UVSOR Users Association
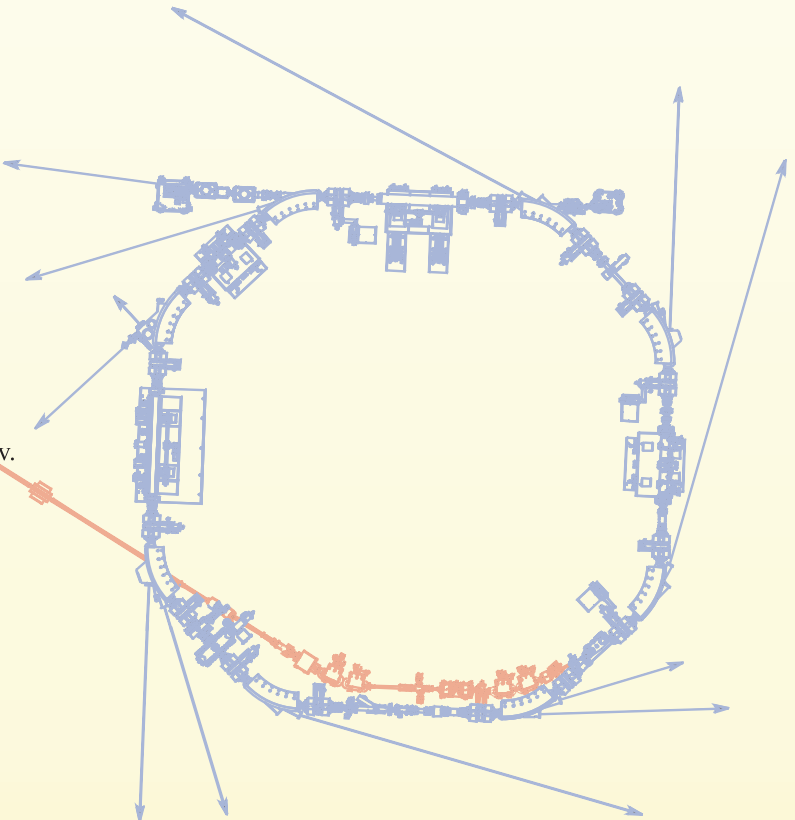
SODA, Kazuo	Chair, Nagoya Univ.
FUKUI, Kazutoshi	Fukui Univ.
NAKAGAWA, Kazumichi	Kobe Univ.
YOSHIDA, Tomoko	Nagoya Univ.
ITO, Takahiro	Nagoya Univ.

Graduate Students

IIZUKA, Takuya	Grad. Univ. Adv. Studies	takuizk@ims.ac.jp	
TANIKAWA, Takanori	Grad. Univ. Adv. Studies	tanikawa@ims.ac.jp	(until Mar. 2011)
TAIRA, Yoshitaka	Nagoya Univ.		
HAJIRI, Tetsuya	Nagoya Univ.		
KIKUCHI, Yoshitaka	Nagoya Univ.		(until Sep. 2010)
GOTO, Yoshiaki	Nagoya Univ.		(since Oct. 2010)
NIWA, Ryosuke	Nagoya Univ.		(since Oct. 2010)
WASA, Naoki	Nagoya Univ.		(since Oct. 2010)

SONG, Dong-Joon	Yonsei Univ.	Apr. 2010
CHOI, Hwan-Young	Yonsei Univ.	Apr. 2010
KWON, Yong-Seung	Sungkyunkwan Univ.	May 2010, Jan. 2011
HONG, Jeong-Beom	Sungkyunkwan Univ.	May 2010
LABLANQUIE, Pascal	LCPMR, Univ. Pierre et marie Curie	June 2010, Feb. 2011
WEENAWAN, Somphon	Kasetsart Univ.	Jun. - Jul. 2010
KIM, Hyeong Do	Pohang Accelerator Laboratory	Aug. 2010
KIM, Chang-Young	Yonsei Univ.	Aug. 2010
JUNG, Won-Sig	Yonsei Univ.	Aug. - Sep., Nov. - Dec. 2010
KOH, Yoon-Young	Yonsei Univ.	Aug. - Sep. 2010
KIM, Bum-Young	Yonsei Univ.	Aug. - Sep., Nov. - Dec. 2010
SZWAJ, Christophe	Univ. of Lille	Nov. - Dec. 2010, Mar. 2011
BIELAWSKI, Serge	Univ. of Lille	Nov. - Dec. 2010, Mar. 2011
JUNG, Min-Cherl	POSTECH	Jan. 2011
JUNG, Sung-Won	POSTECH	Jan. 2011
HE, Cheng	Fudan Univ.	Jan. 2011
ZHANG, Yan	Fudan Univ.	Jan. 2011
XU, Haichao	Fudan Univ.	Jan. 2011
MIN, Gyeong-Im	Sungkyunkwan Univ.	Jan. 2011
OH, Hyunjin	Masan College	Jan. 2011
CARR, G. Lawrence	Brookhaven National Laboratory	Jan. 2011
PONG, Way-Faung	Tam Kang Univ.	Feb. 2011
CHIOU, Jan-Wern	National University of Kaohsiung	Feb. 2011
YANG, Li-Da	Tam Kang Univ.	Feb. 2011
LIU, Ming-Thsung	Tam Kang Univ.	Feb. 2011
ZHONG, Jun	Soochow Univ.	Feb. - Mar. 2011
XIE, Tian	Soochow Univ.	Feb. - Mar. 2011
PRZYBYLSKI, Marek	Max Planck Institute of Microstructure Physics	Feb. - Mar. 2011
YILDIZ, Firkret	Max Planck Institute of Microstructure Physics	Feb. - Mar. 2011
DABROWSKI, Maciej	Max Planck Institute of Microstructure Physics	Feb. - Mar. 2011

Light Sources in 2010

1. Status of UVSOR Accelerators

In the fiscal year 2010, we operated the UVSOR-II accelerators from June '10 to March '11. We had a total of 36 weeks of user operation, 34 weeks of which were in the multi-bunch mode, 1 week in the single-bunch mode, and 1 week in the single-bunch/multi-bunch hybrid mode, which was newly started this year. In the hybrid mode, we basically operate the machine in single-bunch mode during the daytime and multi-bunch mode in the nighttime. We had no week dedicated for machine studies this year, otherwise it was typically a few weeks a year. Because we had a long shutdown period in spring '10, we gave up the study weeks this year to secure beam time for users as in a usual year. We had a three-month shutdown, starting in March '10, for reconstruction work on the storage ring and the beam transport line. We had a one-week shutdown in September and a two-week one around New Years Day.
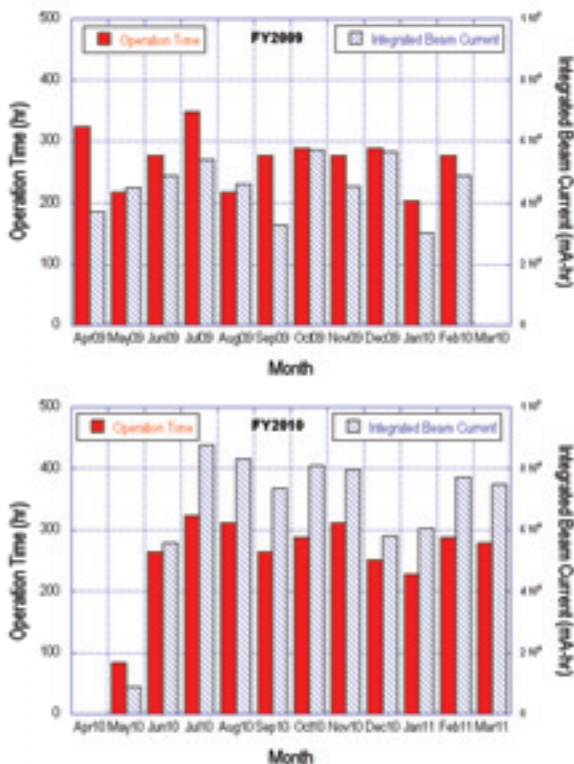

Fig. 1. Monthly statistics in FY2009 (upper) and FY2010 (lower) of the operation time (red bars) and of the integrated beam current (blue dashed bars).

The monthly statistics of the operation time and the integrated beam current are shown in Fig. 1. The operation time per month did not increase compared with last year, but the integrated beam current did. This is because of the start of the full top-up operation, as described later.

The weekly operation schedule is as follows. On Monday, from 9 am to 9 pm, the machine is operated for machine studies. On Tuesday and Wednesday, from 9 am to 9 pm, the machine is operated for users. From Thursday 9 am to Friday 9 pm, the machine is operated for 36 hours continuously for users. Thus, the user beam time is 60 hours per week. This year, we have started operating the machine in the top-up mode 100% of the user time. The beam current is kept at 300 mA in the multi-bunch mode and 50 mA in the single-bunch mode.

This fiscal year, we had a few troubles regarding the pulse magnet power supplies for beam injection, which may be due to the increase in the operation time of the beam injection system caused by the start of the top-up operation. We had a few troubles with the klystron pulse modulator for the linear accelerator. One switching circuit had difficulties three times in a year. Thus, we are going to improve the circuit in 2011. Fortunately, in all cases, the beam time for users could be secured by extending the operation time.

2. Improvements

Top-up Operation

We introduced the top-up operation for 100% of the users beam time this year in both the multi-bunch mode and the single-bunch mode. Because the orbit movement during the injection is large, we deliver timing signals to the beam lines to stop the data acquisition during the injection if necessary.
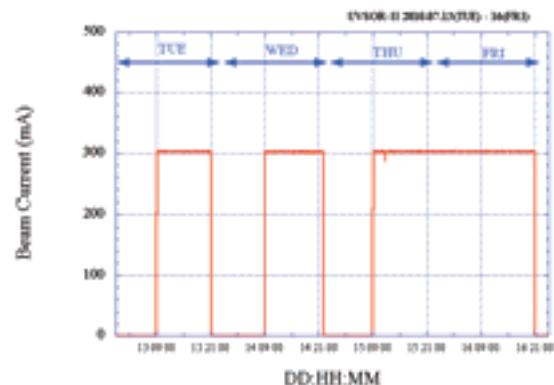

Fig. 2. Typical beam current history in users time from Tuesday to Friday.

Reconstruction of Beam Transport Line

In March 2010, we started the reconstruction of the beam transport line and the storage ring, aiming to produce a 4 m straight section in the ring for a new undulator. We moved the injection point to a short straight section from the 4 m straight section previously used for the injection. The main RF cavity that was installed in the short straight section was moved to another short straight section. The injection septum magnet and the kicker magnets were moved. The beam transport line was extended to the new injection point. All reconstruction works were completed in three months, as shown in Fig. 3. In May, the new beam transport line was successfully commissioned with the same injection efficiency as before.
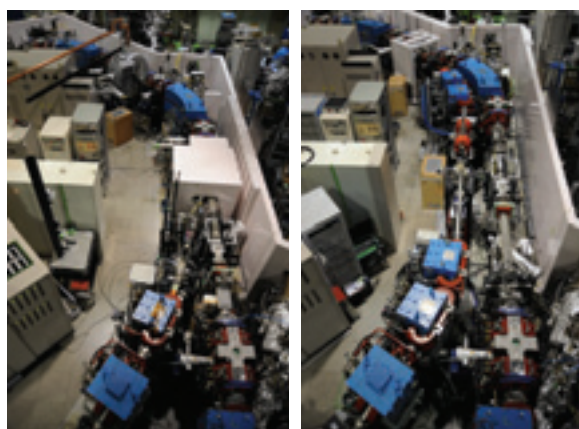
Fig. 3. Beam transport line and injection point of the UVSOR-II storage ring before (left) and after (right) the reconstruction.

Accelerator Technologies

Four undulators are operational at UVSOR-II. They produce various effects on the accelerator performance. One of the undulators, the APPLE-II type one for BL7U, has a significant effect on the beam life time and the injection efficiency. To suppress these effects, we have tested a novel correction method using current wires on the beam duct. By optimizing the electric current on the wires, we could recover the beam lifetime successfully [1]. This method will be introduced to the users beam time soon in the next fiscal year.

3. Research and Development

Coherent Terahertz Synchrotron Radiation

We have been developing technologies to produce coherent synchrotron radiation in the terahertz range by using laser slicing/modulation technologies. By using an external laser source, we can produce various kinds of microdensity structures on the electron bunches. They emit coherent synchrotron radiation in the terahertz range.

This year, we investigated the laser power dependence of the terahertz radiation. We found that the terahertz intensity is proportional to the square of the laser power in the relatively low power range [2].

Coherent Harmonic Generation

Coherent harmonic generation (CHG) is under investigation, aiming to develop a coherent VUV light source and to investigate the basic mechanism of the laser seeding in free electron lasers.

We have succeeded in observing the CHG up to the ninth harmonics in the wide range of the pulse energy of the seed laser. We observed that the CHG power was saturated in the high energy range and oscillates with the laser energy. This was explained by a micro-bunching process in the over-bunching regime [3].

Laser Compton Scattering Gamma-rays

The generation of gamma-rays based on the laser Compton scattering technique has been investigated. This technique is well established and is demonstrated in many accelerator facilities. Usually, the laser and the electron beam collide in a head-on configuration. In contrast, we injected the laser beam into the electron beam in the vertical direction to their orbital plane. With this 90-degree configuration, we have succeeded in producing ultra-short gamma-ray pulses. In addition, we have succeeded in changing the gamma-ray energy continuously by changing the colliding angle around 90 degrees [4].

[1] Y. Kikuchi et al., in this report
[2] M. Hosaka et al, in this report
[3] T. Tanikawa et al., in this report
[4] Y. Taira et al., in this report

Masahiro KATOH (UVSOR Facility)

UVSOR Accelerator Complex

Injection Linear Accelerator

DC Gun	
Electron Source	EIMAC Y-646B
Applied Voltage	75 kV
Accelerator Tube	
Length	2.5 m
Frequency	2856 MHz
Structure	2π/3 Traveling Wave
Repetition Rate	2.6 Hz
Beam Energy	~15 MeV
Electron Beam Macro-pulse Duration	
Short Pulse Mode	~5 ns
Long Pulse Mode	~1.5 μs
Beam Charge	
Short Pulse Mode	0.8 nC/Macro-pulse
Long Pulse Mode	130 nC/Macro-pulse

Booster Synchrotron

Energy	750 MeV
Injection Energy	15 MeV
Beam Current	32 mA (uniform filling)
Circumference	26.6 m
RF Frequency	90.1 MHz
Harmonic Number	8
Bending Radius	1.8 m
Lattice	FODO×8
Betatron Tune	
Horizontal	2.25
Veritcal	1.25
Momentum Compaction	0.138
Repetition Rate	1 Hz (750 MeV)

UVSOR-II Storage Ring

Energy	750 MeV
Injection Energy	750 MeV
Maximum Stored Current	500 mA (multi bunch)
	100 mA (single bunch)
Normal Stored Current	300 mA (multi bunch)
(Top-up operation)	50 mA (single bunch)
Natural Emittance	27.4 nm-rad
Circumference	53.2 m
RF Frequency	90.1 MHz
Harmonic Number	16
Bending Radius	2.2 m
Lattice	Extended DBA×4
Straight Section	(4 m×4)+(1.5 m×4)
RF Voltage	100 kV
Betatron Tune	
Horizontal	3.75
Veritcal	3.20
Momentum Compaction	0.028
Natural Chromaticity	
Horizontal	-8.1
Vertical	-7.3
Energy Spread	4.2×10^{-4}
Natural Bunch Length	108 ps

15 MeV Linear Accelerator

750 MeV Booster Synchrotron

Beam Transport

BL5U
BL5B
BL6U
BL6B
FEL Optical Cavity
BL4B
BL7U
U7
U6
3rd Harmonic Cavity
Main Cavity
BL7B
U5
FEL Optical Cavity
750 MeV Electron Storage Ring
U3
BL3U
BL8B
BL2B
BL1B
BL1A
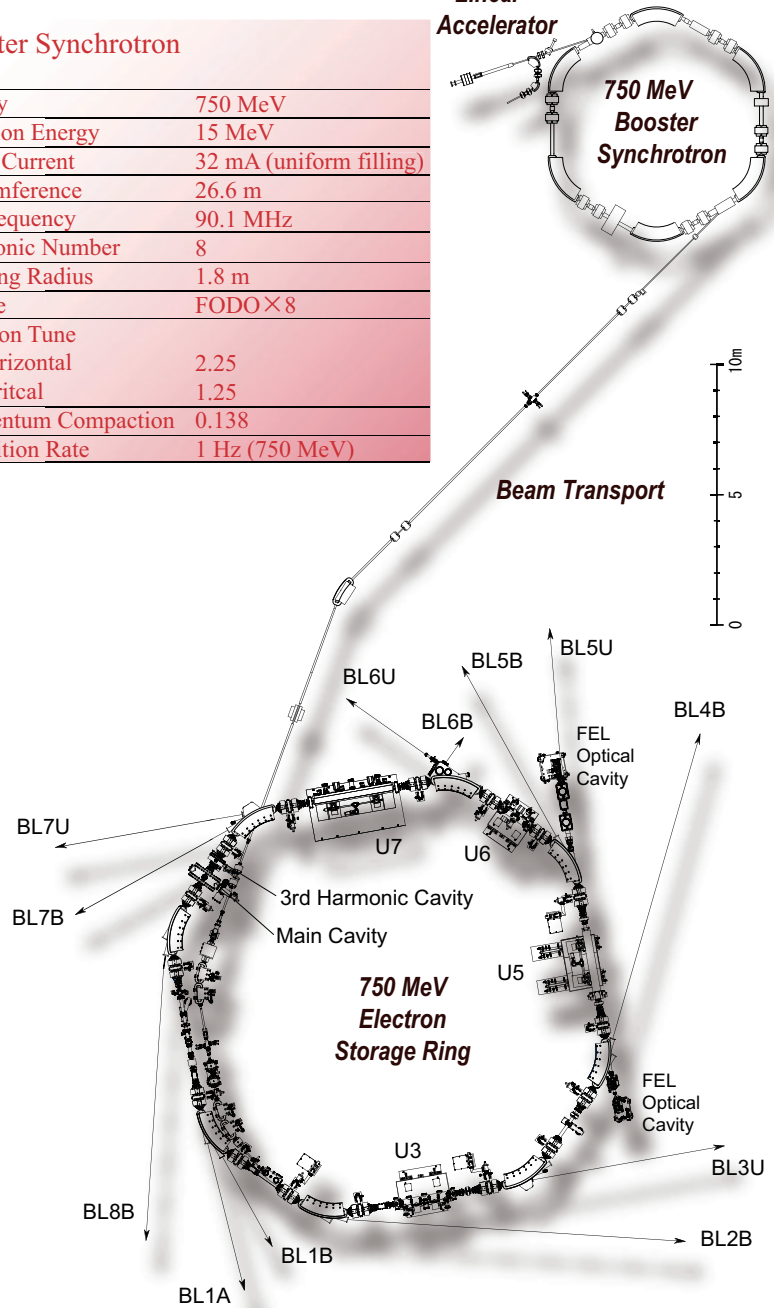
Electron Beam Optics of UVSOR-II Storage Ring

ε = 27.4 nm-rad
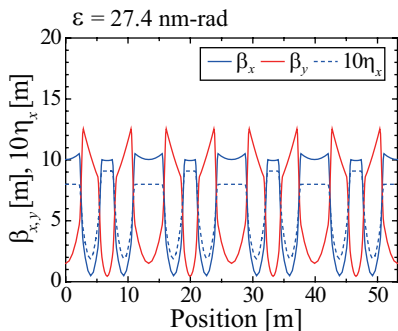
Horizontal / vertical betatron functions and dispersion function

ε = 27.4 nm-rad, 10% Coupling
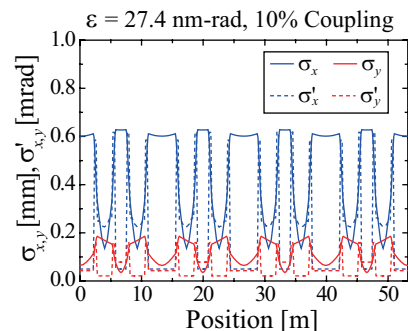
Horizontal / vertical electron beam sizes and beam divergences

11

Insertion Devices

Brilliance of Radiation
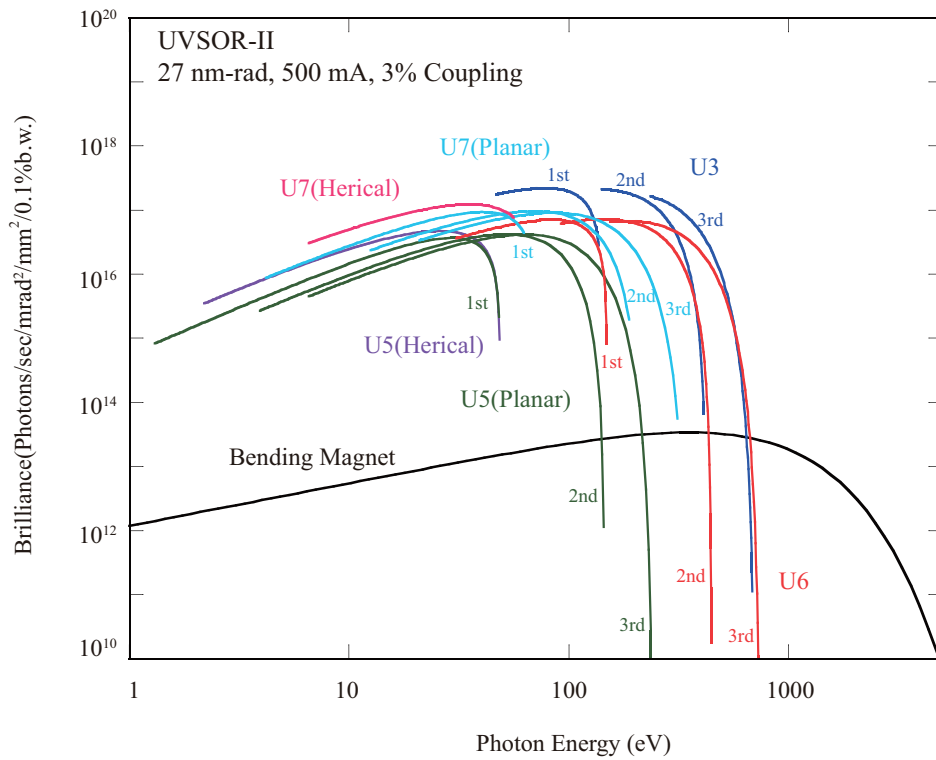
Brilliance of radiation from the insertion devices (U3, U5, U6 and U7) and a beding magnet of UVSOR-II

U3 In-vacuum Undulator

Number of Periods	50
Period Length	38 mm
Pole Length	1.9 m
Pole Gap	15 - 40 mm
Deflection Parameter	2.00 - 0.24

U5 Herical Undulator / Optical Klystron

Number of Periods	21 / 9+9 (Opt. Kly.)
Period Length	110 mm
Pole Length	2.35 m
Pole Gap	30 - 150 mm
Deflection Parameter	4.6 - 0.07 (Helical)
	8.5 - 0.15 (Linear)

Bending Magnets

Bending Radius	2.2 m
Critical Energy	425 eV

U6 In-vacuum Undulator

Number of Periods	26
Period Length	36 mm
Pole Length	0.94 m
Pole Gap	15 - 40 mm
Deflection Parameter	1.78 - 0.19

U7 Apple-II Variable Polarization Undulator

Number of Periods	40
Period Length	76 mm
Pole Length	3.04 m
Pole Gap	24 - 200 mm
Deflection Parameter	5.4 (Max. Horizontal)
	3.6 (Max. Vertical)
	3.0 (Max. Helical)

Beamlines in 2010

Eiji SHIGEMASA

UVSOR Facility, Institute for Molecular Science

Following the successful realization of the upgrade project on the UVSOR storage ring (UVSOR-II project), in which the creation of four new straight sections and the achievement of much smaller emittance (27 nm-rad) were planned, the UVSOR facility has become one of the highest brilliance extreme-ultraviolet radiation sources among synchrotron radiation facilities with electron energy of less than 1 GeV. Eight bending magnets and four insertion devices are available for utilizing synchrotron radiation at UVSOR. There has been a total of 12 operational beamlines in 2010, which have been classified into two categories. Nine of them are so-called "Open beamlines," which are open to scientists of universities and research institutes belonging to the government, public organizations, private enterprises, and those of foreign countries. The other three beamlines are the so-called "In-house beamlines," and are dedicated to the use by research groups within IMS.

The improvements and upgrades of the beamlines at UVSOR have been continuously discussed with users in a series of UVSOR workshops. The newly constructed (BL3U, BL7U, and BL6U) as well as the upgraded (BL5U and BL6B) beamlines synchronized with the UVSOR-II project have been routinely operated, and a number of outcomes have emerged through the utilization of these beamlines. The experimental activities conducted at BL4A and BL8B1 were terminated in August 2009 and in February 2010, respectively. As a consequence, we have one soft X-ray station equipped with a double-crystal monochromator, seven extreme ultraviolet and soft X-ray stations with a grazing incidence monochromator, three vacuum ultraviolet stations with a normal incidence monochromator, and one infrared (IR) station equipped with Fourier-transform interferometers, as shown in the appended table (next page) for all available beamlines at UVSOR in 2010.

"Development and Application of Light Source Technology Based on Electron Storage Ring and Laser" proposed by the UVSOR machine group was accepted in 2008 as a research program in the "Quantum Beam Technology Program" conducted by MEXT/JST. In connection, the straight section S1 will be used for generating coherent THz and VUV radiation, where two beamlines will be constructed. In response, BL1A and BL1B must be moved to vacant lots. Because spectroscopic research works on solids have been conducted very actively at these beamlines, it is essential that all users' activities there should segue at new locations. Based upon the result of the discussion at the users' meetings, which were organized by the UVSOR User's Union, it was decided that BL1A will be moved to the location of the previous BL2A without any changes on the beamline components, and BL1B will be newly constructed at the place of the previous BL3B, where the Ti:Sa laser system for the machine group occupies. For the monochromator at BL3B, a 2.5-m off-plane Eagle type has been chosen. The practical movement and construction of the related beamlines have just started in the spring of 2011.

A supplementary budget for upgrading the UVSOR facility was approved in the autumn of 2010; it had originally been submitted as one of the estimate budget requests of the National Institutes for Natural Sciences. The supplementary budget includes the cost for constructing a new soft X-ray microscopy beamline at BL4U, where a short undulator with a length of approximately 1 m is available as a light source. The period length chosen for this undulator, U4, is 38 mm, which is the same as that for U3. The spectral region from 60 to 800 eV will be covered with the first and higher harmonic radiation. We have decided to choose the entrance slit-less configuration for the monochromator to keep the monochromator throughput as high as possible, as a result of the successful installations of such a configuration to BL7U and BL6U. In order to cover such a wide photon energy region with one single grating, a variable-included-angle Monk–Gillieson mounting has been selected. A scanning transmission soft X-ray microscope (STXM) will be installed at the exit slit position of the new BL4U. A new scientist with the design, installation, commissioning, and maintenance of this STXM beamline is now in the selection process. The introduction of photoemission electron microscopy to a branch beamline of BL4U as well as the upgrades of the undulator U5 and the SGM-TRAIN monochromator at BL5U are in the planning stage. Further discussion toward formulating a basic plan on the beamline construction with users will be carried out.

All users are required to refer to the beamline manuals and the UVSOR guidebook (the latest revision in PDF format uploaded on the UVSOR web page in the summer of 2009), when conducting the actual experimental procedures. Those wishing to use the open and in-house beamlines are recommended to contact the respective beamline master (see next page). For updated information on UVSOR, see http://www.uvsor.ims.ac.jp/.

Beamlines at UVSOR

Beamline	Monochromator / Spectrometer	Energy Range		Targets	Techniques	Contact
BL1A[*]	Double crystal		600 eV - 4 keV	Solid	Absorption	N. Kondo nkondo@ims.ac.jp
BL1B[†]	1-m Seya-Namioka		2 - 30 eV	Solid	Reflection Absorption	M. Hasumoto hasumoto@ims.ac.jp
BL2B[‡]	18-m spherical grating (Dragon)		24 - 205 eV	Gas	Photoionization Photodissociation	K. Mitsuke mitsuke@ims.ac.jp
BL3U[‡]	Varied-line-spacing plane grating (Monk-Gillieson)		60 - 800 eV	Gas Liquid Solid	Absorption Photoemission Photon-emission	N. Kosugi kosugi@ims.ac.jp
BL4B[‡]	Varied-line-spacing plane grating (Monk-Gillieson)		25 eV - 1 keV	Gas Solid	Photoionization Photodissociation Photoemission	E. Shigemasa sigemasa@ims.ac.jp
BL5U	Spherical grating (SGM-TRAIN[§])		5 - 250 eV	Solid	Photoemission	M. Sakai sakai@ims.ac.jp
BL5B	Plane grating		6 - 600 eV	Solid	Calibration Absorption	M. Hasumoto hasumoto@ims.ac.jp
BL6U[‡]	Variable-included-angle varied-line-spacing plane grating		30 - 500 eV	Gas Solid	Photoionization Photodissociation Photoemission	E. Shigemasa sigemasa@ims.ac.jp
BL6B	Martin-Puplett FT-FIR, Michelson FT-IR		0.6 meV - 2.5 eV	Solid	Reflection Absorption	S. Kimura kimura@ims.ac.jp
BL7U	10-m normal incidence (modified Wadsworth)		6 - 40 eV	Solid	Photoemission	M. Matsunami matunami@ims.ac.jp
BL7B	3-m normal incidence		1.2 - 25 eV	Solid	Reflection Absorption	M. Hasumoto hasumoto@ims.ac.jp
BL8B	Plane grating		1.9 - 150 eV	Solid	Photoemission	T. Nishi tnishi@ims.ac.jp
FEL	Free electron laser		1.6 - 6.2 eV			M. Katoh mkatoh@ims.ac.jp
CSR	Coherent synchrotron radiation		0.5 - 5 meV			M. Katoh mkatoh@ims.ac.jp

Yellow area: undulator beamline
[*] This beamline will be moved to BL2A after June 2011.
[†] This beamline will be moved to BL3B after June 2011.
[‡] In-house beamline
[§] Spherical grating monochromator with translating and rotating assembly including normal incidence mount

BL1A

Soft X-Ray Beamline for Photoabsorption Spectroscopy

BL1A is a soft X-ray beamline for photoabsorption spectroscopy.   The beamline is equipped with a focusing premirror and a double crystal monochromator [1].   The monochromator serves soft X-rays in the energy region from 585 to 4000 eV using several kinds of single crystals, such as β-Al_2O_3, beryl, KTP ($KTiOPO_4$), quartz, InSb, and Ge.   The throughput spectra measured using a Si photodiode (AXUV-100, IRD Inc.) are shown in Fig. 1. The typical energy resolution ($E/\Delta E$) of the monochromator is approximately 1500 for beryl and InSb.   There are no experimental setups that are specific to this beamline, except for a small vacuum chamber equipped with an electron multiplier (EM) detector.   Photoabsorption spectra for powdery samples are usually measured in a total electron yield mode, with the use of the EM detector.

This beamline will be moved to BL2A after June 2011.

[1] Hiraya *et al.*, Rev. Sci. Instrum. **63** (1992) 1264.
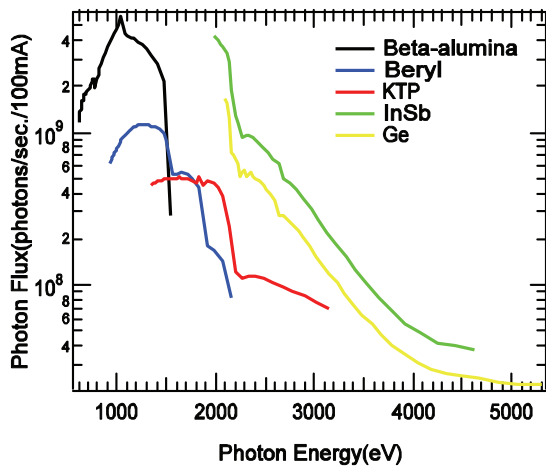
Fig. 1. Throughput spectra of the double crystal monochromator at BL1A.
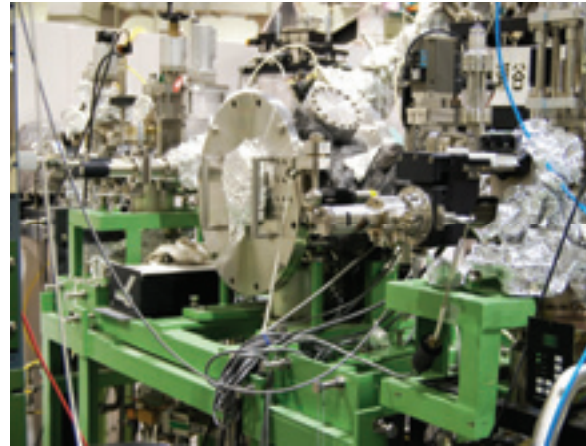
Fig. 2. Side view of BL1A.

Beamline Specifications

Monochromator	Double crystal monochromator
Monochromator crystals: (2d value, energy range)	β-Al_2O_3 (22.53 Å, 585–1609 eV), beryl (15.965 Å, 826–2271 eV), KTP (10.95 Å, 1205–3310 eV), quartz (8.512 Å, 1550–4000 eV), InSb (7.481 Å, 1764–4000 eV), Ge (6.532 Å, 2094–4000 eV)
Resolution	$E/\Delta E$ = 1500 for beryl and InSb
Experiments	Photoabsorption spectroscopy

BL1B

Seya-Namioka Monochromator for General Purposes

BL1B has been constructed to perform various spectroscopic investigations, such as absorption, reflectivity, and luminescence in condensed matters. This beamline consists of a pre-focusing mirror, a 1-m Seya-Namioka-type monochromator, and post-focusing mirrors with different focal lengths. Three gratings of 600, 1200, and 2400 l/mm can cover the wavelength region ranging from 40 to 650 nm (hv = 2–30 eV). The post mirror with a longer focal length is usually used with an LiF window to separate the vacuum condition of the monochromator from the main experimental station, which make experiments for liquids and bio-specimens possible; the other is mainly utilized for solid-state spectroscopy. The output flux from this monochromator is approximately 1010 photons/s around 200 nm with 0.1 mm slit openings. The spectral distributions for two gratings measured using a conventional photomultiplier are shown in Fig. 1. A second monochromator (Spex 270M) and a LN-cooled charge-coupled device (CCD) detector (Princeton Inc.) are available for luminescence measurements, together with a liquid helium-flow-type cryostat. To perform time-resolved experiments, a TAC system is also available.

This beamline will be moved to BL3B after June 2011.
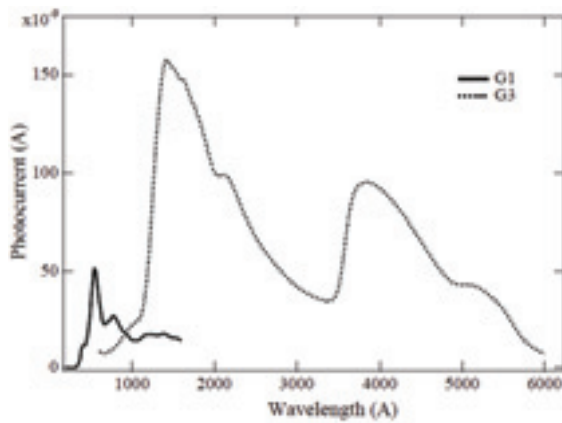
Fig. 1. Photocurrent at the sample position at BL1B.
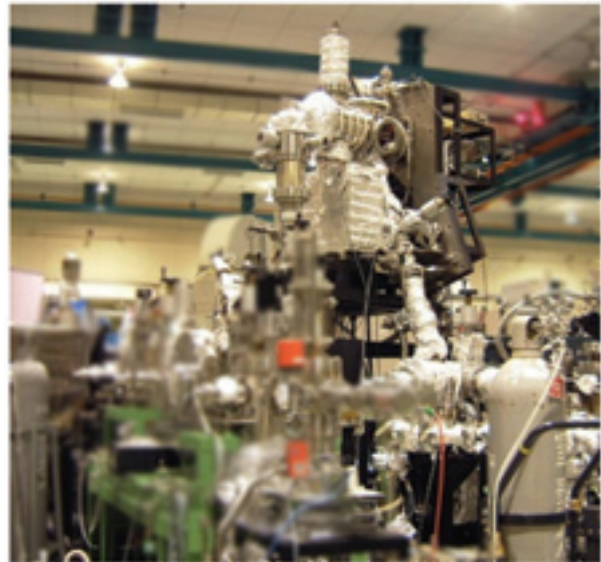
Fig. 2. Photo of BL1B.

Beamline Specifications

Monochromator	1-m Seya-Namioka type
Wavelength Range	40 to 600 nm (2–30 eV)
Resolution	$E/\Delta E$~1000 at 100 nm (10 eV)
Experiments	Absorption, reflection, and luminescence spectroscopy for solids

BL2B

Beamline for Gas Phase Photoionization and Reaction Dynamics

This beamline has been developed to study ionization, excitation, and decay dynamics involving inner-valence electrons, $2p$ electrons of the third row atoms, and 4d electrons of the lanthanides. The monochromator is a spherical grating Dragon type with 18-m focal length. High throughput (1×10^{10} photons s^{-1}) and high resolution ($E/\Delta E$ = 2000 - 8000) are achieved simultaneously under the condition of the ring current of 100 mA [1]. The optical system consists of two pre-focusing mirrors, an entrance slit, three spherical gratings (G1 - G3), two folding mirrors, a movable exit slit, and a refocusing mirror [2]. The monochromator is designed to cover the energy range of 23–205 eV with the three gratings: G1 (2400 lines mm^{-1}, R = 18 m) at 80–205 eV; G2 (1200 lines mm^{-1}, R = 18 m) at 40–100 eV; G3 (2400 lines mm^{-1}, R = 9.25 m) at 23–50 eV. The percentage of the second-order light contamination at $h\nu$ = 45.6 eV is 23% for G2 or 7% for G3.

We have been measuring the yield curves of various fullerene ions [3]. Geometrical structures and electronic properties of fullerenes have attracted widespread attention because of their novel structures, novel reactivity, and novel catalytic behaviors as typical nanometer-size materials. However, spectroscopic information was very limited in the extreme UV region, owing to difficulties in acquiring sufficient sample amounts. This situation has rapidly changed since the start of this century, because the techniques related to syntheses, isolation, and purification have advanced so rapidly that an appreciable amount of fullerenes can now be readily obtained.

[1] M. Ono, H. Yoshida, H. Hattori and K. Mitsuke, Nucl. Instrum. Meth. Phys. Res. A **467-468** (2001) 577.
[2] H. Yoshida and K. Mitsuke, J. Synchrotron Radiation **5** (1998) 774.
[3] J. Kou, T. Mori, Y. Kubozono and K. Mitsuke, Phys. Chem. Chem. Phys. **7** (2005) 119.
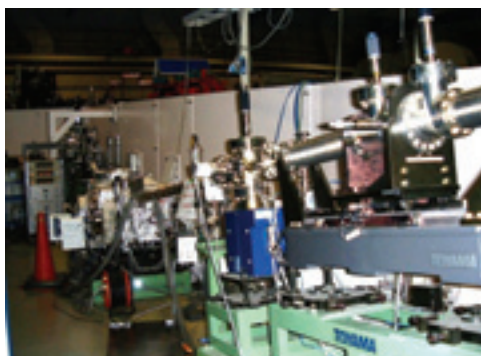
Fig. 1. 18-m spherical grating
monochromator at BL2B.

Fig. 2. End station of BL2B for gas phase
spectroscopy of refractory materials.

Beamline Specifications

Monochromator	18-m spherical grating Dragon-type
Wavelength Range	6–55 nm; 24–205 eV
Resolution	2000–8000 depending on the gratings
Experiments	Mass spectrom.; photoelectron spectrosc.; momentum imaging spectrosc.; e$^-$-ion coincidence spectrosc.; fullerene beam source

BL3U

Varied-Line-Spacing Plane Grating Monochromator for Molecular Soft X-Ray Spectroscopy

The beamline BL3U is equipped with an in-vacuum undulator composed of 50 periods of 3.8 cm period length. The emitted photons are monochromatized by the varied-line-spacing plane grating monochromator (VLS-PGM) designed for various spectroscopic investigations in the soft X-ray range including soft X-ray emission studies. Three holographically ruled laminar profile plane gratings are designed to cover the photon energy range from 60 to 800 eV. The beamline has two endstations, namely, XES setup and multi-purpose setup. The XES setup is used for soft X-ray emission spectroscopy. The beam is horizontally focused onto the sample position by a plane-elliptical mirror, M2X. In the multi-purpose setup, the beam is focused by the toroidal mirror M2. Between the sample position and M2, the differential pumping is placed.
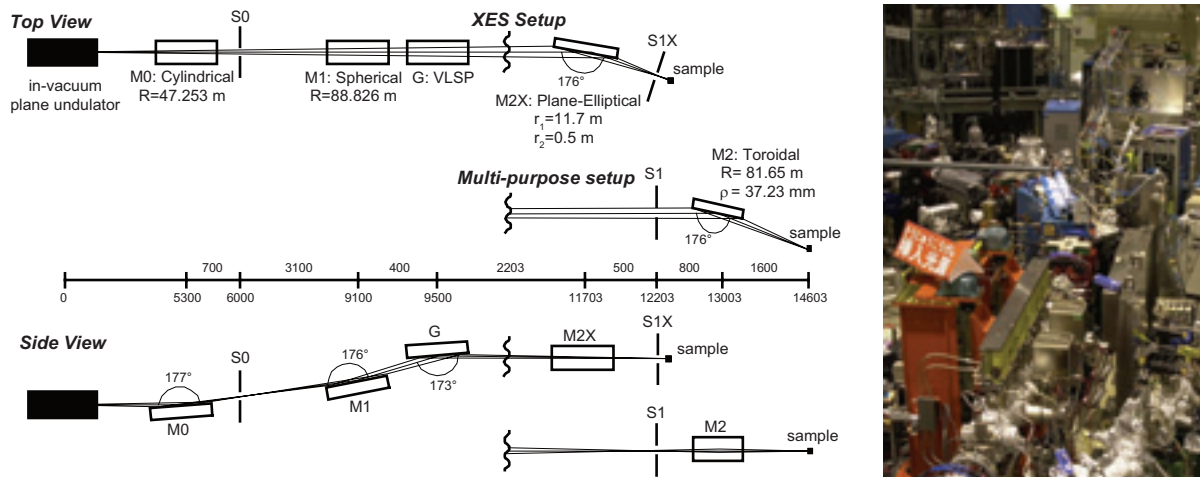
Fig. 1. Schematic layout (left) and the photography (right) of the BL3U. The distances along the beam from the center of the in-vacuum plane undulator are shown in millimeters. S1X and M2X can be replaced with the other exit slit S1 so that experiments can be carried out at either the XES or the multipurpose endstation. In the XES setup, the sample is placed 5–10 mm downstream of S1X.

Beamline Specifications

Monochromator	Varied-line-spacing plane grating monochromator
Energy Range	60–800 eV
Resolution	$E/\Delta E > 10\,000$
Experiments	Soft X-ray spectroscopy (XPS, XES, XAS)
Beam Size (XES Endstation)	Gaussian shape Vertical 5–20 μm; Horizontal 41 μm (FWHM)

BL4B

Varied-Line-Spacing Plane Grating Monochromator for Molecular Soft X-Ray Spectroscopy

The beamline BL4B equipped with a varied-line-spacing plane grating monochromator (VLS-PGM) was constructed for various spectroscopic investigations in a gas phase and/or on solids in the soft X-ray range. Three holographically ruled laminar profile plane gratings with SiO_2 substrates are designed to cover the photon energy range from 25 to 800 eV. The gratings with groove densities of 100, 267, and 800 l/mm cover the spectral ranges of 25–100, 60–300, and 200-1000 eV, respectively, and are interchangeable without breaking the vacuum. Fig. 1 shows the absolute photon flux for each grating measured using a Si photodiode (IRD Inc.), with the entrance- and exit-slit openings set at 50 and 50 μm, respectively. The maximum resolving power ($E/\Delta E$) achieved for each grating exceeds 5000.
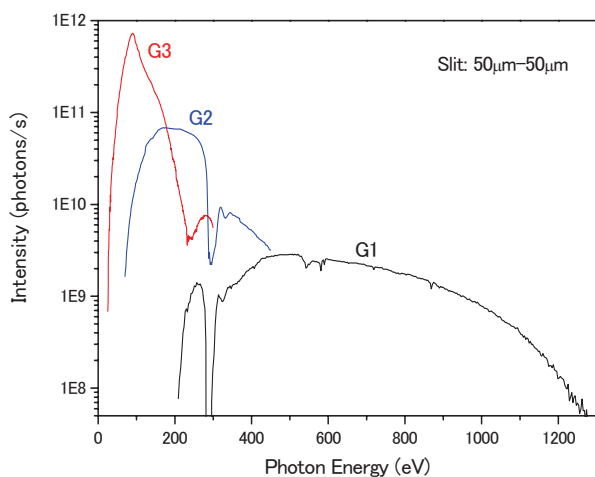
Fig. 1. Throughput from the VLS-PGM monochromator on BL4B.
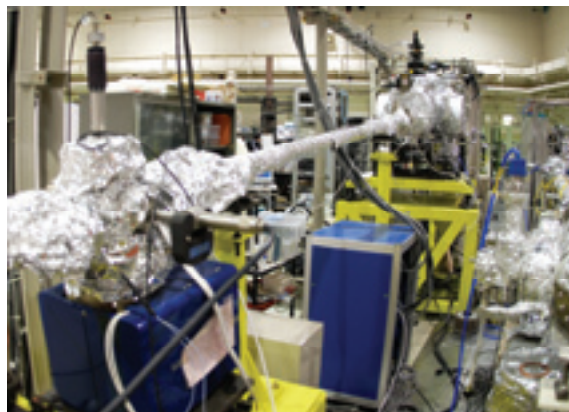
Fig. 2. Photo of BL4B.

Beamline Specifications

Monochromator	Varied-line-spacing Plane Grating Monochromator
Energy range	25–1000 eV
Resolution	$E/\Delta E > 5000$ (at maximum)
Experiments	Soft X-ray spectroscopy (mainly, angle-resolved photoion spectroscopy for gaseous targets and photoelectron spectroscopy for gaseous and solid targets)

BL5U

Photoemission Spectroscopy of Solids and Surfaces

This beamline is designed for high-resolution angle-resolved photoemission study of solids and surfaces with horizontal-linearly and circularly (CW, CCW) polarized synchrotron radiation from a helical undulator.   The beamline consists of a Spherical Grating Monochromator with a Translational and Rotational Assembly Including a Normal incidence mount (SGM-TRAIN) and a high-resolution angle-resolved photoemission spectrometer.

The SGM-TRAIN is an improved version of a constant-length SGM that aims at realizing the following points: (1) covering the wide energy range of 5–250 eV, (2) high energy resolving power, (3) use of linearly and circularly polarized undulator light, (4) reduction of higher-order light, and (5) two driving modes (rotation and translation of gratings) by computer control. The second-order light is well suppressed using laminar profile gratings and combinations of mirrors and gratings.
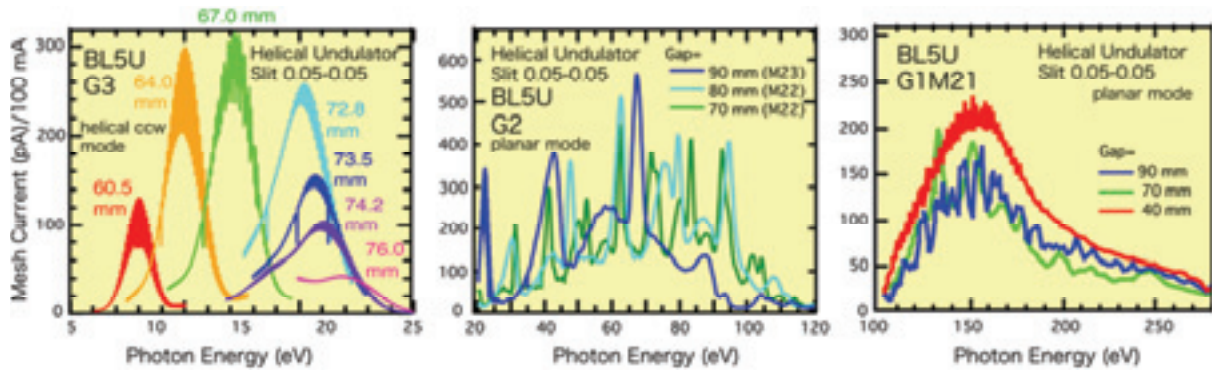
Fig. 1. Throughput spectra from the SGM-TRAIN monochromator at BL5U.

Beamline Specifications

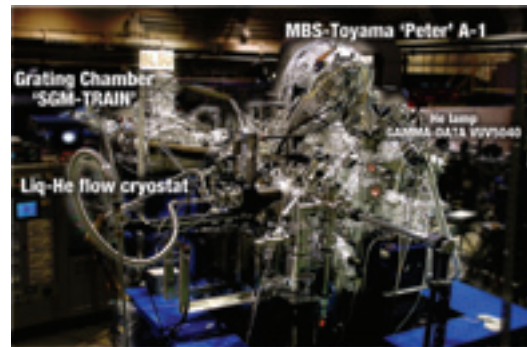| Monochromator	SGM-TRAIN
Energy Range	5–250 eV
Resolution	$h\nu/\Delta E > 2,000$ for < 40 μm slits
Experiment	ARPES, AIPES, XAS
Flux	$<10^{11}$ photons/s for <40 μm slits (in the sample position)
Main Instruments	Hemispherical photoelectron analyzer (MBS-Toyama 'Peter' A-1), LEED of reverse type (OMICRON), Liq-He flow cryostat (5–400 K)

Fig. 2. High-resolution angle-resolved photoemission apparatus at BL5U.

BL5B

Calibration Apparatus for Optical Elements and Detectors

BL5B has been constructed to perform calibration measurements for optical elements and detectors. This beamline is composed of a plane grating monochromator (PGM) and three endstations in tandem. The most upstream station is used for the calibration measurements of optical elements, the middle one for optical measurements for solids, and the last for photo-stimulated desorption experiments. The experimental chamber at the most downstream station is sometimes changed to a chamber for photoemission spectroscopy. The calibration chamber shown in Fig. 2 is equipped with a goniometer for the characterization of optical elements, which has six degrees of freedom, X-Y translation of a sample, and interchanging of samples and filters. These are driven by pulse motors in vacuum. Because the polarization of synchrotron radiation is essential for such measurements, the rotation axis can be made in either the horizontal or vertical direction (s- or p-polarization).
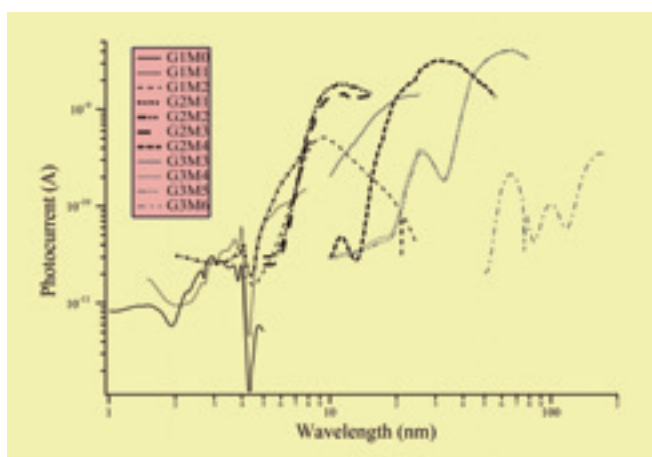
Fig. 1. Throughput spectra for possible combinations of gratings and mirrors at BL5B measured by a gold mesh.
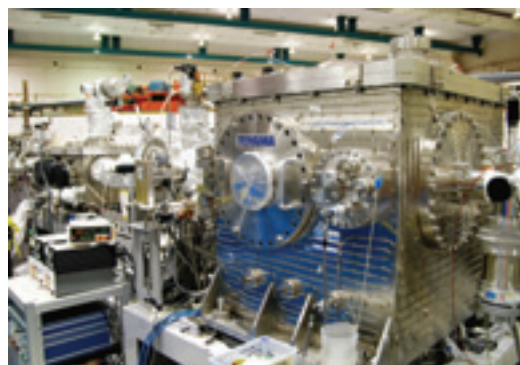

Fig. 2. A side view of the experimental chamber for calibration measurements.

Beamline Specifications

Monochromator	Plane Grating Monochromator
Energy range	6–600 eV (2–200 nm)
Resolution	$E/\Delta E \sim 500$
Experiments	Calibration of optical elements, absorption of solids, photo-stimulated desorption from rare-gas solids

BL6U

Variable-Included-Angle VLS-PGM for Molecular Soft X-Ray Spectroscopy

The beamline BL6U equipped with a variable-included-angle Monk-Gillieson mounting monochromator with a varied-line-spacing plane grating was constructed for various spectroscopic investigations requiring high-brilliance soft X-rays in a gas phase and/or on solids. Through a combination of undulator radiation and sophisticated monochromator design (entrance slit-less configuration and variable-included-angle mechanism), using a single grating, the monochromator can cover the photon energy ranging from 30 to 500 eV, with resolving power of greater than 10000 and photon flux of more than 10^{10} photons/s. Figure 1 shows an example of the monochromator throughput spectra measured using a Si photodiode, with the exit-slit opening set at 30 μm, which corresponds to the theoretical resolving power of 10000 at 80 eV.
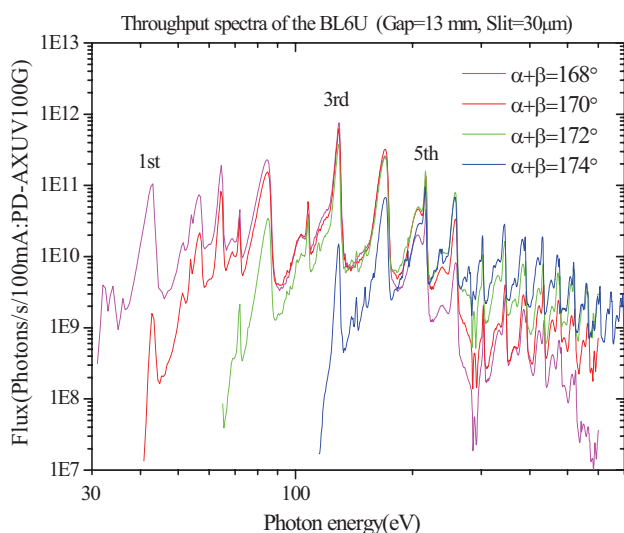
Fig. 1. Throughput spectra of the BL6U monochromator at various included angles.
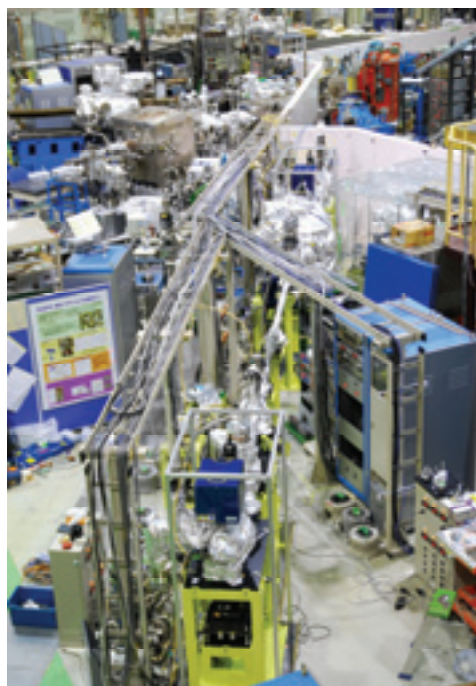

Fig. 2. Photo of BL6U

Beamline Specifications

Monochromator	Variable-included-angle Varied-line-spacing Plane Grating Monochromator
Energy range	40–500 eV
Resolution	$E/\Delta E > 10000$ (at maximum)
Experiments	High-resolution soft X-ray spectroscopy (mainly photoelectron spectroscopy for gaseous and solid targets)

BL6B (IR)

Infrared and Terahertz Spectroscopy of Solids

SR has good performance (high brilliance and high flux) not only in the VUV and SX regions but also in the infrared (IR) and terahertz (THz) regions. BL6B covers the IR and THz regions. The previous beamline BL6A1 that was constructed in 1985 was the pioneer of infrared SR research. The beamline was terminated at the end of FY2003 and a new IR/THz beamline, BL6B (IR), was constructed in FY2004. The front-end part, including the bending duct #6, was replaced with a new one with a higher acceptance angle (215 (H) × 80 (V) mrad^2) using a magic mirror, as shown in Fig. 1 [1]. The brilliance and photon flux at the sample were markedly improved.

The beamline is equipped with two interferometers, one is Michelson type (Bruker Vertex 70v) and the other is Martin–Puplett type (JASCO FARIS-1), which cover the wide spectral region from 5 to 30,000 cm^{-1} ($h\nu = 0.6$ meV–3.7 eV), as shown in Fig. 2. There are two end-stations: one is reflection/absorption spectroscopy for large samples (several millimeters) and the other is IR/THz microscopy for tiny samples (several tens of micrometers).

[1] S. Kimura, E. Nakamura, T. Nishi, Y. Sakurai, K. Hayashi, J. Yamazaki and M. Katoh, Infrared Phys. Tech. **49** (2006) 147.
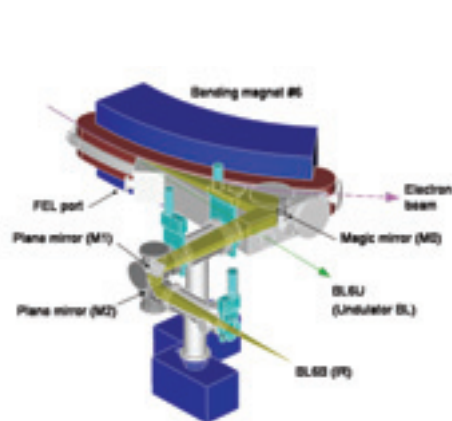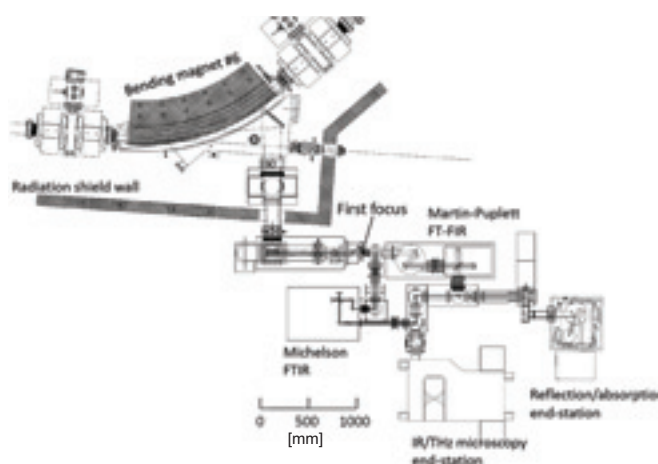
Fig. 1. The design of optics and front end of BL6B.

Fig. 2. Schematic figure of top view of BL6B.

Beamline Specifications

Interferometer	Michelson (Bruker Vertex 70v), Martin-Puplett (JASCO FARIS-1)
Wavenumber Range (Energy range)	5–30,000 cm^{-1} (0.6 meV–3.7 eV)
Resolution in cm^{-1}	0.1 cm^{-1} for Vertex 70v 0.25 cm^{-1} for FARIS-1
Experiments	Reflectivity and transmission, microspectroscopy, and magneto-optics
Miscellaneous	User can bring their experimental system in this beamline

BL7U (SAMRAI)

Angle-Resolved Photoemission of Solids in the VUV Region

The beamline BL7U, named Symmetry- And Momentum-Resolved electronic structure Analysis Instrument (SAMRAI) for functional materials, was constructed to provide photon flux with high energy resolution and high flux, mainly for the high-resolution angle-resolved photoemission spectroscopy of solids. An APPLE-II-type variable polarization undulator was equipped for the light source. The undulator can make high-intensity VUV light with horizontal/vertical linear and right/left circular polarization. The undulator light is monochromatized using a modified Wadsworth-type monochromator with three gratings (R = 10 m; 1200, 2400, and 3600 lines/mm optimized at $h\nu$ = 10, 20, and 33 eV). The energy resolution of light ($h\nu/\Delta h\nu$) is more than 10^4 with a photon flux of more than $10^{11} - 10^{12}$ ph/s on samples in the entire energy region.

The beamline has a photoemission end-station that equips a 200-mm-radius hemispherical photoelectron analyzer (MB Scientific AB, A-l analyzer) with a wide-angle electron lens and a liquid-helium-cooled cryostat with a 6-axes pulse motor control (A-VC Co. Ltd., i-GONIO). The main purpose is to determine the three-dimensional Fermi surface and electronic structure of solids at low temperatures and their temperature dependence in order to reveal the origin of the physical properties.
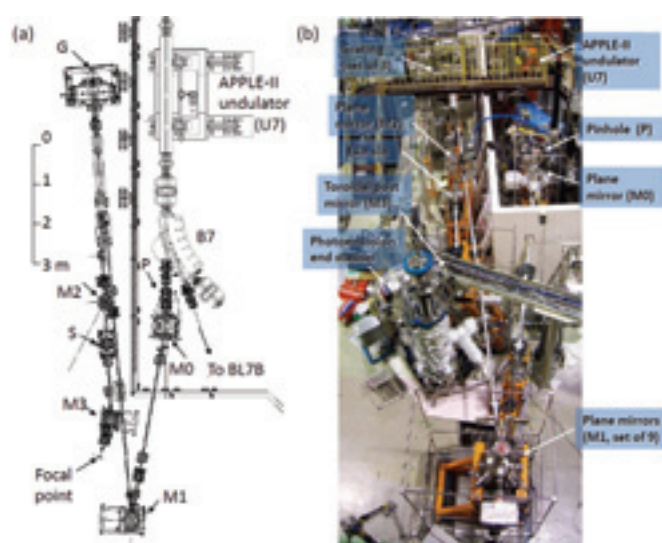

Fig. 1. Layout (a) and photograph (b) of the SAMRAI beamline consisting of the APPLE-II type undulator (U7), the modified Wadsworth-type monochromator (M0 – S), and the high-resolution photoemission analyzer at the focal point. The monochromator has five main optical components: two plane mirrors (M0 and M1) with water cooling, one set of three spherical gratings (G), an exit slit (S), and one toroidal refocusing mirror (M3). The spherical gratings with a radius of 10 m are located 22 m from the center of the undulator. There is no entrance slit. S is located 6.47 m from G. A second branch for a VUV microscope end-station is planned to be constructed after the plane mirror (M2) located between G and S.

Beamline Specifications

Light source	APPLE-II-type undulator (λ_u = 76 mm, N = 36)
Monochromator	10-m Normal Incidence Monochromator (modified Wadsworth type)
Photon energy range	6–40 eV (λ = 30–200 nm)
Resolution ($h\nu/\Delta h\nu$)	1×10^4–5×10^4
Photon flux on sample	$\geq 10^{12} - 10^{11}$ ph/s (depends on $h\nu$)
Beam size on sample	200 (H) × 50 (V) μm^2
Experiments	Angle-resolved photoemission of solids (MB Scientific A-1 analyzer)

BL7B

3-m Normal Incidence Monochromator for Solid-State Spectroscopy

BL7B has been constructed to provide sufficiently high resolution for conventional solid-state spectroscopy, sufficient intensity for luminescence measurements, wide wavelength coverage for Kramers–Kronig analyses, and minimum deformation to the polarization characteristic of incident synchrotron radiation. This beamline consists of a 3-m normal incidence monochromator, which covers the vacuum ultraviolet, ultraviolet, visible, and infrared, i.e., the wavelength region of 40–1000 nm, with three gratings (1200, 600, and 300 l/mm). Two interchangeable refocusing mirrors provide two different focusing positions. For the mirror with the longer focal length, an LiF or a MgF$_2$ window valve can be installed between the end valve of the beamline and the focusing position. Fig.1 shows the absolute photon intensity for each grating with the entrance and exit slit openings of 0.5 mm. A silicon photodiode (AXUV-100, IRD Inc.) was utilized to measure the photon intensity and the absolute photon flux was estimated, taking the quantum efficiency of the photodiode into account.
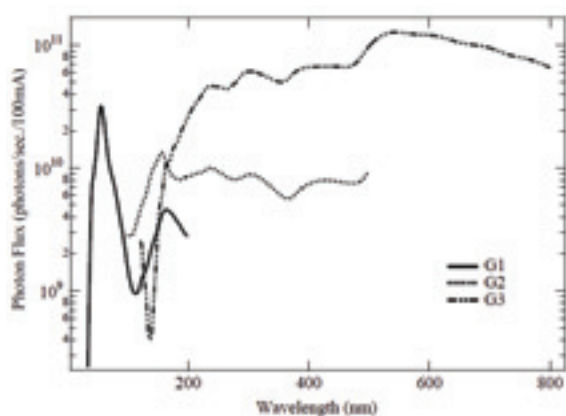

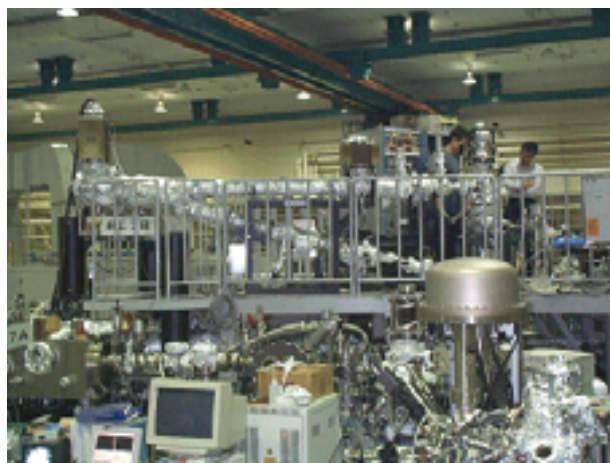Fig. 1.   Throughput spectra of BL7B measured using a silicon photodiode.

Fig. 2.   Photo of BL7B.

Beamline Specifications

Monochromator	3-m Normal Incidence Monochromator
Wavelength Range	50–1000 nm (1.2–25 eV)
Resolution	$E/\Delta E$ = 4000–8000 for 0.01 mm slits
Experiments	Absorption, reflection, and fluorescence spectroscopy, mainly for solids

BL8B

Angle-Resolved Ultraviolet Photoelectron Spectrometer for Solids

BL8B is a beamline for the angle-resolved ultraviolet photoemission spectroscopy (ARUPS) system, which is designed to measure various organic solids such as molecular crystals, organic semiconductors, and conducting polymers. This beamline consists of a plane-grating monochromator (PGM), a sample preparation chamber with a fast-entry load-lock chamber, a measurement chamber (base pressure 1×10^{-10} Torr), a cleaning chamber (base pressure 1×10^{-10} Torr), and a sample evaporation chamber (base pressure 3×10^{-10} Torr). The cleaning chamber is equipped with a back-view LEED/AUGER, an ion gun for Ar^+ sputtering, and an infrared heating unit. The PGM consists of premirrors, a plane grating, focusing mirror, and a post-mirror, with an exit slit. It covers the wide range from 2 to 130 eV with two exchanging gratings (G1: 1200 l/mm, G2: 450 l/mm) and five cylindrical mirrors. The toroidal mirror focuses the divergent radiation onto the sample in the measurement chamber. The spot size of the zeroth-order visible light at the sample surface is approximately 1×1 mm^2. Figure 1 shows the throughput spectra of PGM (slit = 100 μm). The energy resolution at a slit width of 100 μm was found to be $E/\Delta E = 1000$ in the wavelength range from 2 to 130 eV. A hemispherical electron energy analyzer of 75 mm mean radius with an angular resolution less than 2° can be rotated around the vertical and horizontal axes. The sample mounted on a manipulator (temperature range 14–320 K) can also be rotated around two axes.
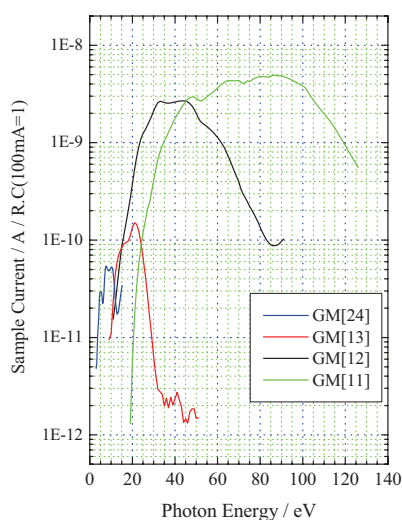

Fig. 1. Throughput spectra of plane-grating monochromator at BL8B2 (slit = 100 μm).

Fig. 2. A photo of BL8B2.

Beamline Specifications

Monochromator	Plane-grating monochromator
Wavelength Range	9–600 nm
Resolution	$E/\Delta E = 1000$
Experiments	Angle-resolved ultraviolet photoemission spectroscopy

FEL

Free Electron Laser

The free electron laser (FEL) at UVSOR-II is parasitically installed at BL5U. The FEL is equipped with a variably polarized optical klystron of 2.35 m in length and an optical cavity of 13.3 m in length. By using various multi-layer mirrors for the cavity, the FEL can provide coherent light in a wide wavelength range from 800 nm to 199 nm. The pulse width is typically several picoseconds. The repetition rate is approximately 11 MHz. The average output power depends on the wavelength but its typical value is several hundred milliwatts. Output power higher than 1W was recorded at 230 nm and 570 nm. The FEL can be operated in a top-up injection mode. Users can use the FEL for several hours with quasi-constant output power. The laser pulses are naturally synchronized with the synchrotron radiation pulses that are provided at other synchrotron radiation beam-lines. The laser beam can be transported to the beam lines by using a mirror system for pump and probe experiments if requested.

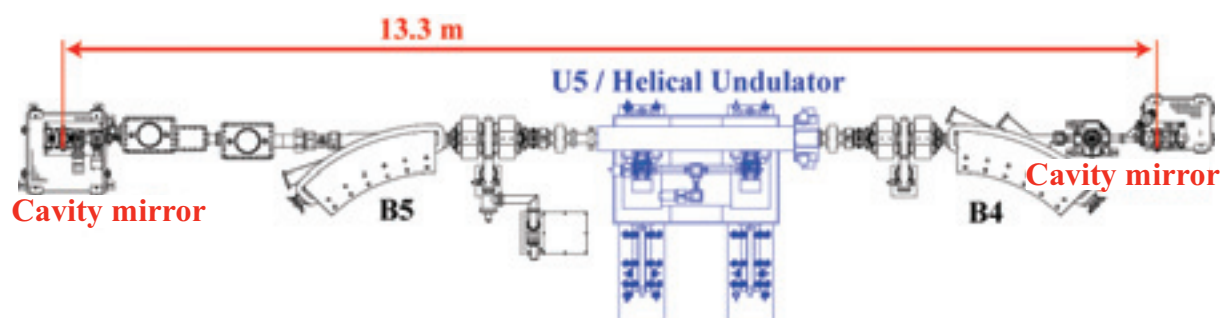The FEL system will be moved to a dedicated long straight section (S1) in fiscal year 2011.

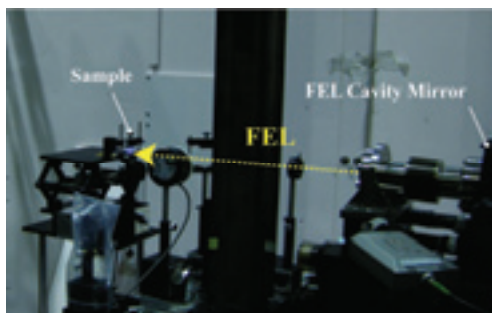Fig. 1. The schematic of the 13.3-m-long optical cavity.

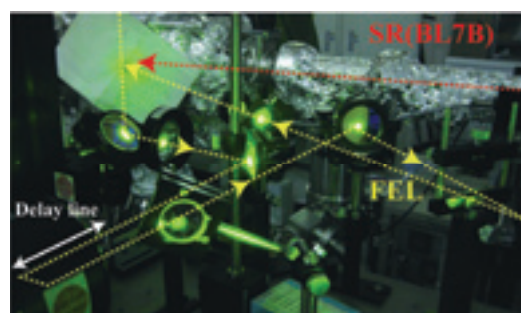Fig. 2. Left and right circular-polarized FEL is delivered to B4.

Fig. 3. The FEL is delivered to BL7B. The FEL is irradiated on a target simultaneously with the SR.

FEL Specifications

Wavelength	199−800 nm
Spectral Band Width	$\sim 10^{-4}$
Polarization	Circular / Linear
Pulse Rate	11.26 MHz
Max. Average Power	~1 W
Cavity Type	Fabry-Perot
Cavity Length	13.3 m
Cavity Mirror	HfO_2, Ta_2O_5, Al_2O_3 multi-layer

Ⅱ. CURRENT STATUS OF
LIGHT SOURCES
AND BEAMLINES

Correction of Dynamic Multipoles for APPLE-II Undulator with Flat Wires

Y. Kikuchi[1], M. Hosaka[1], N. Yamamoto[1], Y. Takashima[1], M. Adachi[2], H. Zen[2] and M. Katoh[2]

[1]*Graduate School of Engineering, Nagoya University, Nagoya 464-8603, Japan*
[2] *UVSOR Facility, Institute for Molecular Science, Okazaki 444-8585, Japan*

Introduction

APPLE-II undulator can produce quasi-monochromatic light of variable polarization though its magnetic circuit is relatively simple. Therefore, it has been installed in many synchrotron radiation facilities and will be installed in Central Japan Synchrotron Radiation Research Facility under construction in Aichi prefecture.

APPLE-II undulator also has been installed in UVSOR-II electron storage ring [1]. When the undulator is operated in vertical polarization mode with narrower gap than 40 mm, the lifetime of electron beam circulating in the storage ring significantly decreases. The reason is considered as dynamic multipole kicks in the undulator, which strongly depends on the undulator gap. At UVSOR-II, multi-wires [2], which are glued in the upper and lower surface of undulator beam duct, are candidate to compensate the multipole effects. In order to evaluate the validity of this method, we numerically studied the dynamic multipoles of the undulator and experimentally examined the correction capability of multi-wires.

Numerical Study on Dynamic Multipoles

In order to evaluate dynamic multipoles generated in the undulator operated in vertical polarization mode, we calculated the relation between the horizontal beam injection point x and the horizontal beam angle in undulator terminus x' using a 3D magnetostatic code RADIA [3]. The result is shown in Fig.1. The quadrupole magnetic field is strong within x = ±5 mm and the higher order multipole magnetic field is strong in the other range. Expected multipole kick with multi-wire correction is also shown in Fig.1 as red line. Since the amplitude of multipole kick is comparative with that of 40-mm-gap condition, we expected significant improvement of the electron beam lifetime with the correction method.

Experimental Examination

Multi-wires were installed in APPLE-II undulator in UVSOR-II (Fig. 2) and we tested the effect of multipole correction on the beam lifetime. The result is shown in Table 1. When the multipoles were corrected by the multi-wires, the electron beam lifetime is significantly improved than that without correction. This multi-wires will enables us to use the undulator with vertical and narrow gap condition. Such operational condition is quite important for angle-resolved photoelectron spectroscopy application of APPLE-II undulator.
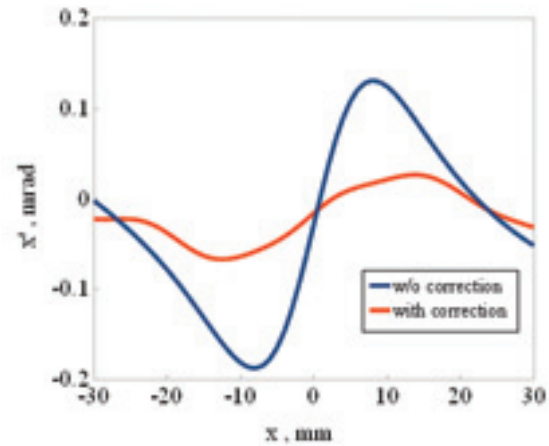

Fig. 1. The relation between x and x', when the undulator gap is operated with 30 mm gap and vertical polarization mode. (Blue:Without correciton, Red:With correction).

Fig. 2. Multi-wires installed in APPLE-II undulator.

Table 1. Result of correction of multipole field with multi-wires.

Gap [mm]	Beam liftime [mA hr]	
	W/o correction	With correction
100	300	—
30	100	290

[1] UVSOR Activity Report **37** (2010) 12.
[2] J. Bahrdt *et al*., Proceedings of EPAC08 (2008) 2222.
[3] P. Elleaume *et al*., Proceedins of PAC97 (1997) 3509.

III-1. ACCELERATORS AND LIGHT SOURCES

Laser-Power-Dependence of Coherent THz Radiation from Electron Bunches Circulating in a Storage Ring

N. Yamamoto[1], M. Shimada[2], M. Adachi[3,4], H. Zen[3,4], T. Tanikawa[4], Y. Taira[1], S. Kimura[3,4], M. Hosaka[1], Y. Takashima[1], T. Takahashi[5] and M. Katoh[3,4]

[1]*Graduate School of Engineering, Nagoya University, Nagoya 464-8603, Japan*
[2]*High Energy Accelerator Research Organization, KEK, Tsukuba 305-0801, Japan*
[3]*UVSOR Facility, Institute for Molecular Science, Okazaki 444-8585, Japan*
[4]*School of Physical Sciences, The Graduate University for Advanced Studies (SOKENDAI), Okazaki 444-8585, Japan*
[5]*Research Reactor Institute, Kyoto University, Kumatori 590-0494, Japan*

Introduction

In order to study in detail the formation of the micro-structure in electron bunches, we have performed laser slicing experiments at the UVSOR-II electron storage ring. Coherent synchrotron radiation (CSR) in the THz region, which contains information on the micro-structure, was observed under various laser energies.

Experiments

The intensity of the THz light was measured by an InSb hot-electron bolometer (QMC, QFI/2) and the spectrum was analyzed at the IR/THz beamline (BL6B) using an in-vacuum Martin–Puplett interferometer (JASCO, FARIS-1), which was used to measure the spectra in the 2–50 cm^{-1} range with a resolution of 1 cm^{-1}. Pulse processing for the CSR measurement was done using a gated integrator (SRS, SR250) to reduce the back ground from normal SR. The gated integrator was triggered by a 1-kHz repetition signal of the laser system, and a width of about 5 μs was chosen. In our measurements, the THz light intensity was evaluated to be 10^4–10^5 times larger than that of normal SR.

Results and Discussion

CSR spectra shown in Fig. 1 were taken for four different laser energies —2.0, 1.5, 1.0, and 0.5 mJ— with same laser pulse duration of 322 fs. The measured spectra are divided by that of normal SR in order to exclude the sensitivity dependence of the bolometer. Each spectrum has two peaks in different frequency ranges. The peaks in the higher and lower frequencies correspond to CSRs emitted in the first turn and in the second turn of the storage ring. Since the temporal resolution of the detector is about 1 μs and the spectra were time-averaged, it cannot resolve the emission from each turn. The measured double peak can be explained as a multi-turn effect [1].

As the laser energy increases, especially for the peak in the higher frequency range, the peaks shift to the lower frequency component increases gradually. The difference in spectral shape with different laser energies arises from the growth of the micro-structure in electron bunches. The dip structure becomes larger and wider as the laser energy increases, and this leads to an increase in the lower-frequency components.
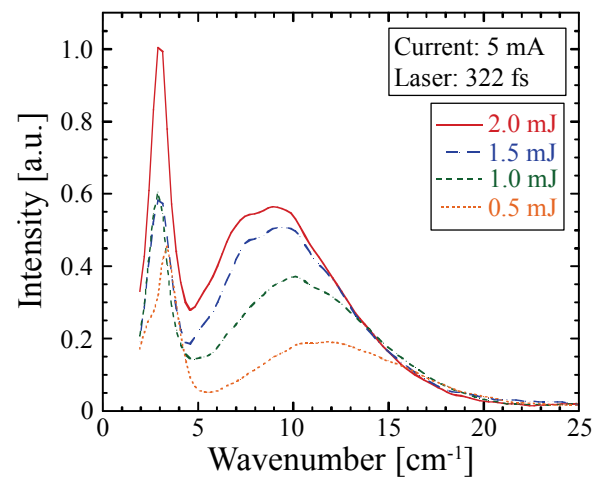

Fig. 1. THz CSR spectra with different energies of slicing laser pulse introduced.

Conclusions

The formation of micro-structure in electron bunches by the laser slicing technique was experimentally studied. The THz CSR spectra were measured for various laser energies. The measured spectra have double-peak structure, which can be attributed to the contributions of the first and second turns. The spectral shape depends strongly on the laser parameters.

The THz CSR spectra were compared with numerical calculations. The spectral shapes agree with the numerical calculations qualitatively, but some discrepancies in the wave number remains. Details of those results are described in Ref. [2].

[1] M. Shimada, *et. al*., Phys. Rev. Lett. **103** (2009) 144802
[2] N. Yamamoto, *et. al.*, Nuclear Instruments and Methods in Physics Research A, in press.

Practical Introduction of Vertical Beam Position Feedback System

H. Zen[1], K. Hayashi[1], M. Adachi[1], N. Yamamoto[2], J. Yamazaki[1] and M. Katoh[1]

[1]*UVSOR Facility, Institute for Molecular Science, Okazaki 444-8585, Japan*
[2]*Graduate School of Engineering, Nagoya University, Nagoya 464-8603, Japan*

Introduction

In 2008, an orbit feedback system was developed for stabilizing the vertical electron beam position in the UVSOR-II storage ring [1]. Then, it was confirmed that the feedback system could suppress the slow drift of the vertical beam position. In this fiscal year, we have introduced the feedback system to user operations with a modification of the system.

Feedback System

The feedback system consists of 24 Beam Position Monitors (BPMs), 16 Steering Magnets (SMs) and control PCs. Firstly, the electron beam orbit was measured by the BPMs, which measures the beam position at 24 points of the ring. Secondly, control PCs calculates the applicable strength of SMs, which minimizes the displacement of orbit. Finally, strength of SMs is changed according to the calculated values. This system minimizes the displacement of electron beam along the storage ring.

Result of Test Operation

During night operations, usually done from Thursday night to Friday morning, we carried out some test operations of the orbit feedback system before introducing the system to normal user operation. A result of test operation is shown in Fig. 1. We found that the feedback system caused sudden orbit change shown in Fig. 1. At the same time, sudden intensity change of synchrotron radiation was observed in user beamlines. The origin of sudden orbit change was determined as a lack of resolution of SMs, whose minimum variation of the beam position is around 4 µm. Therefore, we made a modification on the system to have higher resolution.
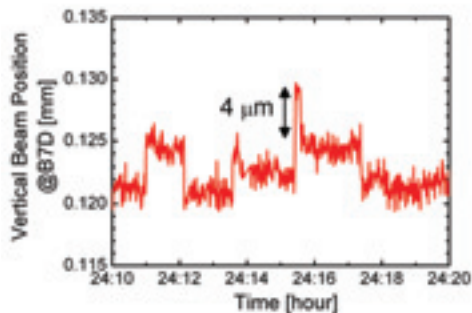
Improvements

To improve the resolution, we newly added 100-turn coils to outside of the SMs. And for the power supply of the additional coil, DC power supplies (KIKUSUI, PMC-18-2A) were introduced. We also installed a 12 bit ADC board (INTERFACE, PCI-3341A) for controlling the new power supplies. The achieved resolution of the beam position with the improved system is around 0.15 µm. After installation, it was confirmed that the improved system did not make sudden orbit change.

Fig. 2. Photographs of additional equipments. Left: Additional small coil around the steering magnet. Right: Remotely controllable DC power supply.

Introduction to User Operation

The improved orbit stabilization system has been introduced to user operations since December 2010. A typical temporal evolution of the vertical beam position during 36-hour operation is shown in Fig. 3. As shown in the figure, the drift of vertical beam position is drastically suppressed by the feedback control. And the orbit feedback system may contribute to suppress the photon energy variation in user beamlines and to achieve higher reproducibility of user experiments.

Fig. 1. Temporal evolution of vertical beam position during a test operation of the orbit feedback system.
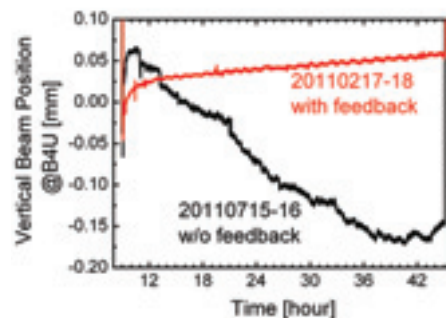

Fig. 3. Temporal evolution of vertical electron beam position at the downstream of bending magnet No. 4.

[1] Y. Suzuki *et al.*, UVSOR Activity Report **36** (2009) 32.

Ⅲ-1. ACCELERATORS AND LIGHT SOURCES

Stabilization of the Accelerated Charge of UVSOR-II Injector

H. Zen, K. Hayashi, J. Yamazaki, M. Adachi and M. Katoh

UVSOR Facility, Institute for Molecular Science, Okazaki 444-8585, Japan

Introduction

In fiscal year 2009, a stabilization system for injection septum of UVSOR-II booster synchrotron has been developed [1]. By using the system, the stability of accelerated charge in the synchrotron was drastically improved. However, we found another source of fluctuation of the accelerated charge, which was fluctuation of the RF power fed to the linac of UVSOR-II injector. In this fiscal year, we added feed-forward system for stabilizing the accelerated charge of the injector.

Principle of Stabilization Method

The energy gain of an RF Linac can be described in the formula,

$$\delta E_{kin} = A\sqrt{P_0} - BI_b , \qquad (1)$$

where δE_{kin} is the energy gain, P_0 is the fed power to the linac, I_b is the averaged electron beam current injected to the Linac, A and B are constant. The best way to stabilize the energy gain is stabilize the fed power and beam current. However, we don't have remote control for the fed power. Thus we decided to vary the averaged beam current for stabilizing the energy gain.

Feed-Forward System

The schematic diagram of developed feed-forward system is shown in Fig. 1. In this system, strength of the solenoid coil between the electron gun and linac is used for changing the average beam current (I_b) injected to the linac. Amplitude of fed RF power (P_0) to the linac is measured with an RF detector and an oscilloscope. The measured waveform is sent to control PC, which determines the optimum excitation current of solenoid coil from a look-up table or an equation.
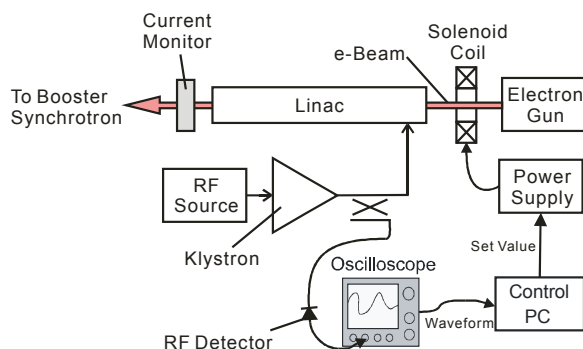
The relationship between the measured RF power and the optimum excitation current of solenoid coil was experimentally obtained. It was found that the optimum current had quadratic dependence on the measured RF power.

Results

The results of 12-hour top-up operation are shown in Figs. 2. According to the changes of RF power fed to the Linac, the excitation current of the solenoid coil was controlled as shown in Fig. 2 (a). Then the accelerated charge in the booster synchrotron was kept more than 0.4 nC for 12 hours. This value corresponding to the injected rate of 6.1 mA/minute in the case of extraction efficiency = 30%, injection efficiency = 70% and maximum number of injection in one minute = 13. At the same time, the stored beam current in UVSOR-II storage ring was kept almost constant around 300 mA.

This feed-forward system is now always running during user operations for stabilizing the accelerated charge in the synchrotron.
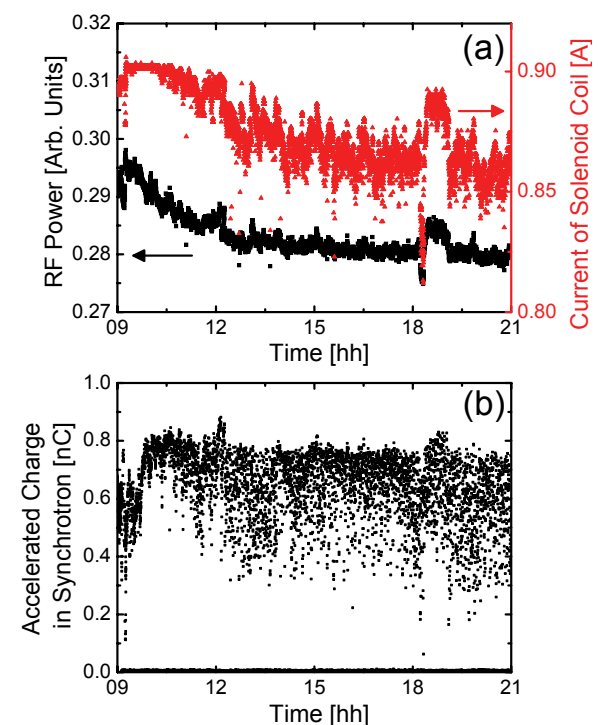

Fig. 2. Temporal evolution of the RF power, excitation current of solenoid coil and accelerated charge in the synchrotron.

Fig. 1. Schematic diagram of feed-forward system.

[1] H. Zen *et al.*, UVSOR Activity Report **37** (2010) 35.

Stabilization of Pulsed Kickers for Creating Injection Bump Orbit in UVSOR-II Storage Ring

H. Zen, K. Hayashi, J. Yamazaki, M. Adachi and M. Katoh

UVSOR Facility, Institute for Molecular Science, Okazaki 444-8585, Japan

Introduction

Injection of UVSOR-II storage ring is done with three pulsed dipole magnets (kickers) and creating bump orbit near the injection point. The height and timing of those kickers have large drift. Such large drift changes the amplitude of bump orbit, which causes decreasing of injection efficiency or electron beam dump. For stable top-up operation of UVSOR-II, the amplitude of bump orbit should be stabilized. Therefore a feedback system to stabilize the pulsed kickers was developed.

Feedback System

Figure 1 shows the schematic diagram of the developed feedback system. By using an oscilloscope, the excitation current signals of the bump kickers are measured as shown in Fig. 2. The oscilloscope is triggered with an external trigger which generated by a digital delay generator (DG535). We set a threshold level to determine the timing of the kicker and recognized that the operational timing of the kicker is the timing when the current waveform crossing the threshold level as shown in Fig. 2. And the pulse height of the kicker is recognized as the maximum value of the waveform as shown in Fig. 2. In the control PC, measured timing and amplitude are compared with ordered timing and amplitude which are given by machine operators. Based on PID algorithm, the control PC calculates the optimum delay and charging voltage of the kicker. Those values are sent to DG535 and power supply of the kicker.

Since the oscilloscope and DG535 have 4 channels, three bump kickers are controlled by one oscilloscope, one DG535 and one control PC at the same time.

Results

Figure 3 shows the result of feedback control. By properly changing the control value of charging voltage of power supply of the kicker and delay of trigger signal of the kicker, we succeeded in stabilizing the pulse height and operational timing of the kicker.

Though the height and timing of all kickers are stabilized, the injection efficiency of the UVSOR-II ring is not so stable. To keep high injection efficiency, we should slightly vary the strength of steering and focusing magnets of beam transport line between the ring and injector. Counter measures for the fluctuation will be developed near future.
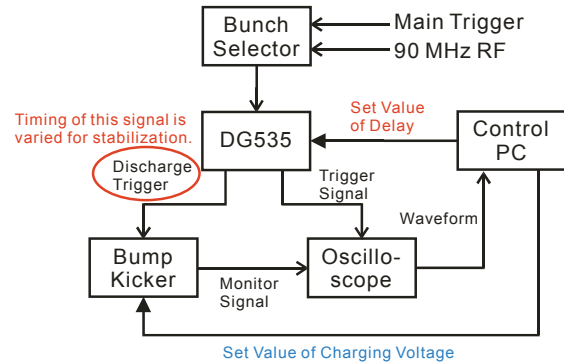

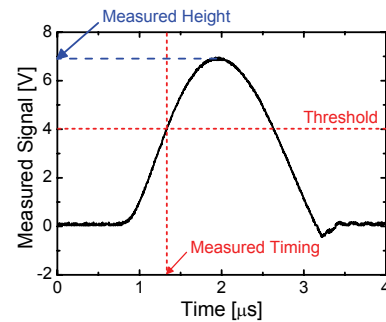Fig. 1. Schematic diagram of the developed feedback system.

Fig. 2. Typical waveform of excitation current of a pulsed kicker.
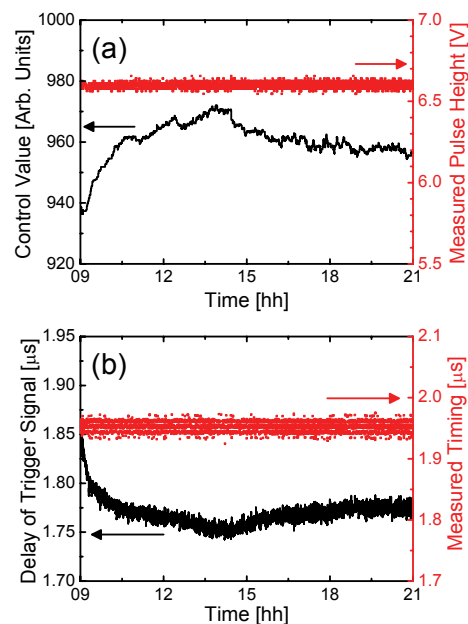

Fig. 3. Temporal evolution of operational condition of a pulsed kicker, (a) control value of charging voltage of the kicker and measured pulse height, (b) delay of discharge trigger signal and measured operational timing of the kicker.

Accelerators

Timing Stabilization of Extraction Kicker of UVSOR-II Injector

H. Zen, K. Hayashi, M. Adachi, J. Yamazaki and M. Katoh

UVSOR Facility, Institute for Molecular Science, Okazaki 444-8585, Japan

Introduction

From this fiscal year, we have started top-up operation of UVSOR-II storage ring during all user operation. In usual operation, 14 buckets of UVSOR-II storage ring are filled by electrons and remained 2 buckets are empty in order to prevent instability caused by ion trapping in the ring [1]. For keeping 2 empty buckets during long time top-up operation, we developed a feedback system for stabilizing the timing of extraction kicker of UVSOR-II injector.

Extraction Scheme and Problem

A fast kicker and an extraction septum are used for extracting electron bunches from UVSOR-II injector, 750 MeV booster synchrotron. At first, the fast kicker suddenly changes the electron beam orbit in the injector. Then 4 bunches in 8 circulating bunches are successfully injected to the extraction septum. Those bunches are bent in the septum and transported to the ring. For filling 14 buckets of the storage ring, the timing of the fast kicker is properly controlled. Although the trigger signal sent to the fast kicker is well controlled, the operational timing of the kicker has long term drift of larger than 40 ns, which corresponds to time interval of 4 buckets. To reduce the drift, a feedback system was developed.

Developed Feedback System

The diagram of the feedback system is shown in Fig. 1. By using an oscilloscope, the excitation current signals of the fast kicker are measured as shown in Fig. 2. The oscilloscope is triggered with the external trigger which generated by a digital delay generator (DG535). We set a threshold level to determine the timing of the kicker and recognized that the extraction timing of bunches is the timing when the current waveform crossing the threshold level as shown in Fig. 2. In control PC, the extraction timing is compared with the ordered timing which is given by machine operators. The control PC calculates the optimum delay of DG535 based on PID algorithm, and sends commands to set the timing delay of DG535 to the calculated delay.

Results

Figure 3 shows the result of feedback control. The fast kicker timing was stabilized around 90 ns, which was the ordered timing of this operation. Then the timing jitter was around 3 ns in FWHM. Figures 4 show the waveforms of bunch pick-up signal after 12-hour top-up operation. As shown Fig. 4 (a), all buckets were filled by electrons without the feedback system. In contrast, we succeeded in keeping the 2 empty buckets with the feedback system as shown in Fig. 4 (b).
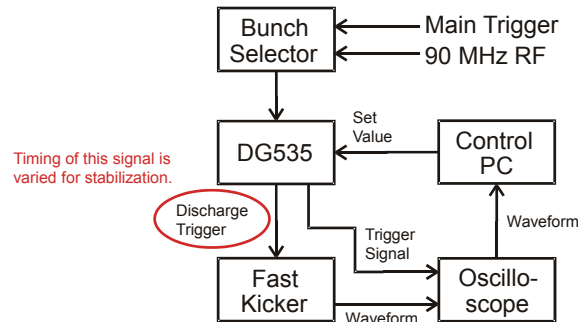

Fig. 1. Diagram of the timing feedback system for the fast kicker.
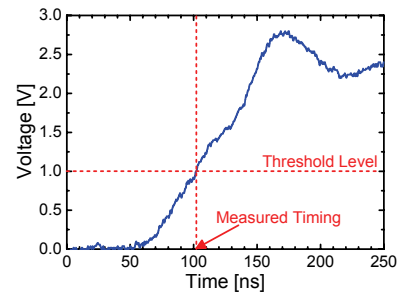

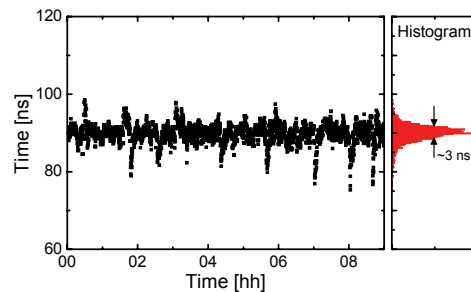Fig. 2. Way to determine the operational timing of the fast kicker.

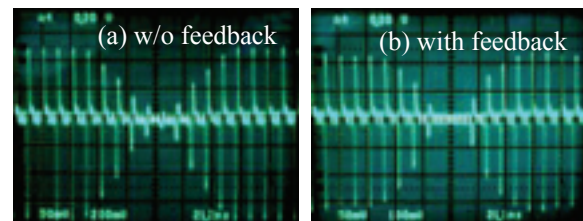Fig. 3. Temporal evolution of operational timing of fast kicker with developed timing feedback system.

Fig. 4. Photographs of an analog oscilloscope showing an electron bunch pick-up signal after 12-hour top-up operation without (a) and with (b) the timing feedback for the fast kicker.

[1] J. M. Byrdt *et al.*, SLAC-PUB-7389 (1996).

Experiments on the Narrowband Coherent Synchrotron Radiation

M. Hosaka[1], Y. Takashima[1], C. Evain[2], C. Szwaj[2], S. Bielawski[2], M. Shimada[3],
A. Mochihashi[4], Y. Takahashi[5], S. Kimura[6] and M. Katoh[6]

[1]*Graduate School of Engineering, Nagoya University, Nagoya 464-8603, Japan*
[2]*Université des Sciences et Technologies de Lille, Villeneuve d'Ascq Cedex, France*
[3]*High Energy Accelerator Research Organization, KEK, Tsukuba 305-0801, Japan*
[4]*Japan Synchrotron Radiation Research Institute (JASRI), SPring-8, Sayo-cho,
Hyogo 679-5198, Japan*
[5]*Research Reactor Institute, Kyoto University, Osaka 590-049, Japan*
[6]*UVSOR Facility, Institute for Molecular Science, Okazaki 444-8585, Japan*

Narrowband terahertz coherent synchrotron radiation can occur from an electron bunch whose longitudinal distribution is sinusoidaly modulated. We have already demonstrated this by creating the modulation using interaction inside an undulator between the electron beam and laser pulse containing a sinusoidal amplitude modulation: the resulting narrowband terahertz spectra were observed using a Martin-Pupplett Fourier transform far infra-red spectrometer [1]. In this paper, we report a detail study on the emission, focusing on the efficiency dependence on modulation (or resulting coherent synchrotron radiation) frequency and laser power.

The experimental setup is the same as that we used previously [1], but we simplify the laser pulse shaping system. Instead of using a pair of gratings to achieve dispersion, we extract the pulse of our regenerative amplifier just before the compressor, and send it to a Michelson interferometer. The major improvement over the previous system is higher pulse energy and wider tuning range of the modulation frequency.

To investigate the efficiency dependence of the coherent terahertz emission on the modulation frequency, we recorded the emission intensity as a function of the modulation frequency by changing the Michelson interferometer position. At the same time, we measured the spontaneous synchrotron radiation spectrum using the same setup in order to take into account the frequency dependence of the detecting system. The relative efficiency is deduced dividing the frequency response by the spontaneous synchrotron radiation spectrum. The result is presented in Fig.1. The broad 20 cm^{-1} peak structure agrees well to theoretical calculations based on a slowly-varying envelope approximation [2]. The low frequency emission (around 3-5 cm^{-1}) is attributed to emission after long transport of the storage ring (one full turn and more).

To investigate the efficiency dependence the coherent terahertz emission on the laser power, we attenuated the laser using a half-wave plate followed by a polarizer. By rotating the half-wave plate, we obtained the dependence of terahertz power with incident laser power [Fig. 2]. This dependence appears to be quadratic with good approximation. The quadratic scaling is generally expected in the limit of low laser powers [2]. However, at higher laser power departure from the scaling law is theoretically prospected [2]. As a next step of this study, we are going to examine the behavior with higher laser energy.

[1] S. Bielawski, *et al*., Nature Physics **4** (2008) 390.
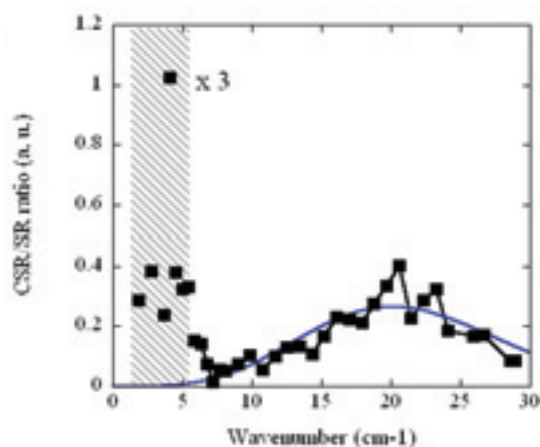[2] C. Evain, *et al*., Phys. Rev. ST Accel. Beams **13** (2010) 090703.

Fig. 1. Ratio between CSR and spontaneous SR versus modulation wavenumber. The blue solid line is theoretically deduced form factor.
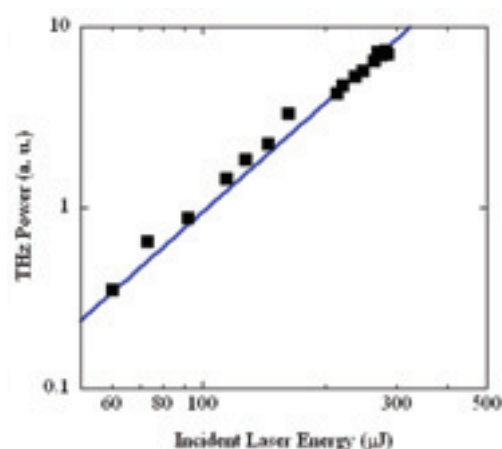

Fig. 2. Terahertz energy versus laser pulse energy. The blue solid line is quadratic law fit.

Generation of Energy-Tunable Gamma Rays via Inverse Compton Scattering in an Electron Storage Ring

Y. Taira[1], M. Adachi[2,3], H. Zen[2,3], T. Tanikawa[3], N. Yamamoto[1],
M. Hosaka[1], Y. Takashima[1], K. Soda[1] and M. Katoh[1,2,3]

[1]*Graduate School of Engineering, Nagoya University, Nagoya 464-8603, Japan*
[2]*UVSOR Facility, Institute for Molecular Science, Okazaki 444-8585, Japan*
[3]*School of Physical Sciences, the Graduate University for Advanced Studies, Okazaki 444-8585, Japan*

Gamma rays in the MeV-region can be generated via inverse Compton scattering of laser photons with a relativistic electron beam of sub-GeV or GeV circulating in an electron storage ring. This technology is called laser Compton scattering (LCS) [1]. LCS gamma rays are tunable in energy, quasi-monochromatic, intense, and high polarized, and are used in nuclear science, positron generation, and electron beam diagnosis.

The methods available for tuning the energy of LCS gamma rays include 1) selecting electron beam energy, 2) selecting the laser wavelength, 3) choosing the scattering angle of the gamma rays using a collimator and an absorber, and 4) controlling the collision angle between a laser and an electron beam. Since LCS experiments were usually carried out at electron storage rings operated with fixed electron energy, method 1) cannot be applied to generate LCS gamma rays of tunable energy.

Ohgaki *et al.* [2] performed analytic calculations and computer simulations on the energy spread and intensity of LCS gamma rays using methods 2) - 4) for a 1.4-GeV electron storage ring. The energy spreads obtained using methods 2) and 4) (1 %) were smaller than the spread obtained using method 3) (7-9 %), and the intensity obtained using method 3) ($\sim 10^5$ photons s^{-1}) was the highest of the three. However, the intensity obtained from method 4) is expected to be increased to $\sim 10^6$ photons s^{-1} when a mode-lock pulse laser was used. Thus Ohgaki *et al.* concluded that method 4) with a mode-lock laser was preferable for generating gamma rays of continuous tunable energy using a laser of fixed wavelength with fixed electron energy.

However, method 4) has never been studied experimentally because LCS gamma rays are usually generated via head-on collision between the electron beam and the laser by injecting the laser through an optical port used for extracting synchrotron radiation. To generate gamma rays of tunable energy using method 4), we installed an optical port in the electron storage ring UVSOR-II which a laser can be injected from the vertical direction with an adjustable collision angle.

Laser pulses of 2.0 W power were provided by a Ti:Sa laser system (COHERENT, LEGEND-HE) synchronized with an RF frequency of the storage ring, 90.1 MHz. The wavelength and the frequency of the laser were 800 nm and 1 kHz, respectively. Gamma rays were detected by an NaI scintillator (1600 cm^3), and the absorption energy was measured.

Experimental data of the absorbed energy spectrum for various collision angles are shown in Fig. 1. Maximum gamma-ray energy and intensity varied in a range from 4 to 9 MeV and from 350 to 850 photons s^{-1}, respectively. It was successfully demonstrated for the first time that the energy of the gamma rays could be tuned by changing the collision angle.
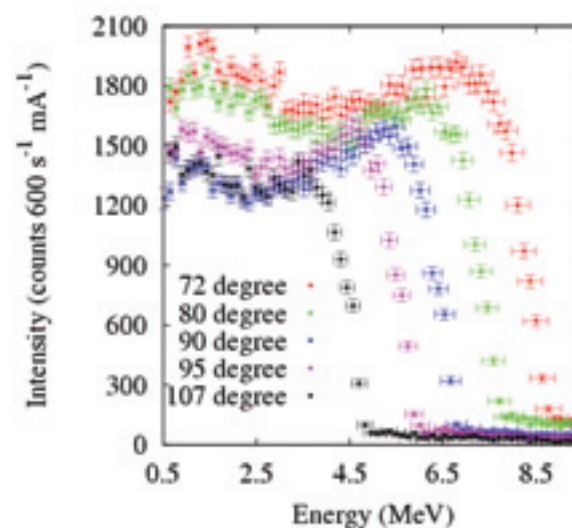

Fig. 1. Experimental data of the energy spectrum for each collision angle listed in the figure. Intensity was standardized by the beam current values. Measurement data of every 100 channels were summed. Error bars in the vertical and horizontal directions are statistical error and energy calibration error, respectively.

[1] J. Stepanek, Nucl. Instr. and Meth. A **412** (1998) 174.
[2] H. Ohgaki, *et al.*, J. Nucl. Sci. and Tech. **44** (2007) 698.

Saturation Phenomena on Coherent Harmonic Generation at UVSOR-II

T. Tanikawa[1], M. Adachi[1,2], H. Zen[1,2], M. Hosaka[3], N. Yamamoto[3], Y. Taira[2,3], J. Yamazaki[2] and M. Katoh[1,2,3]

[1]*The Graduate University for Advanced Studies, Okazaki 444-8585, Japan*
[2]*UVSOR Facility, Institute for Molecular Science, Okazaki 444-8585, Japan*
[3]*Graduate School of Engineering, Nagoya University, Nagoya 464-8603, Japan*

Coherent harmonic generation (CHG) is a method for producing high-order harmonics of a laser light by using a relativistic electron beam. This electron beam interacts with the laser in a sinusoidal magnetic field of an undulator, resulting in microbunching of the electrons at the laser wavelength and in the emission of coherent harmonics (CHs) with a fully coherence, an ultrashort pulse, and a variable polarization [1].

As results of measuring CH spectra by using a vacuum ultraviolet spectrum measurement system constructed in last year at UVSOR-II [2], they have been observed up to 9th harmonic. Figure 1 shows the intensities of the 5th, 7th, and 9th CHs as functions of the peak laser power. Figure 2 shows the intensity of the 5th CH over a wide range of peak laser powers. Dots in Fig. 1 and Fig. 2 represent measured value. In Fig. 1, the CH intensities increase with increasing the peak laser power, reaching a maximum at a value of the power that decreases slightly with the order of the CH. In Fig. 2, the CH intensity oscillates after the maximum.

The dashed and solid curves in Fig. 1 and 2 represent the results of a one-dimensional analytical calculation based on a simple equation for the form factor at each harmonics [3]. The calculation on dashed curve assumes that the longitudinal distribution of the laser is uniform, and that on solid curve assume that the distribution is a Gaussian. As shown in Fig. 1, the calculations reproduced the observed variation in the width and position of the intensity peak for the three harmonics. The peak position shifts to lower peak laser powers with increasing order of the CH. Fig. 2 shows that calculations also reproduced several other peaks observed in the deep saturation regime qualitatively. To understand these results, we carried out a one-dimensional particle tracking simulation of the bunching process in the saturated regime. In Fig. 1, in the case of higher-order CHs, the Fourier component of a longitudinal distribution on the electron beam is largest near the optimal bunching condition, where the bunching is sharpest. However, for lower-order CHs, the Fourier component is largest when the electrons are slightly overbunched because of the contribution of more electrons. For this reason, the lower-order CHs reach their maximum intensity at larger peak laser power. In Fig. 2, the experiments and simulations show several peaks appearing beyond the first maximum, which can be explained by an "additive interference" of the double-peak structure shown in Fig. 3. When the separation of the peaks equals a multiple of the harmonic wavelength, interference produces peaks in the Fourier components, and hence in the CH intensities.

In summary, we have demonstrated that CHG is a useful probe for investigating the formation and evolution of the microbunching caused by laser-electron interactions, which contributes to the next-generation seeded free-electron lasers [4].
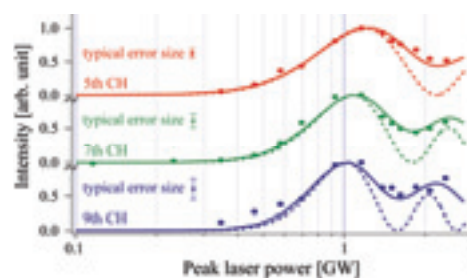

Fig. 1. Measured intensities of the 5th (red), 7th (green), and 9th (blue) CHs plotted as functions of the peak laser power.
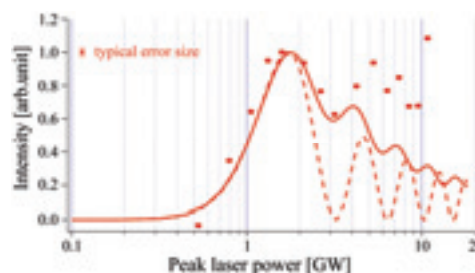

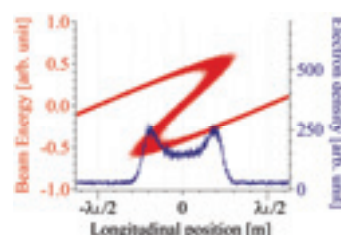Fig. 2. Measured intensity of the 5th CH plotted as a function of the peak laser power.

Fig. 3. Simulation result of the bunching process on the overbunching condition in the OK.

[1] M. Labat *et al.*, Phys. Rev. Lett. **101** (2008) 164803.
[2] T. Tanikawa *et al.*, UVSOR Activity Report **37** (2010) 40.
[3] P. L. Csonka, Part. Accel. **11** (1980) 45.
[4] T. Tanikawa *et al.*, Appl. Phys. Exp. **3** (2010) 122702.

Performance of a High-Precision Transmission Grating for High-Resolution Soft X-Ray Emission Spectroscopy

H. Yamane and N. Kosugi

Dept of Photo-Molecular Science, Institute for Molecular Science, Okazaki 444-8585, Japan

The X-ray emission spectroscopy (XES) is to measure X-rays emitted as a photon-in/photon-out process arising from the decay of the inner-shell excitation and resonant Raman or inelastic scattering. The XES technique combined with the synchrotron radiation is a powerful method to study occupied partial density of states and element-specific excitations of materials. However, a serious problem exists in XES using a reflection grating, that is, a rather low efficiency in detecting emitted X-rays due to (i) the limited number of X-ray focusing optics in the Rowland circle mount (vertical direction only) and (ii) the low acceptance angle and low quantum efficiency at charge coupled devices (CCD) detector with the grazing-incident configuration in the soft X-ray region. Such problems are in general solved by the use of high brilliant X-ray beam of 10^{13} photons/sec. In this case, however, one has to take care of radiation damage, in particular in soft matters.

In order to overcome the above problems, we have developed a new X-ray emission spectrometer based on a transmission grating (TG) at UVSOR BL3U. The spectrometer adopts a novel optical design with a Wolter type I mirror, a free-standing TG, and a back-illuminated CCD, which enables high efficiency and high energy resolution due to an omnidirectional focusing for emitted X-rays and the normal-incident configuration for the CCD detector.

Very recently, we have installed a new TG, which was fabricated by NTT-AT Co. Ltd. In order to achieve the high precision of the TG spectrometer, the new TG is focused on the stability and accuracy of the groove structure. In the high-precision TG, the SiC thickness is about 540 nm, the groove density is 5555 lines/mm (180 nm periods), and the size of the slit is 108 nm at the surface side and 64 nm at the backside as illustrated in Fig. 1. In this report, we show the result of evaluation of the performance for the high-precision TG spectrometer in the energy region of 60–300 eV.

Figure 2 shows an example of resonant XES in the elastic peak region of a LiF(100) single crystal, measured at an incident photon energy $hv = 61.0$ eV. We observed a very sharp elastic peak in the Li Kα spectrum with the full-width at half-maximum of about $\Delta E_{out} = 0.02$ eV, *i.e.*, $E/\Delta E_{out} \sim 3050$. Such a performance has been examined for various photon energies using Si(111), InP(100), CdS(0001), *h*-BN, and HOPG as summarized in Table 1. Note that, the emission intensity is reasonably high for all XES data, e.g., 0.5–1 spectrum/hr. As for the energy resolution, the high precision TG spectrometer shows a high

performance below $hv = 100$ eV with the resolving power of $E/\Delta E_{out} \sim 3000$, which is the advantage in our XES system; e.g., the present spectrometer may offer new insight into the field of Li-based functional materials such as energy-storage devices.
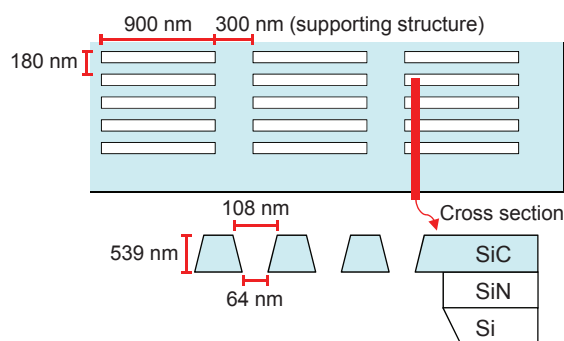

Fig. 1. Scheme of the high-precision transmission grating with the 5555 lines/mm groove density.
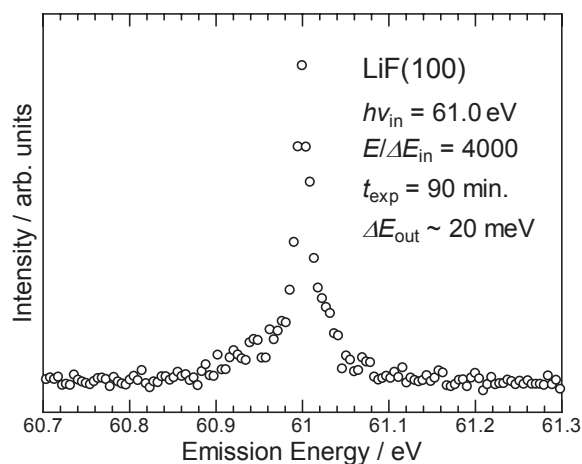

Fig. 2. Elastic peak of the Li Kα XES spectrum ($hv = 61.0$ eV) for the LiF(100) single crystal.

Table 1. Performance of the transmission grating spectrometer with the 5555 lines/mm groove density.

hv / eV	ΔE_{out} / eV	$E/\Delta E_{out}$	Material
61.0	0.02	3050	LiF(100)
100.0	0.03	3333	Si(111)
139.6	0.08	1745	InP(100)
164.1	0.16	1026	CdS(0001)
196.0	0.20	980	*h*-BN
285.5	0.30	952	HOPG

Ⅲ-2. INSTRUMENTAL DEVELOPMENTS

New VIS-VUV Bending Magnet Beamline Design for BL3B

R. Ikematsu[1], K. Fukui[1], T. Ejima[2], E. Nakamura[3], M. Hasumoto[3] and S. Kimura[3]

[1]*Dept. Elec. Elec. Engi, University of Fukui, Fukui 910-8507, Japan*
[2]*IMRAM, Tohoku University, Sendai 980-8577, Japan*
[3]*UVSOR, Institute for Molecular Science, Okazaki 444-8585, Japan*

The solid state optical devices in ultraviolet (UV) region will bring dramatic improvements in not only the telecommunication applications but also the illuminating, environmental and medical applications. To achieve both technological and scientific investigations of these device materials, the light sources which cover wide photon energy region from visible (VIS) to vacuum ultraviolet (VUV) are required. Then, BL3B normal incidence monochromator beamline has been planned for photoluminescence (PL) studies in VIS – VUV regions. This beamline will be constructed as the successor beamline of the BL1B (1-m Seya Namioka type monochromator beamline) which will be shutdown at the end of March 2011. In this report, we present the optical design of a new 2.5-m Eagle type monochromator beamline.

The design parameters for the beamline monochromator dedicated to the PL are usually both the brilliance and the linear polarization degree together with the photon energy coverage, photon flux, resolution and purity. These design specifications of this beamline are as follows; **Photon energy coverage** : $2 \sim 24$ eV, **Photon flux** ($E/\Delta E = 1000$) : $\geq 10^{10}$ photons/sec, **Resolution** ($E/\Delta E$) : ≥ 10000, **Beam spot size** (H × V) : $\leq 0.8 \times 0.8$ mm^2, **Linear polarization degree** (P) : ≥ 0.7.

Figures 1 and 2 show the schematic side view and top view layouts of the BL3B, respectively. The first plane mirror (M_0) only reflects the synchrotron radiation up to increase the design freedom of this beamline optics in a limited area with the radiation shield wall which is located between M_0 and M_1. The

photon flux specification requires 40 mrad horizontal acceptance angle. Then, a toroidal mirror (M_1) has ~ 210 mm width. S (source point) – M_1 to M_1 – S_1 (entrance slit) distance ratio is almost 1:1 to prevent the shape deformation of the focal spot. The M_2 is a plane mirror reflects the light to the x direction (xy plane and y axis are defined as the plane of incidence and the light axis). The roles of M_2 are to give wide space at the sample position (Q) and to cancel the source point (S) horizontal movement under the UVSOR feature version up. An off-plane Eagle type monochromator consists of S_1, G (gratings), and S_2 (exit slit). The focal length is 2.5 m satisfies both the F number matching to the pre-mirror system (M_0 – M_2) and the resolution specification. Three gratings ($G_1 \sim G_3$) with the different glazing angles cover $2 \sim 24$ eV region. The blazing angles and the additional optical filters prevent the higher order lights. The deviation angle of the G is 4 degree. The post-mirror system with Kirkpatrick - Baez optics consists of both spherical mirrors M_3 and M_4 which focus x and z directions, respectively. The reflected light by the M_4 becomes the parallel to the floor. Both the VIS – UV and VUV spectrometers with CCD sensors for the PL measurements will be installed into the sample chamber at Q.

The ray tracing results of this optical configuration are as follows; **Photon flux** ($E/\Delta E = 1000$) : $1 \sim 4 \times 10^{10}$ photons/sec, **Resolution** ($E/\Delta E$) : $12000 \sim 46000$, **Beam spot size** (H × V): 0.5×0.8 mm^2, **Linear polarization degree** (P) : $0.7 \sim 0.8$. This beamline will be constructed within FY2011.

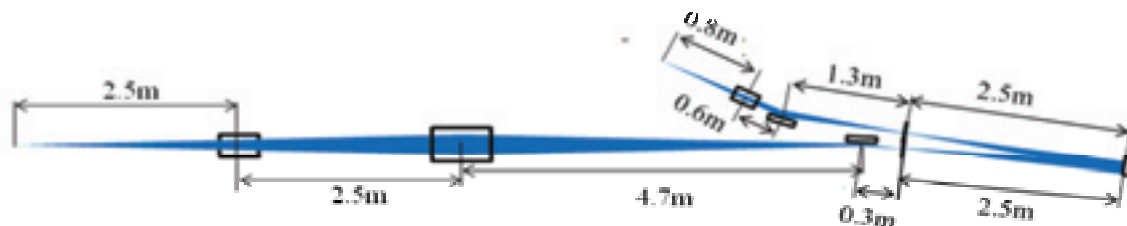Fig. 1. Schematic layout of the BL3B (side view).

Fig. 2. Schematic layout of the BL3B (top view).

Measurement for the Quantum Efficiencies of Microchannel Plates

K. Sakai[1], K. Yoshioka[2], G. Murakami[1], T. Homma[1] and I. Yoshikawa[1]

[1]*Department of Earth and Planetary Science, Graduate School of Science,*
The University of Tokyo, Tokyo 113-0033, Japan
[2]*Department of Physics, Rikkyo University, Tokyo 171-8501, Japan*

Introduction

We are developing the space-based imagers for plasma emissions from the plasmasphere that is torus-shaped dense region filled with plasmas flowing upward from the earth's ionosphere. The main targets of our instruments are the He II and O II ions in the plasmasphere. The He II and O II ions have resonantly scattered emission lines at 30.4 nm and 83.4 nm respectively. Column densities along the field of view of instruments can be obtained because intensities of emissions are proportional to them under the assumption that observational targets are optically thin. Therefore, the accuracies of the detective efficiencies for the instruments are critical for estimation of the densities and to achieve the science goals of our missions. The detective efficiencies are absolutely calibrated at UVSOR.

Microchannel plates (MCPs) detect photons of UV and high-energy particles with incident positions by using position encoder, with extremely low noises. MCPs produce single charge pulses of thousands of electrons via secondary emissions. They have heritages as detectors of the space-based optical instruments. It is essential to obtain the quantum efficiencies (QE) of the MCP for the calculation of the incident intensities. It is commonly used method that photocathodes are deposited to achieve high quantum efficiencies in the spectral range of the ultraviolet. Even in this case, relative QEs of MCPs with photoelectric materials to the bare one are easily measured. Therefore, absolute QEs can be estimated.

In this experiment, the QE of one bare MCP at the wavelength of 30.4 nm is measured. This result leads calibrations of the detectors for various space-based instruments.

Measurement and result

The Al/Mg/Al (744 Å/3958 Å/747 Å) filter and the Sn (1730Å) filter are installed on the entrance of the beam line to achieve the pure 30.4 nm light. The purity is investigated from the consistency between the wavelength characteristics of the Al/C and the Al/Mg/Al sample filters for the light at UVSOR dispersed by the gratings and for the emission line of the RF excited helium gas light at the EUV facilities of Institute of Space and Astronautical Science (ISAS). Fig. 1 shows the transmittances of the Al/C sample filter measured at UVSOR and at ISAS, Fig. 2 shows those of the Al/Mg/Al filter. It is clear that both transmittances of the filter are consistent at 30.4 nm. Therefore, it is shown that the pure 30.4 nm light

is achieved at UVSOR with entrance filters.

With the pure lines, the QE of the MCP detector for the 30.4 nm light is measured. The QEs are calculated by the rate of the MCPs counts to the electron yield of the photo diode which is absolutely calibrated. As a result, the QE of the MCP detector for the 30.4 nm light is 9.83% with the accuracy of 0.41%.

The QE of the MCPs for the 83.4 nm light has to be measured as the future work in addition to the 30.4 nm light. The O II ions have emission line at 83.4 nm and also known as one of main components in the plasmasphere. The pure 83.4 nm light is essential for the measurements and is going to be achieved by using entrance filters and one more UV diffraction grating.
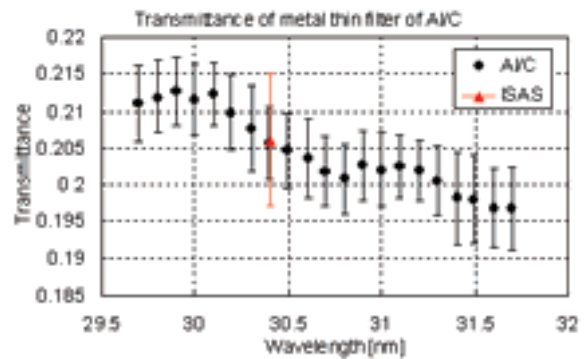

Fig. 1. The transmittances of the Al/C sample filter measured at UVSOR and at ISAS.
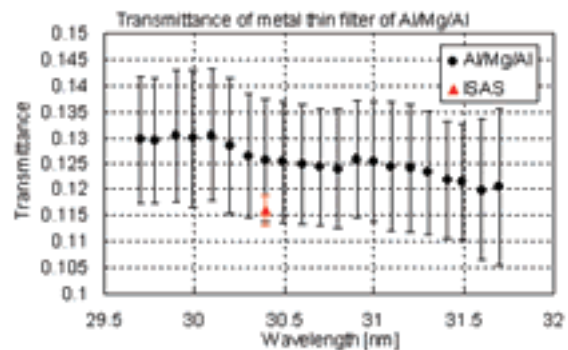

Fig. 2. The transmittance of the Al/Mg/Al sample filter. It is showed that the pure 30.4 nm light is at UVSOR achieved through Al/C filter and the Sn filter as the entrance filters.

Two-Dimensional Electron Spectroscopy on BL6U

E. Shigemasa[1], H. Iwayama[1], E. Nakamura[1], N. Kondo[1], T. Horigome[1] and M. Nagasaka[2]

[1]*UVSOR Facility, Institute for Molecular Science, Okazaki 444-8585, Japan*
[2]*Department of Photo-Molecular Science, Institute for Molecular Science,*
Okazaki 444-8585, Japan

A new project for constructing the undulator beamline BL6U has been started since 2007. A variable-included-angle Monk-Gillieson mounting has been selected, in order to cover a wide photon energy region (30-500 eV) with one single grating. It has been confirmed through its performance tests that the monochromator designed can cover the photon energy ranging from 40 to 400 eV with the resolving power higher than 5000 and the photon flux more than 10^{11} photons/sec, when the storage ring is operated in the top-up mode.

A new electron spectrometer for gas phase spectroscopy has successfully been installed, in parallel with the construction program of BL6U. It is well known that high-resolution electron spectroscopy is a powerful tool to investigate electronic structures of atoms and molecules, especially when high-resolution electron spectra and their polarization dependences are measured as a function of photon energy in high-resolution mode. The ability of this two dimensional (2D) electron spectroscopy has been demonstrated in our recent work at SPring-8 [1, 2], where special attention is paid to detect slow electrons following core excitations. In order to apply high-resolution 2D electron spectroscopy to the investigation of the L-shell excitations of the second row elements, a new experimental setup for BL6U has been designed and constructed. As a high performance hemispherical electron energy analyzer, MBS-A1, developed by the MB Scientific AB company, has been selected.

In order to realize 2D electron spectroscopy, software development for controlling both the beamline monochromator and MBS-A1 analyzer has been performed. For the beamline monochromator, not only its output but the gap of the undulator should be controlled. After careful optimizations for the undulator gaps, 2D electron spectroscopy on BL6U has become feasible, thanks to the stable operation of the UVSOR-II storage ring.

Figure 1 and 2 demonstrate the 2D maps for the de-excitation spectra following the double excitations near the carbon 1s photoionization threshold in CO, measured in the horizontal and vertical directions, respectively, as examples of successful measurements. The exit slit opening of the monochromator was set at 30 μm, which corresponds to the photon energy resolution of about 60 meV. The pass energy and slit width of the MBS-A1 analyzer were set to 100 eV and 0.2 mm, which results in the electron energy resolution of about 60 meV. The straight lines with a

slope of 1 in the high kinetic energy (KE) region in each 2D map are due to the valence photoelectrons with vibrational structures. The vertical lines around KE of 275 eV in Fig. 2 are assigned to the atomic Auger line from oxygen atoms after the dissociation of CO molecules. Some island-like structures are seen in the KE range of 267-270 eV in Fig. 1 and Fig. 2, which seem to be specific to the decay processes of the double excitations. The complicated photon energy dependences of the structures may indicate that the de-excitation processes of the doubly excited states are not so simple.

[1] T. Kaneyasu, Y. Hikosaka, P. Lablanquie, F. Penent, L. Andric, G. Gamblin, J.H.D. Eland, Y. Tamenori, T. Matsushita and E. Shigemasa, Phys. Rev. Lett. **101** (2008) 183003.
[2] E. Shigemasa, T. Kaneyasu, T. Matsushita, Y. Tamenori and Y. Hikosaka, New J. Phys. **12** (2010) 063030.
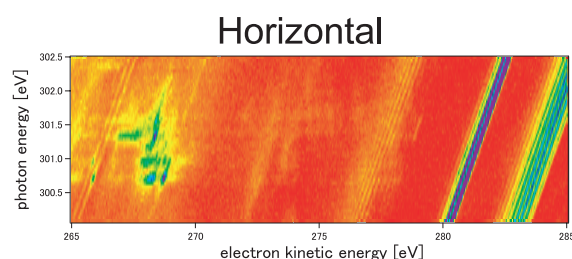
Fig. 1. 2D map of de-excitation spectra following the double excitations around the carbon K-edge of CO measured in horizontal direction.
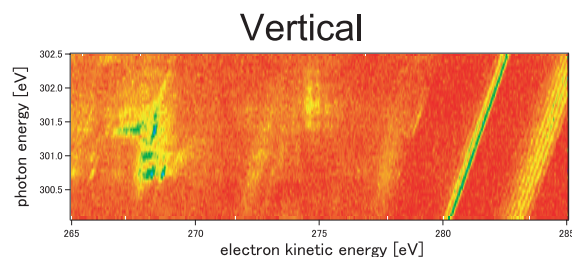

Fig. 2. 2D map of de-excitation spectra following the double excitations around the carbon K-edge of CO measured in vertical direction.

BL7B

Reflection Measurement on [SiC/W/Co]$_2$ and SiC/W/Ir/Ti Sub-Quaterwave Multilayers for Use in 50−110 nm Region

T. Ejima[1], H. Iwai[2], K. Fukui[2], M. Yanagihara[1], M. Watanabe[3],
J. Zhu[4], H. Li[4], Q. Huang[4] and Z. Wang[4]

[1]*IMRAM, Tohoku University, Sendai 980-8577, Japan*
[2]*Faculty of Engineering, University of Fukui, Fukui 910-8507, Japan*
[3]*Tohoku University (Prof. Emeritus), Sendai 980-8577, Japan*
[4]*Institute of Precision Optical Engineering, Tongji University, Shanghai 200092, China*

Traditional multilayers consisting of high- and low-Z materials alternatively having high normal incidence reflectance with broad bands in 50−110 nm region have been developed [1]. In this region, however, because of the strong absorption of all material, the reflectance is rather low. In order to improve this situation, a theory of sub-quarterwave multilayer has been developed [2], basing on the multi-material combination. The layer thicknesses of sub-quarterwave multilayer are less than a quarter of the wave-length. Comparing with traditional multilayer, sub-quarterwave multilayer provides more interfaces per constant optical path. This provides a high reflectance with a broad band by the interfaces close to the outer surface, thus reducing absorption.

Preliminary measurement of reflectance on such multilayers of [Si/W/Co]$_2$ and [Si/W/C]$_2$ had been performed [3]. The subscript "2" means 2 trilayers of different layer thicknesses. In the present study, the measurements on the multilayers, [SiC/W/Co]$_2$, [SiC/W/Ir]$_2$, SiC/W/Ir/Co and SiC/W/Ir/Ti have been performed. The multilayers were designed to have high reflectance of 40−50% in this region at incident angle of 20° for p-polarization. In the multilayers, the top layers were SiC layers and the substrates were Si wafers. Here we report the reflectance measurement on the [SiC/W/Co]$_2$ and SiC/W/Ir/Ti multilayers. In the former, the designed value of layer thickness was respectively 10.59, 11.06, 12.67, 17.51, 10.02 and 8.69 nm from the top SiC layer, and in the latter, 10.42, 5.97, 9.49 and 9.18 nm. They were deposited by using magnetron sputtering method in Tongji University. Near normal incidence reflectance was measured at BL7B, which is equipped with a 3 m McPherson type monochromator. The p-reflectance was measured at incident angles of 20°.

The measured reflectances are shown in Figs.1 and 2 with the calculated results. It can be seen that all the measured reflectances are lower than those of the calculated ones. The possible reasons are as follows. (1) In design, the optical constants used were those from the optics handbook. There is a possibility that the optical constants used in the calculation are different from the actual ones. (2) During and after deposition, the materials reacted with atmosphere and oxidized. Some improvement should be required in next research, such as higher base vacuum condition

and capping layer to protect the multilayers from oxidization when they are exposed to air.
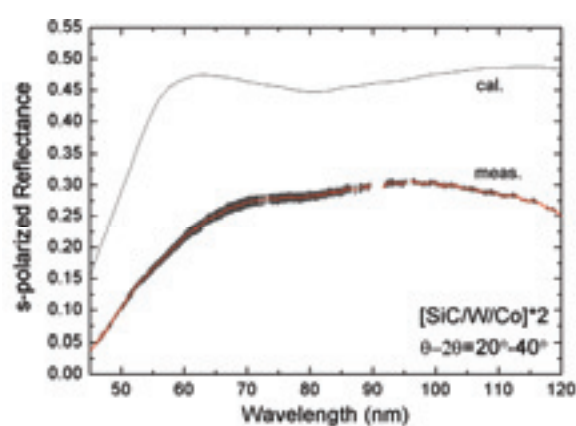
Fig. 1. Calculated and measured p-reflectances of [SiC/W/Co]$_2$ multilayer at incident angle of 20°.
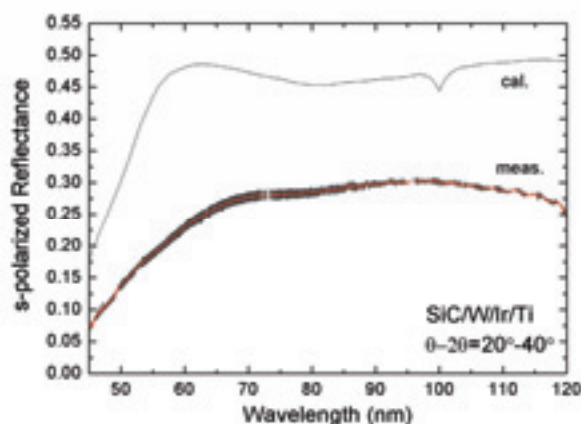

Fig. 2. Calculated and measured p-reflectances of SiC/W/Ir/Ti multilayer at incident angle of 20°.

[1] Y. Kondo *et al*., Nucl. Instr. Meth. A **467-468** (2001) 333.
[2] J. I. Larruquert, J. Opt. Soc. Am. A **18** (2001) 2617.
[3] T. Ejima *et al*., UVSOR Activity Report **36** (2009) 130.

Ⅲ-2. INSTRUMENTAL DEVELOPMENTS

Diffraction Efficiency Measurement on Sub-Quarterwave-Multilayer -Coated Grating for Seya-Namioka Mount in 50−110 nm Region

Y. Liu[1], J. Zhu[2], S. He[1], H. Li[2], Q. Huang[2], Z. Wang[2], S. Fu[1],
T. Ejima[3], H. Iwai[4], K. Fukui[4], M. Yanagihara[3] and M. Watanabe[5]

[1]*National Synchrotron Radiation Laboratory, University of Science and Technology of China, Anhui 230029, China*
[2]*Institute of Precision Optical Engineering, Tongji University, Shanghai 200092, China*
[3]*IMRAM, Tohoku University, Sendai 980-8577, Japan*
[4]*Faculty of Engineering, University of Fukui, Fukui 910-8507, Japan*
[5]*Tohoku University (Prof. Emeritus), Sendai 980-8577, Japan*

The multilayer-coated gratings can provide high diffraction efficiency. They have been widely used in X-ray region and vacuum-UV (VUV) region below 50 nm. However, multilayer coated gratings have been precluded in the VUV region of 50–110 nm because of the strong absorption of materials in this region. As reported in this issue sub-quarterwave multilayers having high normal incidence reflectance with broad bands in 50–110 nm region have been developed. In this study, one of these multilayers, SiC/W/Ir/Ti designed to enhance diffraction efficiency in the 50–110 nm region for Seya-Namioka mount at the −1st order is coated on a grating. Its efficiency was compared with those of the gratings coated with SiC and Ir monolayers. In Seya-Namioka mount, the deviation angle between incident and diffracted rays is constant and about 70°.

The gratings of laminar type were designed to have high efficiency in the 50−110 nm region using the modified integral method [1]. The gratings were fabricated holographically by ion-beam etching. Their line density was 1200/mm. The SiC/W/Ir/Ti multilayer, and SiC and Ir monolayers were deposited on the gratings using magnetron sputtering at Tongji University. Figure 1 shows the surface profile of the multilayer-coated grating. It can be seen that the grooves are still sharp after multilayer deposition. The diffraction efficiency for p-polarization was measured at BL7B equipped with a 3 m McPherson type monochromator in the 45−120 nm. The measurement was made keeping the deviation angle of Seya-Namioka mount.

The measured diffraction efficiency spectra of the gratings coated with SiC/W/Ir/Ti multilayer, and SiC and Ir monolayers are shown in Fig. 2 with calculated ones. The relative trend of the measured spectrum of each grating agrees with that of calculated one. However, the measured efficiencies are lower than the calculated ones except the result at 56 nm for the grating coated with Ir. The plausible reasons of this fact are the deviation of the actual groove depth from the designed one, which causes a wavelength shift of efficiency peak and the deviation of performance of the coating materials. In spite of this, the diffraction efficiency of the grating coated with SiC/W/Ir/Ti multilayer is more than 10% in the 55-100 nm region. This value seems to be satisfactory for practical use in VUV range. Further analysis and experiments are necessary to find the factors that affect the efficiency and to obtain higher efficiency.
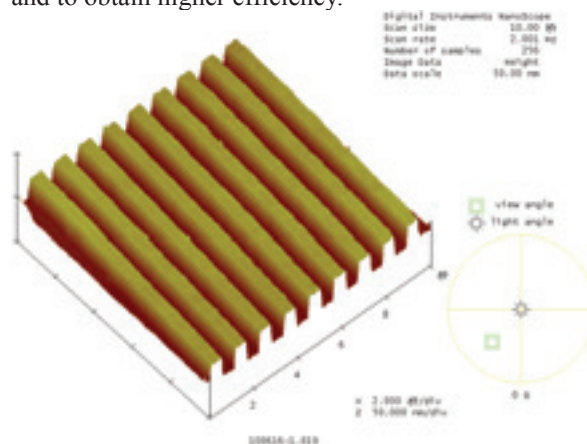

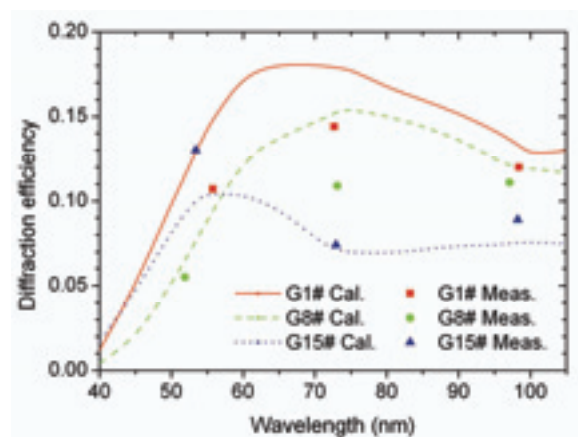Fig. 1. AFM-measured profile of the grating after SiC/W/Ir/Ti multilayer deposition.

Fig. 2. Measured and calculated −1st order efficiency spectra of the gratings coated with three kinds of materials (G1#: SiC/W/Ir/Ti, red squares; G8#: SiC, green circles; G15#: Ir, blue upper triangles).

[1] L. I. Goray and J. F. Seely, Appl. Opt. **41** (2002) 1434.

Development and Verification of CLASP Polarimeter

H. Watanabe[1], N. Narukage[2], T. Bando[2], M. Kubo[2], R. Kano[2], T. Kobiki[2], R. Ishikawa[2],
K. Ueda[2], D. Song[3] and S. Tsuneta[2]

[1]Kwasan and Hida observatories, Kyoto University, Yamashina-ku, Kyoto 607-8417 Japan
[2]National Astronomical Observatory of Japan, Osawa, Mitaka, Tokyo 181-8588, Japan
[3]Department of Physics and Astronomy, Seoul National University, Seoul 151-742, Korea

We developed a polarimeter for the "Chromospheric Lyman-Alpha Spectro-Polarimeter (CLASP)" rocket experiment, which is an international project in collaboration with solar researchers in U.S., Spain, Norway, and Japan. CLASP will detect the weak linear polarization signal produced by the Hanle effect [1] and directly measure the chromospheric magnetic field using Lyman-alpha emission line (121.567 nm) for the first time. Since no practical polarimeter for Lyman-alpha has been developed, we designed and developed the polarimeter, and verified its system performance with an engineering model.

To measure the linear polarization with a high accuracy of 0.1%, we will take the spectra of two orthogonal polarization states simultaneously with a rotating half waveplate and two MgF_2 plates at Brewster's angle. The first MgF_2 plate ("beam splitter" in Fig.1) is a polarization beam splitter that reflects pure s-polarized light to Channel 1. The transmitted light is purified to be p-polarized by the second MgF_2 plate ("polarization analyzer" in Fig.1) and reflected to Channel 2. The rotating waveplate allows measurement of any direction of linear polarization with the fixed beam splitter.

Based on the measurements of reflectivity, transmissivity, and retardation for MgF_2 plate performed in 2009 at UVSOR, components of the polarimeter are designed as follows: The half waveplate is composed by stacking two MgF_2 plates with slightly different thicknesses (14.7 μm) in such a configuration that the slow axes are perpendicular to each other. The beam splitter is a 2-mm thickness MgF_2 plate with its slow axis parallel to the s-polarized light. The reflectivity for s-polarization is 22% and the transmissivity for p-polarization is 78%. The polarization analyzer at Channel 2 is a 15-mm thickness MgF_2 plate with its slow axis parallel to the p-polarized light, i.e., perpendicular to that of the beam splitter.

Using these components described above, the engineering model of the CLASP polarimeter was developed as shown in Fig. 1. By using a pair of autocollimated theodolites, we confirmed that both the beam splitter and the polarization analyzer were mounted at the Brewster's angle (59 degree) to the beam within 3 arcmin accuracy.

The engineering model of the CLASP polarimeter was tested with the synchrotron radiation at the UVSOR BL7B beamline. We input a highly linearly polarized light to the polarimeter and observed the output signal at both channels with a CCD camera. The expected results of the designed polarimeter are the followings: (1) the output signals show a $\cos 4\theta$ modulation with respect to the rotation angle of the waveplate, and (2) the phases of modulations at Channel 1 and Channel 2 are shifted by a half cycle each other, i.e., the maximum at Channel 1 corresponds to the minimum at Channel 2. We indeed observed such modulation patterns as shown in Fig. 2, and verified that the polarimeter for CLASP has been developed.

We note that the wavelength of BL7B beam was calibrated with the absorption lines of molecular oxygen (O_2) around Lyman-alpha (121.567 nm), at a pressure of 0.3 Torr and with a beam line slit width of 50 μm. This method can determine the wavelength within 0.1 nm accuracy.
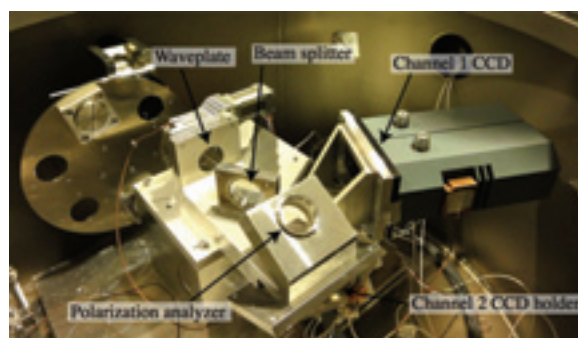

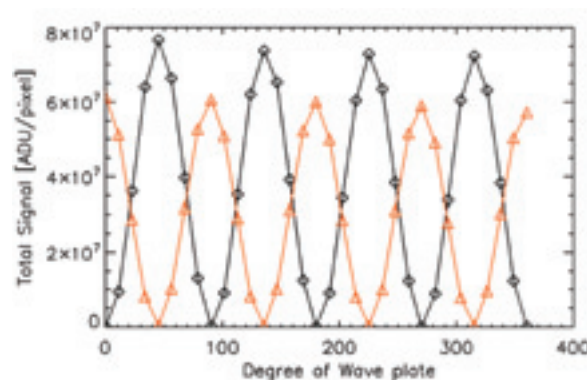Fig. 1.   Photo of the polarimeter engineering model

Fig. 2.   Observed modulation patterns in Channel 1 (black) and Channel 2 (orange).

[1] J. Trujillo Bueno and A. Asensio Ramos, Astrophysical Journal **655** (2007) 642.

III-2. INSTRUMENTAL
DEVELOPMENTS

Asymmetric Reactions of Amino-Acids and Their Precursor Molecules by Circularly Polarized Light from Free Electron Laser

P. K. Sarker[1], T. Kaneko[1], K. Kobayashi[1], J. Takahashi[2], H. Mita[3], M. Adachi[4], H. Zen[4],
M. Hosaka[5] and M. Katoh[4]

[1]*Yokohama National University, Yokohama 240-8501, Japan*
[2]*NTT Microsystem Integration Laboratories, Atsugi 243-0198, Japan*
[3]*Fukuoka Institute of Technology, Fukuoka 811-0295, Japan*
[4]*UVSOR Facility, Institute for Molecular Science, Oakazaki 444-8585, Japan*
[5]*Nagoya University, Nagoya 464-8601, Japan*

Introduction

The origin of homochirality in terrestrial biological molecules (dominant L-body amino acids and D-body sugars) remains an unresolved important problem in the study for the origins of life. One of the most attractive hypotheses for the origin of homochirality is nominated as "Cosmic Scenario"; some chiral impulses from asymmetric excitation sources in space triggered asymmetric reactions on the surfaces of such space materials as meteorites or interstellar dusts. According to this scenario, the enantiomeric excesses in terrestrial amino acids can be advocated that asymmetric reactions of complex organic molecules including amino acid precursors were induced by circularly polarized light (CPL) from synchrotron radiation (SR) source in space prior to the existence of terrestrial life. Recently, a wide-field and deep near-infrared circularly polarized light has been observed in the Orion nebula, where massive stars and many low-mass stars are forming [1]. This observation result strongly support the "Cosmic Scenario" with CPL in space for the origin of homochirality in terrestrial bioorganic compounds.

Presently, we are conducting verification ground experiments for the extraterrestrial scenario by using CPL from SR facilities as a simulating polarized energy source. We have already reported the experimental results of asymmetric reactions in solid films of racemic mixtures of amino acids by irradiating them with CPL in ultraviolet (UV) region from free electron laser (FEL) of UVSOR [2]. The emergence of optical anisotropy in the irradiated films was detected by measurements of circular dichroism (CD) spectra. These results have suggested that the UV-CPL irradiation caused not only preferential photolysis between enantiomers but also asymmetric reactions including conformation changes or some other construct distortions. We have carried out UV-CPL irradiation experiments for aqueous solution of amino acids (DL-isovaline and DL-histidine) and for the films of the precursor molecules of amino acids, such as hydantoins (five-membered heterocyclic molecules).

Experimental

Aqueous solution of IVal, His, or copper complex of His (*pH* = 3, 7 or 11 in all cases) was irradiated with CPL-UV at 215 nm from an FEL of UVSOR-II (IMS, Japan). Amino acids were determined by ion-exchange HPLC (Shimadzu LC-10A). Enantiomers of amino acids were separated by HPLC with a chiral column (Sumichiral OA-50000).

Vacuum-evaporated thin film of hydantoin (5, 5-dihydrogen; Fig. 1) was also irradiated with CPL-UV: hydantoin is an achiral molecule and a precursor of glycine. After the irradiation, optical anisotropy of the resulting thin films were observed with circular dichroism (CD) spectra.
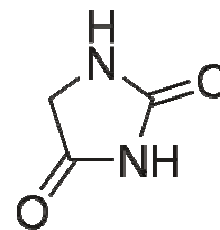

Fig. 1.   Hydantoin

Results and Discussion

After R-CPL irradiation of DL-isovaline aqueous solution, small D-excess was observed, and the L-CPL irradiation caused L-excess. Amino acid analysis showed that the major amino acid product from isovaline was alanine.

Achiral hydantoin has presented apparent optical anisotropy in the CD spectra of the irradiated films, suggesting that asymmetric reactions peculiar to the heterocyclic ring molecules can induce chiral constructions in the starting achiral molecules.

These results suggest that UV-CPL played an important role to produce homochirality of terrestrial amino acids from their precursor molecules. Additional experiments for both chiral and achiral hydantoins and analyses including both identification of reaction product molecules and theoretical calculation of photo-induced constructions are important for the solution of the origins of biological homochirality.

[1] T. Fukue *et al.*, Orig. Life Evol. Biosph. **40** (2010) 335.
[2] J. Takahashi *et al.*, Int. J. Mol. Sci. **10** (2009) 3044.

Ⅲ-3. MOLECULAR SPECTROSCOPY AND DYNAMICS

Effect of the Magic Number "60" on the Photodissociation Process of C_{70}

H. Katayanagi[1,2] and K. Mitsuke[1,2]

[1]*Dept. of Photo-Molecular Science, Institute for Molecular Science, Okazaki 444-8585, Japan*
[2]*Graduate University for Advanced Studies, Okazaki 444-8585, Japan*

We have developed a photofragment imaging spectrometer suitable for synchrotron radiation (SR) excitation of gaseous molecules of refractory materials [1]. Using this apparatus we have observed the scattering distributions of the fragments produced by the photodissociation of C_{60} such as C_{60-2n}^{2+} [2]. We found that the kinetic energy release (KER) of the reaction step to produce C_{50}^{2+} fragments was smaller than those of the other reaction steps. This shows that the C_{50}^{2+} fragment is more stable than the other C_{60-2n}^{2+} fragments. The relative stability of the fragments can thus be obtained. In the present study, we apply this method to observe fragments produced by the photodissociation of the higher fullerene, C_{70}, which decays into C_{60} fragments through stepwise C_2 emission.

The experiments were performed at BL2B in UVSOR. The experimental procedure is almost identical to that of the photofragment imaging of C_{60} [2].

Figure 1 shows two-dimensional (2D) maps of time-of-flight (TOF, t) and arrival position along y-direction of ion signals on a position sensitive detector (PSD). The y-direction on the figure is orthogonal to the path of the parent C_{70} beam. The conspicuous three spots in Fig. 1 (a) are ascribable from left to right to the parent ions of C_{70}^{3+}, C_{70}^{2+} and C_{70}^{+}, respectively. These spots have narrow y-distributions since the C_{70} neutral beam is well collimated. In Figs. 1 (b) and (c) subtle stripes with much broader y-distributions are seen on the left of the parent ions' spots; these stripes are assigned to the fragments produced by successive ejection of C_2 units from the parent ions. The broader y-distributions of the stripes indicate larger velocity, or higher translational temperatures of the fragments acquired by the dissociation than those of the parent ions.

Figure 2 shows the translational temperatures, T, of the fragments determined from the y-distributions of the fragments on Fig. 1. The smaller fragments have the higher temperatures. We can regard the gap between curves of $n = 4$ and 5 are smaller than the other gaps between the curves. This means that the temperature increase between C_{62}^{2+} ($n = 4$) and C_{60}^{2+} ($n = 5$) is exceptionally smaller than those between other fragments. The small increase in the C_{60}^{2+} production process reflects small KER in this reaction step. This is partly because of relative stability of C_{60}^{2+} fragment having the magic number of 60. In addition, there might be another reaction pathway to produce C_{60}^{2+} such as one-step two-fragment fission.
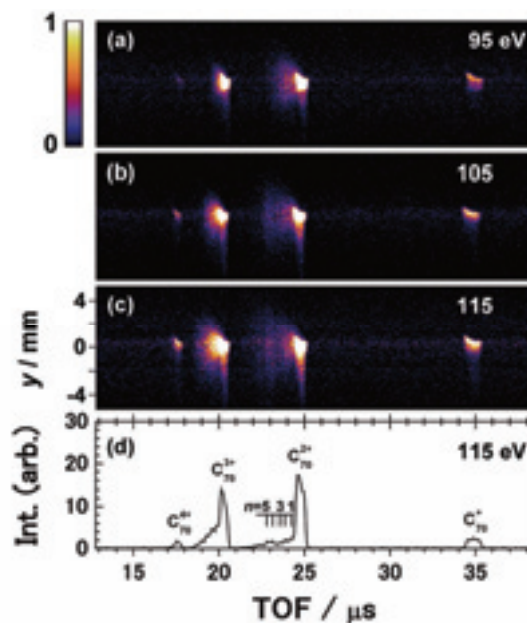

Fig. 1. (a-c) y-t maps of parent and fragment ions produced by the photodissociation of C_{70}. Excitation photon energies are shown in each panel. (d) TOF profile obtained from (c) by integration with respect to y. Assignments of peaks are shown in the panel.

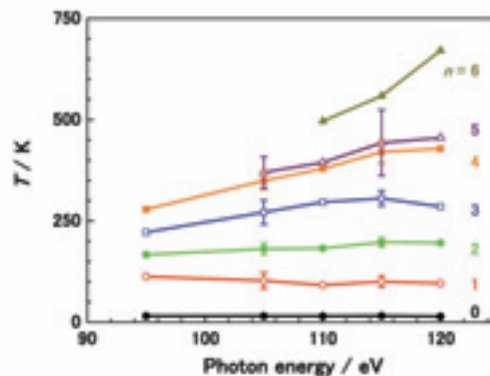Fig. 2. Excitation photon energy dependence of translational temperatures of parent and fragment ions produced at n-th reaction step to produce C_{70-2n}^{2+} evaluated from y-t maps shown in Fig. 1 (a-c). Error bars show deviations among experimental runs on different days.

[1] Md. S. I. Prodhan *et al.*, Chem. Phys. Lett. **469** (2009) 19.
[2] H. Katayanagi and K Mitsuke, J. Chem. Phys. **133** (2010) 081101.

Mass-Analyzed Velocity Map Imaging of Thermal Photofragments from C_{60}

H. Katayanagi[1,2] and K. Mitsuke[1,2]

[1]*Dept. of Photo-Molecular Science, Institute for Molecular Science, Okazaki 444-8585, Japan*
[2]*Graduate University for Advanced Studies, Okazaki 444-8585, Japan*

Dissociation mechanisms of fullerenes have been extensively studied since the fullerenes are systems which have well-defined, highly-symmetric molecular structure despite their large number of degrees of freedom, F (e.g. C_{60}, $F = 174$). The knowledge on the dissociation mechanisms of such large F systems provides a severe benchmark for various statistical theories of reaction dynamics. In the present study, the velocity distributions of the fragments produced by dissociative photoionization of C_{60} have been measured in the extreme UV region for the first time, using a flight-time resolved velocity map imaging technique combined with a high-temperature molecular beam and synchrotron radiation [1]. From the velocity distributions, detailed properties reflecting the dissociation mechanism can be obtained such as kinetic energy release (KER) of dissociation and partitioning of internal energies of reactants among the degrees of freedom.

The experiments were performed at BL2B in UVSOR. Fullerene (C_{60}) powder was loaded in a quartz tube and heated up by an electric heater at around 700-800 K in vacuum. The C_{60} vapor passed through two apertures and reached the ionization region, where the C_{60} molecular beam (x axis) intersected the monochromatized synchrotron radiation (y axis) at right angles. Ions produced at the ionization region were extracted by a velocity map imaging electrode assembly and projected along z axis on to a position sensitive detector (PSD) of 40 mm in diameter and 375 mm away from the ionization region. Photolectrons were extracted to the opposite direction to the ions and detected by a microchannel plate (MCP) detector. Time of flight (TOF, t) and arrival position (x, y) of ions on the PSD were recorded using the signal of photoelectrons as a start trigger. Three-dimensional (3D) lists of data, (x, y, t), were thus obtained.

Integration of the 3D listdata with respect to x, 2D y-t distributions were obtained (not shown here, see Ref. 1). Further integration with respect to y gives us ordinary TOF profiles. Distributions along y-direction on the y-t map with limited TOF ranges which correspond to mass-to-charge ratios (m/z) of each fragment were then extracted. The y-distribution of each fragment is 1D projection of 3D velocity distribution and is converted to translational temperature.

Figure 1 shows the translational temperatures of the fragments. From the temperatures, average KER for respective reaction steps were obtained assuming stepwise C_2 emission and shown in Fig. 2.

In Fig. 2, the values of KER in the first to fourth

steps increase with increasing $h\nu$, reflecting statistical redistribution of the excess energy in the transition state, whereas that in the fifth step leading to C_{50}^{2+} was exceptionally small. This might reflect C_{50} has a cage structure and the number 50 is a magic number although C_{50} cannot satisfy the isolated pentagon rule. In addition, knowledge on the energy partitioning can be obtained from the KER curves. We can estimate the internal energies, E_{int}, of parent C_{60}^{2+} ions from the excitation photon energy, ionization potential and thermal energy of the parent ion. The dashed line in Fig. 2 shows the internal energy divided by the degree of freedom, E_{int} / F. The KER values of n=1 agree with the dashed line. This means that the internal energy partitioned to one degree of freedom is dissipated to the reaction coordinate of C_2 emission among the vibrational degrees of freedom.
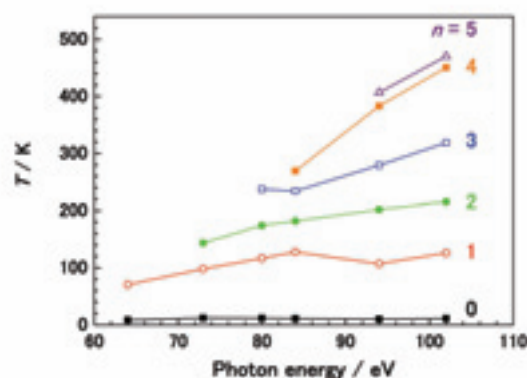

Fig. 1. Excitation photon energy dependence of translational temperatures of the fragments (C_{60-2n}^{2+}).
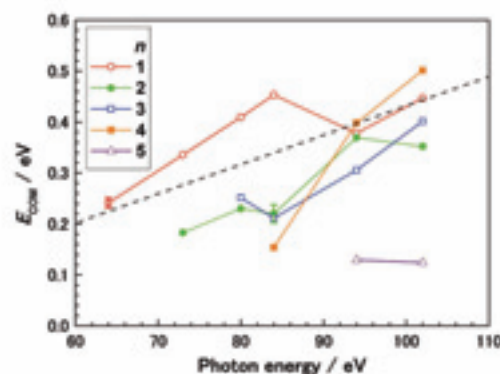

Fig. 2. Excitation photon energy dependence of total average KER generated at the n-th reaction step to produce C_{60-2n}^{2+}. Error bars show the uncertainty caused in the fitting procedure. Dashed line indicates the value of E_{int} / F in the first reaction step.

[1] H. Katayanagi and K Mitsuke, J. Chem. Phys. **133** (2010) 081101.

III-3. MOLECULAR SPECTROSCOPY AND DYNAMICS

BL2B

Breakdown Pathways of Doubly-Charged Perfluorocyclobutane and *cis*-1,1,2,2,3,4-Hexafluorocyclobutane

K. Okada[1], T. Nakashima[1], M. Sakai[1], A. Suemitsu[1], H. Katayanagi[2,3] and K. Mitsuke[2,3]
[1]Department of Chemistry, Hiroshima University, Higashi-Hiroshima 739-8526, Japan
*[2]Institute for Molecular Science, Okazaki 444-8585, Japan*
[3]Graduate University for Advanced Studies, Okazaki 444-8585, Japan

Molecular photoionization and ionic fragmentation processes are of fundamental importance in the upper-atmospheric chemistry and plasma physics. Perfluorocyclobutane (c-C_4F_8) is extensively used as a reagent for dry etching of semiconductors. However, the use of the gas in industry has atmospheric implications for global warming. In our previous study [1] we report yield spectra of the fragment ions of c-C_4F_8 and *cis*-1,1,2,2,3,4-hexafluorocyclobutane (*cis*-c-$C_4H_2F_6$), a candidate for replacing c-C_4F_8, in the photon energy range of 25–170 eV. Due to the shortage of the knowledge of the photochemical process, ion pairs originating from charge separation of the multiply-charged molecular ions were detected in this study using a photoelectron–photoion–photoion coincidence (PEPIPICO) technique to obtain information on the breakdown pathways.
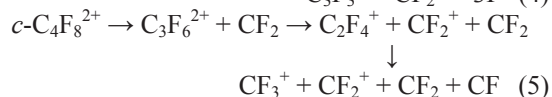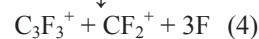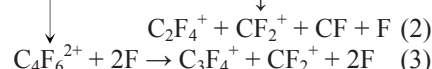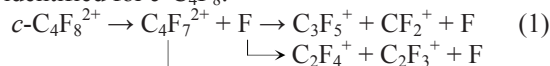
The experiments have been performed on the beamline BL2B at the UVSOR facility. The experimental setup has been described in a previous paper [1]. Electrons and ions produced by the photoabsorption were extracted toward the opposite directions. The detection signals of the electrons and ions were fed into the start and stop pulse inputs of a multi-stop time-to-digital converter (FAST ComTec, P7888), respectively, to record time-of-flight (TOF) data. The data were acquired at 35.0, 40.0, 45.0, 50.0 and 90.0 eV. PEPIPICO spectra were constructed from the ion–ion coincidence events as maps.

Figure 1 depicts a typical PEPIPICO spectrum obtained for c-C_4F_8 at the excitation energy of 45.0 eV. Several coincidence islands can be found in the spectrum, along with ridges arising from false coincidences. In this study we focus on the slopes of the islands. The coordinate tells us the masses of the two fragment ions, while the slope gives information about the fragmentation mechanism to produce such ions.

The most abundant fragment ion pair detected is $C_2F_4^+$/CF^+. Its coincidence island has round shape, indicating that the ion pair can be formed by some decomposition processes. A long parallelogram of slope −1.01 is observed for the island corresponding to the $C_3F_5^+$/CF_2^+ ion pair. This can be explained by the two-body fragmentation of $C_4F_7^{2+}$. The measured slope for the $C_2F_4^+$/CF_2^+ coincidence island is −1.63, which is well described by the three-body secondary decay mechanism:

$$C_4F_7^{2+} \rightarrow C_2F_4^+ + C_2F_3^+,$$
$$C_2F_3^+ \rightarrow CF_2^+ + CF.$$
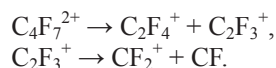
In this way, the following breakdown pathways can be identified for c-C_4F_8:

$$c\text{-}C_4F_8^{2+} \rightarrow C_4F_7^{2+} + F \rightarrow C_3F_5^+ + CF_2^+ + F \quad (1)$$
$$\rightarrow C_2F_4^+ + C_2F_3^+ + F$$
$$\downarrow$$
$$C_2F_4^+ + CF_2^+ + CF + F \quad (2)$$
$$C_4F_6^{2+} + 2F \rightarrow C_3F_4^+ + CF_2^+ + 2F \quad (3)$$
$$\downarrow$$
$$C_3F_3^+ + CF_2^+ + 3F \quad (4)$$
$$c\text{-}C_4F_8^{2+} \rightarrow C_3F_6^{2+} + CF_2 \rightarrow C_2F_4^+ + CF_2^+ + CF_2$$
$$\downarrow$$
$$CF_3^+ + CF_2^+ + CF_2 + CF \quad (5)$$
$$\text{etc.}$$

Similar breakdown pathways are found for the fragmentation of *cis*-c-$C_4H_2F_4$. Reaction channels deduced from the slope analysis correspond to Reactions 1, 2, 4 and 5, with formally replacing one or two F atoms with H atoms.
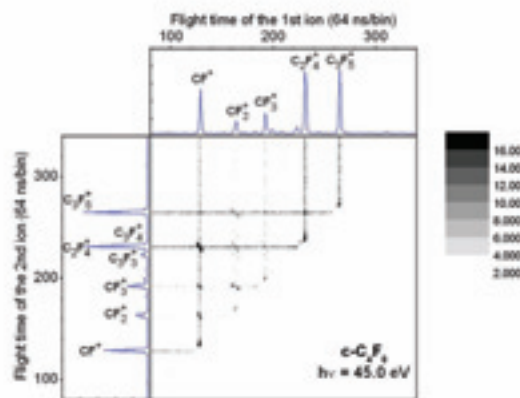

Fig. 1. Overview of a typical PEPIPICO map for c-C_4F_8 acquired at 45.0 eV. The top and left panels indicate the corresponding TOF spectrum.

[1] K. Okada, T. Nakashima, M. Sakai, A. Suemitsu, C. Huang, H. Yagi, H. Katayanagi, K. Mitsuke and K. Tabayashi, J. Phys. Conf. Ser., accepted.

III-3. MOLECULAR SPECTROSCOPY AND DYNAMICS

56

Electronic Structure of Liquid Methanol Studied by Carbon K-Edge Soft X-Ray Absorption Spectroscopy

M. Nagasaka and N. Kosugi

Institute for Molecular Science, Myodaiji, Okazaki 444-8585, Japan

Methanol (CH_3OH) is a liquid at room temperature and is the simplest of the amphiphilic molecules with both hydrophilic and hydrophobic groups. It is known that some mixtures of methanol and water show characteristic hydrogen bonding networks by the cluster formation [1]. The microscopic structure of the hydrogen bonding network of liquid methanol is not fully understood. X-ray absorption spectroscopy (XAS) is a promising method to study the local electronic structure of the hydrogen bond in liquid water [2] and so on. Combination of the O and C K-edge XAS spectra of methanol is useful to reveal the local electronic structures around C and O atoms separately. Wilson et al. reported XAS spectra of methanol in the total electron yield of liquid microjet of methanol [3]. It is difficult to extract liquid XAS spectra from the spectra of gas and liquid mixture. Recently, we have developed a liquid cell for the measurement of XAS in the transmission mode [4]. In the present work, we apply this transmission C K-edge XAS technique to investigate the local electronic structure of liquid methanol.

The experiments were performed at BL3U. The liquid thin layer was sandwiched between two 100 nm-thick $SiNx$ (NTT AT Co.). Thickness of the liquid layer was optimized to be 250 nm by adjusting the helium backpressure. The energy resolution was set to be 0.19 eV at 280 eV. The photon energy was calibrated by the C 1s - π^* peak (290.77 eV) of the CO_2 gas mixture in He [5]. XAS spectra for methanol gas mixture in He were also measured.

Figure 1 shows C K-edge XAS spectra of molecular (gas) and liquid methanol at 25 ºC. Two peaks around 288 and 289.5 eV and several Rydberg states are observed in the molecular spectra. The 288 eV and 289.5 eV peaks contain O-H and C-H components and the 292.5 eV peak contains a σ^* C-O component. Our C K-edge XAS spectrum of liquid methanol shows a simple structure with three contributions around 288.5, 290, and 293 eV as shown in Fig. 1(b); on the other hand, the microjet experiment did not give such a large spectral difference between gas and liquid [3]. The XAS spectra for methanol clusters [6] are similar to our liquid spectrum. The contribution from the methanol gas would be not completely removed in the microjet experiments.

As shown in Fig. 1 (b), the peak around 288.5 eV in liquid methanol is shifted to higher photon energy compared to that of methanol gas. The energy shift (0.53 eV) would be caused by the formation of the hydrogen bonding networks between methanol

molecules. The peak around 290 eV in liquid methanol is also shifted to the higher photon energy compared to that of methanol gas, but the energy shift (0.20 eV) is smaller than in the first peak. This may be explained by a dominant contribution from the hydrophilic OH component in the first band and a dominant contribution from the hydrophobic CH component in the second peak. The peak around 293 eV does not show a noticeable difference between gas and liquid because the σ^* (C-O) orbital is not influenced by the hydrogen bonding network.
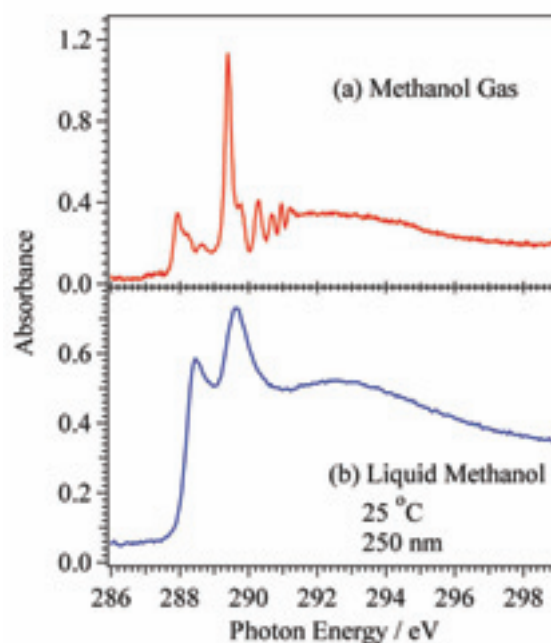

Fig. 1. Carbon K-edge XAS spectra for (a) methanol gas and (b) liquid methanol at 25 ºC. The thickness of liquid methanol layer is estimated to be 250 nm.

[1] C. Corsaro *et al.*, J. Phys. Chem. B **112** (2008) 10449.
[2] Ph. Wernet *et al.*, Science **304** (2004) 995.
[3] K. R. Wilson *et al.*, J. Phys. Chem. B **109** (2005) 10194.
[4] M. Nagasaka *et al.*, J. Electron Spectrosc. Relat. Phenom. **177** (2010) 130.
[5] T. Tanaka *et al.*, Phys. Rev. Lett. **95** (2005) 203002.
[6] Y. Tamenori *et al.*, J. Chem. Phys. **128** (2008) 124321.

Ⅲ-3. MOLECULAR SPECTROSCOPY AND DYNAMICS

Hydration Structures of Li Cations in LiCl Aqueous Solutions Studied by Oxygen K-Edge Soft X-Ray Absorption Spectroscopy

M. Nagasaka[1], T. Hatsui[2] and N. Kosugi[1]

[1]*Institute for Molecular Science, Myodaiji, Okazaki 444-8585, Japan*
[2]*XFEL Project Head Office, RIKEN, Sayo-cho, Hyogo 679-5148, Japan*

Macroscopic properties of aqueous solutions, such as viscosity, boiling point, and freezing point, are influenced by the interaction between ions and water molecules because the hydrogen bonding networks are formed or broken by the interaction of the ions. In aqueous salt solutions, the cation is near the oxygen site of water molecules, whereas the anion is near the hydrogen site. The interaction of the anion with water has been studied by using the OH stretch vibration mode in the Raman spectroscopy [1]. On the other hand, the hydration of the cation has not been studied in detail by vibrational spectroscopies because the OH vibration is insensitive to the cation. Recently, the electronic structure of liquid water has been studied by oxygen K-edge X-ray absorption spectroscopy (XAS) [2]. The pre-edge peak of liquid water (535 eV) corresponds to the transition from the oxygen 1s electron to the $4a_1^*$ unoccupied orbital, which is mainly distributed on the oxygen atom and is dominated by the short-range interaction. The energy shift of the pre-edge peak would be sensitive to the nearest neighbor cation coordination to the water oxygen. In this work, we have studied the hydration shell of Li cations in the LiCl aqueous solutions by using oxygen K-edge XAS.

The experiments were performed at BL3U. The details of the liquid cell for the XAS measurements in the transmission mode were described previously [3]. The liquid thin layer was sandwiched between two 100 nm-thick SiNx (NTT AT Co.). The thickness of the liquid layer was optimized from 50 to 1000 nm by changing the He backpressure [3]. The photon energy was calibrated by the O 1s - π^* peak (530.8 eV) of the O_2 gas mixture in He.

Figure 1 shows O K-edge XAS spectra for the LiCl aqueous solutions with different concentrations at 25 ºC. As the concentration increases, the pre-edge peak is gradually shifted to the higher photon energy. As shown in the inset, the isosbestic points were observed in the pre-edge region, which suggests the existence of two components in the pre-edge region dominated by the short-range interaction. We also measured the O K-edge XAS for different cations and anions (NaCl, KCl, NaBr, and NaI); the energy shift of the pre-edge region is dependent on the alkali ion but is not on the halide ion. This indicates that the two components in the spectra (Fig. 1) are derived from the bulk water and the Li$^+$-solvating water.

In order to extract the contribution of the Li$^+$-solvating water from the spectra, the numbers of the bulk and solvating water molecules were

calculated, assuming the coordination number of water molecules to Li$^+$ is 4 [4]. In the XAS spectra for the nearest neighbor water solvating the different cations, the pre-edge peak in the Li ion shows a larger energy shift than in the Na and K ions. The neutron diffraction studies showed that the bond between the Li cation and water is 0.190 nm, which is shorter than those of the Na and K ions [4]. This indicates that the pre-edge peak shift arises from the nearest-neighbor interaction of the cation with the oxygen site of solvating water molecules and the hydration to the Li ion is stronger than the Na and K ions.

We also measured O K-edge XAS for the LiCl aqueous solutions with different temperatures (4, 25, and 60 ºC); the pre-edge peak corresponding to the Li$^+$-solvating water is not shifted irrespective of the temperature. This agrees that the interaction of the Li ion with liquid water is strong enough to keep the hydration shells even in different temperatures.
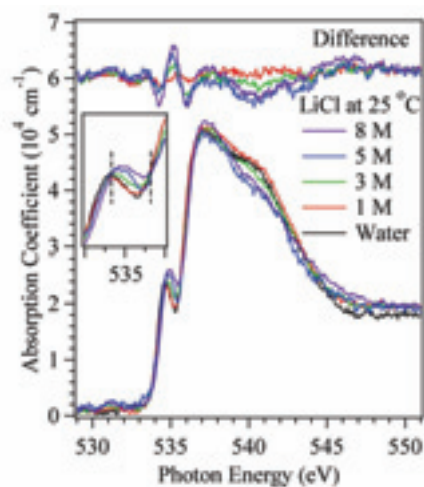

Fig. 1. Oxygen K-edge XAS spectra for the pure water and the LiCl aqueous solutions with different concentrations at 25 ºC. The spectral differences between aq. LiCl and bulk water are also shown. The inset shows isosbestic points (dashed lines) in the pre-edge region.

[1] J. D. Smith *et al.*, J. Am. Chem. Soc. **129** (2007) 13847.
[2] L.-Å. Näslund *et al.*, J. Phys. Chem. A **109** (2005) 5995.
[3] M. Nagasaka *et al.*, J. Electron Spectrosc. Relat. Phenom. **177** (2010) 130.
[4] N. Ohtomo and K. Arakawa, Bull. Chem. Soc. Jpn. **52** (1979) 2755.

Ⅲ-3. MOLECULAR SPECTROSCOPY AND DYNAMICS

Structures of Small Mixed Argon-Nitrogen Clusters Studied by Soft X-Ray Photoelectron Spectroscopy

M. Nagasaka[1], E. Serdaroglu[2], R. Flesch[2], E. Rühl[2] and N. Kosugi[1]

[1]*Institute for Molecular Science, Myodaiji, Okazaki 444-8585, Japan*
[2]*Physikalische Chemie, Freie Universität Berlin, Takustr. 3, D-14195 Berlin, Germany*

The structure of heterogeneous clusters is dependent on the cluster size and composition. The structure of small clusters is very important from the viewpoint of the cluster formation mechanism. The cluster structures have been extensively investigated by theoretical simulations [1]; on the other hand, there are few experiments to study the structures of small mixed clusters because of several experimental difficulties. Recently, we have measured X-ray photoelectron spectroscopy (XPS) of small homogeneous Kr and Xe clusters [2, 3] and small mixed Kr-Xe clusters. Different binding energy shifts in the Kr 3d and Xe 4d edges, which are observed in different sites of the Kr-Xe mixed clusters. These arise from the two different induced polarization effects of surrounding Kr and Xe atoms. In the present study, we have investigated the structures of small mixed Ar-N_2 clusters of different composition by analyzing the core level shifts. N_2 is a linear molecule. Therefore, the core level shift of mixed Ar-N_2 clusters would be influenced by anisotropic interactions of the N_2 molecules.

The experiments were performed at BL3U. The mixed Ar-N_2 clusters were formed in a supersonic expansion of the gas mixtures containing an Ar mixing ratio between 10 % and 40 %. The nozzle temperature and gas pressure were 163 K and 0.5 MPa, respectively. The average size of the homogeneous Ar clusters becomes 200, as estimated from the expansion conditions.

Figure 1 shows the Ar $2p_{3/2}$ XPS spectra for the Ar cluster and the mixed Ar-N_2 clusters of different composition. The surface and bulk sites of the clusters are distinguished by a fitting procedure, as shown in Table 1. The cluster size of 200 corresponds to icosahedral multilayer structures with 4 or 5 layers. The intensity ratio of the surface and bulk sites observed for the Ar $2p_{3/2}$ XPS spectra of the pure (100 %) Ar_{200} cluster is consistent with such icosahedral multilayer structures. On the other hand, in the expansion containing 10 % Ar, the intensity of the surface sites is smaller than that of the bulk sites. This intensity ratio suggests a core-shell structure, where the Ar aggregates are located in the bulk and are covered by a N_2 shell. We have roughly estimated the composition of N_2 bound in clusters from the partial pressure of N_2, and confirmed that the surface-to-bulk ratio of Ar is consistent with a core-shell structure, where Ar is covered by the N_2. These core-shell structures are also observed in expansions containing 20 % and 40 % Ar.
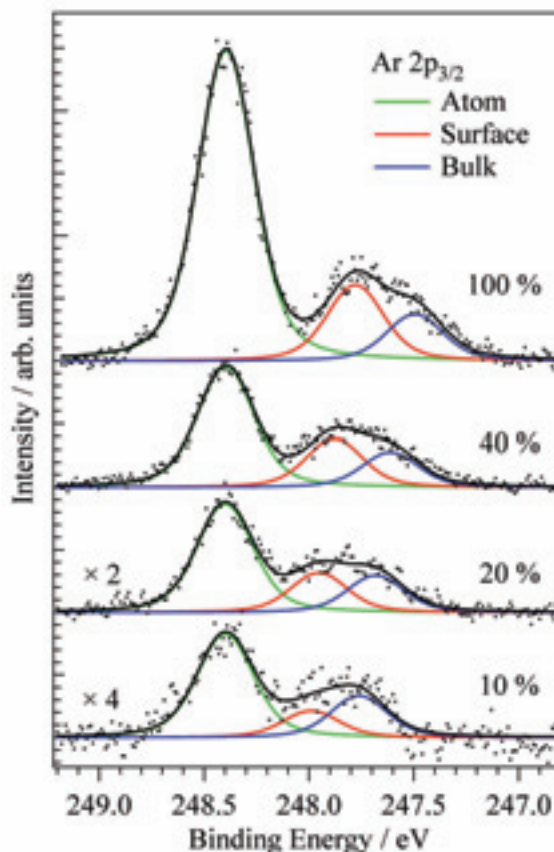

Fig. 1. Ar $2p_{3/2}$ XPS spectra of mixed Ar-N_2 clusters prepared from different mixing ratio of Ar. The surface and bulk sites of the mixed clusters are obtained from a fitting procedure.

Table 1. Binding energy shifts in the Ar $2p_{3/2}$ regime at different sites of the mixed clusters relative to the atomic value in eV. The values in parentheses correspond to the relative intensities of the Ar atoms.

Ar (%)	Surface	Bulk
100	-0.62 (124)	-0.90 (76)
40	-0.52 (79)	-0.79 (57)
20	-0.45 (32)	-0.72 (30)
10	-0.41 (11)	-0.64 (17)

[1] For example, J. W. Hewage and F. G. Amar, J. Chem. Phys. **119** (2003) 9021.
[2] T. Hatsui *et al.*, J. Chem. Phys. **123** (2005) 154304.
[3] M. Nagasaka *et al.*, J. Electron Spectrosc. Relat. Phenom. **183** (2011) 29.

Ⅲ-3. MOLECULAR SPECTROSCOPY AND DYNAMICS

Chemical Environment Effect on Doubly Charged Ion States after Auger Decay of Ethyl Trifluoroacelate Molecules

H. Iwayama[1], E. Shigemasa[1] and P. Lablanquie[2]

[1]*UVSOR Facility, Institute for Molecular Science, Okazaki 444-8585, Japan*
[2]*LCPMR, Université Pierre et Marie Curie, 75231 Paris Cedex 05, France*

Inner-shell photoionization of light elements is generally accompanied by an Auger decay process. A photoelectron and Auger electron are thus ejected, and a doubly charged ion is produced. The binding energy of an inner-shell electron in a molecule depends not only on the atomic energy level but also its chemical environment, which gives rise to a small shift in the energy spectrum. This is the so-called chemical shift. Based on the observation of such chemical shifts in X-ray photoelectron spectra, we can qualitatively discuss chemical bond character and atomic charge in molecules.

The chemical shifts may also be reflected in the binding energies of the doubly charged ion state after Auger decay, because the Auger transition probability depends on a spatial overlap between the inner- and outer-shell electron wavefunctions. In the present work, we investigated the binding energy spectra after Auger decay for ethyl trifluoroacelate molecules ($C_4H_5F_3O_2$) which have four carbon atoms in different chemical environment. This sample was used to demonstrate the importance of chemical shifts in X-ray photoelectron spectra by K. Siegbahn [1].

In order to obtain the binding energy spectra of doubly charged ion states after Auger decay, we performed a high resolution electron spectroscopy on the soft X-ray beamline BL6U at UVSOR. We measured kinetic energies of photoelectrons and Auger electrons of the C1s, O1s and F1s ionizations with a high performance hemispherical electron energy analyzer MBS-A1, developed by the MB Scientific AB company. The photon energies were set at 330, 575 and 730 eV for the C1s, O1s and F1s ionizations, respectively.

Figure 1 shows the C1s photoelectron spectrum, where four peaks corresponding to the four different carbon sites are clearly observed: the chemical shifts in binding energies of the $C1s^{-1}$ states are detected. By varying the photon energy, binding energies of $F1s^{-1}$ and $O1s^{-1}$ states are also determined to be 694 and 539 eV, respectively.

We measured Auger electron spectra for the F1s and O1s ionizations. From the Auger electron spectra and binding energies of the $F1s^{-1}$ and $O1s^{-1}$ states, we obtained binding energy spectra of doubly charged ion states after Auger decay, which are shown in Fig. 2. Here the binding energies for the C_F and C_O sites were measured on the undulator beamline PLÉIADES at SOLEIL with using a magnetic bottle electron spectrometer. We found that the binding energy spectra after the Auger decays of the $F1s^{-1}$ and

$O1s^{-1}$ states are close to those for the $C1s^{-1}$ states of the carbon sites neighboring to the F and O atoms, respectively. These results indicate that the doubly charged ion states after Auger decay reflect the chemical environment near the core-shell ionized atoms. Our results suggest that the doubly charged ion states after Auger decay can be also used as a sensitive tool for a chemical analysis.

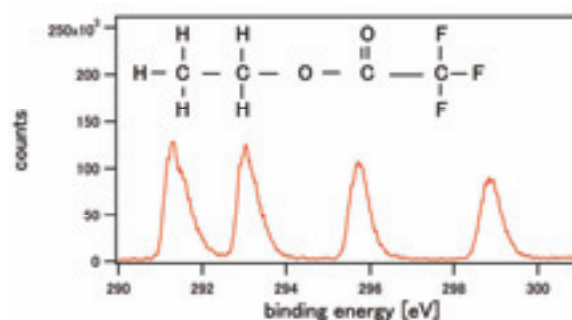[1] U. Gelius *et al.,* J. Electron Spectrosc. **2** (1973) 405.

Fig. 1. The chemical shifts in X-ray photoelectron spectrum for ethyl trifluoroacelate. The energy resolutions for the monochromator and analyzer were both set to 30 meV.
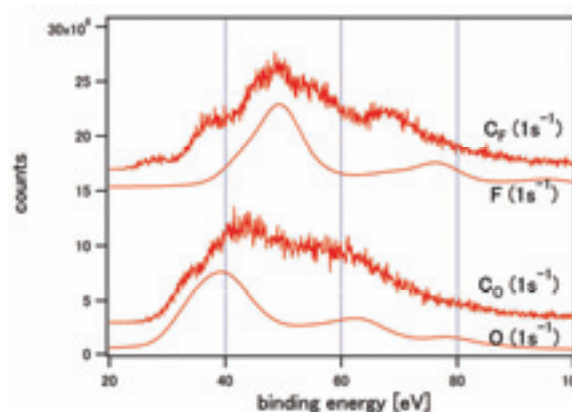

Fig. 2. The binding energy spectra of the doubly charged ion states after Auger decay for the C1s, F1s and O1s ionizations. C_F and C_O denote the carbon atoms neighboring to the F and O atoms, respectively.

Salt Effect on the Photoelectron Emission Threshold from the Wet Surface of TiO$_2$

S. Hitaka, K. Tomita, T. Ishioka and A. Harata

Molecular and Material Sciences, Kyushu University, Kasugakoen 6-1, Kasuga, Fukuoka 816-8580, Japan

Introduction

Titanium oxide (TiO$_2$) has attracted much interest for its unique characteristics of photocatalytic ability such as oxidation of organic compounds without any harmful oxidizing agent. It is widely applied to decompose various organic wastes with solar energy by illuminating the pollutant-adsorbed surface of TiO$_2$. Though some wastewater treatment systems with TiO$_2$ have already been developed, their application to seawater is limited because salt in the seawater usually affect the photocatalytic reaction.

Makita *et al.* [1] reported enhanced photocatalytic reactions in aqueous solutions containing dilute inorganic salt. It is essential to understand salt-enhancement or suppression mechanism to apply photocatalytic reaction for seawater treatment. However, it is still obscure and precise analysis on the mechanism is needed.

In this report, threshold photon energy was measured on photoelectron emission process on the surface of wet TiO$_2$ containing salts. From the results, electronic structures on the TiO$_2$ surfaces were analyzed.

Experimental

Monochromated synchrotron light (4-8) was emitted from the beamline chamber to a He-purged cell through an MgF$_2$ window. The emitted light was reflected on an Al mirror and vertical irradiated on the sample surface through a Cu-mesh electrode. The electrode was set above the wet TiO$_2$ surface and high voltage (400 V) was applied to the electrode. The emitted electron was trapped to the electrode and the total current was monitored by a picoammeter.

The sample was prepared by spreading TiO$_2$ powder (Degussa P-25, anatase:rutile = 8:2) on filter paper covering the bottom of a Pt cell and aqueous salt solution was added to the cell with the volume enough to keep all the powder wet. The salt concentration was 5 mM.

Threshold energy value was derived from the mathematical fitting of empirical formula:

$$S(\nu) = \Sigma\, S_i (h\nu - E_{th,i})^n \qquad (1)$$

where S(ν) is total signal intensity and $E_{th,i}$ is the threshold energy of the i th component. As for index number, $n = 2$ was used in analogy with the case of metal substrates.

Results and Discussion

Photon energy dependence of the photoelectron intensity is shown in Fig. 1. The intensity is well fitted by formula (1) with single component and

derived threshold energy is listed in Table 1. The threshold energy for wet TiO$_2$ with no salt is 5.20 eV. As for single crystalline TiO$_2$(111), the threshold energy is reported to be 5.1 eV. Since single crystal (111) surface is dominant for the used TiO$_2$ powder, it is considered the presence of moisture at the surface has little effect on the band structure of TiO$_2$.

The threshold energy is clearly dependent on the salt species. The threshold value order of cation Mg^{2+}~Li$^+$<Na$^+$<no salt agrees well with the reversed order of photocatalytic activity. Smaller threshold suggests narrower band gap for the surface. The narrower band gap would improve the efficiency of photoexcitation because photons with weak energy become available for excitation.

From above discussion, it is considered that the enhancement by the salt is originated from the distortion of the valence band structure of TiO$_2$. The result can be applied to evaluate photocatalytic activity before actual long-term photochemical experiments.
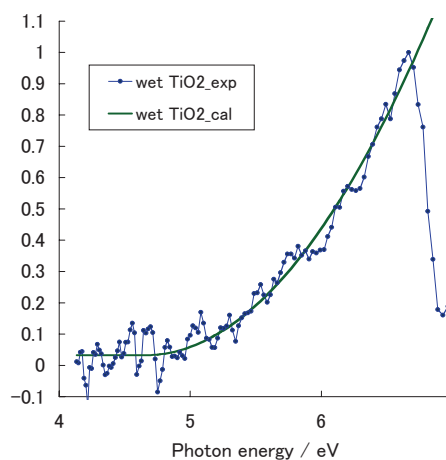

Fig. 1. Photon energy dependence on photoelectron intensity from wet TiO$_2$ surface.

Table 1. Salt dependence on the threshold energy of photoelectron emission from wet TiO$_2$.

Substrate	Threshold / eV
TiO$_2$	5.20
TiO$_2$+ 5 mM LiNO$_3$	4.72
TiO$_2$+ 5 mM NaNO$_3$	5.02
TiO$_2$+ 5 mM Mg(NO$_3$)$_2$	4.71

[1] M. Makita and A. Harata, Chem. Eng. Proc. **47** (2008) 859.

Development of Lower Environmental Load and UVSOR Exciting Luminescence Materials Using with Biomaterials Prepared by Soft Chemistry

M. Ohta

Department of Material Science and Technology, Faculty of Engineering, Niigata University, Niigata 950-2181, Japan

It was known that rare earth ions dosed for oral administration to mouse and rat are transferred to blood vessel through the ileum and deposited its teeth and bone, which mainly consists of hydroxyapatite ($Ca_{10}(PO_4)_6(OH)_2$) [1, 2]. Recently, rare earth is also useful as a contrast medium for magnetic resonance imaging, restriction enzyme, biocatalyst, and so on in fields of biochemistry, physiology, medicine, etc. However, the behavior of rare earth in the living body system remains an open question until now. We have found that Eu ion substituted Ba ion in Eu doped $Ba_{10}(PO_4)_6Cl_2$ phosphor, which matrix is apatite structure [3]. The rare earth ion is also found to substitute easily for calcium ion in hydroxyapatite which is soaked in rare earth chloride aqueous solution, and to play on emission center.

In this study, hydroxyapatite samples doped with rare earth phosphate were prepared in order to apply to phosphor. Their characteristics were investigated by photoluminescent property of rare earth ion-doped hydoxyapatite samples excited by ultraviolet synchrotron orbital radiation light.

Eu-doped hydroxyapatite and Gd-doped hydroxyapatite samples were prepared as follows: hydroxyapatite was added with $EuPO_4$ or $GdPO_4$ and mixed homogeneously, and then heated at 1373 K for 1 hr. $EuPO_4$ or $GdPO_4$ was prepared by reaction of $GdCl_3$ or $YbCl_3$ and $Na_3PO_4 \cdot 12H_2O$ and then fired at 1373 K for 1 hr. $GdCl_3$ or $YbCl_3$ was prepared by reaction of Eu_2O_3 or Gd_2O_3 and HCl.

The photoluminescent property of each sample exited by ultraviolet synchrotron orbital radiation light (BL1B) was detected by using with a multi-channel analyzer.

Figure 1 shows photoluminescence spectra of rare earth ion-doped hydroxyapatite samples excited by BL1B.

The data of X-ray powder diffraction indicated that the rare earth ion substituted for calcium ion in hydroxyapatite.

Figure 1 shows the photoluminescent spectra of Eu ion or Gd ion-doped hydroxyapatite samples excited by ultraviolet synchrotron orbital radiation light. Eu ion-doped sample emitted strong peaks due to f-f transition of Eu^{3+} and Gd ion-doped sample emitted a very strong peak due to f-f transition of Gd^{3+} by excitation from 10 nm to 100 nm. These strong emission phenomena due to rare earth ion suggest to the origin of multiphoton excitation.

[1] S. Hirano and K. T. Suzuki, Environ. Health Perspect. **104** (Supplement 1) (1996) 85.
[2] K. Kostial, B. Kargacin and M. Lendeka, Int. J. Radiat. Biol. Relat. Stud. Phys. Chem. Med. **51** (1987) 139.
[3] M. Sato, T. Tanaka and M. Ohta, J. Electrochem. Soc. **141** (1994) 1851.
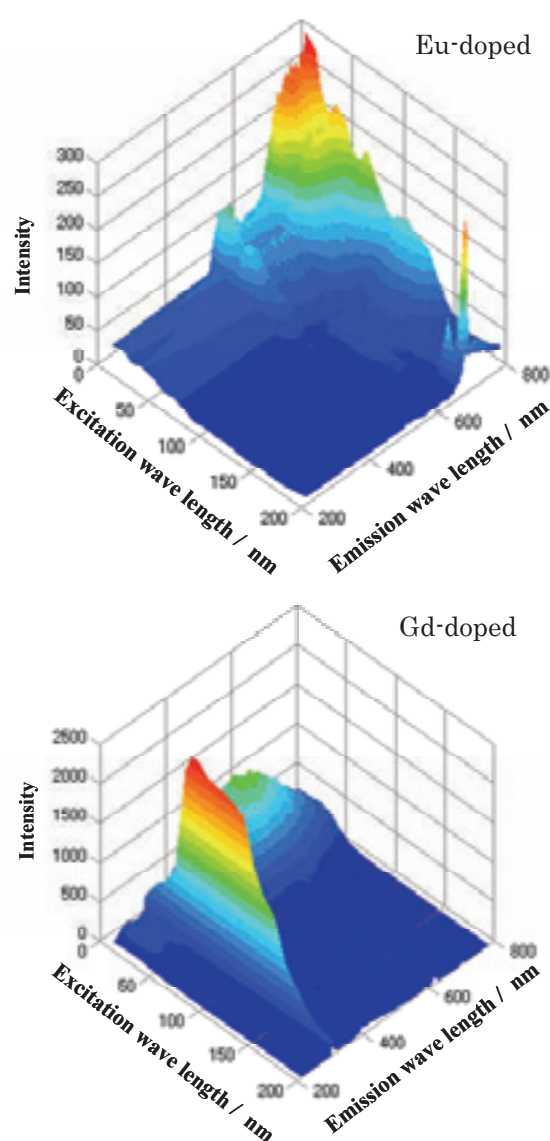

Fig. 1. These figures show the photoluminescent spectra of Eu ion or Gd ion-doped hydroxyapatite samples excited by ultraviolet synchrotron orbital radiation light.

Field Effect on the Electronic States of Organic Thin Films: Incident Angle Dependence of Fluorescence-Yield XAS Spectra

H. S. Kato[1], H. Yamane[2], N. Kosugi[2] and M. Kawai[1,3]

[1]RIKEN (The Institute of Physical and Chemical Research), Wako 351-0198, Japan
[2]Institute for Molecular Science, Okazaki 444-8585, Japan
[3]Department of Advanced Materials Science, University of Tokyo, Kashiwa 277-8501, Japan

Introduction

In order to extend new functionality of electronic devices, the molecular devices have recently been investigated with great efforts. The organic field effect transistor (OFET) is a typical molecular device that controls electric conductivity by injection of carriers into the organic thin film under the applied electric field. Since the organic materials consist of molecular units having their own molecular orbitals, it is not clear that the energy diagram of OFET is exactly the same as that of the inorganic semiconductors, i.e., band bending at the interface in the semiconductor side. Therefore, the direct observation of electronic states in the organic thin films under operative conditions has been required.

In our study, recently, *in situ* element-specific observation of electronic states of organic films beneath metal electrodes is successfully achieved by x-ray absorption spectroscopy (XAS) in the bulk-sensitive fluorescence yield (FY) mode, even under operational conditions. As a result, the bias dependence of the FY-XAS spectra of oligothiophene and pentacene films was detected. Since the obtained spectral changes have included an incomprehensive response, additional experiments were performed.

Experimental

To investigate the electronic states of OFET, pentacene thin films on the SiO_2-covered Si substrates were fabricated at RIKEN. We confirmed that the fabricated pentacene thin films show a *p*-type-like I-V property in the FET configuration. The pentacene films (35 nm thick) were covered homogeneously with a thin Au electrode (25 nm thick) to make uniform electric field in the films under the applied bias. The FY-XAS measurements were performed at the BL3U beamline of the UVSOR facility in IMS. The samples were set in a BL3U end-station through a sample-entry system. The fluorescence intensities were measured using a retarding field detector consisting of MCP plates.

Results and Discussion

Figure 1 shows the incident angle dependence of the C K-edge FY-XAS spectra of the pentacene films, for which the spectra at the incidence angle of 0°, 30° and 60° from the surface normal were measured. At the measurements, the gate bias V_G was applied as a square wave (7 Hz) synchronized to two signal counters for each of the top and bottom bias levels, which enabled us to get two different bias spectra in one photon energy sweep and to compare details of their spectra with sufficient reliability. In Fig. 1, the spectra at the bias of 0 V (blue lines) and -45 V (red lines) are plotted with their difference spectra (bold black lines). It is clear that the spectral changes from 0 V to -45 V increased with increasing incident angle.

In our previous studies, the bias dependence was observed at the normal incidence, so that the electric vector of the x-ray was perpendicular to the direction of the applied electric field. Since the spectral change is claimed to be a result of distorted molecular orbitals under the applied electric field, the previous experimental condition might not be sensitive to the orbital distortion. As the incident angle of the *p*-polarized x-ray increases, in contrast, the parallel component of the electric vector to the direction of applied electric field increases. Therefore, the increase of the difference signals with increasing incident angle, as shown in Fig. 1, rightly supports our previous deduction of the origin of the spectral change under applied bias.
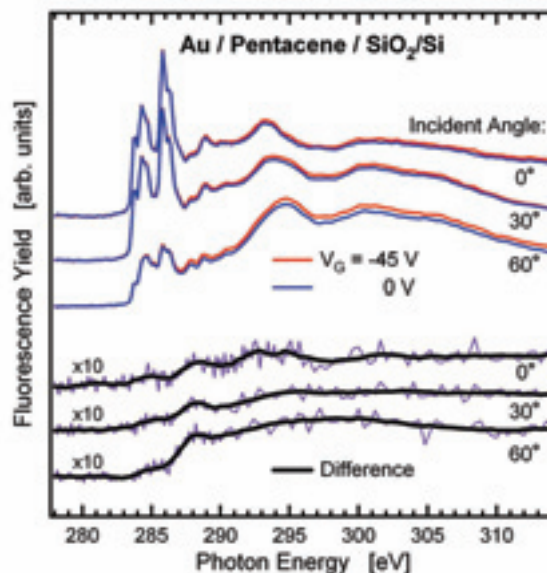

Fig. 1. Incident angle dependence of the C K-edge fluorescence-yield XAS spectra of the Au-covered pentacene films. The spectra were measured at the incident angle of 0°, 30° and 60° from the surface normal. Each set of the spectra at 0 V (blue line) and -45 V (red line) is plotted with their difference spectrum (bold black line).

X-Ray Magnetic Circular Dichroism Study of Suppression of Iron Silicide Formation in Fe/Si$_3$N$_4$/Si(111)

K. Eguchi[1], Y. Takagi[1,2], T. Nakagawa[1,2] and T. Yokoyama[1,2]

[1]*The graduate University for Advanced Studies (SOKENDAI), Okazaki 444-8585, Japan*
[2]*Institute for Molecular Science, Okazaki 444-8585, Japan*

It is known that when transition metals are deposited on silicon substrates, metal silicides are easily formed, which are typically nonmagnetic materials. It is important to suppress the chemical interaction of transition metal atoms with Si substrates by modifying the Si substrate surface. An efficient method to provide well defined surfaces has not been report so far. Previously, we tried to suppress iron silicidation using a Si(111)-($\sqrt{3}\times\sqrt{3}$)Ag substrate, but its effect is not sufficient to exhibit large magnetization [1]. In this work, we have measured Fe L-edge X-ray magnetic circular dichroism (XMCD) of Fe films on a Si$_3$N$_4$/Si(111)-(8×8) substrate.

The experiments were carried out at BL4B. Fe was deposited onto Si$_3$N$_4$/Si(111)-(8×8) and Si(111)-(7×7). The XMCD spectra were taken at *H*=±5 T and *T*=5 K with the incident angles θ of 0° and 55°. The helicity of the X-rays was fixed positively (*P$_c$*:0.41-0.60), while the magnetic field was reversed.

Figure 1 shows magnetization curves of 1.6 ML Fe on Si$_3$N$_4$/Si(111)-(8×8) and Si(111)-(7×7), which were taken at the Fe L$_3$ peaks with the magnetic field normal to the surface. No magnetization can be seen in the Fe film on Si(111)-(7×7), because of the silicidation of iron atoms, while the Fe film on Si$_3$N$_4$/Si(111)-(8×8) was magnetized clearly. The fact indicates that the chemical interaction between Fe and Si atoms is suppressed effectively on the Si$_3$N$_4$/Si(111)-(8×8) substrate.

The spin and orbital magnetic moments were evaluated using the XMCD sum rule and the angle-dependent XMCD measurements. The magnetization of Fe on Si$_3$N$_4$ was fully saturated under the condition of 5 T (See Fig.1). The angle-dependent XMCD spectra taken with the incident angles θ of 0° and 55° are shown in Fig. 2. The spin magnetic moments of each thickness on the Si$_3$N$_4$ surface are found to be much larger than that on the clean surface. Moreover, the spin magnetic moments increases monotonically with increasing the film thickness for the Fe/Si(111) system, because the Fe atom near surface does not form silicides in the thick film. On the other hand, that of the iron atom on Si$_3$N$_4$ surface is 2.62 μ$_B$ at 1.6 ML and the value decreases toward the bulk value of 2.2 μ$_B$ with increasing the film thickness. It is revealed that the Fe atom deposited on the Si$_3$N$_4$ surface does not react chemically with the Si atom.

In summary, the XMCD and M-H curves of iron were measured to evaluate the suppression effect of the iron silicide formation on the Si$_3$N$_4$ surface. The silicidation of iron was found to be suppressed well using the Si$_3$N$_4$ surface.

[1] Y. Takagi, K. Isami, I. Yamamoto, T. Nakagawa and T. Yokoyama, UVSOR ACTIVITY REPORT **37** (2010) 73.
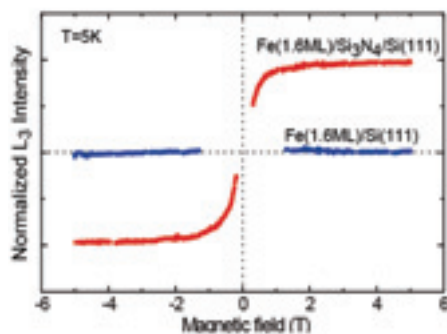

Fig. 1. Magnetization curves for Fe on clean Si(111) and Si$_3$N$_4$/Si(111). Both magnetic field and photon incident direction are perpendicular to the surface.
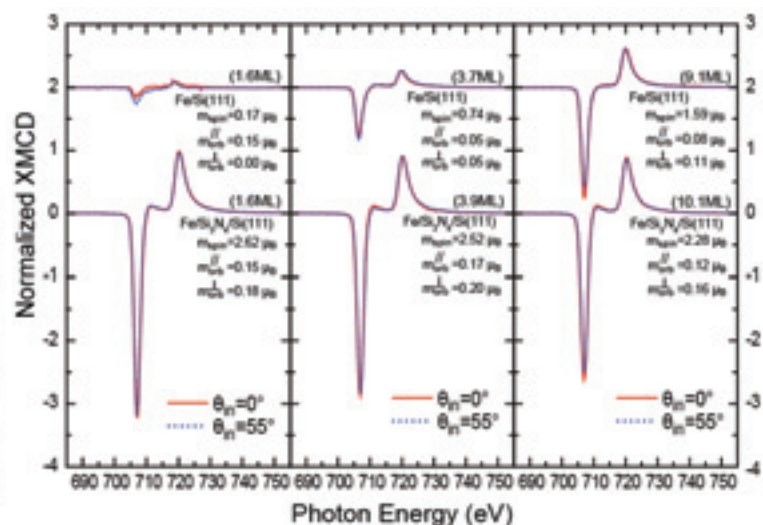

Fig. 2. XMCD spectra at L$_{3,2}$ edge of iron in Fe/Si(111) and Fe/Si$_3$N$_4$/Si(111) systems. Thickness is 1.6, 3.7, 9.1 ML and 1.6, 3.9, 10.1 ML, respectively. Applied magnetic field is 5 T and temperature of samples is 5 K. Incident angles of the light are 0° and 55° to normal direction of the surface.

Magnetic Property of Iron Phthalocyanine on Co Films Studied by XMCD

Y. Takagi[1,2], K. Eguchi[2], T. Nakagawa[1,2] and T. Yokoyama[1,2]

[1] Institute for Molecular Science, Myodaiji-chio, Okazaki 444-8585, Japan
[2]The Graduate University for Advanced Studies, Okazaki 444-8585, Japan

In order to realize the molecular spintronic devices, it is crucial to understand the coupling between molecular spins and a magnetic metal surface. Metal phthalocyanines (Pc's) have attracted much interest due to their characteristic electronic and magnetic properties. Especially, iron(II) phthalocyanine (FePc) is one of these interesting and fundamental compounds because it takes the unusual intermediate triplet spin state and has large orbital moment. In this study, we report on the magnetic property of FePc on clean Cu(001) and magnetic Co layer grown on Cu(001) by means of X-ray magnetic circular dichroism (XMCD) at BL4B, which equipped with a super conducting magnet system.

Sample preparation and XMCD measurement were carried out in UHV chambers. A Cu(001) single crystal was cleaned by repeated cycle of Ar^+ sputtering and annealing. A Co layer was deposited on the clean Cu(001) at room temperature (RT). Purified FePc was deposited on these substrates at RT by sublimation and the thicknesses of the films were monitored by a quartz crystal oscillator. The intensity dependence of N K-edge X-ray absorption spectra (XAS) for the FePc film with X-ray incident angle indicated that the molecular was parallel to the substrate plane. The XAS and XMCD spectra were taken at 5 K and the XMCD spectra were recorded with reversal of magnetic field.

Figure 1 shows Fe L-edge XAS spectra of 25 ML FePc on clean Cu(001) and 1 ML FePc on Co(3ML)/Cu(001) at incident angle θ = 55°. The spectra of 25 ML film represent the electronic state of only FePc film because XAS is very surface sensitive. On the other hand, the shape of 1 ML FePc spectra is quite different from that of 25 ML FePc due to interaction between the FePc molecule and the Co layer.

The XMCD spectra of these films are showed in Fig. 2, which were taken at H = ±0 T (remanence) and ±5 T (saturation) and at temperature of 5 K. Both L_2 and L_3 XMCD signs of the 25 ML FePc film are negative, which indicates that the FePc film has a large orbital magnetic moment. In addition, the magnetic moments were detected in both films in remanence, which means that both films are ferromagnetic at 5 K. The remanent magnetization in the 1 ML FePc on Co layer is larger than that in the 25 ML FePc film on clean Cu(001). Additionally, magnetization curves measured for 1 ML FePc film on Co layer, which were recorded with Fe L_3-edge intensity for FePc films and with Co L_3-edge intensity for underlying Co layer, behaved similar dependence

with magnetic field. This result suggests the presence of a ferromagnetic exchange coupling between the Fe atom in the molecular and the Co atom in the underlying layer.
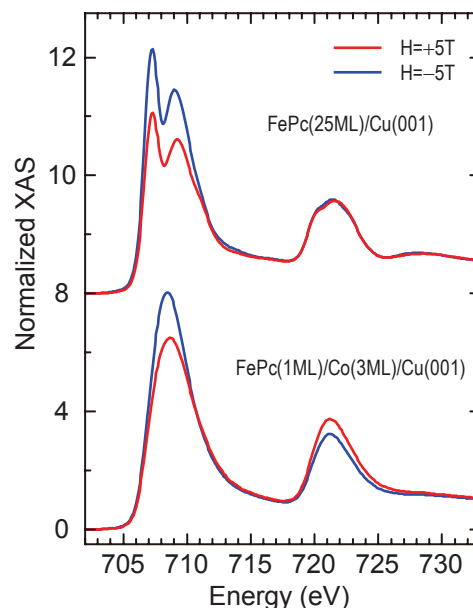

Fig. 1. Fe L-edge XAS spectra of 25 ML FePc on clean Cu(001) and 1 ML FePc on Co(3 ML)/Cu(001) at incident angle θ = 55º from the surface normal at H = 5 T.
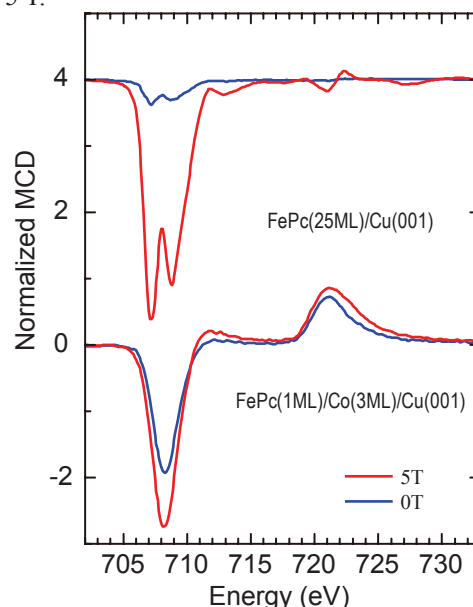

Fig. 2. Fe L-edge XMCD spectra of 25 ML FePc on clean Cu(001) and 1 ML FePc on Co(3 ML)/Cu(001) at incident angle θ = 55º from the surface normal.

Ⅲ-4. SURFACE AND THIN FILMS

Electronic Structure of the Ferromagnetic Semiconductor EuO Ultrathin Films

H. Miyazaki[1], T. Hajiri[2], M. Matsunami[1,3], T. Ito[2] and S. Kimura[1,3]

[1]*UVSOR Facility, Institute for Molecular Science, Okazaki 444-8585, Japan*
[2]*Graduate School of Engineering, Nagoya University, Nagoya 464-8603, Japan*
[3]*School of Physical Sciences, The Graduate University for Advanced Studies,*
Okazaki 444-8585, Japan

Europium monoxide (EuO) is a ferromagnetic semiconductor with the Curie temperature (T_C) at around 70 K [1, 2]. The magnetic moment originates from the half-filled 4f shell of the Eu^{2+} ion with the spin magnetic moment of $S = 7/2$. Recently, we have revealed that the magnetism of EuO is caused by the hybridizations of the Eu 4f – O 2p and Eu 4f – 5d [3-5]. Appling EuO for spintronics devices such as spin filter tunnel barriers [3], it is important to investigate the physical properties as well as the electronic and magnetic structure of EuO thin films with a few nanometer-thicknesses. Three-dimensional angle-resolved photoemission spectroscopy (3D-ARPES) using synchrotron radiation is the most powerful technique to directly determine the electronic band structure. Using this technique, we observed the change of the electronic structure across T_C.

Single-crystalline EuO ultrathin films with thickness of about 2 nm were fabricated by a molecular beam epitaxy (MBE) method. Epitaxial growth of the single-crystalline EuO ultrathin films with the 1 x 1 EuO (100) patterns was confirmed by a low energy electron diffraction (LEED) method. T_C was evaluated to be about 40 K by a magneto-optical Kerr effect (MOKE) *in-situ*. The 3D-ARPES measurements were performed at the beam line BL5U of UVSOR-II combined with the MBE system. The EuO ultrathin films grown in the MBE chamber and were transferred to a 3D-ARPES chamber under UHV condition. The total energy and momentum resolutions for the ARPES measurement were set to 45 meV and 0.014 Å^{-1} at the X point ($h\nu = 38$ eV), respectively.

Figure 1 (a) shows the energy distribution curves (EDCs) of EuO (100) ultrathin film with a thickness of 2 nm near the X point at 5 K (ferromagnetic phase). From a comparison with the band calculation, the observed states at a binding energy E_B of 1.0 – 3.5 eV and 4.0 – 7.0 eV are attributed to the Eu 4f and O 2p states, respectively. From our previous results [5], the observed dispersive features of the Eu 4f states around the X point indicates the hybridization of the Eu 4f and O 2p states, leading to the origin of the ferromagnetic phase transition of EuO. Figure 1 (b) shows the temperature dependence of the peak energies of the Eu 4f states at the X point derived from the second-derivative EDCs. There are two Eu

4f bands at the X point, which shift to the lower binding energy side on cooling across T_C of 40 K. The energy shifts of the higher binding energy peak are small compared to the bulk ones, corresponding to the decrease of T_C. This result indicates that the hybridization intensity between the Eu 4f and other states becomes weaker with decreasing thickness. This result is consistent with our recent thickness-dependent band calculation.
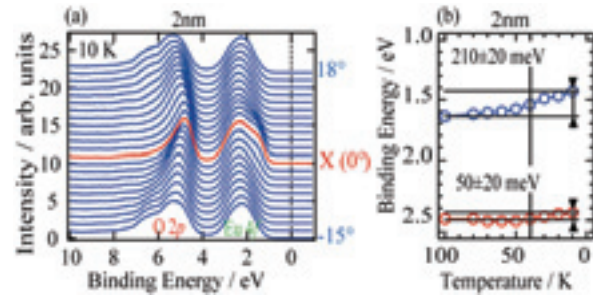

Fig. 1. (a) Energy distribution curves (EDCs) of an EuO (100) ultrathin film (2 nm thickness) near the X point. (b) Temperature dependence of the peak energies at the X point derived from the second-derivative EDCs of the Eu 4f states.

[1] N. Tsuda *et al*., Electronic Conduction in Oxides (Springers College) (1976).
[2] A. Mauger *et al*., J. Phys. (paris) **39** (1978) 1125.
[3] H. Miyazaki *et al*., Physica B **403** (2008) 917.
[4] H. Miyazaki *et al*., Jpn. J. Appl. Phys. **48** (2009) 055504.
[5] H. Miyazaki *et al*., Phys. Rev. Lett. **102** (2009) 227203.
[6] M. Müller *et al*., J. Appl. Phys. **105** (2009) 07C917.

III-4. SURFACE AND THIN FILMS

Quantum Topological Phase Transition in Ultrathin Bi$_2$Se$_3$ Films

Y. Sakamoto[1], T. Hirahara[1], H. Miyazaki[2], S. Kimura[2] and S. Hasegawa[1]

[1]*Department of Physics, University of Tokyo, Tokyo 113-0033, Japan*
[2]*UVSOR Facility, Institute for Molecular Science, Okazaki 444-8585, Japan*

Topological insulators (TI) are a novel state of quantum matter in three dimensions (3D) that have been gaining increased attention. Along with its two-dimensional (2D) counterpart, the quantum spin Hall (QSH) phase, they are mathematically characterized by the so-called Z$_2$ topological number [1]. While the bulk is insulating with an inverted gap, there is a metallic edge or surface state which is topologically protected and hence robust against weak perturbation or disorder.

One of the important aspect in the study of TI is the phase transition between the trivial (normal) and the topological state. The principal issue here is the exchange of the parity of conduction and valence bands by changing some external parameter. One example is the case of HgTe/CdTe quantum well. In this case, it was reported that by reducing the thickness of the well below a critical thickness of d_c = 60 Å, the inverted band gap (band gap Δ<0) once closes (Δ=0) and becomes a normal band gap (Δ>0) as schematically shown in Fig. 1 (a). Thus reducing the system size and changing the dimensionality does not only have the advantage that the surface-sensitivity is enhanced which will make the surface-state property more apparent in terms of 3D TI, but is also important in determining if the system is trivial or topological in 2D.

Bulk Bi$_2$Se$_3$ is a 3D topological insulator with an inverted band gap and its surface states possess a linear band dispersion expressed by the Dirac equation [Fig. 1 (b)]. In a recent theoretical work, it was shown that this Hamiltonian possess similarity to the 2D QSH effective Hamiltonian for the HgTe quantum wells. The authors predicted that an energy gap will open in the surface-state dispersion due to the interaction between the top and bottom surfaces for thin film thicknesses. Furthermore, it was shown that the inverted gap will close at d_c = 25 Å for Bi$_2$Se$_3$, and below d_c a normal band gap will develop so the system will become trivial [Fig. 1 (a)] [2]. Therefore a topological quantum phase transition is predicted to occur in the thin film limit. However this has not been experimentally demonstrated yet.

In the present study, we have performed angle-resolved photoemission spectroscopy (ARPES) measurements on ultrathin Bi$_2$Se$_3$ films on silicon to verify if the phase transition actually takes place. Figure 2 shows the band dispersion for 2 (a), 3 (b) and 8 (c) quintuple layer (1 QL = 9.5 Å) ultrathin Bi$_2$Se$_3$ films measured at the photon energy of 20 eV using circularly-polarized light. The band structure for the 8 QL film is similar to that found in bulk
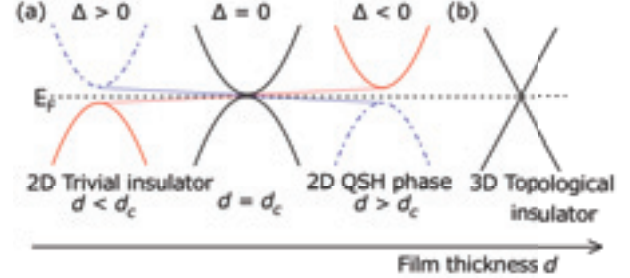

Fig. 1. Schematic drawing of the topological quantum phase transition in 2D. (b) Schematic drawing of the surface-state linear band dispersion of the 3D TI.
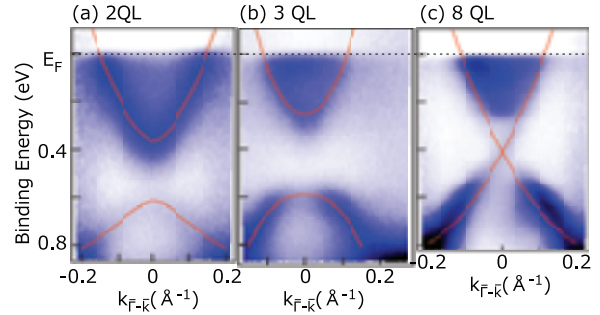

Fig. 2. E-k band dispersion images for the 2 QL (a), 3 QL, and 8 QL ultrathin Bi$_2$Se$_3$ films along the Γ-K direction. The overlapped lines show the fitted curves using Eq. (1).

single crystals, showing the bulk bands just near the Fermi level as well as the Dirac surface states. On the other hand, the 2 and 3 QL films show a clear gap opening in the surface-state dispersion. However, the gap size is larger for the 3 QL film than the 2 QL one, which is counterintuitive to our understanding for particles confined in a potential, suggesting the occurrence of a parity reversal. Moreover, by fitting the measured images to (red solid lines in Fig. 2)

$$E_\pm = E_0 - Dk^2 \pm \sqrt{(v_F \hbar k)^2 + (\Delta/2 - Bk^2)^2} , \quad (1)$$

we are able to deduce the sign of Δ and B which are related to the edge-state Hall conductance. This quantitative analysis also supported the occurrence of a transition from a QSH state (3 QL) to a trivial phase (2 QL). Thus we have found experimental evidence of a quantum topological phase transition in this system [3].

[1] L. Fu and C. L. Kane, Phys. Rev. B **76** (2007) 045302.
[2] H.-Z. Lu *et al.,* Phys. Rev. B **81** (2010) 115407.
[3] Y. Sakamoto *et al.,* Phys. Rev. B **81** (2010) 165432.

Very Narrow Intermolecular Electronic Band Dispersion in a Crystalline Film of Zn-Phthalocyanine

H. Yamane and N. Kosugi

Dept of Photo-Molecular Science, Institute for Molecular Science, Okazaki 444-8585, Japan

The electronic band dispersion, energy *versus* wave vector $E(\boldsymbol{k})$, is a fundamental parameter to understand electric properties of solids such as hole mobility (μ_h). In the field of organic semiconductors, the study of the intermolecular $E(\boldsymbol{k})$ shows a rapid progress due to the needs of the interpretation of the charge transport mechanism in molecular electronic devices. However, due to the very weak intermolecular interaction and the difficulty in preparing crystallized films sufficient for the $E(\boldsymbol{k})$ measurement, the observation of the intermolecular $E(\boldsymbol{k})$ has been limited to the case of high-μ_h materials. In order to elucidate and control the functionality of organic semiconductors, a systematic and quantitative experiment on the intermolecular interaction can play a crucial role. In this work, we have succeeded to observe a narrow intermolecular $E(\boldsymbol{k})$ in crystalline films of Zn-phthalocyanine (ZnPc), which is one of the promising materials in the field of organic electronics. The present observation may pave the way for the systematic band structure analysis in the field of organic semiconductors.

The present experiment was performed using the angle-resolved photoemission spectroscopy (ARPES) system at BL6U. The crystallinity of the sample was confirmed by low-energy electron diffraction (LEED) and by the N K-edge X-ray absorption spectroscopy (XAS) in the sample-current mode. The $E(\boldsymbol{k})$ relation was measured by ARPES at normal emission as a function of the incident photon energy ($h\nu$), which scans the $\boldsymbol{k}$ component along the surface normal. The sample temperature at all measurements was 15 K.

Figure 1 shows the incident angle (α) dependence of N K-edge XAS spectra for the 30-nm-thick films of ZnPc on Au(111). The sharp $1s \rightarrow \pi^*$ transition peaks appear at $h\nu = 398 \sim 405$ eV. These peaks are strongest at grazing incidence ($\alpha = 60°$) and are getting weaker with decreasing α. Other broad $1s \rightarrow \sigma^*$ transition features ($h\nu > 405$ eV) show the opposite trend. From the data analysis, we found that the ZnPc film on Au(111) is well oriented with their molecular plane parallel to the substrate surface.

Figure 2 shows the $h\nu$ dependent ARPES spectra at the normal emission for the ZnPc crystalline film on Au(111). Since the ZnPc crystalline film on Au(111) shows a Stranski-Krastanov growth mode, there are the remanent substrate signal such as a Fermi edge, which we used for the fine $h\nu$ calibration. For the ZnPc-derived peaks A, B, and C, we have observed a clear dispersive behavior with $h\nu$, wherein (i) the periodicities of A–C are same in the $\boldsymbol{k}$ space and (ii) the bandwidth of peak A, originating from the highest occupied molecular orbital (HOMO), is 120 meV.

The present observation clearly indicates that the band-like transport can be realized in phthalocyanine films by the control of the geometric film structure. Moreover, the present result can be a benchmark for the systematic study on the intermolecular interaction, e.g., intermolecular $E(\boldsymbol{k})$ as a function of the central metal atom in the phthalocyanine molecule, which enables to discuss experimentally the intermolecular interaction in terms of the intermolecular distance and the molecular orbital symmetry.
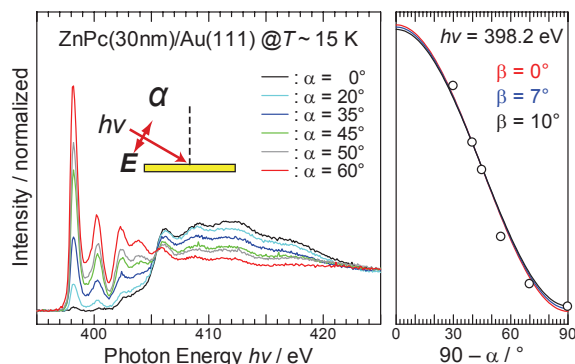
Fig. 1. The α dependence of N K-edge XAS spectra for the crystalline ZnPc films on Au(111) at 15 K.
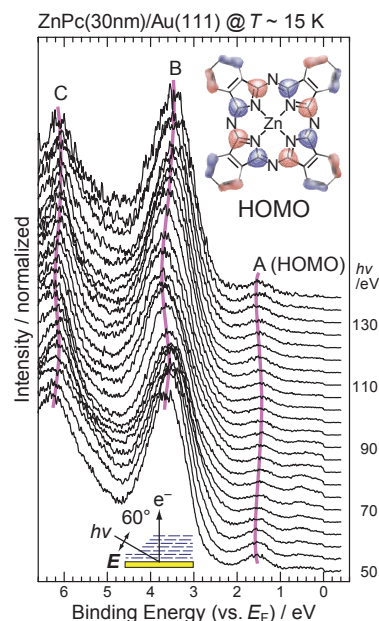

Fig. 2. The $h\nu$ dependence of ARPES spectra (4 eV step) at the normal emission for the crystalline ZnPc films on Au(111) at 15 K.

Interface Electronic Structure of Crownether-Derivatives on Cu(111)

H. Machida[1], K. Yonezawa[1], M. Yamamoto[1], S. Hosoumi[1], T. Hosokai[2], T. Nishi[3], N. Ueno[1], and S. Kera[1,3]

[1]*Graduate School of Advanced Integration Science, Chiba University, Chiba 263-8522, Japan*
[2]*Institut für Angewandte Physik, Universität Tübingen, Tübingen 72076, Germany*
[3]*Institute for Molecular Science, Okazaki 444-8585, Japan*

Studies on the adsorption of large π-conjugated organic molecules on metal surfaces have increased considerable attentions, since the molecule/substrate interaction crucially influences electronic functions of organic devices. A missing study of the interface issue is on a molecular system with structural flexibility by sp^3 bond (σ bond) in its main backbone. To reveal physical properties of such flexible molecules, we studied the valence electronic structure of tetrabromide-dibenzo-18-crown-6 (BDBC) thin films prepared on Cu(111) by using angle-resolved ultraviolet photoelectron spectroscopy (ARUPS).

Experimental

ARUPS spectra were measured at photon incidence angle α=60°, hv=28 and 100 eV and T=295 K. The molecules were evaporated onto the Cu(111). The monolayer (ML) formation was confirmed by the work function of the densely packed ML that shows a clear LEED pattern. High-resolution UPS spectra were also recorded using HeI light source.

Results and Discussion

Figure 1 (a) shows the HeI UPS of BDBC(ML) on Cu(111) together with BDBC(ML)/HOPG and DOS by DFT calculation. The spectrum (1: thick curve) is shown after the background subtraction. All the bands of BDBC/Cu(111) are shifted to low-binding energy (Eb) side by 0.3-0.4 eV compared with BDBC/HOPG. Bands A (HOMO) and B seem to split on Cu(111)

due to strong coupling. An interface state (G) appears at the band-gap region.

Figure1 (b) shows the UPS at Br(3d) region. Bands L and M are due to spin-orbit splitting and shifted to low-Eb side by 2.1 eV (bands L' and M') for BDBC(ML)/Cu(111), indicating Br atoms interact more strongly with Cu(111).

Figures1 (c) and 1 (d) show ARUPS results for annealed-BDBC(ML)/Cu(111) along Γ–K direction. The photoelectron angular distributions (PAD) of split bands A_1 and A_2 are evaluated by curve fitting. These PAD patterns are different but show a nearly similar distribution, indicating both states could originate from the HOMO (π state distributed at phenyl rings) of a free BDBC and may split due to hybridization with the substrate, which may give differences in the π-MOs distribution. Moreover, the PADs have broad distribution around θ=0-30°, leading the phenyl rings (π planes) are inclined to the substrate surface. All these show a clear evidence of chemisorptive interaction at BDBC/Cu(111) interface. An expected BDBC structure on Cu(111) is shown at the bottom of Fig.1 (d). The molecule-substrate distance and molecular deformation evaluated by x-ray standing wave measurements remarks a closer distance to the Cu(111) for Br atoms than other elements, which is consistent with the present UPS results.
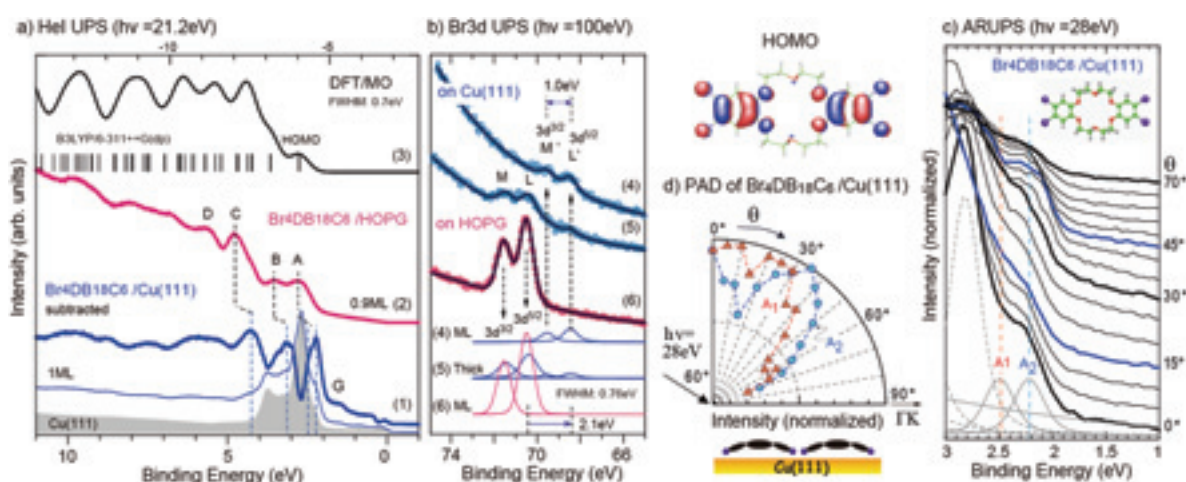

Fig. 1. (a) He I UPS of a clean Cu(111), BDBC(1ML)/Cu(111), and background subtracted BDBC(1ML) spectrum(1) together with BDBC(0.9 ML)/HOPG(2) and DFT-simulated spectrum(3). (b) Br(3d)-region UPS for 1ML/Cu(111)(4), thick-island film(7 nm)/Cu(111)(5) and 1ML/HOPG(6). Deconvoluted features in each spectrum are shown at the bottom. (c) ARUPS along Γ–K direction for BDBC(annealed ML)/Cu(111). (d) PAD for bands A_1(orange triangles) and A_2(blue circles). HOMO distribution on gas-phase and expected molecular conformation on Cu(111) are also shown.

ARUPS Study of Pentacene Thin Film on Uniaxially Oriented PTFE Film

K. K.Okudaira, K. Ito, K. Hotta and N. Ueno

Association of Graduate Schools of Science and Technology, Chiba Univererity,
Chiba 263-8522, Japan

Introduction

Electroactive organic molecules have attracted much attention owing to their versatility and unique electronic properties of interest for the design of optoelectronic and electronic devices. In-plane orientation of pentacene films has been performed in order to improve the transport properties in OFETs. Fabrication of oriented structure such as uniaxially oriented crystallites is important to obtain the oriented growth of materials as a substrate. The uniaxially poly(tetrafluoroethylene) (PTFE) films can be used as orienting media onto various substrate [1]. In this study, we observe angle-resolved ultraviolet photoelectron spectroscopy (ARUPS) and show the anisotropic orientation of pentacene (Pn) film on the uniaxially oriented PTFE thin films by evaporation onto the uniaxially polished Cu plate.

Experimental

ARUPS measurements were performed at the beam line BL8B of the UVSOR storage ring at the Institute for Molecular Science. The take-off angle (θ) dependencies of photoelectron spectra were measured at incident angle of photon (α) = 45° with the photon energy (hν) of 40 eV. At first (PTFE) was deposited on uniaxially polished polycrystal Cu plate by polishing paste (alumina particles with mean radius of about several μm) (PTFE(5nm)/Cu). An additional organic layer of pentacene was subsequently evaporated to a final thickness of 10 nm on the uniaxially PTFE(5nm)/Cu (Pn(10nm)/ PTFE (5nm)/ Cu).

Results and Discussion

Figures 1 (a) and (b) show the take-off angle (θ) dependences of ARUPS spectra of Pn(10nm)/ PTFE (5nm)/Cu with the parallel condition (the polarization plane of incidence photon is parallel to the polishing direction of Cu plate) and the perpendicular condition (the polarization plane of incidence photon is perpendicular to the polishing direction of Cu plate), respectively. The peak located at binding energy of about 1 eV corresponds to the localized π state (HOMO). Figure 2 shows the θ dependence of photoelectron from HOMO band with the parallel and perpendicular condition The θ dependences with parallel condition have a sharp maxima at θ= 65°. On the other hand, with the perpendicular condition, the intensity of HOMO band does not show a strong θ dependence. They indicate that the molecular orientation of pentacene film in parallel to polishing direction for Cu plate is different from that in

perpendicular to polishing direction. It was found that pentacene molecules show anisotropic molecular orientation on uniaxially oriented PTFE film.

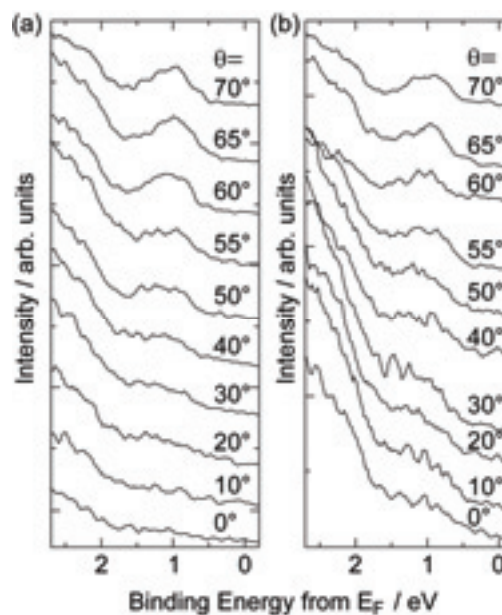[1] J. C. Wittmann et al., Nature **352** (1991) 414.

Fig. 1. Take-off angle (θ) dependences of ARUPS of Pn(10nm)/PTFE(5nm)/Cu with (a) parallel and (b) perpendicular condition , respectively.
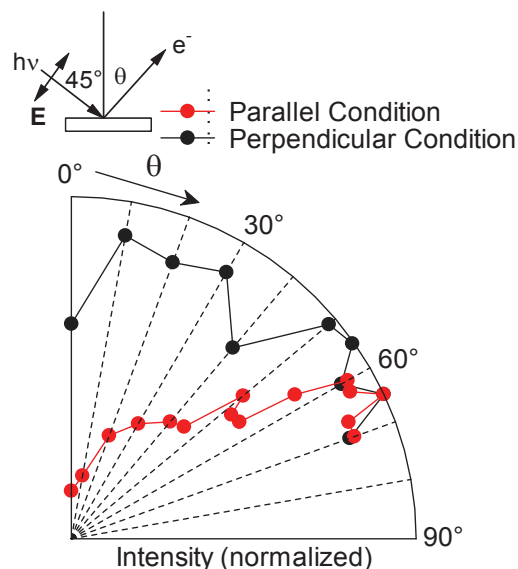

Fig. 2. Take-off angle (θ) dependences of photoelectron intensities of HOMO peak of Pn(10nm)/PTFE(5nm)/Cu with parallel (●) and perpendicular condition (●).

Nodeless Superconducting Gap in $A_xFe_2Se_2$ (A=K, Cs) Revealed by Angle-Resolved Photoemission Spectroscopy

Y. Zhang[1], L. X. Yang[1], M. Xu[1], Z. R. Ye[1], F. Chen[1], C. He[1], H. C. Xu[1], J. Jiang[1], B. P. Xie[1], J. J. Ying[2], X. F.Wang[2], X. H. Chen[2], J. P. Hu[3], M. Matsunami[4], S. Kimura[4] and D. L. Feng[1]

[1] *State Key Laboratory of Surface Physics, Advanced Materials Laboratory, and Department of Physics, Fudan University, Shanghai 200433, China*

[2] *Hefei National Laboratory for Physical Sciences at Microscale and Department of Physics, University of Science and Technology of China, Hefei, Anhui 230026, China*

[3]*Department of Physics, Purdue University, West Lafayette, Indiana 47907, USA*

[4]*UVSOR Facility, Institute for Molecular Science and The Graduate University for Advanced Studies, Okazaki 444-8585, Japan*

Pairing symmetry is a fundamental property that characterizes a superconductor. For the iron-based high-temperature superconductors, an s±-wave pairing symmetry has received increasing experimental and theoretical support. More specifically, the superconducting order parameter is an isotropic s-wave type around certain Fermi surface, but it has opposite signs between the hole Fermi surfaces at the zone center and the electron Fermi surfaces at the zone corners.

Recently, a new series of iron-based superconductors, $A_xFe_2Se_2$ (A=K, Cs), has been discovered with relatively high transition temperature of ~30 K [1]. We have conducted angle-resolve photoemission spectroscopy (ARPES) experiment on $A_xFe_2Se_2$ (A=K, Cs) at beamline BL7U [2].

Figure 1 (a) reveal the photo emission intensity map along out-of-plane momentum (k_z) in the ΓZAM plane. The cross-sections of the κ and δ Fermi surfaces clearly show weak dispersion along the k_z direction, indicative of a rather two-dimensional electronic structure. The spectral weight of κ increases from Γ to Z, and a small electron pocket could be clearly observed for the κ band around Z [Fig. 1 (b)]. This gives an electron pocket around Z with its residual spectral weight extending towards Γ. However, we emphasize that the size of the κ pocket is much smaller than that of the δ pocket, which is rather k_z-independent as illustrated in Fig. 1 (c). The experimental Fermi surface topology clearly shows that there is no hole Fermi surface near the zone centre, and $A_{0.8}Fe_2Se_2$ is indeed the most heavily electron-doped iron-based superconductor by far.

The momentum distribution of superconducting gap is deduced in Fig. 2. The gap of the band around the M point is of the isotropic s-wave type within the experimental uncertainty, which averagely is about 10.3 meV. Further data taken with different photon energies in Fig. 2 (b) indicate such a gap does not vary with the out-of-plane momentum k_z. Smaller gap about 7 meV could be observed for the κ band with little k_z-dependence.

Our data show that the rather robust superconductivity in such a highly electron-doped

iron-based superconductor could mainly rely on the electron Fermi surfaces near M. Thus, the sign change in the s± pairing symmetry driven by the inter-band scattering as suggested in many weak coupling theories becomes conceptually irrelevant in describing the superconducting state here. A more conventional s-wave pairing is probably a better description.
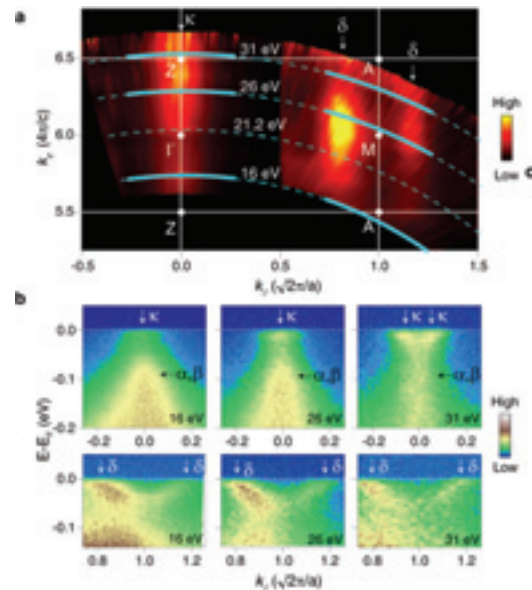

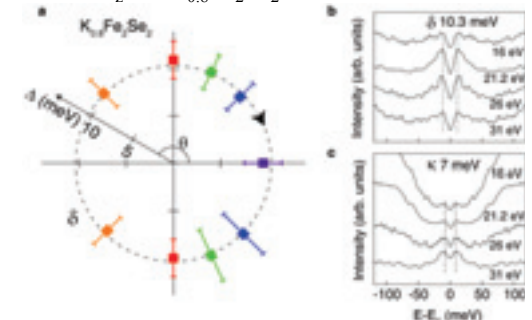Fig.1. The Fermi surface and band structure as a function of k_z for $K_{0.8}Fe_2Se_2$.

Fig. 2. Momentum dependence of the superconducting gap of $K_{0.8}Fe_2Se_2$.

[1] J. Guo *et al*., Phys. Rev. B **82** (2010) 180520.
[2] Y. Zhang *et al*., Nature Materials, **10** (2011) 273.

Ⅲ-5. SOLID STATE PHYSICS

Characterization of Magnesium in Huntite by an XAFS Method

T. Kurisaki[1], D. Tanaka[1], S. Kokubu[1] and H. Wakita[1,2]

[1] *Department of Chemistry, Faculty of Science, Fukuoka University,*
Fukuoka 814-0180, Japan
[2] *Advanced Materials Institute, Fukuoka University Fukuoka 814-0180, Japan*

A huntite was called 'a hanto-ishi' and was used as a pigment of the white in ancient Egypt. This mineral chemical formula is expressed in $CaMg_3(CO_3)_2$. The huntite has very few reports about locality, and it is a rare mineral. However, this mineral is used abundantly in ancient Egypt. On the other hand, the dolomite is a general carbonate that has a similar chemical composition to the huntite. But, the dolomite was not used as a white pigment It is not apparent why the huntite which is a rare mineral was used as a pigment of the white. It is reported that the huntite is produced in Nagasaki. The X-ray absorption spectroscopy is frequently used for steric and electronic structure analyses because it gives good information on the local structure and oxidation state of the absorbing atom [1]. We performed electronic structure analysis of calcium in the huntite using the XAFS method in last year.

In this work, we performed the XANES spectra measurement about various magnesium salts and minerals such as huntite and dolomite. The obtained experimental XANES spectra are analyzed using the calculated theoretical spectra from DV-Xα calculations. The X-ray absorption spectra were measured at BL1A of the UVSOR in the Institute of Molecular Science, Okazaki [2]. The ring energy of the UVSOR storage ring was 750 MeV. Mg K-edge absorption spectra were recorded in the regions of 1275-1380 eV by use of two Beryl crystals. The absorption was monitored by the total electron yield using a photomultiplier. The samples were spread onto the carbon tape on the first photodynode made of CuBe of the photomultiplier.

Figure 1 shows the observed Mg K-edge XANES spectra for the Huntite and Dolomite. The Mg-K XANES spectra of Huntite and Dolomite show different peak profiles at second peaks. This result shows that the magnesium in these minerals has different electronic states. We are going to try to calculate the spectra by DV-Xα molecular orbital calculations. The calculated XANES spectra and the observed XANES spectra of the Huntite and the Dolomite are shown in Fig. 2.

The observed XANES spectra and the calculated XANES spectra showed good agreement. The peak A is estimated to the electron transition (mainly Mg 1s to unoccupied mixed orbital consisting of O 3d, O 3p, O 3s and O 4s). The obtained XANES spectra are analyzed using the calculated spectra from DV-Xα calculations.
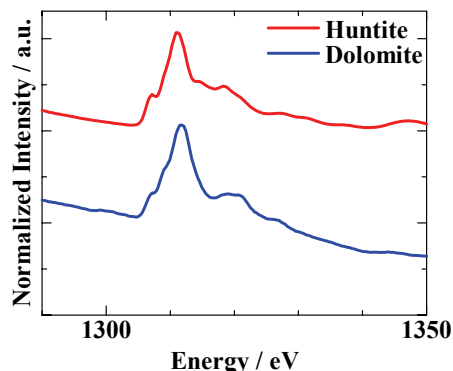

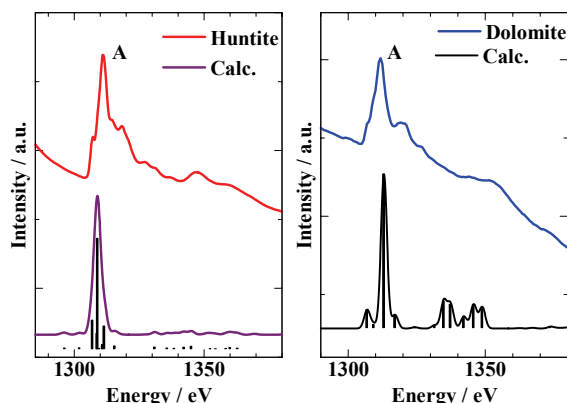Fig. 1. Observed Mg K-edge XANES spectra of Huntite and Dolomite.

Fig. 2. The comparison of observed XANES spectra with calculated XANES spectra for Mg K-edge.

[1] T. Kurisaki, S. Matsuo, I. Toth and H. Wakita, Anal. Sci. **24** (2008) 1385.

[2] S. Murata, T. Matsukawa, S. Naoè, T. Horigome, O. Matsuodo and M. Watatabe, Rev. Sci. Instrum. **63** (1992) 1309.

Temperature Dependence of Polarized Fundamental Absorption-Edge Spectra of PbMoO$_4$

M. Fujita[1] and M. Itoh[2]

[1] Japan Coast Guard Academy, Kure 737-8512, Japan

[2] Dept. Electrical and Electronic Engineering, Shinshu University, Nagano 380-8553, Japan

Lead molybdate (PbMoO$_4$) is well known as a superior medium for acousto-optic devices. This material also attracts attention because of its great potential to be used as an effective cryogenic detector for double β decay experiments. The crystal has the scheelite structure with the optical axis along the *c*-axis. Recently we found remarkable dichroism of the lowest exciton band at 3.6 eV in PbMoO$_4$ [1]. In the present study, we have measured the temperature dependence of the fundamental absorption-edge spectra of PbMoO$_4$ crystals with use of polarized light.

PbMoO$_4$ samples were obtained from Furukawa Company. They were grown by the Czochralski technique from the raw materials of PbO of 99.99% purity and MoO$_3$ of 99.9% purity in 1:1 molar ratio, and was purified by three-time crystallization. The thickness of the sample was 2.0 mm.

The absorption spectra for the polarization parallel to the *a*-axis (**E**//**a**) and *c*-axis (**E**//**c**) measured at various temperatures are shown in Figs. 1 (a) and (b), respectively. Distinct dichroism is observed at each temperature. For **E**//**a**, a weak absorption band is observed as a shoulder superimposed on the tail above 150 K. The band shows significant red shift and becomes remarkable with increasing temperature. Such structure is not observed for **E**//**c**. It should be noted that the exciton absorption band [1] and the shoulder structure in Fig. 1(a) are both observed distinctly for **E**//**a**, while they are extremely weak or not discernible for **E**//**c**. This correspondence suggests that the shoulder structure is attributed to the exciton absorption perturbed by some lattice defects [2].

In contrast to the case of **E**//**a**, no additional structure is observed in the tail region for **E**//**c** at temperatures between 6 and 300 K. In Fig. 2 are plotted the absorption coefficients for **E**//**c** in a logarithmic scale. The straight lines fitted to the linear portions of the experimental curves for $T \geq 100$ K converge to a point. This fact indicates that the Urbach rule, $\alpha = \alpha_0 \exp\{-\sigma(E_0-E)/k_B T\}$, holds for PbMoO$_4$ as in the case of PbWO$_4$ [3]. The parameters of the conversing point are obtained as $\alpha_0 = 1.5 \times 10^4$ cm^{-1} and $E_0 = 3.52$ eV. The steepness parameters σ at $T \geq$ 100 K are plotted by open circles in the inset in Fig. 2. The solid curve in the inset shows the best fit of the equation, $\sigma(T) = \sigma_0(2k_B T/\hbar\omega)\tanh(\hbar\omega/2k_B T)$ to the data points with the high-temperature steepness parameter $\sigma_0 = 0.67$ and average photon energy $\hbar\omega = 26$ meV.

An exciton in three-dimensional lattices becomes self-trapped and gives rise to a luminescence band with large Stokes shift, when the value of σ_0 is smaller than the critical value $\sigma_c = 1.50$. The present value of σ_0 is considerably smaller than this critical value, indicating that the exciton-phonon coupling is strong in PbMoO$_4$. In fact, the intrinsic luminescence due to self-trapped excitons in PbMoO$_4$ is observed with a peak at around 2.3 eV when excited with light of the photon energies above 3.3 eV. The large Stokes shift (~ 1.0 eV) of the intrinsic luminescence band is in satisfactorily agreement with the above conclusion on the strong exciton-phonon coupling in PbMoO$_4$.
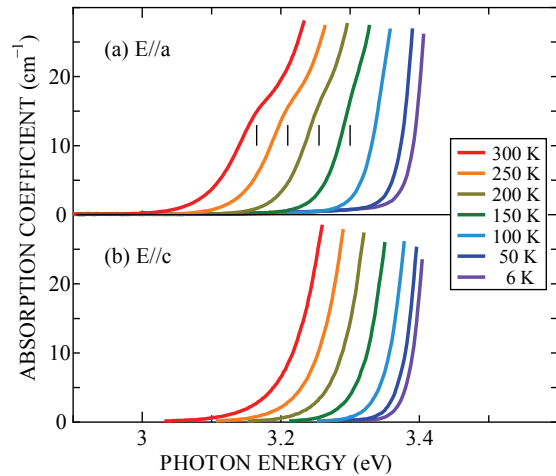

Fig. 1. Absorption-edge spectra of PbMoO$_4$ at various temperatures for (a) **E**//**a** and (b) **E**//**c**.
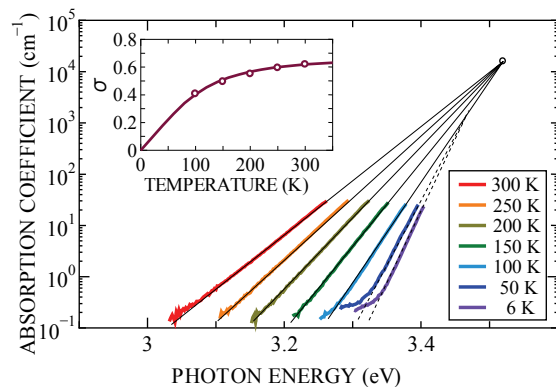

Fig. 2. Logarithmic plot of the absorption spectra for **E**//**c**. In the inset is shown the temperature dependence of σ.

[1] M. Fujita *et al*., Phys. Status Solidi B **247** (2010) 405.

[2] M. Fujita and M. Itoh, Phys. Status Solidi B **247** (2010) 2240.

[3] M. Itoh *et al*., Phys. Status Solidi B **231** (2002) 595.

III-5. SOLID STATE PHYSICS

Luminescence Properties of KCl:Ag⁻ Crystals under the Excitation around the Fundamental Absorption Edge

T. Kawai[1] and T. Hirai[2]

[1]*Graduate School of Science, Osaka Prefecture University, Sakai 599-8531, Japan*
[2]*Faculty of Science and Engineering, Ritsumeikan University, Kusatsu 525-8577, Japan*

In KCl crystals containing iodine ions as hetero halogen ions, the absorption bands due to the I⁻ ions are observed around the fundamental absorption edge of the KCl crystals. The excitation on these absorption bands induces the several luminescence bands due to the localized exciton [1-3]. Among these luminescence bands, the luminescence bands observed in the visible energy region are called the BG and B bands and are attributed to the radiative decay from the relaxed exciton state which consists of a hole localized on a pair of an iodine and chlorine anion and a bound electron, $[(Cl\ I)^- + e^-]$.

In this study, we have investigated luminescence properties of KCl crystals doped with Ag⁻ centers under the excitation around the fundamental absorption edge. Since the Ag⁻ anions doped in alkali halide crystals are substituted for the halogen ions, the Ag⁻ anions would be regarded as pseudo halogen ions. Therefore, the localized excitons related with the Ag⁻ ions would be existed in the same way as the localized excitons in KCl:I crystals.

Figure 1 shows the luminescence spectra of KCl: Ag⁻ crystals at 10 K, which are measured at BL1B of the UVSOR facility. Under the excitation on the various energies between 6.42 and 7.21 eV, the luminescence band peaking at 2.91 eV is observed. The 2.91 eV luminescence band is attributed to the radiative transition from the relaxed excited state of $^3T_{1u}$ in the Ag⁻ center and is called the A' luminescence band [4, 5]. The excitation on 8.26 eV above the intrinsic exciton band of KCl crystals brings about a broad luminescence band at 2.30 eV, which is ascribed to the intrinsic STE in KCl single crystals [6]. It should be noted that a broad luminescence band having a halfwidth of 0.52 eV is observed at 2.60 eV under the excitation on the energy region between 6.66 and 7.21 eV, in addition to the A' luminescence band. The excitation spectra for the 2.60 eV and STE luminescence bands are shown in the insert of Fig. 1. The excitation spectrum for the STE luminescence band exhibits the sharp response at 7.65 and 8.27 eV and is consistent with that reported previously [6]. On the other hand, the excitation spectrum for the 2.60 eV luminescence band exhibits the sharp responses at 6.70, 7.14, and 7.59 eV.

The 2.60 eV luminescence band in KCl:Ag⁻ is very similar to the BG luminescence band in KCl:I in the energy position and lineshape [1-3]. The excitation spectrum for the 2.60 eV luminescence band exhibits three sharp responses in the energy region between 6.70 and 7.60 eV. The excitation spectrum for the BG luminescence band in KCl:I also has the three responses in the same energy region [1-3]. The similarity between them leads us to the idea that the 2.60 eV luminescence band in KCl:Ag⁻ has it's origin in the two-center type localized exciton such as $[(Ag\ Cl)^- + e^-]$.
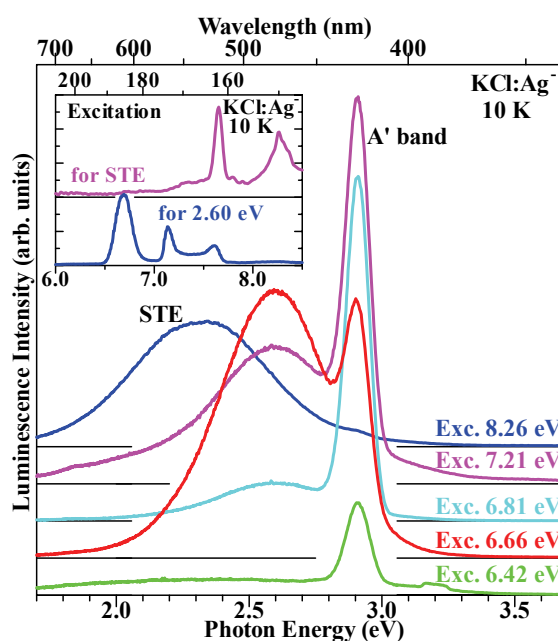

Fig. 1. Luminescence spectra of KCl:Ag⁻ crystals under the excitation around the fundamental absorption edge. Inset is excitation spectra for the STE and 2.60 eV luminescence bands.

[1] K. Kan'no, M. Itoh and Y. Nakai, J. Phys. Soc. Jpn. **47** (1979) 915.
[2] T. Higashimura, H. Nakatani, M. Itoh, K. Kan'no and Y. Nakai, J. Phys. Soc. Jpn. **53** (1984) 1878.
[3] A. Ohno and N. Ohno, Phys. Status Solidi C **8** (2011) 112.
[4] K. Kojima, S. Shimanuki, M. Maki and T. Kojima, J. Phys. Soc. Jpn. **28** (1970) 1227.
[5] W. Kleemann, Z. Physik **249** (1971) 145.
[6] K. Kan'no, T. Matsumoto and Y. Kayanuma, Pure & Appl. Chem. **69** (1997) 1227.

Optical Study in the Vacuum-Ultraviolet Energy Region of BaFe$_2$As$_2$

M. Nakajima[1,2,3], K. Kihou[2,3], C. H. Lee[2,3], A. Iyo[2,3], H. Eisaki[2,3] and S. Uchida[1,3]

[1]*Department of Physics, University of Tokyo, Tokyo 113-0033, Japan*
[2]*National Institute of Advanced Industrial Science and Technology, Tsukuba 305-8568, Japan*
[3]*JST, Transformative Research-Project on Iron Pnictides (TRIP), Tokyo 102-0075, Japan*

Introduction

The parent compounds of iron-arsenide superconductors, with BaFe$_2$As$_2$ as a representative example, are unique metals which exhibit a structural phase transition accompanied or followed by a magnetic phase transition. The magnetostructural state has attracted much attention as a proximate phase to a superconducting phase. To elucidate the mechanism of superconductivity in iron-based compounds, it is important to investigate the electronic properties in the normal state as well as those in the superconducting state.

Optical spectroscopy is one of the most useful methods for investigating the electronic dynamics in solids. If reflectivity is obtained for a wide energy range, optical conductivity can be derived through the Kramers-Kronig (K-K) transformation of the reflectivity spectrum. In this work, we measured reflectivity in the vacuum-ultraviolet (VUV) region of BaFe$_2$As$_2$. Reflectivity measurement in this energy region is necessary to obtain reliable optical conductivity for multi-band/orbital systems such as iron-pnictides or cuprates [1], since a number of intraband and interband excitations overlap in the same energy region and extend up to 10 eV or higher.

Experimental

Single crystals of BaFe$_2$As$_2$ were synthesized by a self-flux method [2]. The in-plane reflectivity spectrum in the VUV region between 4 and 35 eV was measured at room temperature using a Seya-Namioka-type grating at BL1B of UVSOR facility. The optical conductivity spectrum was obtained via K-K transformation of the measured reflectivity spectrum connected to the lower-energy one.

Results and Discussion

The in-plane reflectivity spectrum up to 32 eV is shown in Fig. 1. The reflectivity shows good coincidence with the result measured in the laboratory. Three distinct reflectivity edge appear at $\sim$ 1, $\sim$ 10, and $\sim$ 25 eV. Each edge indicates the end point of a series of intraband or interband excitations.

Figure 2 shows the conductivity spectra obtained by various extrapolations above 4.5 eV. If we use conventional extrapolation schemes for the K-K transformation, the obtained conductivity appreciably deviates from the present result, particularly in the region higher than 0.3 eV. Thus, the measurement in the VUV region is essential for quantitative analysis.
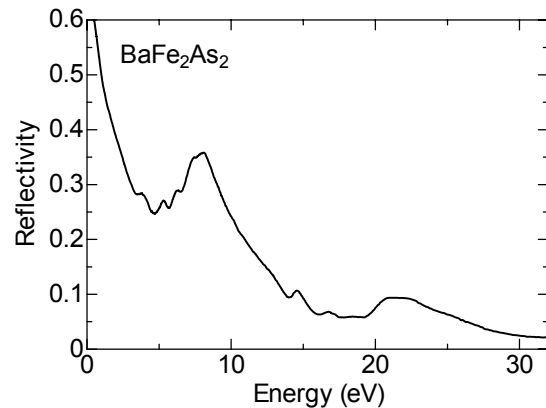

Fig. 1. Reflectivity spectrum of BaFe$_2$As$_2$ measured at room temperature in the energy range up to 32 eV.

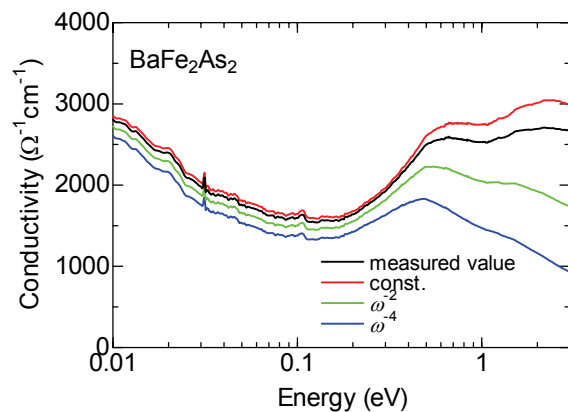
Fig. 2. Kramers-Kronig transformed optical conductivity spectra for various high-energy extrapolations.

[1] S. Tajima *et al.*, J. Opt. Soc. Am. B **6** (1989) 475.
[2] M. Nakajima *et al.*, Phys. Rev. B **81** (2010) 104528.

Ⅲ-5. SOLID STATE PHYSICS

Identification of Cr^{3+} Impurity Contained in $YAlO_3$ by Photoluminescence

K. Nakahara and Y. Ohki

Dept. Electrical Engineering and Bioscience, Waseda University, Tokyo 169-8555, Japan

Introduction

Yttrium aluminate ($YAlO_3$) has been attracting much attention as a promising candidate for a gate insulator in advanced metal-oxide-semiconductor devices [1]. By analyzing photoluminescence (PL) properties of $YAlO_3$, we have been examining the localized states present in the band gap that are assumed to cause leakage current.

Experimental

The samples examined are $YAlO_3$ (100) single crystals grown by the Czochralski method and $YAlO_3$ thin films prepared by a spin-coating method. The films were annealed in oxygen at designated temperatures between 600 and 1000 $^{\circ}$C. Using synchrotron radiation under multibunch operation at the BL1B line of UVSOR Facility as a photon source, PL spectra were measured at 10 K. Crystallization of thin films were confirmed by in-plane X-ray diffraction (XRD) measurements.

Results and Discussion

Figure 1 shows PL spectra induced by 6.4 eV photons, obtained at 10 K for the crystal and the films deposited and annealed on Si substrates. The crystal sample has PL peaks at 1.65 and 1.70 eV. On the other hand, the two PL peaks are similar to those of R-lines of Cr^{3+} ions in Cr-doped $YAlO_3$ [2]. The films annealed at 600, 700 and 800 $^{\circ}$C have no PL peaks, while those annealed at 900 and 1000 $^{\circ}$C have PL peaks at 1.70, 1.75 and 1.79 eV. Similar differences in peak energy between the crystal and the deposited film are also seen in $LaAlO_3$ thin films deposited on different substrates [3], which is possibly due to the lattice distortion.

The XRD patterns shown in Fig. 2 indicate that the films annealed at 900 $^{\circ}$C or higher are polycrystalline, while those annealed at 600, 700 and 800 $^{\circ}$C are amorphous. As indicated by the broken lines, the two large peaks almost agree with those that should be assigned to $YAlO_3$, and subtle differences would be due to lattice distortion. However, the presence of other small peaks suggests that $Y_3Al_5O_{12}$ and $Y_4Al_2O_9$ are included in the films.

These results indicate that the PL is caused by the crystallization and that the corresponding spin-forbidden transition in Cr^{3+} becomes possible owing to spin-orbit mixing induced by the crystal field [3]. Therefore, there is a possibility that the present $YAlO_3$ samples contain Cr^{3+} ions as an impurity. Detection of Cr^{3+} ions by inductively coupled plasma atomic emission spectrometry (ICP-AES) failed, indicating that the Cr^{3+} ion content in the present samples is below 1 ppm.
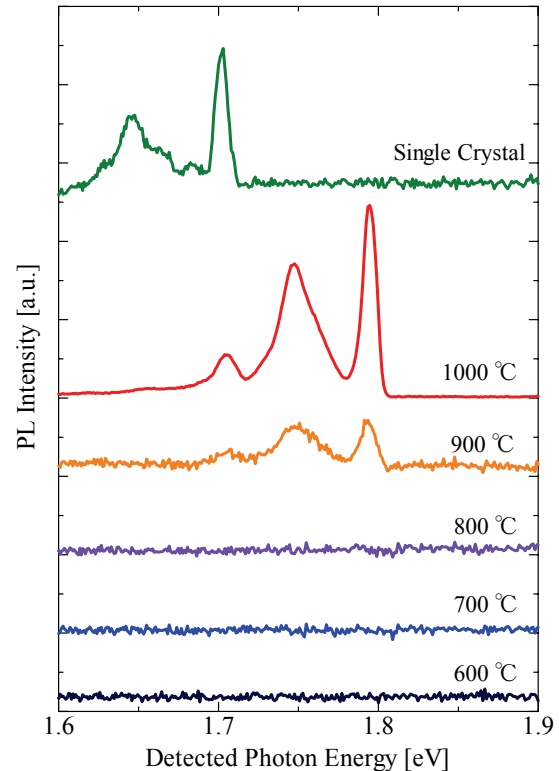

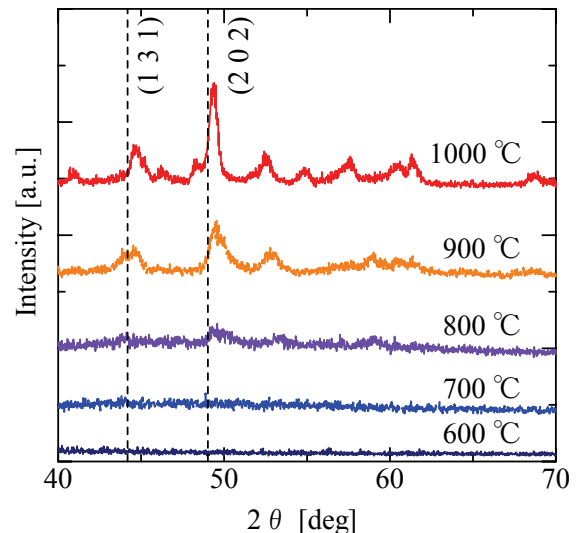Fig. 1. PL spectra induced by 6.4 eV photons in $YAlO_3$.

Fig. 2. In-plane XRD patterns of $YAlO_3$ thin films.

[1] S. A. Shevlin *et al.*, Phys. Rev. Lett. **94** (2005) 146401.

[2] M. Yamaga *et al.*, J. Phys.: Condens. Matter **5** (1993) 8097.

[3] E. Hirata *et al.*, Jpn. J. Appl. Phys. **49** (2010) 091102.

Ⅲ-5. SOLID STATE PHYSICS

Relaxed Exciton Luminescence of KCl Heavily Doped with KI

A. Ohno and N. Ohno

Graduate School of Engineering, Osaka Electro-Communication University, Neyagawa, Osaka 572-8530, Japan

Extensive studies have been made on luminescence arising from localized relaxed excitons in KCl containing iodine impurities. Stimulation in iodine absorption bands of dilute I⁻-doped KCl (KCl:I) produces two characteristic luminescence bands under excitation with UV light or with X-rays at low temperatures. These luminescence bands have been well explained in terms of localized relaxed excitons at ICl⁻ molecule (I⁻ monomer) and a complex of two iodine ions (I⁻ dimer), respectively [1-3]. However, optical and luminescence properties of heavily doped KCl:I crystals have not been examined sufficiently for applying to highly efficient scintillation material.

Single crystals of KCl:I were grown by the Bridgeman method from reagent grade KCl added with an appropriate amount of KI. The obtained crystals were transparent up to 5 mol %. The optical measurements were made at 6 K.

The luminescence spectra excited with photons near the exciton absorption region of KCl were almost the same as those of the previous studies; two luminescence bands peaking at 2.64 eV (monomer emission) and 4.64 eV (dimer emission) at 6 K. Photoexcitation spectra detected at 4.64 eV for various KI mol % of KCl:I crystals are shown in Fig. 1. The each spectrum has been normalized at unity at the maximum. As can be seen clearly, the excitation peaks at 6.46 and 7.07 eV for the 0.01 mol % crystal move toward the lower energy side with increasing KI concentration. The low energy shift of these excitation bands suggests that there coexist dimers, trimers and lager sizes of I⁻ ions (KI cluster) in heavily doped KCl:I crystal [1].

The luminescence energies of the trimers and clusters of I⁻ ions in heavily doped KCl:I crystals are expected to be different from that of I⁻ dimers. We have examined the photoluminescence spectra excited at various photon energies. The results for 3 mol % crystal are shown in Fig. 2. It is clearly confirmed that the peak energy of the luminescence band moves from 4.62 eV excited at 6.46 eV to 4.32 eV at 5.90 eV. These luminescence bands are supposed to be the composite bands due to radiative annihilation of the relaxed exciton at dimers, trimers and clusters of I⁻ ions.

In KCl:I crystals containing KI above 1 mol %, there exists a small amount of dimer centers as compared with monomers, and moreover the amount of trimers and clusters of KI is supposed to be extremely smaller than those of monomers and dimers. However, the luminescence intensities of such large-sized centers are found to be comparable with

that of the dimer emission. This fact suggests that the excitons trapped in KI clusters in heavily doped KCl:I crystals would give the high luminescence efficiency. The similar mechanism has been reported in CsI:Na system [4], where the observed luminescence enhancement originates from self-trapped excitons in NaI nanoparticles in host crystals.
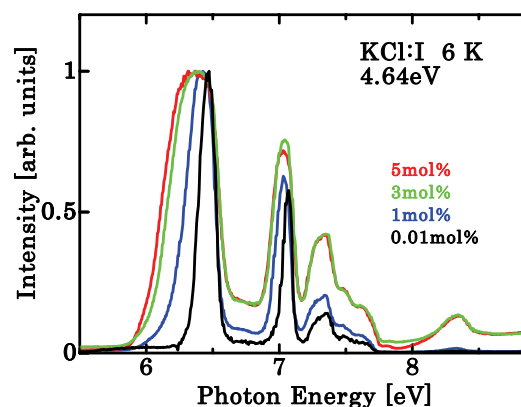

Fig. 1. Photoexcitation spectra of KCl:I crystals detected at 4.64 eV for various KI mol % at 6 K.
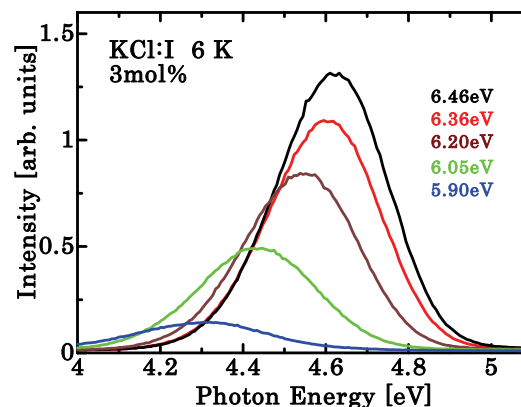

Fig. 2. Photoluminescence spectra of KCl:I (3 mol %) excited at various photon energies at 6 K.

[1] N. Nagasawa, J. Phys. Soc. Jpn. **27** (1969) 1535.
[2] K. Toyoda, K. Nakamura and Y. Nakai, J. Phys. Soc. Jpn. **39** (1975) 994.
[3] K. Kan'no, M. Itoh and Y. Nakai, J. Phys. Soc. Jpn. **47** (1979) 915.
[4] M. Nakayama, N. Ando, T. Miyoshi, J. Hirai and H. Nishimura, Jpn. J. Appl. Phys. **41** (2002) L263.

Ⅲ-5. SOLID STATE PHYSICS

Optical Study of the Current-Induced Mott Transition in Ca_2RuO_4

R. Okazaki[1], Y. Nishina[1], Y. Yasui[1], I. Terasaki[1], F. Nakamura[2], Y. Kimura[2],
M. Sakaki[2] and T. Suzuki[2]

[1]*Department of Physics, Nagoya University, Nagoya 464-8602, Japan*
[2]*ADSM, Hiroshima University, Higashi-Hiroshima 739-8530, Japan*

The Mott insulating state, which is driven by the Coulomb interaction U, has attracted increasing research interests since it manifests a significance of many-body effects in condensed matter physics. Various exotic electronic states emerge in the vicinity of the Mott insulating phase as seen in high-T_c cuprates and organic conductors.

The $4d$-electron transition metal oxide Ca_2RuO_4 provides various interesting phenomena around the Mott insulating phase. Systematic isovalent Sr-doping study revealed that the ground state of $Ca_{2-x}Sr_xRuO_4$ changes from the antiferromagnetic Mott insulator ($x = 0$) to the spin-triplet superconductor ($x = 2$) [1]. Pressure study also indicates the wide variety of electronic ground states [2].

Very recently, Nakamura *et al.* reported the electric-field-induced Mott transition in Ca_2RuO_4 by applying relatively low electric field of ~ 50 V/cm at room temperature [3, 4]. Furthermore the current-induced metallic state persists down to $T = 4.2$ K and the ferromagnetic (FM) order emerges below $T \sim 15$ K, which is reminiscent of the pressure-induced FM state [2]. The origin of this current-induced electronic state is still an open question. To shed further light on a nature of this nonequilibrium electronic state, we have investigated the optical property of the Mott insulating phase in Ca_2RuO_4 under external electrical currents. We used the beam line BL1B in UVSOR facility to measure the reflectivity spectra of Ca_2RuO_4 in an energy region of 2 – 30 eV, which enables us to evaluate the optical conductivity through the Kramers-Kronig (KK) analysis. The reflectivity spectra of Ca_2RuO_4 single crystals measured at room temperature with different currents are shown in Fig. 1. We find an increase of the reflectivity by the currents in low-energy region, as well as several pronounced peaks corresponding the interband transitions as reported in previous optical studies [5]. Figure 2 shows the optical conductivity spectra of Ca_2RuO_4 transformed by the KK analysis. An optical gap decreases as a function of the external currents, implying a possible current-induced metallic state in Ca_2RuO_4. We are now developing an evaluation of self-heating effects under the large external currents.

[1] S. Nakatsuji and Y. Maeno, Phys. Rev. Lett. **84** (2000) 2666.
[2] F. Nakamura *et al.*, Phys. Rev. B **65** (2002) 220402(R).
[3] M. Sakaki *et al.*, JPS meeting (2010) 20pPSA-28; Y. Kimura *et al.*, (2010) 24aPS-3.
[4] F. Nakamura *et al.*, submitted.
[5] J.S. Lee *et al.*, Phys. Rev. Lett. **89** (2002) 257402; J.H. Jung *et al.*, **91** (2003) 056403.
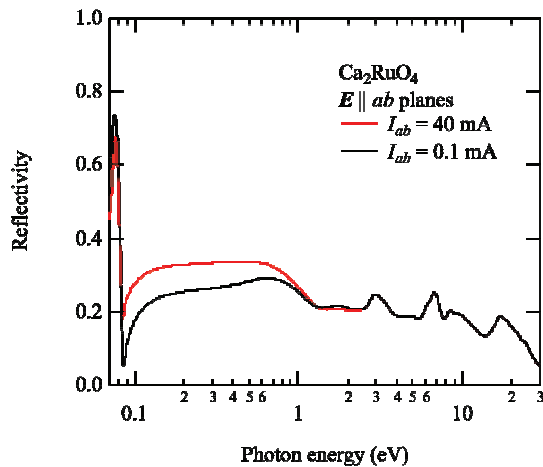
Fig. 1. Reflectivity spectra of Ca_2RuO_4 single crystal measured at room temperature with external currents for $I \parallel ab$. The electric field of incident light is parallel to the *ab* planes.
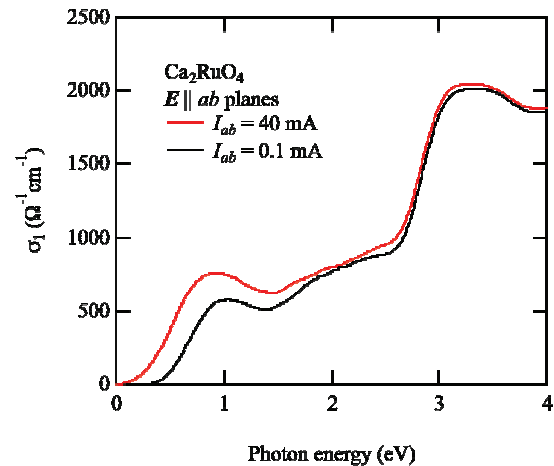

Fig. 2. Optical conductivity σ_1 of Ca_2RuO_4 obtained from the Kramers-Kronig transformation of the reflectivity spectra.

Metal-Insulator Transition in $V_{1-x}W_xO_2$

J. S. Lee[1], K. Shibuya[2], M. Kawasaki[1,2] and Y. Tokura[1,2,3]

[1]*Department of Applied Physics and Quantum Phase Electronics Center (QPEC), University of Tokyo, Tokyo 113-8656, Japan*

[2]*Correlated Electron Research Group (CERG) and Cross-Correlated Materials Research Group (CMRG), ASI, RIKEN, Wako 351-0198, Japan*

[3]*Multiferroics Project, ERATO, Japan Science and Technology Agency (JST), Tokyo 113-8656, Japan*

The metal-insulator transition in VO_2 takes place at around 340 K accompanying the structural transition from high-temperature rutile to low-temperature monoclinic phases. Dimerization of V ions occurs in the latter with a tilting of the V–V bond from *c*-axis. 3*d* electrons localize on V sites forming spin singlet dimers. The driving mechanism of the metal-insulator transition has long been argued whether Mott–Hubbard or Peierls transitions. It has been recently suggested that both mechanisms are active and thus the transition is viewed as a many-body Peierls type.

From the viewpoint of device application, dramatic change in electrical resistivity as well as infrared transmission across the transition above room temperature makes VO_2 potentially useful for optical, electrical, and electro-optical switches by exploiting the phase control through the electron injection into pure VO_2 by electric field or light absorption. There has been an enduring interest in controlling the metal-insulator transition temperature (T_{MI}) of VO_2 by chemical substitution. Electron doping with use of higher valence elements such as W, Mo, and Nb was shown to reduce the transition temperature. Among them, W is known to be the most effective, reducing the transition temperature by 21–28 K/at.%. The valence of W was confirmed to be 6+, which corresponds to adding two electrons per W atom. However, physical properties of electron-doped VO_2 are not well understood because only few studies have been carried out in single crystals.
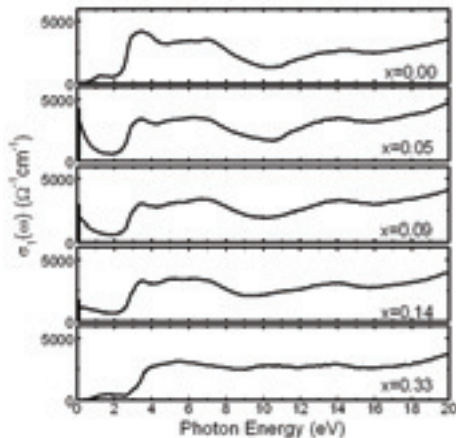
Here, we have investigated optical properties of solid-solution $V_{1-x}W_xO_2$ epitaxial films in a wide range of doping concentration ($0 \leq x \leq 0.33$). We found there are systematic variations of the optical conductivity spectra in the high energy region (as shown in Fig. 1). Detailed examination of the optical gap reveals that the ground state changes from the insulator, to metal, and to insulator as x (the W content) increases (upper panels in Fig. 2). As a signature of the dimerization of V ions there appear the splitting of the phonon around 300 cm⁻¹ for the pure VO_2. As x increases, the splitting becomes less prominent and is absent for $x=0.33$ (lower panels in Fig. 2). This indicates that while the insulating state for $x = 0.0$ is closely related to the Peierls instability, that for $x = 0.33$ can be understood by considering purely the electron-correlation.
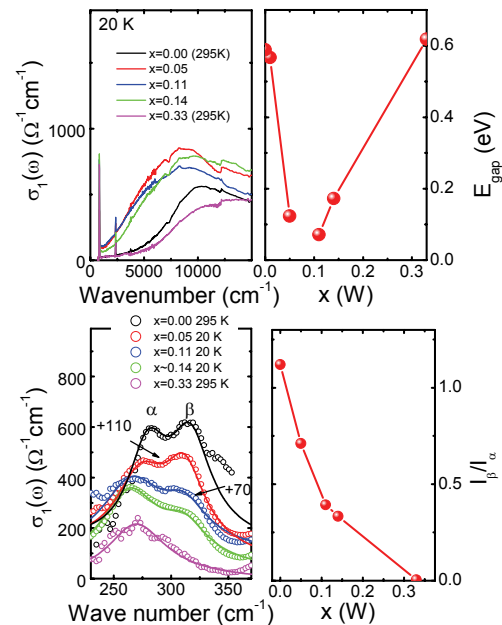
Fig. 2. Left panels: the optical conductivity spectra up to the visible region (upper) and in the far-infrared region (lower). Right panels: doping-dependences of the optical gap energy (upper) and the intensity ratio of two phonon modes (lower).

[1] F. J. Morin, Phys. Rev. Lett. **3** (1959) 34.
[2] J. B. Goodenough, J. Solid State Chem. **3** (1971) 490.
[3] K. Shibuya et al., Appl. Phys. Lett. **96** (2010) 022102.

Fig. 1. Optical conductivity spectra $\sigma_1(\omega)$ of $V_{1-x}W_xO_2$ obtained at the room temperature.

Analysis of 4f-5d Excitation Spectra of Pr^{3+}-Doped SrY$_2$O$_4$

S. Watanabe[1], Y. Ichikawa[2], M. Yoshino[2], T. Yamada[2] and T. Nagasaki[3]

^{1}*Venture Business Laboratory, Nagoya University, Nagoya 464-8603, Japan*

^{2} *Department of Materials, Physics and Energy Engineering, Graduate School of Engineering,*
Nagoya University, Nagoya 464-8603, Japan

^{3} *EcoTopia Science Institute, Nagoya University Nagoya 464-8603, Japan*

Trivalent praseodymium (Pr^{3+})-doped oxides have been widely studied for application as a luminescent material in devices such as solid-state lasers and phosphors. Because of strong recent desire for luminescent materials in high-energy regions, the $4f^2$-$4f^1 5d^1$ transitions of Pr^{3+} in wide band-gap host crystals have drawn attention for potential application as UV and VUV phosphors.

We make a report of the analysis of the emission and excitation spectra for Pr^{3+}-doped SrY$_2$O$_4$. The Pr^{3+}-doped SrY$_2$O$_4$ sample was prepared by the solid-state reaction at 1323 K and identified as single phase by x-ray diffraction measurement. The concentration of Pr^{3+} ion in the sample was 3 mol%. The excitation spectrum at 10 K was measured monitoring the emission at 516 nm.

In addition, we also analyzed the spectra based on first-principles calculations for multiplet energy and absorption spectrum using the 4-component relativistic configuration interaction (CI) method [1, 2]. This calculation method has been successfully applied to analysis of the multiplet energy levels and optical spectrum between the multiples for impurity ions in host crystals. The SrY$_2$O$_4$ host crystal has three cation sites, which are Y1 site, Y2 site and Sr site. The occupied sites of the Pr^{3+} ions were analyzed by comparison between the experimental spectrum and theoretical spectra. The solution energies of Pr^{3+} into the host crystal were also estimated by first-principles band calculations. These calculations were performed using VASP code [3].

The calculated solution energies of Pr^{3+} into SrY$_2$O$_4$ host crystal were 0.11 eV for Y1 site, 0.31 eV for Y2 site and 0.64 eV for Sr site, respectively, at oxidation limits. For the substitution in Sr site by Pr^{3+} ion, the oxygen vacancy in host crystal, SrY$_2$O$_4$, required for the charge compensation. Therefore it is natural that the solution energy of Pr^{3+} into the Sr site was much higher than the solution energy of Pr^{3+} into other two sites.

Figure 1 shows the experimental excitation spectrum and theoretical absorption spectra. The peaks A – F were observed in the experimental spectrum. The peak E originates in the fundamental absorption of the SrY$_2$O$_4$ host crystal. The theoretical spectra were calculated with three models, which were occupied three sites mentioned above, respectively (Y1, Y2 and Sr site). While the intensity of the experimental excitation spectrum is not directly compared with the theoretical absorption spectra,

relative peak energy can compared between each spectra. The absorption of the Pr^{3+} ions in all three sites , Y1, Y2 and Sr site, contributed to the peaks A, B and C. On the other hand, the peak D can clearly attributed the absorption of Pr^{3+} in Sr site and the broad peak F can attributed the absorption of Pr^{3+} in Y1 and Y2 site.

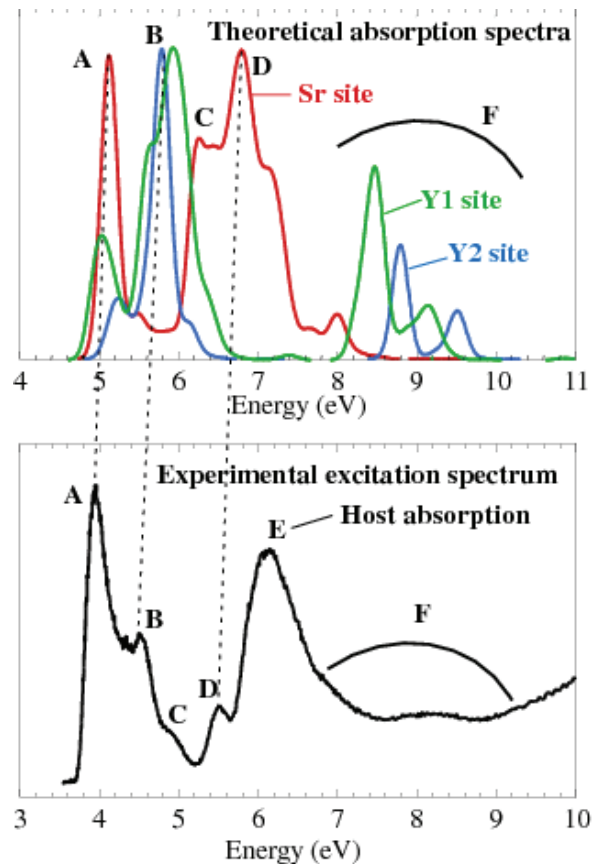Consequently, we can conclude that the Pr^{3+} ions occupied in all three sites, Y1, Y2 and Sr site.

Fig. 1. Experimental excitation spectrum and theoretical absorption spectra of Pr^{3+}-doped SrY$_2$O$_4$ materials.

[1] K. Ogasawara, T. Iwata, Y. Koyama, T. Ishii, I.Tanaka and H. Adachi, Phys. Rev. B **64** (2001) 143.
[2] S. Watanabe, K. Ogasawara, M. Yoshino and T. Nagasaki, Phys. Rev. B **81** (2010) 125128.
[3] G. Kresse and D. Joubert, Phys. Rev. B **59** (1999) 1758.

Charge State Analysis of Co Ions in $Pr_{1-x}Sr_xCoO_{3-\delta}$

T. Yoshioka, H. Kanamori and T. Yamamoto

Faculty of Science and Engineering, Waseda University, Tokyo 169-8555, Japan

Introduction

Perovskite-type cobalt oxides $R_{1-x}A_xCoO_{3-\delta}$ (R and A are rare-earth and alkaline-earth ions, respectively) have been extensively studied, because of their unique electronic and magnetic properties such as colossal magnetoresistance and metal-insulator transition [1-3]. In order to understand such properties, it is essential to know the charge state, i.e., valence, of Co ions in these materials. When the alkaline-earth ion is incorporated into $PrCoO_3$, i) valence of Co ions controls the system, i.e., from Co^{3+} to Co^{4+} or ii) oxygen vacancy is created, to keep the system electrically neutral. However, these mechanisms of charge compensation have not yet been fully understood. Then the charge state analysis of Co ions in $Pr_{1-x}Sr_xCoO_{3-\delta}$ are carried out here by the Co-$L_{2,3}$ X-ray absorption near-edge structure (XANES) measurements changing a concentration of Sr (x=0, 0.1, 0.3, 0.5, 0.7).

Experiments

$Pr_{1-x}Sr_xCoO_{3-\delta}$ samples were synthesized by the conventional solid-state reaction method. Co-$L_{2,3}$ XANES spectra were collected at BL4B in UVSOR by the total electron yield (TEY) method. All the sample powders were mounted on the first Be-Cu dinode using the carbon adhesive tape. The incident beam was monochromatized by the varied-line-spacing plane grating (800 lines/mm). The energy resolution of the incident beams, E/ΔE was set to 3000 by tuning the slit height settled at the upper and lower reaches of the grating.

Results

Prior to the XANES analysis, all the samples were characterized by the X-ray diffraction (XRD). No extra peaks were found in the observed XRD patterns except for those of the perovskite structured $Pr_{1-x}Sr_xCoO_{3-\delta}$, which yield the $Pr_{1-x}Sr_xCoO_{3-\delta}$ crystallizes orthorhombic perovskite structure (Pbnm) at ambient condition.

Observed Co-L_3 XANES spectra of $Pr_{1-x}Sr_xCoO_{3-\delta}$ are shown in Fig. 1, in which fine structure of Co-L_3 XANES spectra of $Pr_{1-x}Sr_xCoO_{3-\delta}$ changes as increment of the concentration of doped Sr^{2+} ions. From the deconvolution of the experimental spectra using the Gaussian function (red lines in Fig. 1), it is found that relative intensity of peak A to B increases as increment of Sr concentration (Fig. 2). These experimental results suggest that electronic structure of Co ions in $Pr_{1-x}Sr_xCoO_{3-\delta}$ changes continuously as increment of Sr concentration.
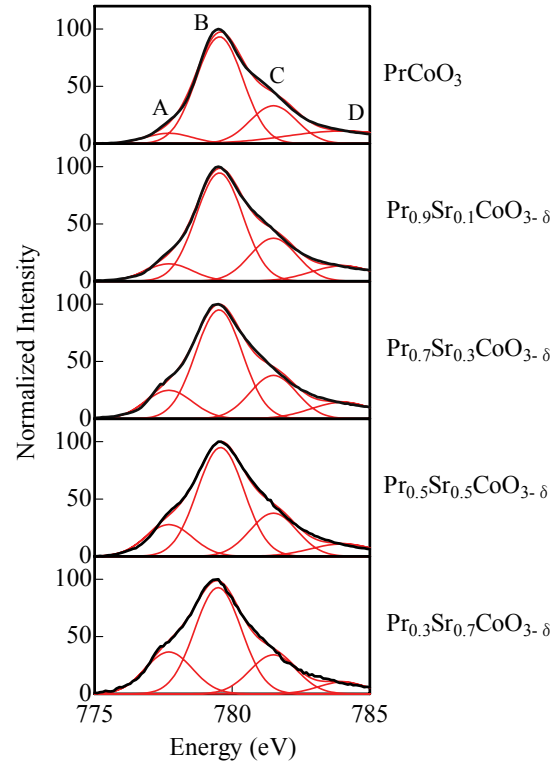

Fig. 1. Observed Co-L_3 XANES spectra of $Pr_{1-x}Sr_xCoO_{3-\delta}$.
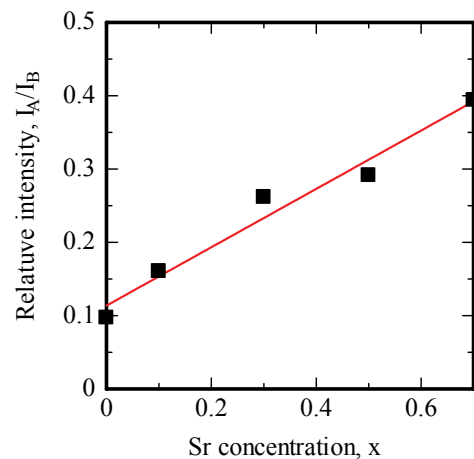

Fig. 2. Relative intensity of peak A to B as a fnction of Sr concentration, x, in $Pr_{1-x}Sr_xCoO_{3-\delta}$.

[1] S. Tsubouchi *et al.*, Phys. Rev. B **69** (2004) 144406.
[2] H. Masuda *et al.*, J. Phys. Soc. Jpn. **72** (2003) 873.
[3] V. Golovanov and L. Mihaly, Phys. Rev. B **53** (1996) 8207.

Ⅲ-5. SOLID STATE PHYSICS

Electronic Structure of Heusler-Type Alloys Fe$_{2-y}$M$_y$VAl (M = Co, Rh, Ir)

S. Harada[1], M. Kato[1], S. Yagi[1], K. Soda[1], Y. Nishino[2] and H. Miyazaki[3]

[1]*Graduate School of Engineering, Nagoya University, Nagoya 464-8603, Japan*
[2]*Graduate School of Engineering, Nagoya Institute of Technology, Nagoya 466-8555, Japan*
[3]*UVSOR Facility, Institute for Molecular Science, Okazaki 444-8585, Japan*

Heusler-type Fe$_2$VAl and its related alloys have attracted much attention because of the enhancement of its thermoelectric power S by partial substitution of the forth element M [1]. Universal dependence of S is found on the partial substitution, which can be qualitatively explained by a rigid-band-model. However, it is also noticed that S depends on a substituted element M even in the same group, as shown in Fig. 1 [2]. To develop new thermoelectric materials, it is important to understand the origin of the dependence of their thermoelectric properties on the substitution. In this report, we will show the results of the 3p-3d resonance photoemission measurement of Fe$_{2-y}$M$_y$VAl (M = Co, Rh, and Ir) to clarify the change in their electronic structure on the substitution.

Photoemission spectra of polycrystalline samples of Fe$_{2-y}$M$_y$VAl were recorded under ~2 x 10^{-8} Pa at 20 K for clean surfaces prepared by *in situ* fracturing.

Figure 1 summaries valence-band spectra of Fe$_{1.9}$M$_{0.1}$VAl recorded at the excitation photon energy $h\nu$ of 52 and 37 eV just below the Fe and V $M_{2,3}$ thresholds, where the Fe and V 3d photoemissions are suppressed due to so-called anti-resonance effect, respectively. Thus the spectra at $h\nu$ = 52 eV may represent the density of states (DOS) other than the Fe 3d states, *i.e.* the V and M d states, while the spectra at $h\nu$ = 37 eV show the Fe and M d DOS. In all the spectra, there are features recognized at the binding energy of $E_B \sim$ 0.4, 0.8, 1.5, and 3 eV. As seen in the spectra at $h\nu$ = 52 eV, the d DOS of V and substituted M, is almost the same for all the studied alloys. At $h\nu$ = 37 eV, the 0.8-eV band for the Co substitution becomes prominent, while the spectra for the Rh and Ir substitution are similar to each other. Small band shift towards the high binding energy side as a whole is also noticed for the Ir substitution.

Observed similarity is ascribed to the common band formation with the substituted M d states incorporated into the main Fe-V 3d band. According to Harisson [3], the characteristic radius r_d of Co 3d states compared with the Fe 3d ones is slightly reduced but those of the Rh 4d and Ir 5d ones are much increased. Thus the interaction of the Rh and Ir d states with the Fe 3d ones, proportional to r_d^3, is expected to be larger than the Co-Fe interaction. On the other hand, the average d state energy ε_d of Co is low and those of Rh and Ir are high, compared with that of Fe. Therefore the Fe 3d states are expected to be pushed towards the high and low binding energy side for the Ir and Co substitutions, respectively; the

large interaction of Ir with Fe suggests larger shift than that of Co. This seems consistent with the present results.

Further study of the dependence on the substitution is now in progress and will be reported elsewhere.
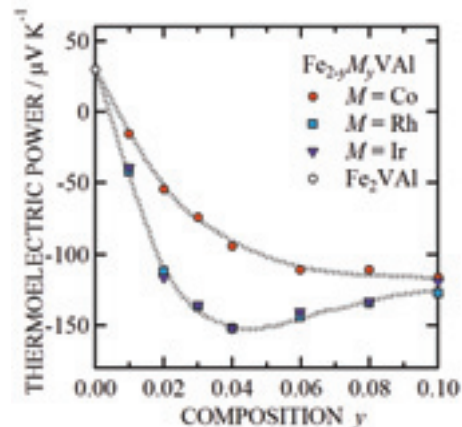
Fig. 1. Thermoelectric power of Heusler-type alloys Fe$_{2-y}$M$_y$VAl (M = Co, Rh, and Ir).
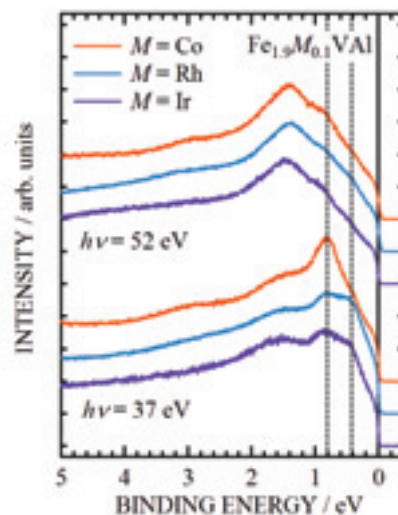
Fig. 2. Valence-band photoemission spectra of Heusler-type alloys Fe$_{1.9}$M$_{0.1}$VAl (M = Co, Rh, and Ir)

[1] Y. Nishino, "The Science of Complex Alloy Phases," (TMS, Warrendale, 2005) 325.
[2] T. Sugiura and Y. Nishino, J. Jpn. Inst. Metals **73** (2009) 846.
[3] W. A. Harisson, "Electronic Structure and the Properties of Solids," (Dover Publications Inc., New York, 1989).

A Photon Energy-Dependent Angle-Resolved Photoemission Study of CaCu$_3$Ti$_4$O$_{12}$

H. J. Im[1], T. Sakurada[1], M. Tsunekawa[2], M. Toita[1], T. Watanabe[1], K. Takegahara[1],
H. Miyazaki[3] and S. Kimura[3,4]

[1]*Department of Advanced Physics, Hirosaki Univerisy, Hirosaki 036-8561, Japan*
[2]*Faculty of Education, Shiga University, Shiga 522-8522, Japan*
[3]*UVSOR Facility, Institute for Molecular Science, Okazaki 444-8585, Japan*
[4]*School of Physical Sciences, The Graduate University for Advanced Studies,
Okazaki 444-8585, Japan*

Recently, the discovery of the extremely high dielectric constant (as high as 10^4-10^5) of A-site perovskite CaCu$_3$Ti$_4$O$_{12}$ (CCTO) over a wide range of temperature from 100 to 500 K has generated considerable attention because of the expectation of developing a high-efficient and small capacitor [1, 2]. However, its electronic structures are not still clear due to the absence of observation of band dispersion. Furthermore, discrepancy between the results of electrical transport measurements and that of band calculation has stressed an importance of the observation of band dispersion; while CCTO has a metallic phase in LDA band calculation, the electrical resistivity measurements exhibit an insulator phase. Here, we clearly observed the band dispersions in valence band regime and found the high symmetry points (Γ and H), using photon energy (hv)-dependent angle-resolved photoemission spectroscopy (ARPES).

High-quality CCTO single crystal was prepared by TSFZ method. ARPES experiments were performed at the beamline BL5U. The range of photon energies is from 54 eV to 93 eV. The clean surface was prepared in the (100) plane by cleaving *in situ*. Measurements were carried out at room temperature (T = 300 K) in a vacuum better than 2×10^{-8} Pa. A wide angle acceptable MBS analyzer is used with energy resolution of 50 meV at hv = 60 eV.

Figure 1 (a) shows the energy distribution curves (EDCs) of CCTO in the valence-band region along Δ-direction. With increasing hv, ARPES spectra trace the blue dashed arrow in the Brillouin zone of body-centered cubic structure depicted as in Fig. 1 (b). Valence bands can be divided into three regions, 1 - 2.5 eV, 2.5 - 5 eV, and 5 - 8 eV. The bands in the regions of 2.5 - 5 eV and 5 - 8 eV relatively highly disperse with intense features, while the bands in the region of 1 - 2.5 eV are not well distinguished due to weak intensity and broad band width. In the region of 1- 2.5 eV, we observe the intensity variation of the small shoulder as a function of hv, reflecting the band dispersion. The shoulder becomes prominent closing hv = 60 eV. This suggests that hv = 60 eV is a symmetry point. In the region of 2.5 - 5 eV, there are two kinds of bands. One disperses from 2.9 to 3.5 eV with a top at hv = 90 eV, while the other shows very small dispersion around 3.9 eV, reflecting the

localized character. In the region of 5 - 8 eV, bands are well split with top around 5.5 eV and bottom around 7.4 eV around hv = 90 eV. These indicate that both hv = 60 and 90 eV correspond to symmetry point. According to the free electron final state model, the inner potential is estimated to be 16 eV and the symmetry points are designated as shown in Fig. 1 (a): the EDC at hv = 90 eV corresponds to Γ-point and that of hv = 60 eV to H-point. Finally, we find the negligible intensity at the Fermi level (E_F), which directly explains why CCTO shows the insulator phase.

We performed hv-dependent ARPES measurements on A-site perovskite CCTO, which shows extremely high-dielectric constant and has an insulator phase in contrast to band calculation results. We observed the clear band dispersions and the negligible spectral weight at E_F in good agreement with the electrical resistivity measurements.
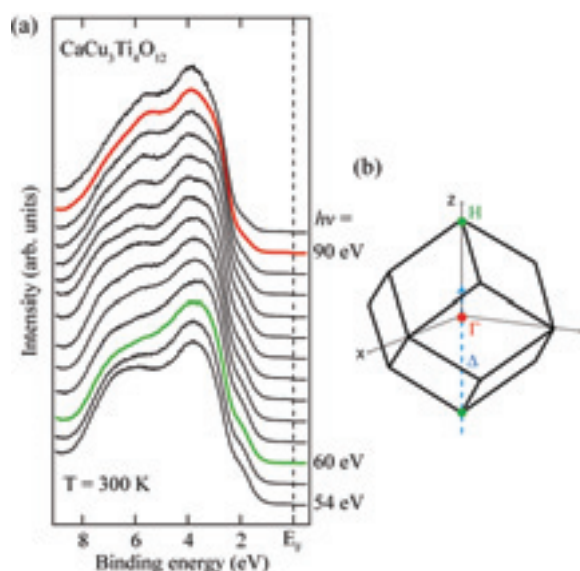

Fig. 1. (a) The EDCs along Δ-direction obtained by ARPES measurements at photon energies between hv = 54 and 93 eV in normal emission. (b) The Brillouin zone and the momentum spaces (blue dashed arrow) measured in experiments.

[1] M. A. Subramanian *et al*., J. Solid State Chem. **151** (2000) 323.
[2] Y. Zhu *et al*., Phys. Rev. Lett. **99** (2007) 037602.

Ⅲ-5. SOLID STATE PHYSICS

Angle-Resolved Photoemission Study on GdTe$_2$

R. Niwa[1], S. Hirate[2], T. Ito[1,4], T. Hajiri[1], H. Miyazaki[3], B. H. Min[6],
S. Kimura[3,5] and Y. S. Kwon[6]

[1]*Graduate School of Engineering, Nagoya University, Nagoya 464-8603, Japan*
[2]*School of Engineering, Nagoya University, Nagoya 464-8603, Japan*
[3]*UVSOR Facility, Institute for Molecular Science, Okazaki 444-8585, Japan*
[4]*Nagoya University Synchrotron radiation Research Center, Nagoya University, Nagoya 464-8603, Japan*
[5]*School of Physical Sciences, The Graduate University for Advanced Studies (SOKENDAI), Okazaki 444-8585, Japan*
[6]*Department of Physics, Sungkyukwan University, Suwon 440-749, Korea*

Rare-earth ditellurides (RTe$_2$; R = rare earth) have attracted much attention because of their anomalous physical properties due to their two dimensionality, especially the charge density wave (CDW) transition [1]. However, there are not many reports of CDW formation from the electronic structure viewpoint except for LaTe$_2$ and CeTe$_2$ [2].

In this study, we have performed angle-resolved photoemission spectroscopy (ARPES) on single-crystalline GdTe$_2$ [3] to clarify the CDW formation and its relation to the anomalous properties.

Figure 1 shows the Fermi surface (FS) of GdTe$_2$ at the temperature T of 10 K obtained by the intensity plot of the ARPES spectra in the binding energy region of $E_F \pm 20$ meV with the incident photon with the energy of 63 eV. The perfectly symmetric FS images are consistent with the bulk Brillouin zone. This result implies that the observed electronic structure corresponds to the bulk electronic structure. From band structure calculations on RTe$_2$ [2], FSs dominate with Te $5p_x$ and $5p_y$ characters.

Figure 2 (a) shows the ARPES image near E_F along the ΓX high-symmetry line. Two symmetric bands with respect to the Γ point are observed. These bands are attributed to a hole pocket at around the Γ point and an electron pocket at around the X point. The intensity of these bands are suppressed at the binding energy (E_B) of 0.25 eV. Similar suppression was observed in the whole Brillian zone. To check the suppression of intensity at $E_B = 0.25$ eV in detail, the energy distribution curves are plotted in Fig. 2 (b). This figure clearly indicates that the conduction band is folded at around $E_B = 0.25$ eV and the gap opens in between $E_B = 0.1$ and 0.4 eV. The band folding as well as the energy gap is the evidence of the CDW formation.

[1] J. Chung *et al.*, J. Kor. Phys. Soc. **38** (2001) 744.
[2] K. Y. Shin *et al.*, Phys. Rev. B **72** (2005) 085132.
[3] Y. S. Kwon and B. H. Min, Physica B **281&282** (2000) 120.
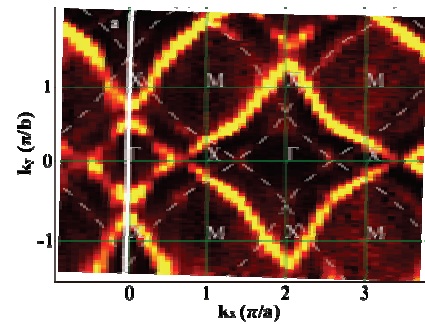
Fig. 1. The intensity map of the ARPES spectra of GdTe$_2$ in the binding energy width of $E_F \pm 20$ meV plotted in the ΓXM plane of the Brillouin zone. The ARPES spectra were taken at $T = 10$ K using $hv = 63$ eV photons. The plot can be regarded as a Fermi surface.

Fig. 2. (a) ARPES image along the ΓX symmetry line. White dashed lines are guides for eyes. (b) ARPES spectra near E_F of GdTe$_2$ enlarged around FS crossing point of the electron pocket at the X point (green line in inset). These data were taken at $T = 10$ K using $hv = 63$ eV photons.

Terahertz Spectroscopy of Copper Ion Conducting Glasses

T. Awano

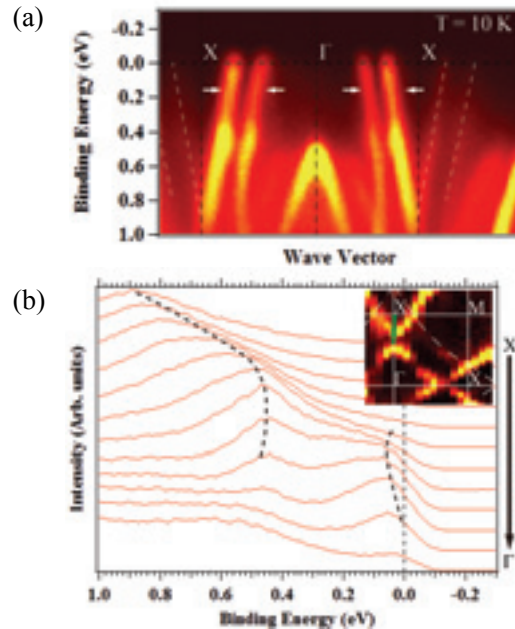*Department of Electronic Engineering, Tohoku Gakuin University, Tagajo 985-8537, Japan*

An optical absorption band by a collective motion of mobile ions may appear in terahertz region, in which motion of mobile ions changes from translation in microwave region to vibration motion in far-infrared region. I had investigated far-infrared and millimeter wave spectra of some silver or copper ion conductors to study the dynamics of mobile ions. In AM_4X_5 (A=alkali metal; M=Ag or Cu; X=halogen) crystal, a structure by "ionic plasmon" was observed in the spectral region below 10 cm^{-1} in silver ion conductors or 30 cm^{-1} in copper ion conductors in energy loss function spectra at temperatures of superionic conducting phase [1].

Such collective motion may be one reason of the high ionic conductivity of superionic conducting glasses even at low temperature. I had investigated whether such "ionic plasmon" exists in the non-periodic structure in glass of various frameworks. The AgI-Ag_2MoO_4 glass has no network structure in contrast with the AgI-$AgPO_3$. The alkylammonium ions (TMA, TEA) disperse randomly into AgI in organic-inorganic glasses.

In this study, I have investigated on copper ion conducting glasses of CuI-$CuPO_3$, CuI-Cu_2MoO_4 and TMAI-TEAI-CuI glasses to compare ionic motion with silver conducting glasses.

Figure 1 shows absorption spectra of CuI-$CuPO_3$, CuI-Cu_2MoO_4 and TMAI-TEAI-CuI glasses obtained from reflectivity spectra by K-K analysis. They are put in order of their CuI-contents. There observed two broad absorption bands around 130, 60, 30 cm^{-1} and at low energy tail. These absorption bands were observed in silver conducting glasses, however, peak positions are slightly shifted toward high energy side in copper conducting glasses. This seems to be due to the difference of mass of conduction ion. Expected frequency ratio of silver and copper motion is 1.3 and is in good agreement with observed ones. This means that these bands are due to motions of conducting ion.

Figure 2 shows absorption spectra of silver ion conducting AgI-Ag_2O-V_2O_5 glasses for comparison. This glass has dispersive structure as the AgI-Ag_2MoO_4 glass, therefore is able to contain much AgI. Peak positions of broad absorption bands are 110 and 20 cm^{-1}. These positions are the same as those in other silver conducting glasses [2].

[1] T. Awano, Infrared Phys. and Tech. **51** (2008) 458.
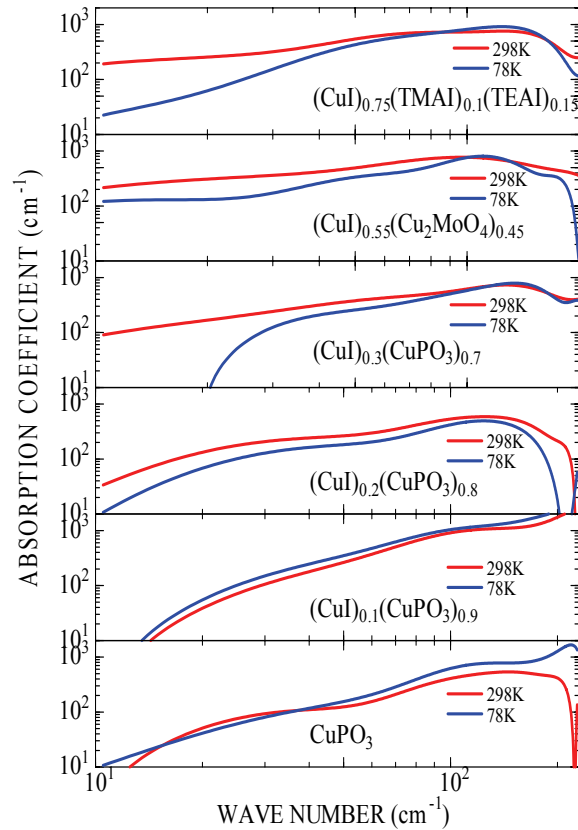[2] T. Awano and T. Takahashi, J. Phys. Soc. Jpn. **79** Suppl. A (2010) 118.

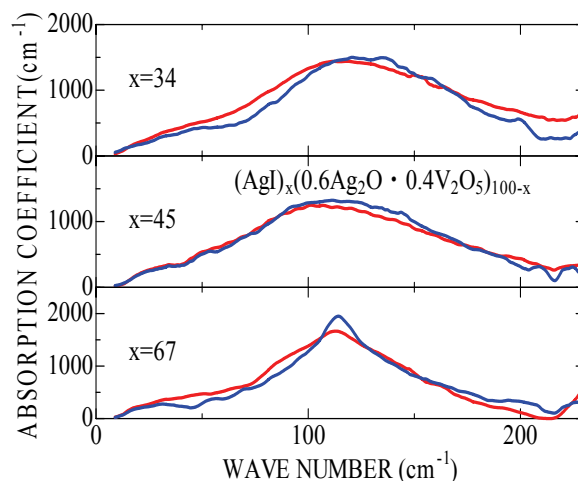Fig. 1. Absorption spectra of CuI-containing superionic conducting glasses.

Fig. 2. Absorption spectra of AgI-containing superionic conducting glasses.

Ⅲ-5. SOLID STATE PHYSICS

Pressure-Dependent Reflectivity Spectra of α-(BEDT-TTF)$_2$I$_3$ in the THz Region

T. Iizuka[1], T. Mori[2], K. Yakushi[1,3] and S. Kimura[1,2]

[1]*School of Physical Sciences, The Graduate University for Advanced Studies (SOKENDAI), Okazaki 444-8585, Japan*
[2]*UVSOR Facility, Institute for Molecular Science, Okazaki 444-8585, Japan*
[3]*Institute for Molecular Science, Okazaki 444-8585, Japan*

Introduction

Recently, a quasi-two-dimensional organic conductor, α-(BEDT-TTF)$_2$I$_3$ [BEDT-TTF = bis(ethylenedithio)tetrathiafulvalene, here after BEDT-TTF is abbreviated as ET] is attracting attention because of its rich physical properties, e.g., superconductivity under uniaxial pressure along the *a*-axis and a zero gap state, namely "Dirac-cone" as observed in graphite [1]. α-(ET)$_2$I$_3$ shows metal-to-insulator (M-I) transition on cooling due to charge ordering (T_{CO} = 135 K), at ambient pressure. T_{CO} decreases with applying pressure, and then disappears at around 2.0 GPa. Previously reported temperature-dependent hall coefficient and electrical resistivity data imply that the carrier density and mobility compensate each other above 1.9 GPa [2]. The anomalous carrier property is discussed to originate from the Dirac-cone-type conduction band [3]. However, there has been no direct observation of the electronic structure yet. In this study, the polarized optical reflectivity spectrum $R(\omega)$ of α-(ET)$_2$I$_3$ was measured under pressures to investigate the electronic structure.

Experimental

Single crystals of α-(ET)$_2$I$_3$ were grown by an electrochemical oxidation method. Polarized $R(\omega)$ of α-(ET)$_2$I$_3$ along the *a*-axis was measured in the terahertz (THz) region of 70 - 450 cm^{-1} (2.1 - 13.6 THz), from the insulator to metallic phases by applying pressure from 0.3 to 2.9 GPa at the temperature of 8 K. The measurement was performed at the THz micro-spectroscopy end station of BL6B at UVSOR-II. A diamond anvil cell (DAC) was employed to produce high pressure, with a pressure medium of Apiezon® N. The pressure was calibrated by a ruby fluorescence method.

Because of the low signal intensity in the insulator phase, the accumulation was done in form of interferogram. Spectra were calculated from the Fourier transformation of the averaged interferograms.

Results and Discussion

Obtained $R(\omega)$ of α-(ET)$_2$I$_3$ at T = 8 K at pressures from 0.3 to 2.9 GPa are shown in Fig. 1. $R(\omega)$ at ambient pressure after the correction of using diamond window (reflective index n = 2.4) in DAC is shown at the bottom of the figure [4].

TO-Phonon peaks at around 123 cm^{-1}, which mainly appear in the polarization along the *a*-axis, correspond to the antisymmetric stretching mode of I$_3$ [4]. The peaks do not shift below the M-I transition pressure of 2.0 GPa. On the other hand, phonon peaks at around 400 cm^{-1} shift to the lower wavenumber side with elevating pressure. The latter peak comes from the breathing mode of ET molecules which can couple to carriers [4]. In addition, the base line of the spectrum increases with applying pressure due to the appearance of carriers. Even in the metallic phase above 2.0 GPa, the spectra have no Drude response, but the $R(\omega)$ intensity increases with increasing the wavenumber. The Drude response seems to appear in the lower energy region. This result is consistent with Dirac-cone picture which has low carrier density due to the unique electronic structure of Fermi "point", not a surface, in the Fermi level [3].
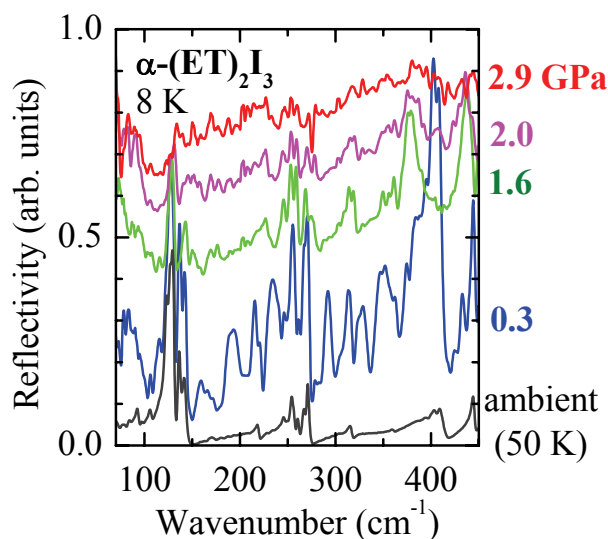
Fig. 1. Pressure-dependent reflectivity spectra [$R(\omega, P)$] of α-(ET)$_2$I$_3$ at the temperature of 8 K with polarization along the *a*-axis. Black line is the simulated reflectivity spectrum at ambient pressure in the case of a diamond window of DAC [4].

[1] A. B. Kuzmenko *et al.*, Phys. Rev. Lett. **100** (2008) 117401.
[2] N. Tajima *et al.*, J. Phys. Soc. Jpn. **69** (2000) 543.
[3] S. Katayama *et al.*, J. Phys. Soc. Jpn. **75** (2006) 054705.
[4] Y. Yue *et al.*, Phys. Rev. B **82** (2010) 075134.

LO-Phonon Plasmon Coupled Mode of ZnO

T. Inushima[1], Y. Ota[1] and K. Fukui[2]

[1]*Department of Electronics, Tokai University, Hiratsuka 259-1292, Japan*
[2]*Department of Electrical and Electronics Eng., University of Fukui, Fukui 910-8507, Japan*

There are several similarities in the electronic structures between InN and ZnO; it is predicted from the first principle calculation that whenever there is a defect, it produces electrons in the conduction band [1]; It is also predicted that neither the phonon structure nor the band structure can be obtained without taking into account the d electrons as valence electrons. So anomaly of the plasmon-longitudinal optical (LO) phonon coupled mode is a common subject to be investigated [2]. In this experiment, we measured the plasmon-LO phonon coupled mode of ZnO as a function of the electron density.

Using BL6B and a MCT detector we measured the reflectivity spectra of c-plane ZnO at a nearly normal incident configuration. Figure 1 shows the electron density dependence of the reflectivity spectra of bulk ZnO samples which were grown by hydrothermal method. The samples contain Li, which is considered to produce electrons as residual carriers in the conduction band. In this experimental configuration, only E_1 optical phonon is observed as a Reststrahren band (TO at 409 cm^{-1} and LO at 587 cm^{-1}). The inset shows that the LO-phonon shoulder melts according to the increase of the electron density, and that linear plasmon-LO phonon coupling (Frölich interaction) is not observed. Another contribution of the electron is the decrease of reflectivity in the energy region higher than 1100 cm^{-1}. There is a cutoff of the second order phonon absorption at 1100 cm^{-1}. Then this decrease of the reflectivity is related to the increase of the impurities or defects in the sample.

Usually Germanium and Silicon are non-polar materials and the optical phonons at $k=0$ are not infrared active. Consequently they do not split at $k=0$ into LO and TO components, and there is no LO-phonon plasmon coupled mode. In these non-polar semiconductors the interaction between free carriers and phonons is non-linear and optical phonons are observed as a result of Fano interference. When interference exists, the LO phonon shows asymmetric broadening at the initial position. On the other hand, in polar semiconductors like InN, LO-phonon-plasmon interaction is so strong that only plasmon-LO phonon coupled modes are observed.

The results shown in Fig. 1 indicate that the LO phonons of ZnO do not couple with the free carriers linearly, but they show instead Fano interference.

From the first principle calculation ZnO has a spontaneous polarization of 0.05 C/m^2, which is comparable to that of the representative polar semiconductor AlN. Hence the absence of Frölich interaction in ZnO should be explained by taking into account the cause of the residual carriers in the conduction band.

In conclusion, polar semiconductor ZnO does not have plasmon-LO phonon coupled mode. To make clear this absence, reflectivity measurements in the far-infrared region are necessary, which will be done in the near future.

[1] Chris G. Van der Walle and J. Newgebauer, Nature **423** (2003) 626.
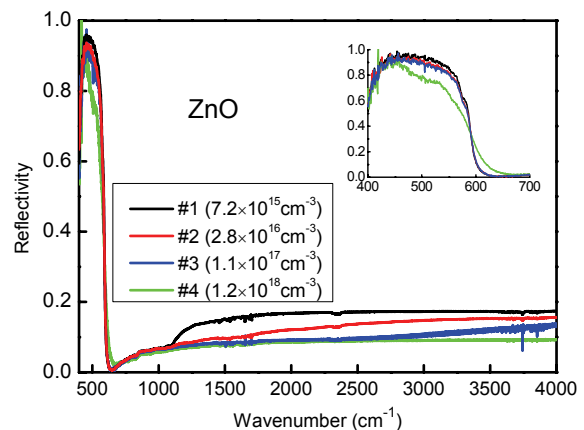[2] T. Inushima, M. Higashiwaki and T. Matsui, Phys. Rev. B **68** (2003) 235204.

Fig. 1. Electron density dependence of the reflectivity spectra of bulk ZnO grown by a hydrothermal method. The incident light is normal to the a-b plane. Inset is the detail of the E_1 phonon Reststrahren band of ZnO.

Observation of Electronic States on Solids Utilizing FIR Synchrotron Radiation

A. Irizawa[1], T. Iizuka[2] and S. Kimura[2,3]

[1]*The Institute of Science and Industrial Research, Osaka University, Ibaraki 567-0047, Japan*
[2]*School of Physical Sciences, The Graduate University for Advanced Studies (SOKENDAI), Okazaki 444-8585, Japan*
[3]*UVSOR Facility, Institute for Molecular Science, Okazaki 444-8585, Japan*

Introduction

The optical study is one of the most powerful techniques for the investigation of electronic states on solids. There can be obtained the great deal of information about the electronic band structure, the symmetry of crystal structure, and the dielectric property. In the respect of experimental affinity, the optical study is extremely compatible with the multiple conditions such as low temperature, high magnetic field, and high pressure. In the case of strongly correlated electron systems, it is well known that the temperature is one of the decisive factors for the electronic state. The considerable types of phase transition are induced by the change of the temperature. Particularly, the multiferroic compounds can be controlled of its physical properties mutually by the external fields such as magnetic, electronic, and elastic ones. The other particular condition, the pressure will directly affect the electron-electron interactions through the change of lattice constants. The beamline BL6B in UVSOR is adjusted for the investigations at low temperature and high pressure in the extremely low-energy region of IR-THz. There equips two type interferometers of both Michelson and Martin-Puplett type. In this report, we have performed the optical reflectivity measurements in the longest wavelength region for the newly synthesized compound having a spinel-related structure.

Experimental

The selected experimental components are the Martin-Puplett type interferometer and the Si-bolometer detector with the liquid-He flow type cryostat for controlling the temperature from 300 K down to 13 K. The reflectivity was obtained from the ratio of optical reflections between the sample and Au as a standard with mirrored surfaces. They were installed on the sample holder and were measured through the tapered hole of 4 mm in diameter.

Results and Discussion

The reflectivities are obtained in the energy range between 20 and 230 cm^{-1} as shown in Fig. 1. Here we can confirm the gradual change from the metallic spectrum at 300 K to the insulating ones with decreasing temperature. The Drude response toward 1 clearly decreases at low temperatures. More than 3 phonons are uprising in the insulating state except the intrinsic noise coming from the Fourier-transform (FT) interferometer at around 40 cm^{-1}. The obtained spectra are well connected to the higher-energy spectra measured at the laboratory using the conventional light source, i.e., black body. The comprehensive reflectivity including this result will develop the reliable optical constants through the Kramers-Kronig (KK) transform.
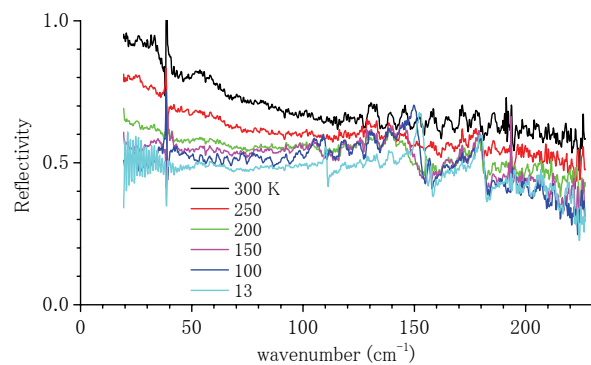

Fig. 1. Temperature change of the reflectivity at the FIR-THz region.

Polarization-Dependent Angle-Resolved Photoemission Study on LiFeAs

T. Hajiri[1], R. Niwa[1], T. Ito[1,2], M. Matsunami[3,4], Y. J. Song[5], S. Kimura[3,4] and Y. S. Kwon[5]

[1]*Graduate School of Engineering, Nagoya University, Nagoya 464-8603, Japan*
[2]*Nagoya University Synchrotron radiation Research Center, Nagoya University, Nagoya 464-8603, Japan*
[3]*UVSOR Facility, Institute for Molecular Science, Okazaki 444-8585, Japan*
[4]*School of Physical Sciences, The Graduate University for Advanced Studies (SOKENDAI), Okazaki 444-8585, Japan*
[5]*Department of Physics, Sungkyunkwan University, Suwon 440-749, Korea*

Iron pnictide superconductor discovered recently [1]. Although they have been intensively studied from both experiment and theory, the mechanism of its anomalous superconductivity has not been revealed yet. So far, the importance of the orbital characters of Fermi surfaces for the nesting condition has been reported [2]. However, there are few reports about the nesting properties on the three-dimensional electronic structure [3].

We have performed angle-resolved photoemission spectroscopy (ARPES) on LiFeAs (T_c = 18 K), to elucidate the three-dimensional electronic structure, especially Fermi surfaces and the orbital characters, by using S and P polarized photons at UVSOR-II BL7U as shown in Fig. 1 (a).

Figure 1 (b) shows the photon-energy-dependent ARPES spectra at $k = 0$ Å^{-1} of LiFeAs measured at T = 12 K (SC state) with the P polarization. The ARPES peak disperses from 0.4 eV (hν = 23 eV) to 0.3 eV (hν = 35 eV). The observed symmetry shows in good agreement with the π/c (ΓZ, see Fig. 1 (c)) period.

Figures 2 (a) and (b) show the polarization-dependent ARPES image near the Γ and Z points, respectively. Red and green color maps are ARPES images for the S and P polarized photons, respectively. In Figure 2, the three (two) hole-pockets near the Γ (Z) point show the clear polarization dependence between S and P polarizations. According to the dipole selection rules [4], ARPES spectra with S polarization are dominated by d_{xy} and d_{yz} orbitals (with odd symmetries), while P polarization with d_{xz}, $d_{x^2-y^2}$ and d_{z^2} (with even symmetries). It should be noted that the d_{xz} orbital cross section is larger than that of $d_{x^2-y^2}$ at this photon energy [5]. Thus we conclude the orbital character of each FS as follows; (1) d_{yz} for the middle hole-pocket at the Γ point and for inner hole-pocket at the Z point, (2) $d_{x^2-y^2}$ for the outer hole-pocket at the Γ and Z point, and (3) d_{xz} for the inner hole-pocket at Γ point, respectively. The above characterizations are in good agreement with the band calculation [6].
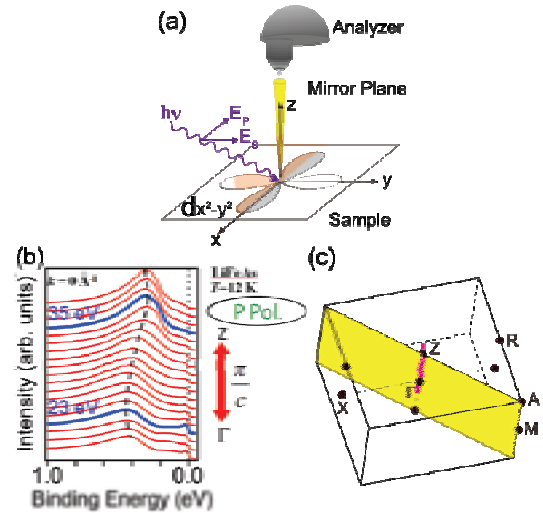

Fig. 1. (a) Experimental configuration of present ARPES. (b) Photon-energy-dependent ARPES spectra at $k = 0$ Å^{-1} of LiFeAs at T = 12 K with the P polarization. (c) Brillouin zone of LiFeAs. The red line corresponds to the measured line in (b) in the ΓMAZ plane (yellow area).
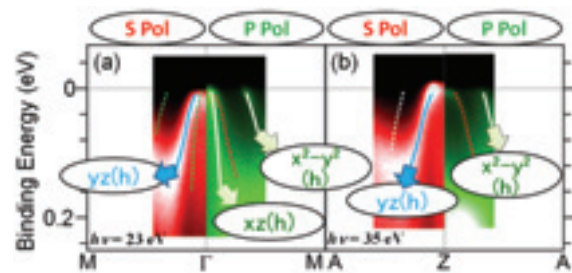
Fig. 2. ARPES image near the Γ (a) and Z (b) points of LiFeAs at T = 12 K measured with the S (red image) and P (green image) polarizations.

[1] Y. Kamihara *et al.*, J. Am. Chem. Soc. **130** (2008) 3296.
[2] K. Kuroki *et al.*, Phys. Rev. B **79** 224511 (2009).
[3] T. Yoshida *et al.*, Phys. Rev. Lett. **106** (2011) 117001.
[4] A. Damascelli, Physica Scripta. **T109** (2004) 61.
[5] B. Mansart *et al.*, Phys. Rev. B **83** (2011) 064516.
[6] S.V. Borisenko *et al.*, Phys. Rev. Lett. **105** 067002 (2010).

Ⅲ-5. SOLID STATE PHYSICS

Three-Dimensional ARPES Study on FeSb$_2$

S. Imada[1], K. Terashima[1], A. Yamasaki[2], K. Mima[1],Y. Miyata[1], R. Yamaguchi[1],
Y. Tachimori[1], Y. Yamanoi[1], H. Eto[1], Y. Matsui[2], J. Yamaguchi[3], S. Komori[3], A. Sekiyama[3],
S. Suga[3] and H. Nakamura[4]

[1]*Faculty of Sci. and Eng., Ritsumeikan University, Shiga 525-8577, Japan*
[2]*Faculty of Sci. and Eng., Konan University, Kobe 658-8501, Japan*
[3]*Grad. School of Eng. and Sci., Osaka University, Osaka 560-8531, Japan*
[4]*Grad. School of Eng., Kyoto University, Kyoto 606-8501, Japan*

FeSb$_2$ shows a metal-insulator crossover; it is metallic around room temperature, while it is insulating at low temperatures with an upturn of the resistivity curve at ~50 K. A number of experimental reports have indicated the existence of the energy gap at low temperatures [1-3], while the mechanism for the formation of the energy gap has not been settled yet. So far, mainly two scenarios have been proposed, one is that FeSb$_2$ is a Kondo insulator [2], and the other is that FeSb$_2$ is a narrow-gap semiconductor [1, 3].

In our previous study on FeSb$_2$ at UVSOR [4], we have measured temperature dependence of the density of states (DOS) near E_F. As we reduce the temperature, the DOS suppression is observed, but finite intensity in the vicinity of E_F remains even at 15 K where the resistivity shows insulating behavior. We also find a free-electron like band crossing E_F at 15 K, indicative of the surface state. Thus it is important to separate the surface contribution from photoemission spectra to discuss bulk property and its mechanism.

In the present study, we have performed angle-resolved photoemission (ARPES) on FeSb$_2$ to reveal the mechanism of the crossover by directly observing the temperature dependence of the energy gap. Since the band calculation predicts three-dimensional band structure and the existence of a couple of small Fermi surfaces [5, 6], we measured $h\nu$-dependence of the normal emission spectra to determine inner potential of the sample.

A single crystal of FeSb$_2$ has been synthesized by Sb-flux method. High-resolution ARPES study has been performed at BL7U in the UVSOR facility. Energy resolution was set at ~15 meV. We have obtained a clean surface of the sample by fracturing in an ultrahigh-vacuum of ~5x10^{-9} Pa.

Figure 1 (a) shows the normal emission spectra using photon energy from 13 to 28 eV, where each $h\nu$ corresponds to different k points along Γ-X axis. As in Fig. 1 (a), we have observed a number of dispersive bands of FeSb$_2$, such as Fe 3$d_{3z^2-r^2}$ band [5] located at ~0.3 eV, Fe 3$d_{x^2-y^2}$ band [5] at ~1 eV, and so on. In fig. 1 (b), the calculated bands [6] are tentatively superimposed on the plot of the second derivative of the normal emission spectra. From the comparison between our experimental results and calculated bands, we estimate that the spectra taken at $h\nu$~23 eV corresponds to Γ. The inner potential of FeSb$_2$ was calculated to be ~21 eV. With this inner potential, X point corresponds to $h\nu$~37 eV, and we find that BL7U can cover the whole Brillouin Zone of FeSb$_2$. Further ARPES study, clarifying (i) the bulk Fermi surfaces near the Zone edge and corner [5], (ii) the location of the surface bands, (iii) the temperature dependence of bulk bands, is necessary to elucidate the origin of the metal-insulator crossover in FeSb$_2$.
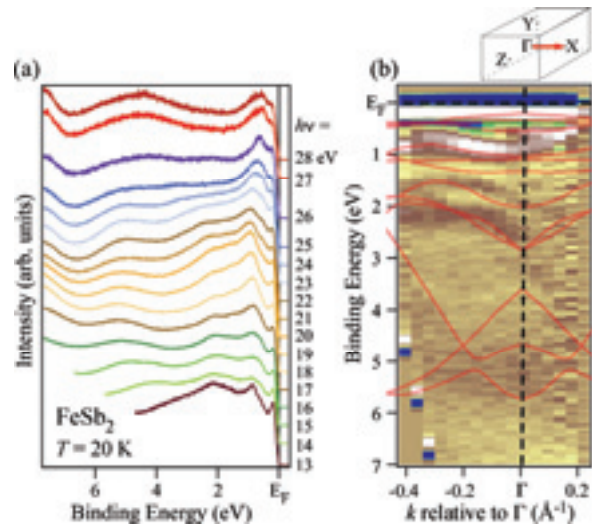

Fig. 1. (a) ARPES spectra derived by normal emission method using $h\nu$ = 13-28 eV at BL7U. (b) Plot of second derivative of (a). White and brown area corresponds to bands. Calculated bands [6] are shown as red lines. Inset shows Brillouin Zone of FeSb$_2$ and the measured k-direction (Red arrow).

[1] Z. Schlesinger *et al*., Phys. Rev. Lett. **71** (1993) 11.
[2] C. Petrovic *et al*., Phys. Rev. B **72** (2005) 045103.
[3] T. Koyama *et al*., Phys. Rev. B **76** (2007) 073203.
[4] S. Imada *et al*., UVSOR activity report **36** (2009) 106.
[5] A. V. Lukoyanov *et al*., Euro. Phys. J. **53** (2006) 205.
[6] J. M. Tomczak *et al*., Phys. Rev. B **82** (2010) 085104.

Angle-Resolved Photoemission Spectroscopy of YbAl$_2$

M. Matsunami[1,2], T. Hajiri[3], H. Miyazaki[1], M. Kosaka[4] and S. Kimura[1,2]

[1]*UVSOR Facility, Institute for Molecular Science, Okazaki 444-8585, Japan*
[2]*School of Physical Sciences, The Graduate University for Advanced Studies (SOKENDAI), Okazaki 444-8585, Japan*
[3]*Graduate School of Engineering, Nagoya University, Nagoya 464-8603, Japan*
[4]*Graduate School of Science and Engineering, Saitama University, Saitama 338-8570, Japan*

The heavy fermion or the valence fluctuation behavior in the strongly correlated f electron systems can be derived from the hybridization between conduction band and 4f state (c-f hybridization). Therefore, to directly probe the c-f hybridized electronic structures in the momentum space is important for understanding the heavy fermion physics. Angle-resolved photoemission spectroscopy (ARPES) is a powerful tool for this purpose. Recently, some ARPES results regarding the c-f hybridized electronic structure were reported [1-4]. These studies were performed on the basis of the surface Brillouin zone [1, 4] or by using the 4d-4f resonant process [2, 3]. However, ARPES for the f electron systems, which usually have three-dimensional electronic structure, should be done along the bulk Brillouin zone.

YbAl$_2$, which crystallizes in the cubic Laves MgCu$_2$ structure, is a prototypical valence fluctuation system. The Yb mean valence has been estimated to be $\sim$ +2.2 by the resonant inelastic x-ray scattering experiment [5]. The electronic specific-heat coefficient as a measure of the electron-mass enhancement exhibits a slightly high value, $\gamma\sim$10-17 mJ/K^{2}mol [6]. These characteristics suggest that a strong c-f hybridization effect can be realized in YbAl$_2$. Hence YbAl$_2$ is well-suited system for studying the c-f hybridized electronic structures including the f electron dispersion.

In this work, we have performed ARPES for YbAl$_2$. The single crystals of YbAl$_2$ were grown by the Lithium flux method [6]. The ARPES experiment was carried out at the undulator beamline BL7U "SAMRAI" in UVSOR-II [7]. The total energy resolution was set to ~10 meV and the measurement temperature was 12 K. The crystal orientation was determined by Laue x-ray diffraction prior to the ARPES measurements. The crystal was cleaved *in situ* at 12 K along the (111) plane.

Figure 1 (a) shows the bulk Brillouin zone of YbAl$_2$. The photon energy $h\nu=20$ eV were chosen so as to obtain the electronic band dispersion in the Γ-K line as shown in Fig. 1 (b). The electron pocket centered at Γ point and the nearly flat bands at the binding energy of 0.15 eV are observed, which are attributed to Yb 5d conduction and Yb 4$f_{7/2}$ bands, respectively. These states are strongly hybridized with each other, providing a fractional dispersion in Yb 4$f_{7/2}$ bands.
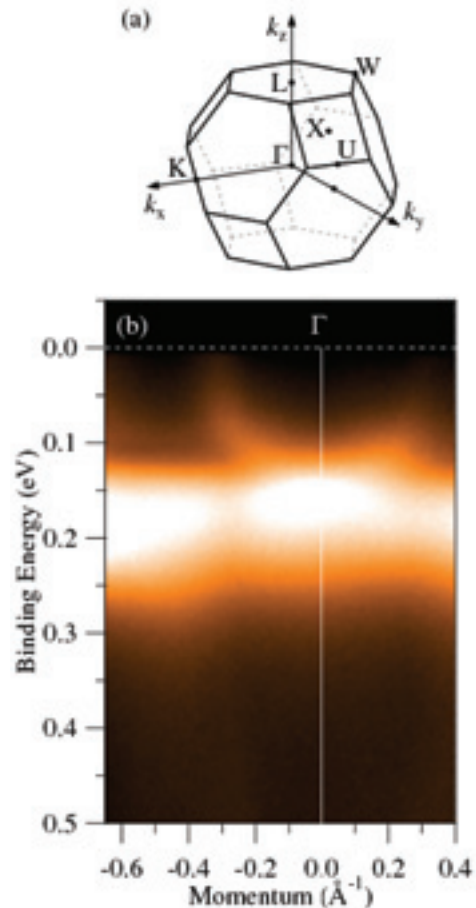

Fig. 1. The Brillouin zone (a) and the ARPES intensity map around Γ point at 12 K (b) of YbAl$_2$.

[1] S. Danzenbacher *et al.*, Phys. Rev. Lett. **96** (2006) 106402.
[2] G. A. Wigger *et al.*, Phys. Rev. Lett. **76** (2007) 035106.
[3] H. J. Im *et al.*, Phys. Rev. Lett. **100** (2008) 176402.
[4] D. V. Vyalikh *et al.*, Phys. Rev. Lett. **105** (2010) 237601.
[5] C. Dallera *et al.*, Phys. Rev. B **68** (2003) 245114.
[6] H. Nowatari *et al.*, J. Phys. Soc. Jpn. **76** (2007) Suppl. A, pp. 80.
[7] S. Kimura *et al.*, Rev. Sci. Instrum. **81** (2010) 053104.

Ⅲ-5. SOLID STATE PHYSICS

Temperature-Dependent Angle-Resolved Photoemission Spectra of SmB₆ (001)

H. Miyazaki[1], T. Hajiri[2], T. Ito[2] and S. Kimura[1,3]

[1]*UVSOR Facility, Institute for Molecular Science, Okazaki 444-8585, Japan*
[2]*Graduate School of Engineering, Nagoya University, Nagoya 464-8603, Japan*
[3]*School of Physical Sciences, The Graduate University for Advanced Studies,
Okazaki 444-8585, Japan*

Rare-earth intermetallic compounds generally become metals with strong electron correlations. However, some compounds become semiconductors with very small energy gap at the Fermi level (E_F), namely "Kondo semiconductor" or "Kondo insulator" [1]. SmB₆ is one of Kondo semiconductors. The energy gap formation of SmB₆ has been debated for a long time because the origin of the energy gap has been unclear yet. To solve this problem, it is important to investigate the detailed electronic structure of SmB₆. Three-dimensional angle-resolved photoemission spectroscopy (3D-ARPES) using synchrotron radiation is the most powerful technique to determine the electronic band structure directly. Then we have performed 3D-ARPES to clarify the momentum-dependent electronic structure near E_F.

A SmB₆ (001) single crystal was cleaned by Ar+ ion sputtering and 1400 °C annealing cycles in the ultrahigh vacuum (UHV) chamber with a base pressure of ~ 2 × 10⁻⁸ Pa. Clean surface of SmB₆ with the 2 × 2 (001) patterns was confirmed by a low energy electron diffraction (LEED) method and no contamination, such as carbon, was checked by an Auger electron spectroscopy (AES). The 3D-ARPES measurements were performed at the beamline 7U of UVSOR-II. The total energy and momentum resolutions for the ARPES measurement were set to 13 meV and 0.006 Å⁻¹ at the Γ point ($h\nu$ = 26 eV) and 12 meV and 0.003 Å⁻¹ at the X point ($h\nu$ = 10.6 eV), respectively.

Figures 1 (a1) and (b1) show the temperature dependence of the energy distribution curves (EDCs) at the Γ and X points, respectively. The Fermi edge of the EDCs is broadened with elevating temperature due to the thermal excitations of electrons. With decreasing temperature, we observed broad and sharp peaks at around 20 meV at the Γ and X points, respectively, and small gap opening at both points. To clarify the temperature-dependent components near E_F, Figs. 1 (a2) and (b2) indicate density of states (DOS) derived from the EDCs derived by the Fermi-Dirac function evaluated from the gold at Γ and X points, respectively. DOS at E_F gradually decreases with decreasing temperature at both the Γ and X points. However, only at the X point, a peak around 15 meV appears below 100 K and becomes larger on cooling. According to the temperature-dependent X-ray adsorption spectra (XAS) at the $L_{2,3}$-edge, the mean valence of Sm ions

is dramatically changed from 2.57 at 120 K to 2.50 at 30 K [2]. The temperature dependence of the 15 meV peak at the X point is consistent with the XAS result, i.e., the 20 meV peak is strongly related to the change of the valence. According to the LDA band structure calculation, the hybridization between the Sm 5d and 4f states appears and the energy gap opens at the X point. Therefore the hybridization scenario is plausible for the semiconducting nature of SmB₆.
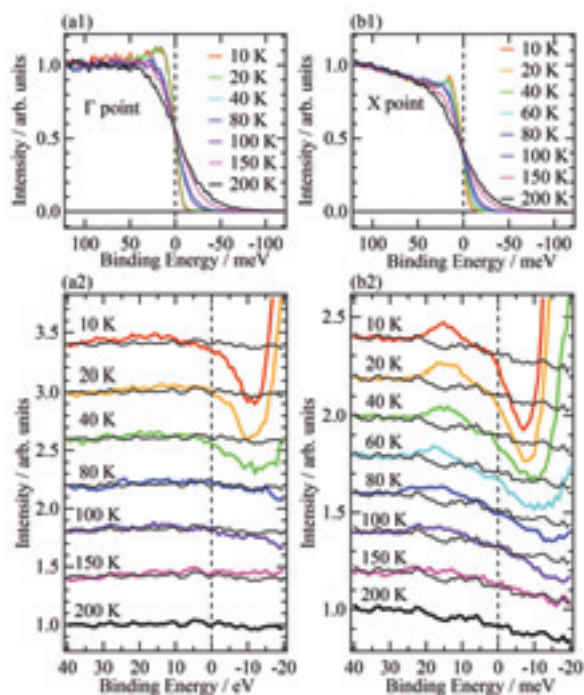

Fig. 1. Temperature dependence of the energy distribution curves (EDCs) and density of states (DOS) of SmB6 derived from the EDCs divided by the Fermi-Dirac function near the Γ point (a1, a2) and X point (b1, b2), respectively.

[1] G. Aeppli and Z. Fisk, Comment Condens. Matter Phys. **16** (1995) 1629.
[2] M. Mizumaki *et al.*, J. Phys.: Conf. Ser. **176** (2009) 012034.

High-Resolution Angle-Resolved Photoemission Study of an Iron Pnictide CaFe$_2$P$_2$: Observation of Strong k_z Dispersion

K. Nakayama[1], T. Kawahara[1] P. Richard[2], K. Umezawa[1], T. Sato[1,3] and T. Takahashi[1,2]

[1]*Department of Physics, Tohoku University, Sendai 980-8578, Japan*

[2]*WPI Research Center, Advanced Institute for Materials Research, Tohoku University, Sendai 980-8577, Japan*

[3]*TRIP, Japan Science and Technology Agency (JST), Kawaguchi 332-0012, Japan*

The discovery of superconductivity in LaFeAsO$_{1-x}$F$_x$ below a transition temperature (T_c) of 26 K [1] has generated great interest. Owing to intensive researches, a lot of related compounds, which contain iron-pnictide (FeAs or FeP) layer, have been discovered. An important current issue is why physical properties show remarkable differences between the FeAs and FeP compounds despite an identical carrier number (Fe $3d$ electrons). For example, the highest T_c is about one order of magnitude different (~56 K and ~7 K for FeAs and FeP compounds, respectively). It is also known that the non-doped FeAs compound exhibits an antiferromagnetic (AF) order accompanied by a structural phase transition, while the FeP compound does not show either magnetic or structural transition. To understand the origin of these differences in terms of electronic structure, angle-resolved photoemission spectroscopy (ARPES) is a powerful technique. Indeed, ARPES has revealed several essential features responsible for the superconductivity and AF order in the FeAs compounds, particularly in AFe$_2$As$_2$ (A = Ca, Sr, and Ba) system, such as Fermi-surface topology, superconducting-gap symmetry, and band folding in the AF phase [2-5]. On the other hand, little is known about the electronic structure of the FeP compounds.

In this study, by utilizing the low energy and variable photon energy ($h\nu$) characters of the beamline BL7U, we have succeeded in directly observing three-dimensional bulk band dispersions in CaFe$_2$P$_2$, which does not show superconducting and AF transitions.

Figure 1 (a) shows ARPES spectral intensity plot along Γ(Z)-M(A) high-symmetry line measured with $h\nu$ = 23 eV. As denoted by black curves in Fig. 1 (a), we identify several highly dispersive bands such as a holelike α band and an electronlike γ band which cross Fermi level (E_F) at the Γ(Z) and M(A) points, respectively. To clarify the dimensionality of the electronic structure, we have performed systematic $h\nu$ dependence at the Γ(Z) point. As clearly seen from Fig. 1 (b), the holelike bands exhibit significant dispersions as a function of $h\nu$. For example, the α band is located at ~100 meV below E_F for $h\nu$ = 15 eV, while it is above E_F for $h\nu$ = 23 eV [Fig. 1 (a)], clearly indicating the presence of three-dimensional closed Fermi surface in CaFe$_2$P$_2$. This result is in sharp contrast to the previous observation of

quasi-two-dimensional cylindrical Fermi surface in the normal state of CaFe$_2$As$_2$ [4]. The observed difference in the dimensionality of the electronic structure may be a key in understanding the differences between the FeAs and FeP compounds. It has been argued that the nesting between hole and electron Fermi surfaces plays an important role for the occurrence of the superconductivity and the AF order in iron pnictides. It is thus inferred that lower T_c and the absence of the AF order in the FeP compound is caused by the deterioration of the nesting condition due to higher dimensionality, which may be associated with the shorter c-axis length compared to the FeAs compound.
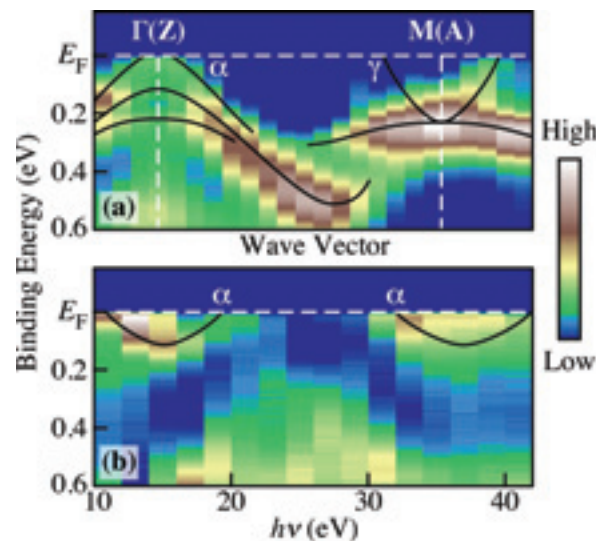

Fig. 1. (a) ARPES intensity of CaFe$_2$P$_2$ plotted as a function of wave vector and binding energy measured at 25 K with $h\nu$ = 23 eV. (b) $h\nu$ dependence of ARPES intensity at the Γ(Z) point. Black curves are guides for the eyes to trace the band dispersion.

[1] Y. Kamihara *et al.*, J. Am. Chem. Soc. **130** (2008) 3296.
[2] H. Ding *et al.*, Europhys. Lett. **83** (2008) 47001.
[3] K. Nakayama *et al*., Europhys. Lett. **85** (2009) 67002.
[4] C. Liu *et al.*, Phys. Rev. Lett. **102** (2009) 167004.
[5] P. Richard *et al.*, Phys. Rev. Lett. **104** (2010) 137001.

Ⅲ-5. SOLID STATE PHYSICS

Intrinsic Quasi-Particle Dynamics in Topological Metallic States

S. R. Park[1], W. S. Jung[1], G. R. Han[1], Y. K. Kim[1], Ch. Kim[1], D. J. Song[1], Y. Y. Koh[1], C. Kim[1],
S. Kimura[2], K. D. Lee[3], N. Hur[3], J. Y. Kim[4], B. K. Cho[4], J. H. Kim[5], Y. S. Kwon[5] and J. H. Han[5]

[1]EInstitute of Physics and Applied Physics, Yonsei University, Seoul, Korea
[2]UVSOR Facility, Institute for Molecular Science, Okazaki 444-8585, Japan
[3]Department of Physics, Inha University, Incheon, Korea
[4]Department of Materials Science & Engineering, GIST, Gwangju, Korea
[5]Department of Physics, Sungkyunkwan University, Suwon, Korea

Topological metallic (TM) states, the metallic surface states of topological insulator (TI), recently have raised great interest in the condensed matter community because of their novel properties. Spin degeneracy which is normally found in solids is lifted in TM states. Electron spins in TM are locked into the momenta, forming chiral spin states. Such spin texture should strongly suppress backscattering by non-magnetic impurities. Due to these properties, TM states are supposed to have high electron mobilities.

High mobilities in the surface states have not been experimentally measured as the transport method can be used only for bulk conductivity. On the other hand, mobility or life time of surface electrons can be measured by ARPES. To obtain the intrinsic quasi-particle life time, we have performed ARPES experiments on Bi_2Se_3, Bi_2Te_3 and Sb. Bi_2Se_3, Bi_2Te_3 and Sb single crystals were grown by flux and Bridgman methods. Samples were cleaved in situ and ARPES measurements were performed at the beamline BL7U [1, 2].

From the earlier experiments at UVSOR, we found out that the quasi-particle dynamics is severely affected by adsorbed atoms and molecules on the surfaces. Therefore, we have raised samples temperatures to anneal off the adsorbed atoms and molecules and obtain clean surfaces. Figure 1 shows ARPES data from Bi_2Se_3, Bi_2Te_3 and Sb surface states taken with 8 eV photons. 8 eV is found to suppress the bulk state spectral weight. The surface band reaches the Γ point near the 0.3 eV binding energy for Bi_2Se_3. This point is called the Dirac point. The binding energies of Dirac points are 0.3, 0.11 and 0.23 eV for Bi_2Se_3, Bi_2Te_3 and Sb, respectively.

Suppression of the bulk ARPES states allows us to perform reliable self energy analysis on the data. The imaginary parts of the self energies from the data are plotted in Fig. 2. In the data, it is noted that $Im\Sigma$ from topological surface states are very much energy independent, at around 25 meV. This casts a stark contrast to the case of high temperature superconductors for which $Im\Sigma$ is very energy dependent. In addition, the width of 25 meV is very small, indicating the quasi-particle life time in the surface states is very long.

Even though 25 meV is already very small, we believe the intrinsic width is even smaller. Generally,

electron-electron interaction gives the energy dependent width. Therefore, the constant width indicates that the electron-electron correlation is extremely small. Other contribution to the width may be from the electron-phonon coupling. However, no electron-phonon kink structure was observed, meaning electron-phonon contribution is negligible. Therefore, the only culprit for the breadth is impurity/inhomogeneity. These results clearly show that the intrinsic life time of the quasi-particles in surface states is extremely long, resulting in peak widths of less than a few meV. This value is smaller than any other cases, including the superconducting coherence peak in the ARPES spectrum from the $(\pi,0)$ point of high temperature superconductors.
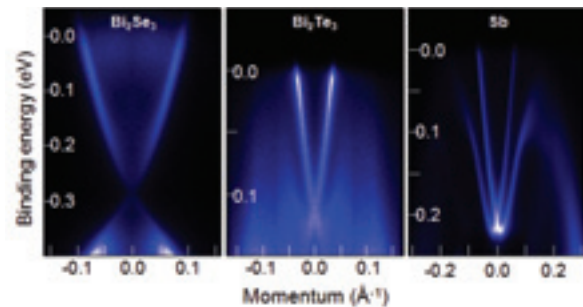

Fig. 1. Near Γ point ARPES data from various topological surface states : (a) Bi_2Se_3 (b) Bi_2Te_3 and (c) Sb [From ref. 2].
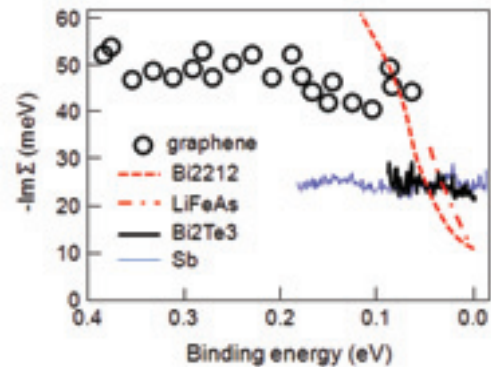

Fig. 2. Plot of $Im\Sigma$ from $Bi_{2-x}Sn_xTe_3$, Sb, graphene, $Bi_2Sr_2CaCu_2O_{8-\delta}$ (Bi2212) and LiFeAs [From ref. 2].

[1] S. R. Park et al., Phys. Rev. B **81** (2010) 041405.
[2] S. R. Park et al., New J. Phys. **13** (2011) 013008.

Angle-resolved Photoelectron Spectroscopy of HOPG with Photon Energies of <16 eV

S. Tanaka[1], M. Matsunami[2] and S. Kimura[2]

[1]*The Institute of Scientific and Industrial Research, Osaka University, Ibaraki 567-0047, Japan*

[2]*UVSOR Facility, Institute for Molecular Science, Okazaki 444-8585 Japan*

Graphite has been regarded as a "textbook" system for investigations of the solid state physics for many years because of its unique characters. It consists of carbon, which is one of the most basic elements, and the network of the sp^2-hybridized orbital makes the quasi-two dimensional electronic structure. The dispersions of the valence band are schematically shown in Fig. 1 [1].
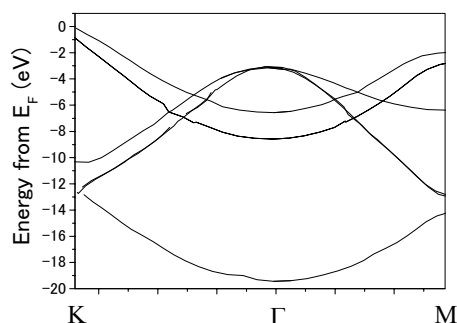

Fig.1 Electronic structure of the graphite.

In this report, we present a photoelectron spectroscopic study of HOPG (Highly Oriente Pyrolytic Graphite) at the photon energy region below 16 eV for the first time.

The experiments were carried out at the BL7U at UVSOR, which covers the photon energy of 6-43 eV, and is equipped with the apparatus for the angle-resolved photoelectron spectroscopy (ARPES). An HOPG sample was cleaved in UHV ($<1\times10^{-8}$ Pa), and its fresh surface was investigated. The reliability of the experiments including the sample condition was checked with the comparison of the ARPES spectra taken at $h\nu$=41 eV with the previous result [2].

Figure 2 shows the series of the surface-normal-photoelectron spectra of HOPG at 11 K with photon energies of 7.3-16 eV. Intensities are calibrated by the photon intensities measured with the photodiode. The most striking feature is the sharp peaks just below the Fermi level, whose intensities are resonantly enhanced at $h\nu$=11.2 eV (the width is about 1 eV).

This is surprising since the band of the graphite crosses the Fermi level at the K-point, and the highest occupied state at the Γ-point is about 3 eV below the Fermi level. We found that these peaks are only observed below 30 K of the sample temperature. The resonance is probably due to the excitation into the unoccupied state at 11.2 eV above the Fermi level.
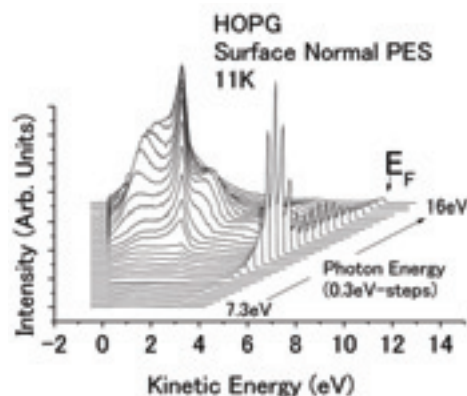

Fig.2 Series of the photoelectron spectra of HOPG.

One may argue that this could be ascribed to an extrinsic origin; the defect or the adsorbed species on the surface. The use of the ARPES, however, enables us to deny this possibility. In Fig. 3, the result of the ARPES at $h\nu$=11.5 eV are shown together with the dispersion of the peak as a function of the $k_{//}$. The dispersion is similar to the calculated one at the K-point along the K-Γ direction of the graphite (solid lines) except a typical quasi-particle behavior.
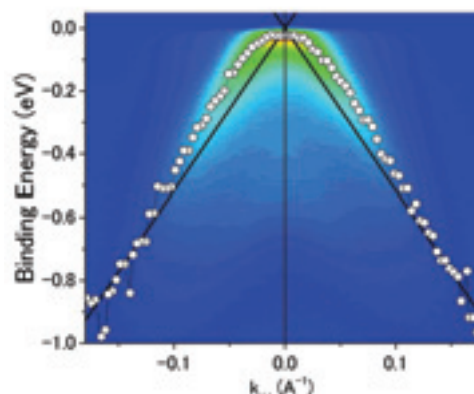
Fig. 3 Dispersion of the peak near the Fermi level.

Most plausible explanation is that the K-point is backfolded to the Γ-point in the two-dimensional Brilloin zone due to the reconstruction of the HOPG lattice which occurs below 30 K. The detailed study to clarify this possibility is now under progress.

[1] R. Ahuja *et al.,* Phys. Rev. B **55** (1997) 4999.
[2] K. Sugawara *et al.,* Phys. Rev. B **73** (2006) 045124.

Ⅲ-5. SOLID STATE PHYSICS

Characterization of Indium Filter for Generation of Single Order Laser Harmonics

M. Fushitani, A. Matsuda and A. Hishikawa

Department of Chemistry, Graduate School of Science, Nagoya University,
Nagoya 464-8602, Japan

An ultrashort laser pulse in the extreme ultraviolet (EUV) region is of great interest as a probe to investigate ultrafast dynamics of molecules because of the capabilities of ionizing most atoms and molecules. Among others, laser high-order harmonic generation using a gaseous nonlinear medium is proved to be a promising frequency conversion process to obtain EUV laser pulses [1].

Due to the up-conversion process occurring every half optical cycle of the driving laser pulse, laser high-order harmonics is often generated as a train of pulses, and the corresponding spectrum exhibits a series of odd-order harmonics. For time-resolved measurements, a single pulse is preferred rather than a pulse train. There are several methods to transform a pulse train into a single pulse. A typical method is to employ optical components such as a grating where the harmonics are spectrally dispersed and one of the harmonic orders is spatially selected by using a slit. The single harmonics, however, are significantly stretched in the time domain. An alternative method is to use a thin metal foil as a narrow-band filter. Because of the thickness in the order of 10^3 Å, less amount of dispersion is introduced in the selected harmonics during the propagation of a metal foil, keeping the pulse duration still short. Here, we investigate the transmission property of an indium foil to obtain ultrashort EUV laser pulse at 80 nm as the 5th order harmonics of the UV laser pulse at 400 nm.

The transmittance of an indium filter with a thickness of 1000 Å was measured at BL7B. The synchrotron radiation (SR) was dispersed by the G2 (600 lines/mm) and G3 (300 lines/mm) gratings in the wavelength range of 40<200 and 120<800 nm, respectively. The reference and transmitted light were detected by a Si photodiode (AXUV100).

Figure 1 shows parts of the transmittance of the indium filter. The maximum transmittance of <10 % is observed around 80 nm with modulations due to the interference effect [2]. The second maximum observed in the region of 150<200 nm is attributed to the second order diffraction of the G2 grating. The transmittance in the 320<480 nm is about 0.1 %.

The expected wavelengths for the 3rd (HH3), 5th (HH5) and 7th (HH7) order harmonics driven by ultrashort laser pulse at 400 nm (UV) are indicated by arrows in Fig. 1. The corresponding transmittances are 0.1 % (UV), 0.07 % (HH3), 10 % (HH5), and 0.3 % (HH7). The present study shows that the indium foil is a suitable narrow-band filter for HH5 to generate ultrashort EUV pulse at 80 nm, with a high contrast ratio (10^3) to the neighboring orders (HH3 and HH7).

[1] T. Brabec and F. Krausz, Rev. Mod. Phys. **72** (2000) 545.
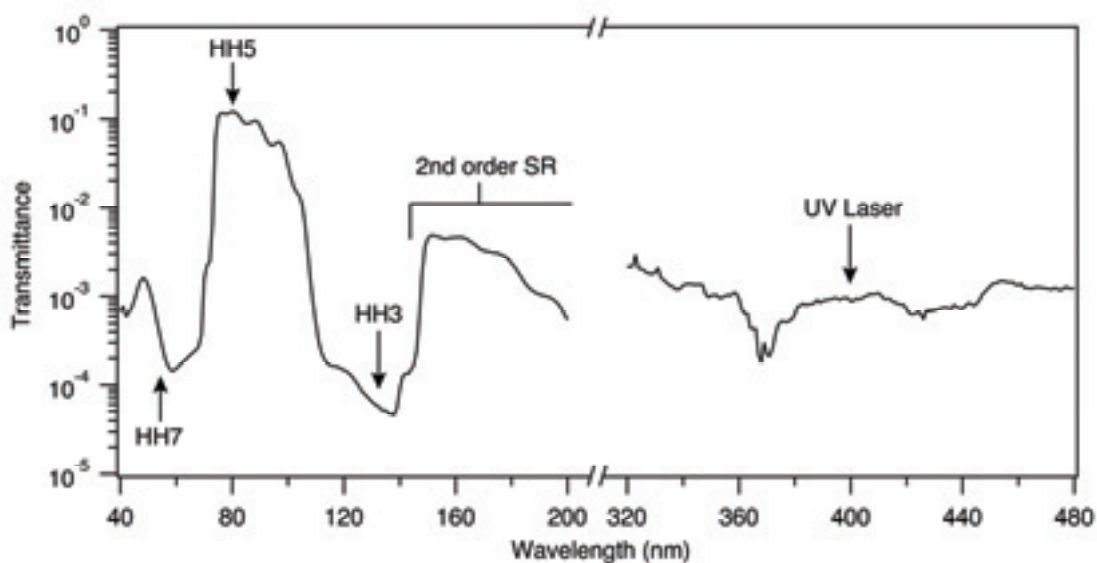[2] W. R. Hunter, D. W. Angel and R. Tousey, Appl. Opt. **4** (1965) 891.

Fig. 1. Parts of the transmittance curve of an indium foil with a thickness of 1000 Å in the wavelength region of 40<200 and 320<480 nm.

Impurity Band of Boron Doped Diamond
Observed in the Ultra-Violet Region

T. Inushima[1], Y. Ota[1] and K. Fukui[2]

[1]*Department of Electronics, Tokai University, Hiratsuka 259-1292, Japan*
[2]*Department of Electrical and Electronics Eng., University of Fukui, Fukui 910-8507, Japan*

We report on the refractive index of the impurity band which formed in a semiconductor in the ultra-violet region.

Since the discovery of superconductivity in boron-doped diamond, its impurity band structure has been a key issue for the understanding of the superconductivity. Recently it is reported that when the boron concentration exceeds $N_B=4\times10^{18}$cm^{-3}, impurity band forms at the first excited levels (2p) of the impurity boron at 0.06 eV above the valence band maximum. At higher N_B, the wave functions of the 2P states begin to overlap and the impurity band spreads in the k-space. Simultaneously, Fermi level rises to the impurity band and a variable range hopping is realized [1]. This mechanism can be seen in the absorption spectra of boron doped diamond, which is shown in Fig. 1.

When N_B is low (<1000 ppm), the prominent absorption peaks are at 0.305 and 0.347 eV, which are the transitions from 1S to $2P_0$ and $2P_{\pm1}$ states, respectively. These transitions form a sharp Gaussian shape and are accompanied by LO-phonon sidebands in the higher energy region. When N_B exceeds 4×10^{18} cm^{-3} (2000 ppm), the absorption spectrum changes into a Lorentzian shape governed by the single absorption at 0.35 eV, and the sharp structure disappears, which indicates a drastic decrease of the relaxation time of the excited carriers, or an appearance of the impurity band.

In order to clarify the energy dependence of the impurity band structure, we measured refractive index of the impurity band in the ultra-violet region using BL7B.

Figure 2 shows the reflection spectra of 2000 ppm boron doped diamond measured at 20 and 300 K by a combination of S2 (6~12 eV) and S3 (3~7 eV) detectors. The spectra have clear sinusoidal interference fringes caused by the transmitting light of the homo-epitaxial diamond film. Using the film thickness of 1.6 μm, refractive index is determined as a function of photon energy, which is shown in the inset of Fig. 2.

The observed refractive index is much smaller than that of the bulk diamond (n~2.4), and shows a minimum at 6 eV. The increase in the higher energy side is due to the direct transition of the bulk diamond at 11.2 eV, and there is no reflection anomaly at the indirect gap at 5.4 eV.

Figure 2 indicates that the impurity band that formed in the bulk diamond has energy dispersion and that it extends up to 10 eV.
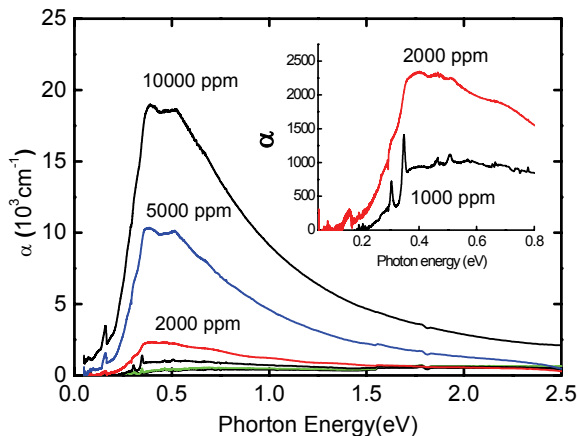

Fig. 1. Boron concentration dependence of the absorption spectra of diamond. The B/C ppm ratio used in the crystal growth is used as the indication of the samples and 10,000 ppm corresponds to N_B of 2×10^{19} cm^{-3}.
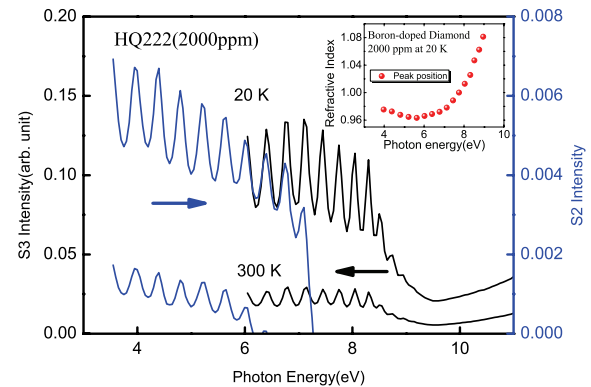

Fig. 2. Reflection spectra of 2000 ppm boron doped diamond at 20 and 300 K. Inset shows the energy dependence of the refractive index.

[1] T. Inushima, R. F. Mamin and H. Shiomi, Phys. Rev. B **79** (2009) 045210.

III-5. SOLID STATE PHYSICS

Spectroscopic Analysis of Electronic States of Solids in Scope of IR-VUV Utilizing BL7B

A. Irizawa[1] and S. Kimura[2,3]

[1]*The Institute of Science and Industrial Research, Osaka University, Ibaraki 567-0047, Japan*
[2]*School of Physical Sciences, The Graduate University for Advanced Studies (SOKENDAI), Okazaki 444-8585, Japan*
[3]*UVSOR Facility, Institute for Molecular Science, Okazaki 444-8585, Japan*

Introduction

The optical study is one of the most effective approaches in terms of the tunability and the wideness of energy range for understanding of electronic states of solids. The accurate analysis can be achieved from the reflectivity in the wide energy range as far as possible where the optical conductivity can be derived from the reflectivity through Kramers-Kronig (KK) transform. In that sense, the reflectivity data from BL7B in the wide energy range between 1.2 and 40 eV (1000-30 nm) is the important part for KK transform. In this machine time, we prepared several solid samples of strongly correlated *d*-electron system. $Sr_2Ir_{1-x}Rh_xO_4$ (x=0-1) is the newly synthesized system having the perovskite-related crystal structure, so called the Ruddlesden-Popper phase [1]. The end members of this system are that Sr_2IrO_4 is the spin-orbital Mott insulator [2, 3] and Sr_2RhO_4 is the 2D-like metal [4, 5], respectively. The metal-insulator transition has been reported for the solid solution $Sr_2Ir_{1-x}Rh_xO_4$ where the electronic state will change at around x=0.8. We measured the reflectivities of all these compounds using a 3-m normal incidence monochromator at BL7B in this beam time.

Experimental

The optical reflectivities of $Sr_2Ir_{1-x}Rh_xO_4$ (x=0-1) were measured at UVSOR-II BL7B. The energy was changed from 1.2 to 40 eV with three gratings (1200, 600, and 300 lines/mm). There are several types of optical window for avoiding the higher degree diffractions. Follow to the former studies in BL7B, we selected the 3 type windows with the 2 gratings for the main experiments. Also we checked the continuity of them by the G2 measurement. The measured temperatures were selected for 300 K and 77 K as a room temperature and the lower temperature.

Results and Discussion

As a result, the spectra can be obtained for all the compositions of $Sr_2Ir_{1-x}Rh_xO_4$ (x=0, 0.5, 0.8, 1). The measurements were repeated twice for all the compositions. The results are stabilized for the different sequences as shown in Figs. 1 instead of the low intensity of the reflection. Although the connectivity among the spectra with the different gratings and the windows still have some controversial point, they can be connected in the single spectrum by the proportional operation. The temperature variation is hardly discriminated within the limits of error in this experiment.
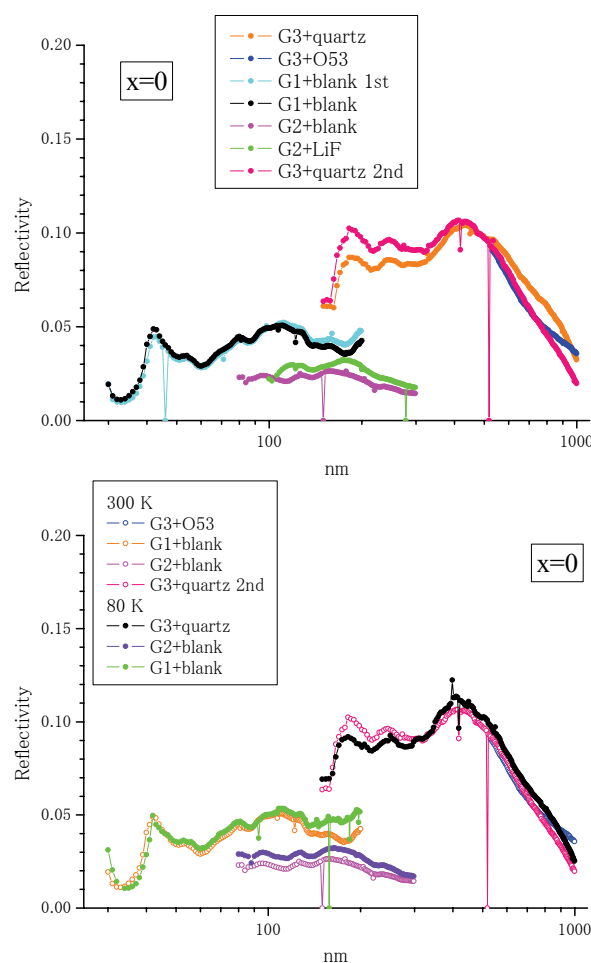

Fig. 1. Stability of reflective spectra for the twice measurements.

[1] M. Isobe, JPS meeting (2010) 24pXP-9.
[2] S. J. Moon *et al.,* Phys. Rev. Lett. **101** (2008) 226402.
[3] B. J. Kim *et al.,* Science **323** (2009) 1329.
[4] F. Baumberger *et al.,* Phys. Rev. Lett. **96** (2006) 246402.
[5] B. J. Kim *et al.,* Phys. Rev. Lett. **97** (2006) 106401.

Optical Study of Rattling Phonons in Clathrate Compounds

T. Mori[1], M. Matsunami[1,2], T. Iizuka[2], S. Kimura[1,2], K. Suekuni[3] and T. Takabatake[3,4]

[1]UVSOR Facility, Institute for Molecular Science, Okazaki 444-8585, Japan

[2]School of Physical Sciences, The Graduate University for Advanced Studies (SOKENDAI), Okazaki 444-8585, Japan

[3]Department of Quantum Matter, ADSM and [4]Institute for Advanced Material Research, Hiroshima University, Higashi-Hiroshima 739-8530, Japan

Recently novel phenomena related to local anharmonic phonons observed in cagelike materials such as intermetallic clathrates have attracted much interest [1-4]. In particular, the so-called rattling phonons of guest ions in polyhedral cages and how they may affect such as electric and thermal properties, have been studied extensively in light of their potential application in thermoelectric devices.

Some of the clathrates classified in type-I structure show not only low thermal conductivity with a high thermoelectric figure of merit, but also glasslike temperature dependence of specific heat and thermal conductivity [1]. Such thermal properties are universally observed in glasses or amorphous materials, though the present materials form a regular lattice. It is thus argued that such anomalous thermal behaviors may be caused by the rattling phonons vibrating in an off-centered anharmonic potential.

In this study we measured reflectivity spectra of type-I $Ba_8Ga_{16}Sn_{30}$ (β-BGS), type-I $Ba_8Ga_{16}Ge_{30}$ (BGG), and type-VIII $Ba_8Ga_{16}Sn_{30}$ (α-BGS) to investigate rattling phonon and electric structure. In those materials, only β-BGS has off-centered rattling phonon and shows glasslike thermal properties.

The single crystals of n- and p-type β-BGS, BGG, and α-BGS were grown by a self-flux method [1, 2]. Reflectivity spectra of those samples were measured in the photon energy range of 2 meV – 30 eV using several spectroscopies. In the energy range between 2 meV and 1.5 eV, two interferometers (Martin-Puplett and Michelson type) were used. In the energy range between 1.5 and 30 eV, a synchrotron radiation at BL7B in UVSOR facility was used in this machine time. The optical conductivity spectra $\sigma(\omega)$ were calculated from the reflectivity spectra using Kramers-Kronig (KK) relations.

Figure 1 (a) shows obtained reflectivity spectrum of n-type β-BGS at room temperature. The spectrum of each energy region is connected smoothly based on far-infrared spectral data. Optical conductivity spectrum calculated from the reflectivity spectrum using KK relation is shown in Fig. 1 (b). The $\sigma(\omega)$ spectrum of n-type β-BGS consists of mainly three features. Firstly, below about 10 meV, there are four peaks of phonons. The lowest broad peak around 3 meV is assigned as off-center rattling phonon of $Ba(2)^{2+}$ ions. This observation of the rattling phonon is consistent with that obtained by another probe [4].

Secondly, below about 0.1 eV, the Drude-like doped carrier contribution is observed. Thirdly, there are two peaks around 1.5 and 20 eV. Including higher-energy structures, these are due to the electronic interband transitions from valence bands to conduction bands.

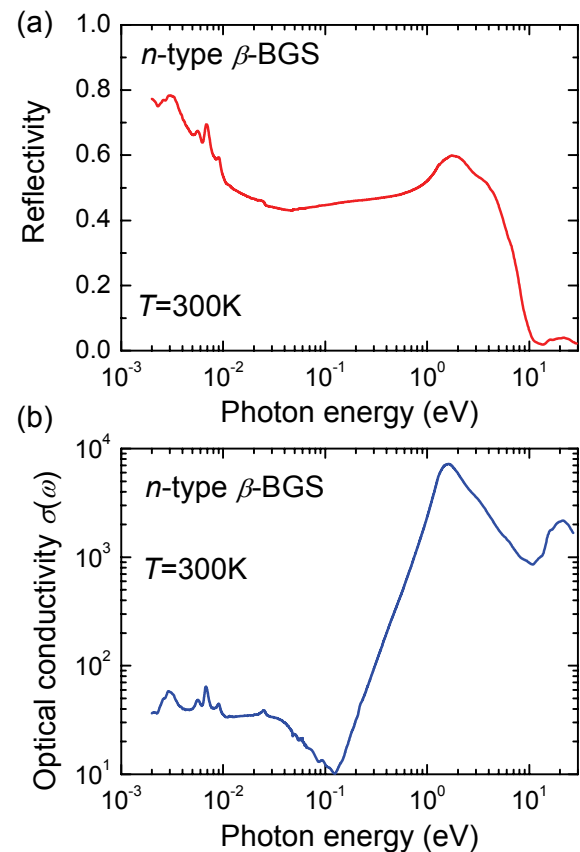Fig. 1. (a) Observed reflectivity spectra and (b) optical conductivity spectra $\sigma(\omega)$ of n-type β-BGS at room temperature.

[1] M. A. Avila *et al*., Phys. Rev. B **74** (2006) 125109.
[2] M. A. Avila *et al*., Appl. Phys. Lett. **92** (2008) 041901.
[3] T. Mori *et al*., Phys. Rev. B **79** (2009) 212301.
[4] T. Mori *et al*., Phys. Rev. Lett. **106** (2011) 015501.

Ⅲ-5. SOLID STATE PHYSICS

Characterization of Wide Bandgap Oxide and Fluoride Crystal in VUV Region

T. Nakazato[1], M. Tsuboi[1], K. Sakai[1], K. Yamanoi[1], T. Shimizu[1], N. Sarukura[1] and T. Fukuda[2]

[1]*Institute of Laser Engineering, Osaka University, Suita 565-0871, Japan*
[2]*WPI-AIMR, Tohoku University, 2-1-1 Katahira, Aobaku, Sendai 980-8577, Japan*

Introduction

All-solid-state lasers, optics, and scintillators in the vacuum ultraviolet (VUV) region are in demand because of the important roles that they play in various fields. Fluoride and oxide crystals are key materials, which meet these demands because of their wide-bandgap. In our previous research, we proved that zinc oxide (ZnO) is a promising fast scintillator [1], having achieved a luminescence lifetime of less than 100 ps by controlled impurity doping [2]. In this research, we measure the photoluminescence (PL) spectra of two different types of ZnO crystals, undoped and impurity-doped, at various temperatures in order to investigate their optical properties in the VUV region. Results provide the necessary database for optimizing this material for various applications.

Experiment

We have measured the PL spectra of undoped and impurity-doped ZnO crystals at 20 K, 50 K, 100 K, 150 K, 200 K, 250 K and 300 K. The excitation wavelength was 70 nm.

Results and Discussion

Figure 1 shows the temperature dependence of the PL spectra. Both the undoped and impurity doped ZnO have two emission peaks at around 380 nm and 600 nm. As shown in Fig. 1 (a), the 380 nm emission peak, which originates from exciton recombination, becomes narrower, more intense, and shifts to a shorter wavelength with decreasing temperature. These indicate that the exciton changes from free exciton to bound exciton with decreasing temperature. On the other hand, shift in wavelength and change in peak width of the 600 nm emission was not observed. Intensity increases with decreasing temperature, reaching maximum at 200 K. However, further decrease in temperature decreases the intensity. The 600-nm emission originates from transition between defect levels in the ZnO crystal. The temperature dependence of the broad emission in the visible region shows a different trend in previous work [3]. Further investigation is being carried out in order to understand this difference. Impurity-doped ZnO also manifests the same temperature dependence, as shown in Fig. 1 (b), except that the intensity of the 600-nm emission reaches maximum at 150 K.

The relative intensity of exciton emission from defect level-transition in impurity-doped ZnO is lower than that in the undoped one. This is because the impurity prevents exciton recombination, wherein
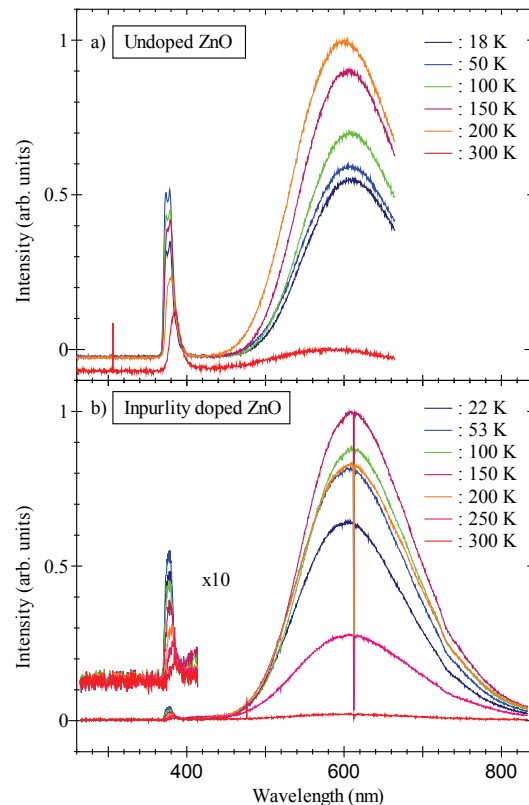

Fig. 1. Photoluminescence spectra of ZnO. Excitation wavelength is 70 nm. a) Undoped ZnO. b) Impurity doped ZnO.

the impurity works as a fluorescence quencher. On the other hand, the wavelength of the emission originating from exciton recombination (380 nm) and from transition between defect levels (600 nm) is the same regardless of impurity doping for all temperatures. These results show that we can control the lifetime without changing emission wavelength and other scintillator properties by impurity-doping. This systematic study will help us in material survey.

[1] M. Tanaka *et al.*, Appl. Phys. Lett. **91** (2007) 231117.
[2] T. Shimizu *et al.*, Rev. Sci. Instrum. **81** (2010) 033102.
[3] H. Mrokoc and U. Ozgur, "Zinc Oxide: Fundamentals, Materials and Device Technology", Wiley-VCH, Weinheim (2009).

Optical Constants of AlN Determined by VUV Ellipsometry

K. Ozaki[1], T. Saito[2], H. Iwai[1], K. Fukui[1] and I. Saito[2]

[1]Dept. Elec. Elec. Engi, Univ. Fukui, Fukui 910-8507, Japan
[2]National Metrology Institute of Japan, National Institute of Advanced Industrial Science and Technology, Tsukuba 305-8563, Japan

Introduction

Recently, the need for quantitative measurements of UV-VUV radiation is increasing with the expanding applications of the radiation for sterilization, curing, etc.. However, most-widely used Si photodiodes, have a serious problem of degradation under UV exposure. Therefore, AlN (AlGaN) photodiodes [1] without this problem are attractive. Accurate optical constants of materials composing a detector are necessary for the design and the characterization. Although commercially available spectroscopic ellipsometers are known as a powerful tool to obtain optical constants with high accuracy, the shortest wavelength limit is typically in the near UV region. Among some trials to go down to the VUV range, an AIST group designed a VUV ellipsometer using a oblique incident photodiode as a polarization analyzer and proved that it worked successfully [2]. Currently, we are tuning up the instrument by optimizing various conditions for the use at BL7B. In addition, we tried to obtain optical constants of an AlN by performing VUV spectroscopic ellipsometry measurement to AlN thin films, which can be used for AlN photodiodes.

Experiment

A VUV ellipsometer used this time is shown in Figure 1. First, the polarizer is not needed in this equipment by the reason that the polarization state of incident light to the sample can be artificially changed by rotating the sample chamber. Due to the characteristics of synchrotron radiation, the incident radiation is nearly linearly polarized. The beam reflected by the sample is detected by an inclined detector, which results in polarization sensitivity. This design eliminates the need of polarizer, which is typically realized by 3-time reflections, and greatly simplifies the mechanism.
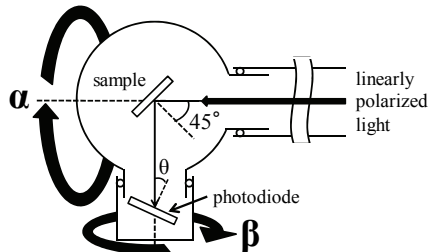

Fig. 1. Schematic layout of a VUV ellipsometer.

Analysis and Discussion

The Stokes vector **S'** at the detector can be expressed by

$$\mathbf{S}' = \mathbf{M_a}(\Psi_a, \Delta_a)\mathbf{R}(-\beta)\mathbf{M}(\Psi, \Delta)\mathbf{R}(-\alpha)\mathbf{S}, \quad (1)$$

where **S** is the Stokes vector of the incident light to the sample, $\mathbf{M}(\Psi,\Delta)$ the Mueller matrix of a sample, $\mathbf{M_a}(\Psi_a,\Delta_a)$ the Mueller matrix of a detector, $\mathbf{R}(-\alpha)$ the Muller matrix of a rotator (angle of rotation -α), $\mathbf{R}(-\beta)$ the Muller matrix of a rotator (angle of rotation -β). The detector is sensitive only to the intensity component S'_0 in **S'**. Hence, the Eq. 1 is expanded on S'_0. At certain βs, the equation is simplified and thus, all Stokes vector component of incident light, Δ, Ψ and Ψ_a are obtained by the fitting to the sample chamber rotation measurement result.

Ellipsometric parameters, Ψ and Δ, were obtained from measurement result of the AlN thin films on Al_2O_3 substrate. Complex refractive indeces ($N=n - ik$) of an AlN derived from Ψ and Δ are shown in Figure 2. A red line is a curve calculated by Kramers-Kronig transform and the fitting to reflectance.

In the energy range lower than 9 eV, optical constants obtained had large measurement errors. This is because the optical axis does not match the mechanical axis, which was brought by the change in the position of the incident optical axis depending on the wavelength. This is inevitable due to the spectral design of BL7B. Another cause is the influence of birefringence possibly due to the strain in LiF used for higher-order rejection. In the energy range higher than 9 eV, optical constants of AlN obtained by the ellipsometry are found to be close to those by K-K method considering the error bars.

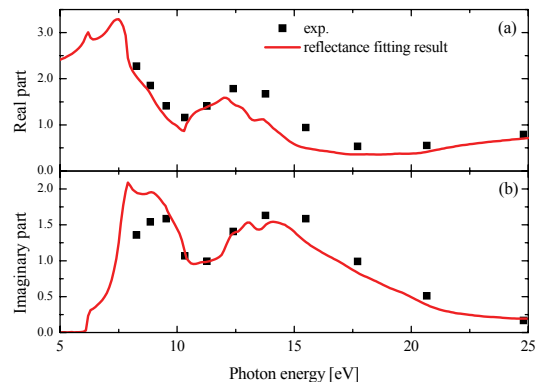For better performance, mechanical improvement and measurement automations are planned.

Fig. 2. Complex refractive indices of an AlN, (a) real part and (b) imaginary part.

[1] T. Saito *et al*., Phys. Stat. Solid. C **6** (2009) S658-S661.
[2] T. Saito, M. Yuri and H. Onuki, Rev. Sci. Instrum. **66** (1995) 1570.

Ⅲ-5. SOLID STATE PHYSICS

Ultraviolet Photoelectron Spectra
of Mono-Metal Endohedral Fullerene Er@C$_{82}$ (I)

T. Miyazaki[1], R. Sumii[2,3], H. Umemoto[4], H. Okimoto[4], Y. Ito[4], T. Sugai[4],
H. Shinohara[4] and S. Hino[1]

[1] *Graduate School of Science and Engineering, Ehime University, Matsuyama 790-8577, Japan*
[2] *Institutes for Molecular Science, Okazaki 444-858, Japan*
[3] *Research Center for Materials Science, Nagoya University, Nagoya 464-8602, Japan*
[4] *Graduate School of Science, Nagoya University, Nagoya 464-8602, Japan*

Erbium atom entrapped fullerenes have been isolated, the cage symmetry of Er@C$_{82}$ (I) has been determined to be C_{2v} (82:9) by NMR structural analysis, and the oxidation state of Er in Er@C$_{82}$ is an issue worth to investigate. In the current work, the ultraviolet photoelectron spectra (UPS) of Er@C$_{82}$(I) will be presented.

The ultraviolet photoelectron spectra (UPS) measurement was carried out at the beamline BL8B of Ultraviolet Synchrotron Orbital Radiation Facility (UVSOR) of Institute for Molecular Science. The base pressure of the measurement chamber was 4×10^{-8} Pa, and the pressure during the measurement went up to about 6×10^{-8} Pa. Specimens for UPS measurement were thin films vacuum deposited onto a gold deposited molybdenum disk from a quartz crucible under 5×10^{-7} Pa. The temperature of the crucible during vacuum deposition of Er@C$_{82}$(I) was 650–700 °C. The UPS were referenced against the Fermi level (E_F) of gold and were plotted as a function of binding energy relative to E_F.

The upper valence band UPS of Er@C$_{82}$ (I) obtained with hv = 20–55 eV incident photons are shown in Fig. 1. Eleven structures labeled A−K and marked with dotted lines were clearly observed. All spectra were normalized by the peak height of the structure E. The intensity of these structures changed, when the incident photon energy was tuned. For example, the intensity ratio of B–D was almost unity at hv = 20 eV and 40 eV but changed to about 1:2 at hv = 30 eV. This is a typical behavior in the UPS of fullerenes. The spectral onset energy (E_{onset}) of Er@C$_{82}$(I) is 0.38 eV below the Fermi level and this is much smaller than that of empty C$_{82}$ (1.2eV). The UPS of Er@C$_{82}$ (I) in the deeper binding energy region (E_b > 5 eV) is due to ó-electrons that constitute the C$_{82}$ skeletal C–C bonds. The seven peaks in this region were at 5.4 eV (E), 6.8 eV (F), 7.7 eV (G), 8.4 eV (H), 10.1 eV (I), 10.9 eV (J) and 12.9 eV (K). The UPS of the upper binding energy region (E_b < 5 eV) are derived from π-electrons and four structures are observed at 0.7 eV (A), 1.6 eV (B), 2.1 eV (C) and 3.3 eV (D).

The UPS of Er@C$_{82}$ is substantially identical with those of La@C$_{82}$ and Tb@C$_{82}$, which suggests their analogous electronic structure. The upper valence band UPS of Er@C$_{82}$ differs significantly from those of three Tm@C$_{82}$ isomers. This observation supports the empirical rule that the electronic structure of metallofullerenes is governed by the cage structure and the oxidation state of entrapped metal atom: the electronic structure is analogous when the cage structure of metallofullerenes and the oxidation state of the entrapped atom is the same, and the electronic structure might be quite different when the cage structure of the metallofullerenes or the oxidation state of the entrapped atom is different. Using this empirical rule we could deduce the cage structure of metallofullerenes or the oxidation state of the entrapped atom from the UPS measurements. The upper valence band UPS of Er@C$_{82}$ (I) is well reproduced by the simulated spectrum assuming a C_{2v}–C$_{82}$$^{3-}$, confirming the cage structure deduced from NMR analysis. It suggests that Er@C$_{82}$ (I) has the C_{2v}–C$_{82}$ cage structure and the oxidation state of the entrapped Er atom is +3.

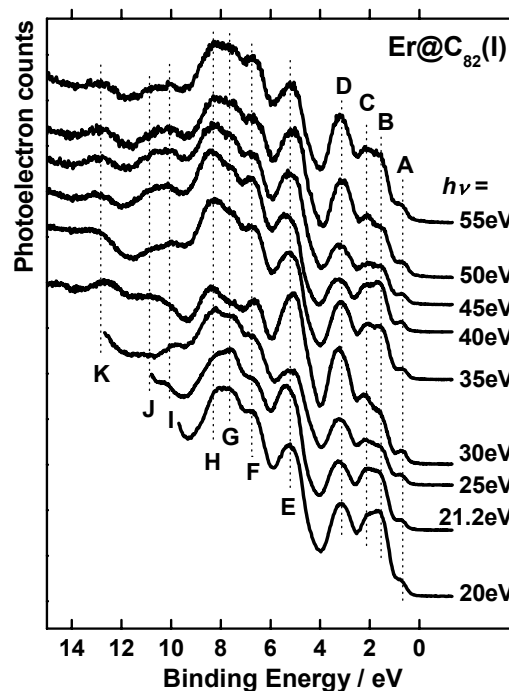Fig. 1. The incident photon energy dependent UPS of Er@C82 (I) at hv = 20 ~ 55 eV. Eleven structures are observed and their intensity changes upon the tuning of the incident photon energy.

Mo L$_3$-XANES Study of Silylation Effect for Methane Dehydroaromatization over Mo/H-MFI Catalysts

H. Aritani, K. Kuramochi and S. Yoshinaga

Faculty of Engineering, Saitama Institute of Technology, Fukaya 369-0293, Japan

A Mo-modified H-MFI zeolite (Mo/H-MFI) catalyst is one of a typical catalyst for direct GTL (Gas to liquid), because it shows high activity for dehydroaromatization of methane in absence of oxygen. In this reaction, reduction of Mo species is brought about in contact with methane in initial step, and reduced Mo ions react methane to form carbide and/or oxycarbide species in next step. It has been accepted that the carbide and/or oxycarbide species are the active center for dehydroaromatization of methane. However, deactivation cannot be avoided by carbon deposition. Hydrogen co-feed with methane is one of an effective method for suppression of coking. However, excess hydrogen may affect a reduction of Mo species during the reaction, and decrease of active Mo-oxycarbide species may give low reactivity. On the other hand, strong acid sites in external H-MFI surface possibly relates to the coking directly. Thus, selective covering of the coking site may be effective for durable activity [1]. Silylation of one of a unique method for selective coverage of external acid sites onto H-MFI. This study focused on the effect of silylation on methane dehydroaromatization over Mo/H-MFI catalysts. Mo L$_{III}$-edge XANES studies were introduced to characterize the active Mo species on bare and silylated H-MFI.

Catalysts were prepared by impregnation of H-MFI (Si/Al$_2$=67) synthesized hydrothermally with MoO$_2$(acac)$_2$−CHCl$_3$ solution, and followed by drying overnight and calcination at 773 K. MoO$_3$-loading amount is 5.0 wt% in whole catalysts. For silylation of Mo/H-MFI catalysts, heptane solution of teiethoxyvinylsilane (Mo/Si=10) was employed for impregnation, and followed by drying and calcination at 873 K. Mo L$_{III}$-edge XANES spectra were operated in BL1A of UVSOR-IMS in a top-up mode. InSb double crystal monochromator was used for the XANES measurements in a total-electron yield mode. The value of photon energy was calibrated by using Mo metal-foil at Mo L$_{III}$-edge, and normalized XANES spectra and their second derivatives were obtained for characterization. Catalytic activity was evaluated in a fixed bed flow reactor. Each catalyst (0.250 g) was placed in a quartz-tube reactor, and pretreated in He−CO(0-2%) flow (30 mL min^{-1}) at 973 K for 1 h. Then CH$_4$(20%)− H$_2$(1%)−He reactant gas was fed at 973 K (30 mL min^{-1}: SV = 7.2 L g^{-1} h^{-1}). Products were analyzed by online GC.

Figure 1 shows the Mo L$_{III}$-XANES spectra of silylated/unsilylated Mo/H-MFI catalysts after dehydroaromatization at 973 − 1073 K for 3 h. As
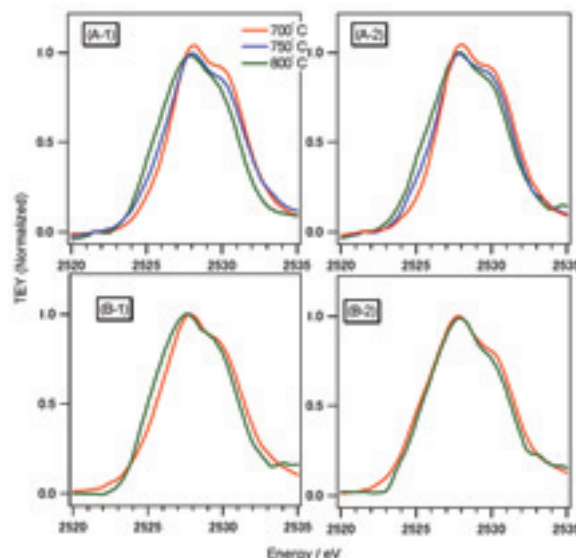

Fig. 1. Mo L$_{III}$-edge XANES spectra of (A) bare- and (B) Silylated- MoO$_3$(5.0wt%)/H-MFI catalysts after methane dehydroaromatization with (1) CH$_4$(20%)-He or (2) CH$_4$(20%)-H$_2$(1.0%)-He at various reaction temperature.

shown in Fig. 1 (A-1 and B-1), According to a higher reaction temperature, the edge energy of XANES threshould becomes lower. It indicates the reduction and/or carbonization of MoO$_x$ species to MoO$_x$C$_y$ ones. Excess reduction of Mo species brings about the deactivation of the catalysts because of excess carbon deposition [1, 2]. In case of silylated Mo/H-MFI [Fig. 1 (B-1) and (B-2)], the reduction degree of Mo species is almost as same as bare Mo/H-MFI [Fig. 1 (A-1) and (A-2)]. On these catalysts, high and durable activity for methane dehydroaromatization is significantly shown by silylation. The effect of silylation is possibly due to the depression of coking from methane, and the reduction of Mo species is almost independent. For Mo/H-MFI catalysts, formation of active MoO$_x$C$_y$ species (partially carbonized MoO$_x$) is one of a key role for high activity. And thus, deactivation of coking sites in H-MFI extrapores is very effective to obtain durable activity. In this study, it is suggested that silylation by using teiethoxyvinylsilane act as the depression of activity on the coking sites because coking amount becomes low. Detailed study about the silylation effect on Mo species is now in progress.

[1] H. Aritani, S. Shinohara, S. Koyama, K. Otsuki, T. Kubo, A. Nakahira, Chem. Lett. **35** (2006) 416.
[2] H. Aritani, H. Shibasaki, H. Orihara, A. Nakahira, J. Environm. Sci. **21-6** (2009) 736.

Ⅲ-6. APPLIED MATERIALS

XANES Analysis of Na-Incorporated β-Tricalcium Phosphate

K. Kawabata[1] and T. Yamamoto[2]

[1]Department of Holistic Human Science, Kwansei Gakuin University, 662-8501, Japan
[2]Faculty of Science and Engineering, WasedaUniversity, 169-8555, Japan

Bioceramics based on the calcium phosphate are now widely used for repairing the bone defects. As it is well known that the main component of the inorganic part of human bone consists of hydroxyapatite (HAp). HAp itself is, of course, used as bioceramics, but other calcium phosphates are also employed, in which β-tricalcium phosphate (β-TCP) is one of the most active one. It was reported that incorporation of trace elements in such bioceramics accelerates the creation of HAp in the human body. To understand the influence of trace elements, it is essential to understand the local environment of trace elements in an atomic scale. We have systematically investigated the local environment of divalent ions, i.e., Mg^{2+} [1], Mn^{2+} [2] and Zn^{2+} [3], by the XANES measurements with the aid of the first-principles calculations. In the present study, local environment of monovalent Na ions in β-TCP is investigated by the Na-K XANES measurements.

Sample specimens were fabricated by the conventional solid-state reaction method. High purity powders of $CaHPO_4$, $CaCO_3$ and $NaHCO_3$ were mixed and ground in an agate mortar, which were calcined at 1273 K for 6 hours in air. Na-K XANES spectra are measured at BL1A in UVSOR by the total electron yield method. Sample powders were mounted on the first dinode of the electron multiplier using the carbon adhesive tape.

Observed Na-K XANES spectrum of Na-incorporated β-TCP is shown in Fig. 1 together with that of NaCl for comparison. It is difficult to determine the local environment of Na ions in β-TCP only from the comparison with the spectra of standard materials. Then the theoretical calculations are mandatory for the quantitative analysis of the local environment of incorporated Na ions. Here the first-principles calculations were carried out to obtain the theoretical Na-K XANES spectra of Na in β-TCP by using the WIEN2k package [4], in which the core-hole effect was directly included by removing the Na 1s electron. Several models by changing the substituted sites of Na incorporation were constructed. Calculated spectrum using the model, in which Na is substituted at Ca(4) site in β-TCP, is compared with the observed one in Fig. 2. Observed Na-K XANES profile of Na-incorporated β-TCP is quantitatively well reproduced by this model. This result confirmed that the incorporated Na ions are substituted at Ca(4) site in β-TCP.
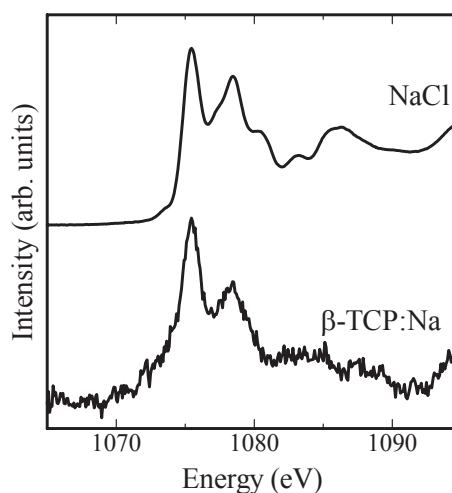

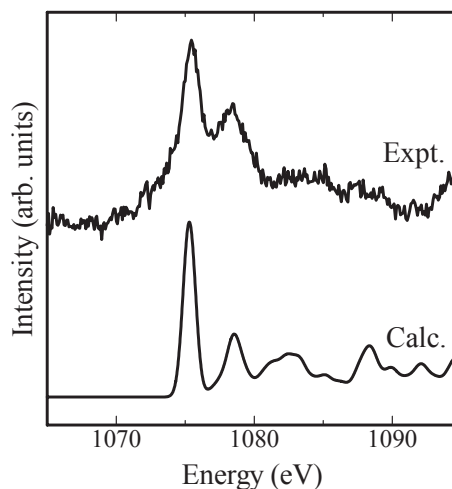Fig. 1. Observed Na-K XANES spectra of Na-incorporated β-TCP ($Ca_{2.7}Na_{0.3}(PO_4)_2$) and NaCl.

Fig. 2. Comparison between observed and calculated Na-K XANES spectra of Na-incorporated β-TCP.

[1] K. Kawabata, H. Sato and T. Yamamoto, UVSOR Activity Report **35** (2007) 108.
[2] K. Kawabata, H. Sato and T. Yamamoto, J. Ceram. Soc. Jpn. **116** (2008) 108.
[3] K. Kawabata, T. Yamamoto and A.Kitada, Physica B **406** (2011) 890.
[4] http://www.wien2k.at

Evaluation of Hydrotalcite-Based Nanosheet by Soft Chemical Process

A. Nakahira[1], S. Yamamoto[1], M. Sato[2], Y. Takamatsu[1], S. Misu[1] and H. Aritani[3]

[1]*Faculty of Engineering, Osaka Prefecture University, Gakuencho, Sakai 599-8531, Japan*
[2]*Osaka Center, IMR, Tohoku University, Gakuencho, Sakai 599-8531, Japan*
[3]*Saitama Institute of Technology, Fukaya 369-0293, Japan*

Introduction

Layered double hydroxide (LDH) is one of unique clay minerals with a layered structure, its composition formula of $[M^{2+}_{1-X} M^{3+}_{X} (OH)_2 \cdot A^{n-}_{X/n} \cdot nH_2O]$. These LDH and its related materials are expected to be one of novel materials because of their potential applications in wide areas, such as catalysis, adsorption, and nanocomposite and drug delivery. Recently, the nanosheets from the exfoliation of layered host compounds have received increasing attention because the resulting unilamellar materials or nanosheets have various attractive aspects. Furthermore, the nanosheets from the LDH are expected to be especially useful among novel nanosheet related materials.

In the present study, we focused on the structural evaluation of the nanosheets from LDH basically composed of Mg^{2+} and Al^{3+}, which is called hydrotalcite, "MgAl-Tal". Furthermore, it is known that these nanosheets are important for the novel nanostructured materials synthesized by the layer-by-layer methods. However, it is not clarified about the detailed structure evaluation of the nanosheets from MgAl-Ta. In the present study, the structure evaluation of the nanosheets from LDH composed of Mg^{2+} and Al^{3+} (MgAl-Tal: hydrotalcite) were performed.

Experiments

From 0.2 mol/dm^3 MgCl$_2$ aqueous solution and 0.1 mol/dm^3 AlCl$_3$ aqueous solution, mixing solution was prepared by the co-precipitation method. MgAl-Tal with M^{2+}/M^{3+} =2~4 were synthesized by adding mixing solution into 0.05 mol/dm^3 NaHCO$_3$ at room temperature. 1 mol/dm^3 NaOH was simultaneously added into the aqueous solution in order to keep pH 10. Products for MgAl-Tal were aged at room temperature for 2 hours. They were separated and sufficiently washed by deionized water and finally air-dried at 50 ℃ for 24 hours. The delamination of obtained MgAl-Tal products were prepared by soft chemical process. The products were obtained from the delamination of MgAl-Tal.

The local structures around Al for the nanosheets were characterized by measuring X-ray adsorption near edge structure (XANES) at BL1A in UVSOR with KTP.

Results and Discussion

MgAl-Tal samples prepared by the co-precipitation method was identified to be a layered double hydroxide consisted of Mg^{2+} and Al^{3+} by powder X-ray diffraction analysis. Then, the delamination of obtained products were successfully prepared by the soft chemical process. The products obtained from the delamination of MgAl-Tal indicated the tyndall phenomenon, suggesting that nanosheets were obtained. It was suggested that products obtained from the delamination of MgAl-Tal had broad peaks derived from XRD results.

Figure 1 shows the results of XANES of Al-*K* edge of the nanosheet products obtained from the delamination of MgAl-Tal. For the comparison, MgAl-Tal samples prepared by the co-precipitation method were similarly evaluated. The spectrum of he nanosheet products obtained from the delamination of MgAl-Tal corresponded approximately to that of MgAl-Tal samples prepared by the co-precipitation. It was elucidated that Al-K edge XANES spectra of the nanosheet products obtained from the delamination of MgAl-Tal were similar to that of MgAl-Tal as a starting material.
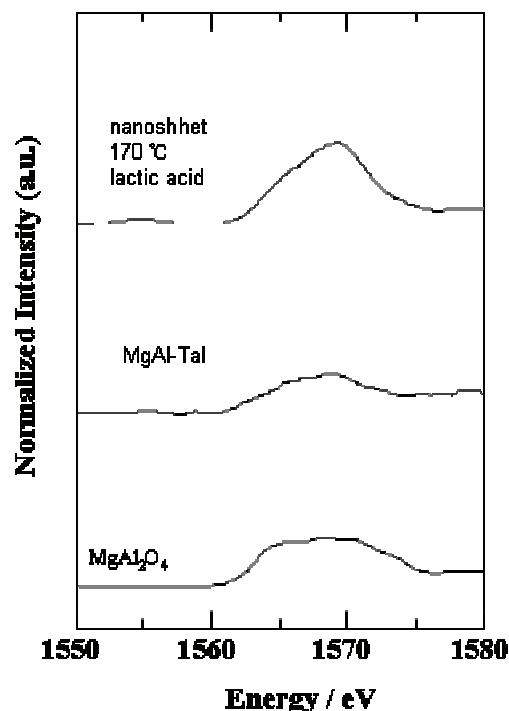

Fig. 1. Results of XANES of Al-*K* edge of the MgAl-Tal nanosheet.

Evaluation of Local Structure of SBF-Type Mesoporous Silica Bulks

A. Nakahira[1,2], S. Yamamoto[1], M. Sato[2], Y. Takamatsu[1], S. Misu[1], Y. Kawabe[1],
Y. Nishio[1] and H. Aritani[3]

[1]*Faculty of Engineering, Osaka Prefecture University, Gakuencho, Sakai 599-8531, Japan*
[2]*Osaka Center, IMR, Tohoku University, Gakuencho, Sakai 599-8531, Japan*
[3]*Saitama Institute of Technology, Fukaya 369-0293, Japan*

Introduction

Much attention has been paid to the mesoporous silica families, MCM, FSM, and SBF and so on. Since SBA-15 powders synthesized by the sol-gel method with triblock copolymer surfactants possess a huge specific surface area and range of relatively uniform pore size and furthermore contain a unique internal structure with uniform arrays of hexagonal mesopore, it is expected to be potentially useful as catalysts supports and adsorbent and so on. In particular, SBA-15 powders have the thicker silica walls around mesopores than that of MCM-type mesoporous silica (MCM and FSM) made with conventional cationic surfactants, leading to the stability for SBA-15 at high temperature and/or under severe conditions. However, the development for the preparation of bulky mesoporous silica SBA-15 is strongly desired, because powdered SBA-15 materials are restricted in their practical application in many fields. We successfully prepared the dense SBA-15 bulk by the modified hydrothermal hot-pressing process. In this study, the local structures for SBF-type mesoporous silica bulks were investigated by XAFS measurements.

In the present study, we focused on the structure evaluation of the bulks of SBF-type mesoporous silica by the modified hydrothermal hot-pressing process. In special, the structure evaluations of the SBF-type bulk were performed.

Experiments

SBA-15 was synthesized by the following method. Silica and block copolymer mesophases were synthesized at room temperature as follows. Pluronic P123 (M_{av}=5800, EO20PO70EO20) as a block copolymer was dissolved in water and HCl solution with stirring at room temperature. Then, TEOS as a silica was added into that solution with stirring at room temperature. The mixture was aged at 80 ℃ for 12 h without stirring. The solid product was filtered, washed, and air-dried at room temperature. Calcination was carried out, slowly increasing temperature from room temperature to 500 ℃ and heating at 500 ℃ for 6 hours. Subsequently, the consolidation of this SBA-15 powder was carried out by the modified thermal hot pressing method with the uniaxial pressure of 30 MPa at 110 ℃ to 150 ℃ for 2 h. After the modified thermal hot pressing treatments, obtained bulks were heat-treated at 600 ℃ in the air atmosphere. The local structures around Si for the products of SBF-type bulk were characterized by measuring X-ray adsorption near edge structure (XANES) at BL1A in UVSOR.

Results and Discussion

Dense SBA-15 bulks were successfully synthesized by the modified hydrothermal hot-pressing possess. These dense SBA-15 bulks with mesoporous structure were similar to that of powdered SBA-15, suggesting that the dense SBA-15 bulks with mesoporous structure as well as powdered SBA-15 were successfully synthesized by the modified hydrothermal hot-pressing possess.

Figure 1 shows the results of X-ray adsorption near edge structure (XANES), Si-K edge, for SBA-15 bulk prepared by the modified hydrothermal hot-pressing at 150 ℃. For the comparison, SiO_2, FSM and SBA-15 powder were similarly evaluated. X-ray adsorption near edge structure (XANES) of the dense SBA-15 bulks indicated the similar pattern of powdered SBA-15. It was obvious that dense SBA-15 bulks obtained by the hydrothermal hot-pressing possess hexagonal regularity similar to powdered SBA-15 from these Si-K edge XANES results.
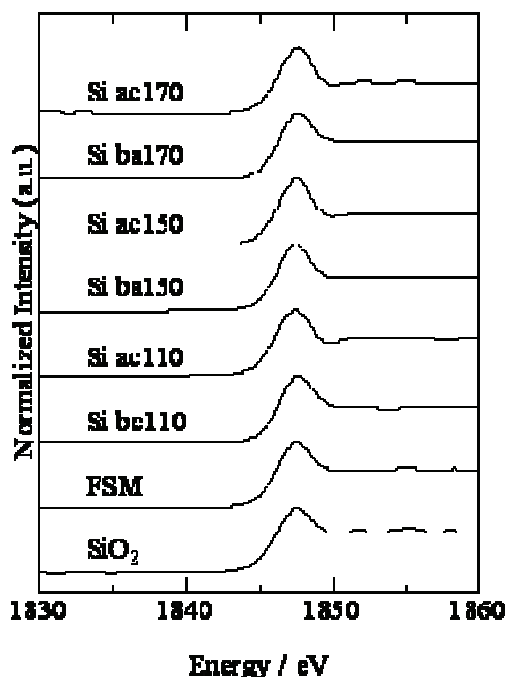

Fig. 1. The results of X-ray adsorption near edge structure (XANES), Si-K edge, for SBA-15 bulks.

Investigation of Local Structure of Mg K-Edge in Chitosan and Mg Co-Addition Calcium Phosphate Materials

T. Onoki[1], Y. Nishio[1], T. Moriguchi[1], Y. Kawabe[1], M. Sato[2] and A. Nakahira[1,2]

[1]Graduate School of Engineering, Osaka Prefecture University, Sakai 599-8531, Japan
*[2]Osaka Center for Industrial Materials Research, Institute for Materials Research,
Tohoku University, Sakai 599-8531, Japan*

Human bone has an organic/inorganic composite structure. Bone replacing biomedical materials, for example hydroxyapatite (HA) ceramics, has been required more biocompatibility and optimal mechanical properties. Recently, bioceramics were fabricated by some hydrothermal techniques at low temperature [1]. Magnesium (Mg) is known to be an important trace element in bone and teeth. Indeed, despite its low concentration (generally between 0.5 and 1.5 wt%), it plays a key role in bone metabolism, in particular during the early stages of osteogenesis where it stimulates osteoblast proliferation, and its depletion causes bone fragility and bone loss. Relationships have been suggested between the magnesium content in enamel and the development of dental caries. Given the biological relevance of magnesium, many research teams have worked on the preparation of apatite and calcium phosphate implant materials containing relatively low levels of Mg, which has been shown to improve their bioactivity [2]. According to the literature, the replacement of calcium by magnesium in HA is difficult.

Chitosan was one of origanic materials derived from crab shell. And has function of accumulating mineral species. So we conducted for making a Mg adding HA/chitosan composite ceramic for more biocompatibility. Calcium hydrogen phosphate di-hydrate (DCPD) is one of starting materials for HA ceramics through a hydrothermal hot-pressing technique at around 100 ºC [1]. As a first step, Mg adding DCPD/chitosan composite powder were prepared. Co-precipitation method was employed in order to prepare Mg adding DCPD/chitosan composite materials. The composite materials were based on the DCPD preparation [3], which 1.0M calcium nitrate solution (99.0%; $Ca(NO_3)_2 \cdot 4H_2O$, KANTO CHEMICAL, Japan) and 1.0M di-ammonium hydrogen phosphate solution (98.5%; $(NH_4)_2HPO_4$; KANTO CHEMICAL, Japan) were mixed. Magnesium chloride (99.0%; MgCl; Wako, Japan) Chitosan powder (LLWP Grade, KIMICA, Japan) was dissolved in water with a little acetic acid. The chitosan and MgCl solution was added to $Ca(NO_3)_2 \cdot 4H_2O$ solution with various concentration before mixing to the $(NH_4)_2HPO_4$ solution. And then the fabricated powder were converted to HA by a hydrothermal treatment (150 ºC, 2h).

Mg K-edge XANES spectra for the fabricated powders were obtained in a total electron yield mode at room temperature using a KTP double-crystal monochrometer at BL1A station of UVSOR. The spectra were collected in the photon energy range from 1295-1330 eV at intervals of 0.05eV with a dwell time of 1s. Mg-K edge XANES of the DCPD/chitosan composite and the HA converted powder were shown in Figure 1. Firstly, we could not detect Mg in the HA sample without chitosan. On the other hand, a little amount of Mg can be observed in both of DCPD and HA with chitosan. These result indicate that chitosan play an important role for Mg adding to calcium phosphate materials. It is shown that chitosan is a good carrier for doping non-HA mineral elements to HA.
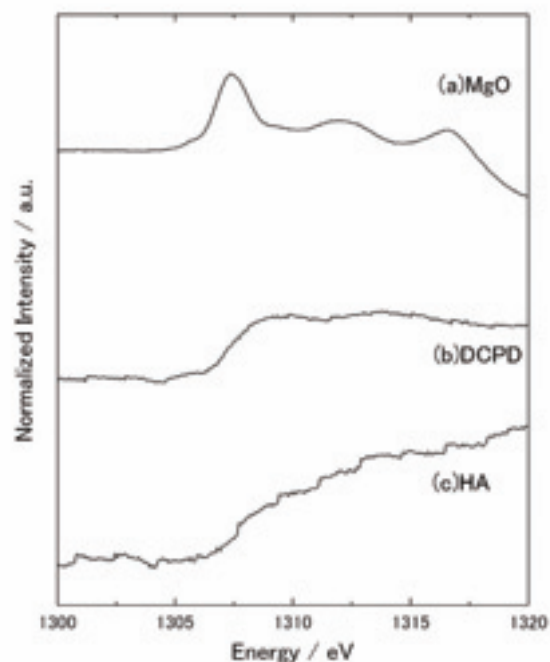

Fig. 1. XANES spectra of Mg K-edge of the DCPD/chitosan composite and the HA converted powder with Mg.

[1] S. Ishihara, T. Matsumoto, T. Onoki, T. Sohmura and A. Nakahira, Mater. Sci. Eng. C **29** (2009) 1885.
[2] S. Gomes, G. Renaudin, E. Jallot and J. M. Nedelec, ACS Appl. Mater. Interfaces **1** (2009) 505.
[3] T. Onoki, K. Hosoi and T. Hashida, Scr. Mater. **52** (2005) 767.

Ⅲ-6. APPLIED MATERIALS

Investigation of Effect of Ions in Seawater for Ettringite Formation

M. Sato[1], S. Yamamoto[2], Y. Nishio[2], Y. Takamatsu[2] K. Kumadani[2] and A. Nakahira[1,2]

[1]*Osaka Center for Industrial Materials Research, Tohoku University, Sakai 599-8531, Japan*
[2]*Graduate School of Engineering, Osaka Prefecture University, Sakai 599-8531, Japan*

Ettringite ($3CaO \cdot Al_2O_3 \cdot 3CaSO_4 \cdot 32H_2O$) is one of calcium sulpho aluminate (CSA) system, and it has a needle-like microstructure belongs to hexagonal system. It is a naturally occurring mineral found in Germany for the first time. This mineral is characterized by the very high content of water molecules. Since ettringite is important material to provide the rapid set and/or high early strength for constructional materials, more effective material design can be expected by investigating the generation behavior in detail. However, there are few reports for the generative mechanism of ettringite. In this study, we prepared ettringite using different aqueous solutions including Mg^{2+}, Na^+, CO_3^{2-}, SO_4^{2-} ions etc. and investigated the generation behavior in different ion enviroments.

In order to obtain the ettringite, tricalcium aluminate (C3A, $3CaO \cdot Al_2O_3$) were firstly prepared by $CaCO_3$ and Al_2O_3 powders as starting materials. After mixed up each powder, it was calcinated at 1573 K for 36 hours in air. And then, obtained C3A and $CaSO_4 \cdot 2H_2O$ were mixed and stirred at 200 rpm from 5 minutes to 24 hours in the different aqueous solutions. After stirring, samples were filtered and dried.

Na-K, Mg-K, Al-K and S-K edge XANES spectra of obtained ettringite powders were measured in a total electron yield mode at room temperature using Beryl, KTP and InSb double-crystal monochrometer at BL1A station of UVSOR, respectively.

Figure 1 shows Mg-K edge XANES spectra of ettringite prepared in 1 mol/l $MgCl_2$ aqueous solution at room temperature for several aging times. In the case of $MgCl_2$ solution with 0.01 mol/l concentration, no peaks derived from Mg compounds were observed. However, spectra derived from Mg compounds were observed in the case of 0.1 and 1 mol/l MgCl solution as shown in Fig. 1. From XANES measurement, it is suggested that the Mg based layered double hydroxide (LDH) is generated within 5 minutes, and the generation of LDH affects the formation of ettringite. Similar trend that the ettringite formation is affected at the concentration of solution more than 0.1 mol/l was obtained in other solution such as NaCl, KCl and Na_2SO_4.
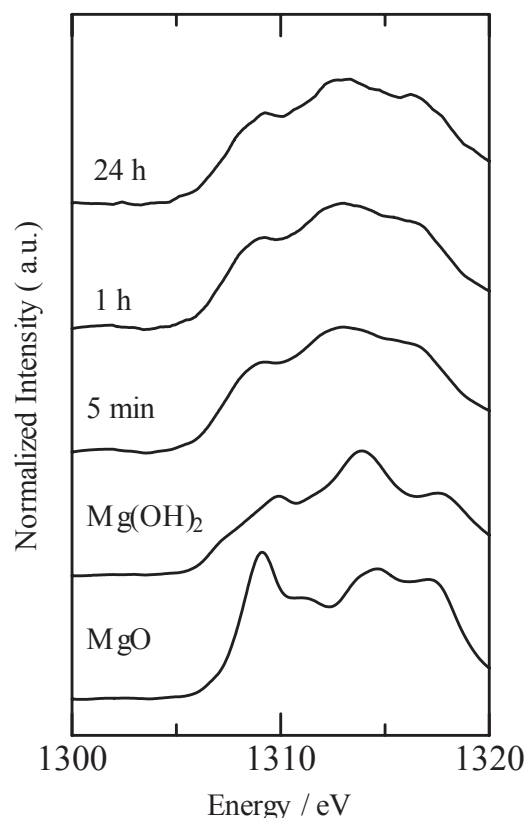

Fig. 1. Mg-K edge XANES spectra of ettringite prepared in 1 mol/l $MgCl_2$ aqueous solution at room temperature for several aging times.

Investigation of Local Structure of P-K Edge in Fe Doped HAp

M. Sato[1], S. Yamamoto[2], Y. Nishio[2], Y. Takamatsu[2] and A. Nakahira[1,2]

[1]*Osaka Center for Industrial Materials Research, Tohoku University, Sakai 599-8531, Japan*
[2]*Graduate School of Engineering, Osaka Prefecture University, Sakai 599-8531, Japan*

So far, many kinds of magnetic beads such as paramagnetic iron oxide particles and surface-modified ones by polymer have been widely used in a medical field. However, those iron oxide based magnetic beads have been pointed out the risk of the elution of iron by long term use. The resolvability of iron strongly depends on its particle size. Since the particle size of magnetic beads is decided by a service space, control of resolvability is one of the problems that we should overcome to use it in a living body. Because the elution of iron affects proliferation and metabolism of cell, there is a possibility to exhibit some toxicity. Therefore, development of non toxic magnetic bead has been strongly desired. Hydroxyapatite ($Ca_{10}(PO_4)_6(OH)_2$, HAp) is a good candidate for drug delivery system materials due to its excellent ion exchange ability and protein adsorption ability. By using these unique abilities of HAp, non toxic magnetic bead can be developed.

In this study, Fe doped HAp was prepared by conventional wet process and local structure around P atom was investigated by XAFS measurement.

0.1 mol/l $Ca(NO_3)_2$, $(NH_4)_2HPO_4$ and $FeCl_3$ solutions were used as starting materials. These solutions were mixed up each other becoming the ratio of Ca to P of 1.67 and the ratio of Fe from 0 to 20 mol% for Ca solution. Mixed solution was aged for 1 h at room temperature and then it was filtered and dried at 323 K for overnight. P-K edge XANES spectra of Fe doped HAp powders were measured in a total electron yield mode at room temperature using InSb double-crystal monochrometer at BL1A station of UVSOR.

Figure 1 shows P-K edge XANES spectra of Fe doped HAp prepared by conventional wet process at room temperature. Obtained P-K edge XANES spectra of samples were similar to that of commercial HAp, and a change of the spectral pattern was not clearly observed within any ratio of Fe. This result indicates that the local structure of around P atom of Fe doped HAp samples is almost same with commercial HAp.
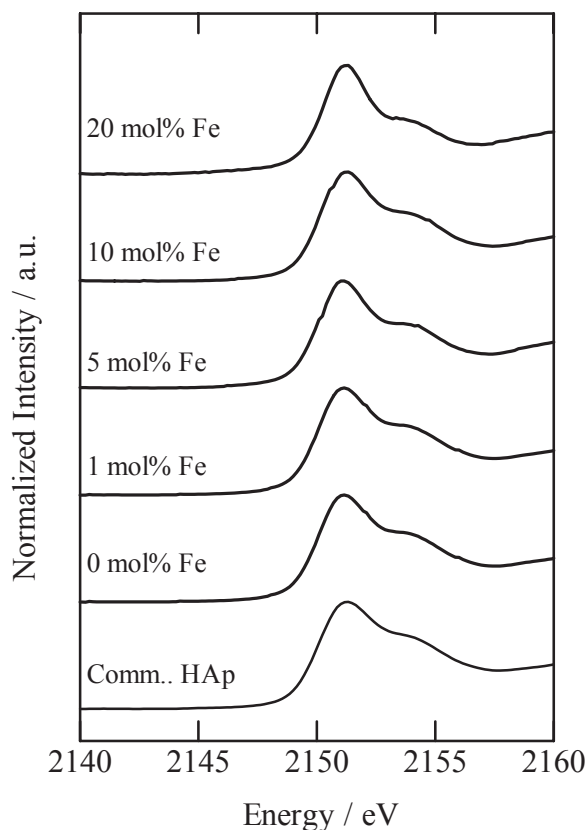

Fig. 1. P-K edge XANES spectra of Fe doped HAp prepared by conventional wet process at room temperature.

Optical Spectroscopy of ZnO Thin Films

N. Kashiwagura, Y. Kubo, T. Hashida, Y. Hayashi and M. Yamaga

Department of Mathematical and Design Engineering, Gifu University, Gifu 501-1193, Japan

Today the most widely adopted TCO (Transparent Conductive Oxides) films for use as electrodes of solar cell and liquid crystal display is ITO (Indium Tin Oxides) films. However, ITO films include so sparse Indium that the substitutive materials are expected. ZnO thin films are one of the hopeful materials as TCO films.

ZnO thin films were deposited on a fused silica glass (10 mm x 20 mm x 0.5 mm) by the DC sputtering method. The sputtering time, the gas (Ar) pressure and the substrate temperature were 240 minutes, 0.40 Torr. and 200 ℃, respectively. The induced electric power was 60 W for sample 1, and 45 W for sample 2.

Optical absorption, luminescence and excitation spectra were measured using the BL1B beam in the temperature range of 10-300 K.

Figure 1 shows the optical absorption spectra for ZnO thin films. The sharp edge at 150 nm for sample 2 is due to the absorption of glass substrate. The several broad bands below 360 nm (3.3 eV) are due to the band-to-band transition of ZnO. The sample 2 is efficiently transparent as TCO thin film above 380 nm (visible light region), while the sample 1 is not so.

Figure 2 shows the luminescence spectra with various excitation wavelengths in sample 2 at 300 K. The band-to-band excitation below 360 nm produces two broad luminescence bands. In these spectra, the additional peaks around 540 and 590 nm are the influence from outer lights, which could not be perfectly eliminated. As the excitation wavelength increases (the energy decreases), the intensity of luminescence band around 570 nm decreases, while that around 420 nm still remains.

Figure 3 shows the luminescence spectra in sample 2 at 10 K. The spectrum with the 100 nm excitation shows no dent around 480 nm, in other words, both bands around 420 nm and 570 nm get broader and closer. With increasing the excitation wavelength, the luminescence intensities decrease. As a consequence, the band around 420 nm remains, whereas that around 570 nm almost disappears.

The band around 420 nm is estimated to be intrinsic luminescence (for example, self-trapped exciton). The broader band around 570 nm is estimated to be the luminescence associated with defects (for example, donor/acceptor recombination).

The relation between the luminescence and electrical conductivity will be examined. In this study, optical properties of pure ZnO thin films were investigated. It seems to be more important to investigate Ga or Al doped ZnO thin films in the point of electrical conductivity.
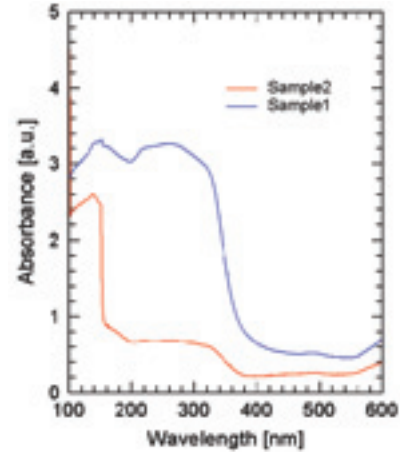

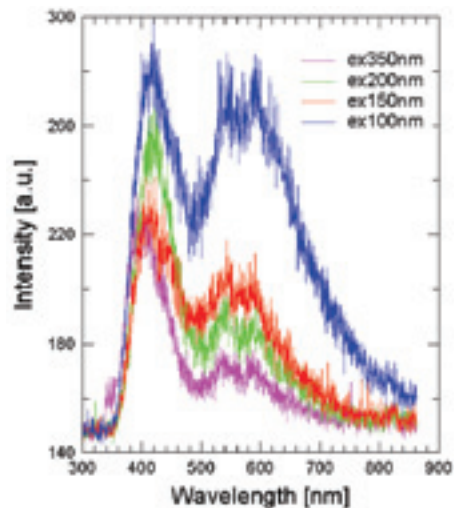Fig. 1. Absorption spectra in ZnO thin films at 300 K.

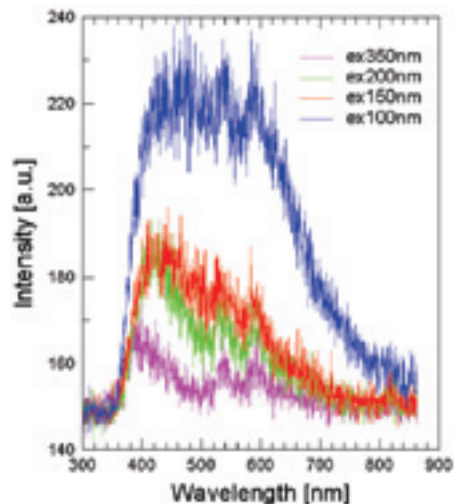Fig. 2. Luminescence spectra in sample 2 at 300 K.

Fig. 3. Luminescence spectra in sample 2 at 10 K.

Optical Spectroscopy of Wide Gap Semiconductors

M. Yamaga, H. Uno, Y. Ogoshi, A. Kanetake, S. Takano and T. Nohisa

Department of Material and Design Engineering, Gifu University, Gifu 501-1193, Japan

$In_xGa_{1-x}N$ and $Cd_{1-x}Mn_xTe$ crystals are wide band-gap semiconductors. Band-gap energies of indium gallium nitride ($In_xGa_{1-x}N$) mixed crystals decrease with increasing x. Absorption edges of $In_xGa_{1-x}N$, corresponding to the band-gap energies, vary from the ultraviolet to visible ranges. Then, $In_xGa_{1-x}N$ mixed crystals are a promising material for multi-junction thin film solar cells. On the other hand, $Cd_{1-x}Mn_xTe$ crystals have magneto-optical properties induced by Mn^{2+} ions. They are useful as an optical isolator material.

$In_xGa_{1-x}N$ thin films were deposited on SiO_2 substrates by rf-sputtering at room temperature. Sputtering targets were In and Ga metals with various weight ratios. The X-ray diffraction (XRD) patterns of the $In_xGa_{1-x}N$ thin films consisting of several peaks in the angle range between 30 and 70 degrees indicate microcrystalline thin films.

$Cd_{1-x}Mn_xTe$ single crystals were grown by the vertical Bridgeman method. The composition of the crystal is the same as the melting composition.

Figure 1 shows absorption spectra observed in $In_{0.2}Ga_{0.8}N$ and $Cd_{0.5}Mn_{0.5}Te$ at 300 K. The absorption edge of the GaN thin film was observed at 360 nm at room temperature, whereas that of $In_{0.2}Ga_{0.8}N$ thin film is shifted toward a longer wavelength of about 450 nm as shown in Fig.1. The absorption spectrum of $Cd_{0.5}Mn_{0.5}Te$ consists of several broad bands in the range from 100 to 600 nm.

It is reported that GaN crystals show sharp exciton luminescence around 360 nm and substitution of In in GaN crystals leads to red-shift and line-broadening of the luminescence. UV excitation for the $In_{0.2}Ga_{0.8}N$ thin film produces broadband luminescence with double peaks at 460 and 560 nm as shown in Fig. 2. The luminescence for the GaN thin film is similar to that for $In_{0.2}Ga_{0.8}N$ thin film. This result suggests that the 460 and 560 nm luminescence broadbands may be associated with N deficits and impurity O ions.

Figure 3 shows temperature dependence of the luminescence spectra excited at 100 nm for $Cd_{0.5}Mn_{0.5}Te$. The peak energy of the luminescence is just below the band edge energy in Fig. 1. The luminescence intensities markedly decrease above 120 K. The luminescence may be due to weakly localized excitons.

Identification of these luminescence centers $In_xGa_{1-x}N$ and $Cd_{1-x}Mn_xTe$ crystals gives information on structure and energy levels of the localized luminescence centers.
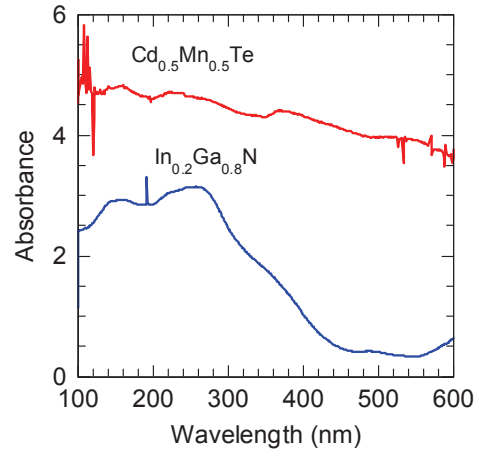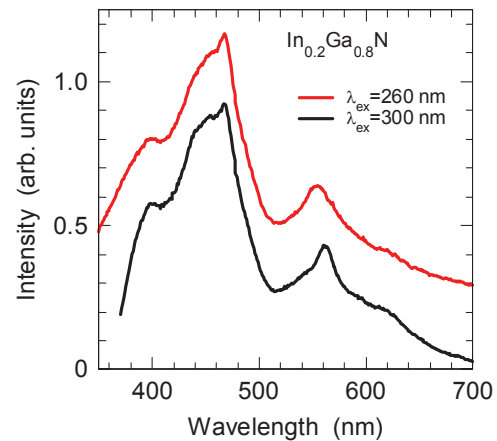

Fig. 1. Optical absorption spectra at 300 K.

Fig. 2. Luminescence spectra in $In_{0.2}Ga_{0.8}N$.

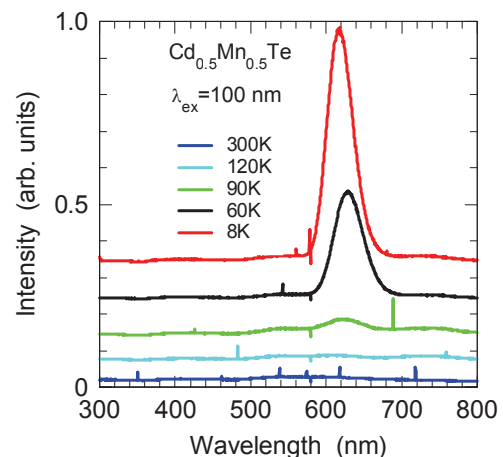Fig. 3. Luminescence spectra in $Cd_{1-x}Mn_xTe$.

Soft X-Ray Emission Spectroscopy in the C K_α of Graphene-Nanoflakes (GNFs) Functionalized with Nitrogen

J. W. Chiou[1], M. T. Liou[2], W. F. Pong[2], H. Yamane[3] and N. Kosugi[3]

[1] *Department of Applied Physics, National University of Kaohsiung, Kaohsiung, Taiwan*
[2] *Department of Physics, Tamkang University, Tamsui, Taiwan*
[3] *Institute for Molecular Science, Okazaki 444-8585, Japan*

Figure 1 shows normal x-ray emission spectra (NXES) and Figure 2 shows resonant inelastic x-ray scattering (RIXS) spectra excited at different photon energies in the spectra of the C K_α of HOPG and GNFs:N deposited on Si(100) substrate, prepared using microwave plasma enhanced chemical vapor deposition process and subsequently functionalized with nitrogen plasma by the electron cyclotron resonance process. Spectral features of these GNFs:N films are essentially similar, consisting of a broad main feature around 277.4 eV (A) and a high-energy shoulder feature near 281.7 eV (B), to those observed by Muramatsu *et al*. [1]. However, the peak-to-height ratio of the shoulder-feature to the main-feature depended on the nitrogen at.% (0 to 20 at.%). These spectral features therefore suggest that local electronic structures and chemical bonding states are essentially similar among the GNFs:N films, but that their ratios, for example of sp^2 and sp^3-configured carbon atoms, differ depending on the nitrogen at. %. Comparing the spectra of GNFs films and reference HOPG, we conclude that the main feature (A) is in same position with HOPG and the high-energy shoulder feature (B) of the GNFs films are not in the same position as slightly shifts towards higher energy than in HOPG. These features A and B are the σ and π orbitals, respectively. The feature height and their ratios are tabulated in Table 1. It is very difficult to draw some conclusion on the (π/σ) ratio presently because on nitrogen functionalization initially it decreases and then increases indicating the change of sp^2/sp^3 ratio.

Figure 2 shows that the spectral features are varied with the excitation energy, indicating sp^2 and/or sp^3 carbons are resonantly excited at certain excitation of energy. The redistribution of intensities in the spectra indicates changes in the occupancies of different molecular orbitals, possibly due to changes in electron density of states upon nitrogen incorporation in GNFs:N. The NXES spectral profile has been used as a means to identify certain chemical states of incorporation of nitrogen in the GNFs structure. However, it is also observed in Fig. 2 that the C K_α RIXS spectra strongly depend on excitation energy and the dependence is believed to stem from the resonant inelastic scattering and related to the band structure of the GNFs:N. This interpretation is important for all the emission experiments with high resolution synchrotron radiation and implies the possible use of photon-in-photon-out technique for electronic band structures. This soft NXES/RIXS

revealed a new picture of the core excitation and the existence of strong vibronic coupling effects in GNFs and GNFs:N.

Fig. 1. NXES spectra of HOPG and GNFs:N.
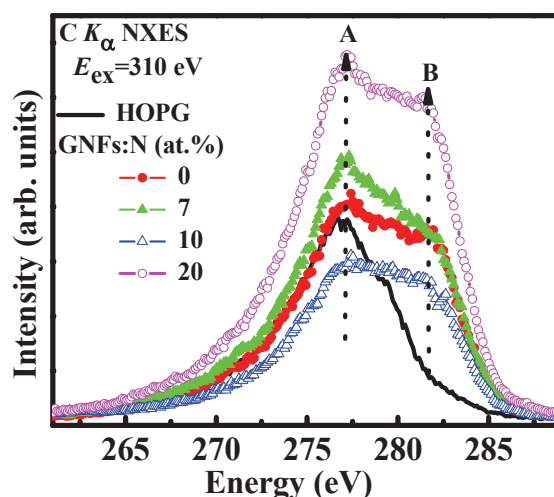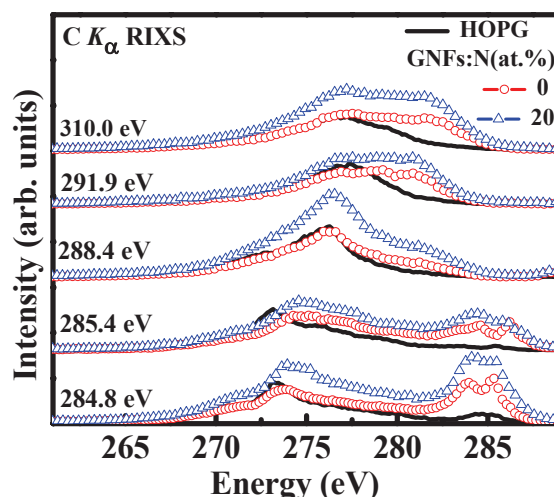

Fig. 2. RIXS spectra of HOPG and GNFs:N.

Table 1. Intensity of σ and π and their ratios.

	Peak B (π)	Peak A (σ)	(π/σ) ratio
HOPG	26.3	37.5	0.70
GNFs	36.2	41.2	0.88
GNFs:N(7at.%)	34.3	47.7	0.72
GNFs:N(10at.%)	26.2	31.2	0.84
GNFs:N(20at.%)	58.2	66.4	0.88

[1] Y. Muramatsu *et al*., Carbon **39** (2001) 1403.

Probing Electronic Structure of Graphdiyne
by Resonant Soft-X-Ray Emission Spectroscopy

J. Zhong[1], T. Xie[1], X. H. Sun[1], S. D. Wang[1], Y. L. Li[2], H. Yamane[3], N. Kosugi[3] and J. H. Guo[4]

[1]*Jiangsu Key Laboratory for Carbon-Based Functional Materials and Devices, Institute of Functional Nano and Soft Materials Laboratory (FUNSOM), Soochow University, Suzhou 215123, China*
[2]*Institute of Chemistry, Chinese Academy of Sciences, Beijing 100190, China*
[3]*Institute for Molecular Science, Okazaki 444-8585, Japan*
[4]*Advanced Light Source, Lawrence Berkeley National Laboratory, Berkeley, CA 94720, USA*

The structural study of carbon is a main fundamental interest and is expected to be widely applied to nanosciences and technology. Due to carbon's three hybridization states (sp^3, sp^2, and sp), having numerous combinations by which atoms of this element can be bonded to each other to produce many carbon allotropes; such as graphite (sp^2), diamond (sp^3) in the nature, and many novel carbon allotropes such as fullerene (sp^2), carbon nanotube (sp^2), and graphene (sp^2), are successfully synthesized. The design and synthesis of new carbon allotropes with definite structure and property is a significant and ongoing challenge within new materials science and there are still a large number of new forms of carbon to be discovered. Graphdiyne proposed is a novel structure in the carbon family and predicted to be the most stable of the various diacetylenic nonnatural carbon allotropes and is one of the most "synthetically approachable" [1]. Recently, the synthesizing of a novel, stable graphdiyne form of carbon has been reported and in this work, we probe the electronic structure of graphdiyne in comparison with that of highly oriented pyrolitic graphite (HOPG), single-walled carbon nanotube (SWNT) and graphene by using resonant soft-x-ray emission spectroscopy (XES).

X-ray absorption spectroscopy (XAS) probes the unoccupied density of states (DOS) and XES probes the occupied DOS. In addition to the inherent elemental selectivity of X-ray spectra, energy selective excitation of the emission spectra allows separation of features that pertain to different atoms or same element in different chemical environments. In previous report [2], the quantum confinement of SWNT with decreased tube diameters has been reported which can be observed in resonant emission spectra by significant changes in the π and σ bands. Figure 1 shows the C K-edge resonant emission spectra of HOPG, SWNT, graphene and graphdiyne at the excitation energy of 285.5 eV. The spectrum for graphdiyne in the σ band shows great changes compared to that for HOPG and SWNT, while similar to that for graphene, indicating a similar hybridization as graphene. Figure 2 shows the C K-edge normal emission spectra at the excitation energy of 305 eV. A difference in the σ band for graphdiyne can be found

compared to all other samples, indicating the specific electronic structure of graphdiyne.

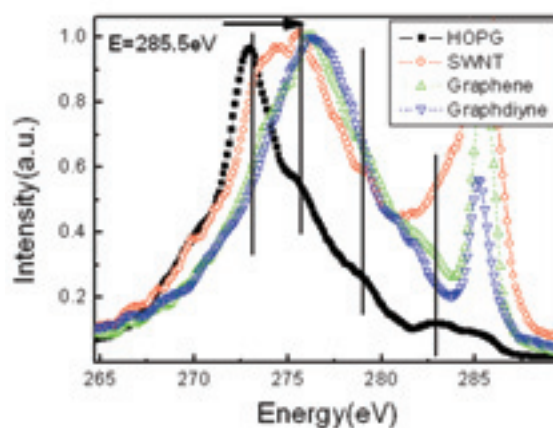Fig. 1. C K-edge resonant emission spectra of HOPG, SWNT, graphene and graphdiyne at the excitation energy of 285.5 eV.
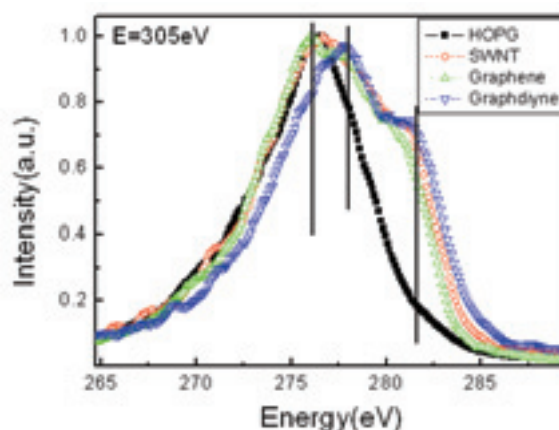

Fig. 2. C K-edge normal emission spectra of HOPG, SWNT, graphene and graphdiyne at the excitation energy of 305 eV.

[1] G. X. Li, Y. L. Li, H. B. Liu, Y. B. Guo, Y. J. Li and D. B. Zhu, Chem. Comm. **46** (2010) 3256.
[2] J. Zhong *et al*., Appl. Phys. Lett. **93** (2008) 023107.

Ⅲ-6. APPLIED MATERIALS

Synchrotron Radiation Effect on the Local Structure of Highly-Hydrogenated Diamond-Like Carbon Film

K. Kanda, M. Uemura and T. Hasegawa

Laboratory of Advanced Science and Technology for Industry, University of Hyogo,
Ako 678-1205, Japan

Diamond-like carbon (DLC) film is expected to use as lubrication material in space, where oil cannot be used, because its some excellent properties such as hard, low friction coefficient, low surface energy and so on. It was known that the DLC films are durable against X-ray exposure, because it was reported that DLC films are not etched by exposure to soft X-ray (SX) in the absence of oxygen gas [1]. However, many kinds of novel DLC films have been fabricated by the remarkable advancement in DLC industry in last decade. Recently, irradiation of SX in a vacuum into DLC films has been reported to lead the desorption of hydrogen and an increase in the film density, hardness, and refractive index [2]. Information on the mechanism of the deterioration of DLC film by X-ray exposure is undoubtedly important for use of DLC films in space safely.

In the previous study [3], we reported that the SX exposure in the vacuum with the absence of oxygen to the DLC films formed using the amplitude-modulated RF CVD method leaded to the desorption of hydrogen and etching. In the present study, we measured NEXAFS spectra of the DLC films at BL8B1 of UVSOR to discuss of the variation of local structure of DLC film by the irradiation of SX.

DLC films were deposited with 200-nm thickness on Si wafers by using the amplitude-modulated RF plasma-enhanced CVD method. Three kinds of DLC film, each with different hydrogen content, were used as samples. The SX irradiation of the DLC film was carried out at beamline 6 (BL-6) of NewSUBARU synchrotron facility in the University of Hyogo. The electron energy of the NewSUBARU ring was 1.0 GeV and the ring current was 220 mA on a top-up mode. The synchrotron radiation (SR) at the BL-6 sample stage had a continuous spectrum from IR to soft X-rays, which are lower than 1 keV. Sample DLC films were exposed to SR at room temperature.

Local structure was evaluated from the Near edge X-ray absorption fine structure (NEXAFS) study performed at the BL4B of UVSOR. The NEXAFS spectra were measured in the energy range 275-320 eV with 0.5 eV FWHM resolution in the total electron yield mode.

A pre-edge resonance at 285.4 eV is not visible in the spectrum of diamond because diamond consists of only carbon atoms in sp^3 (C-C) sites. Therefore, the peak intensity of this resonance is considered as a good index of sp^2 content. The procedure for determination of sp^2 content from the NEXAFS measurements was established in the previous studies [4, 5]. The amount of sp^2 bonded carbon atoms can be extracted by normalizing the area of the resonance corresponding to 1s→π* transitions at 285.4 eV with the area of a large section of the spectrum. The absolute $sp^2/(sp^2+sp^3)$ ratio was determined by the comparison with that from the NEXAFS spectrum of graphite.

The $sp^2/(sp^2+sp^3)$ ratio in the DLC film, estimated from NEXAFS study, was plotted to irradiated SR dose in Fig.1. The $sp^2/(sp^2+sp^3)$ ratio increased steeply from ≈0.5 before irradiation of SR to ≈0.6 after the irradiation of SR of 300 mA·h dose. Beyond 300 mA·h dose, the $sp^2/(sp^2+sp^3)$ ratio keeps ≈0.6. As a result, carbon double bonding can be regarded to formed due to the desorption of hydrogen from highly-hydrogenated DLC film in the dose region under 300 mA·h.
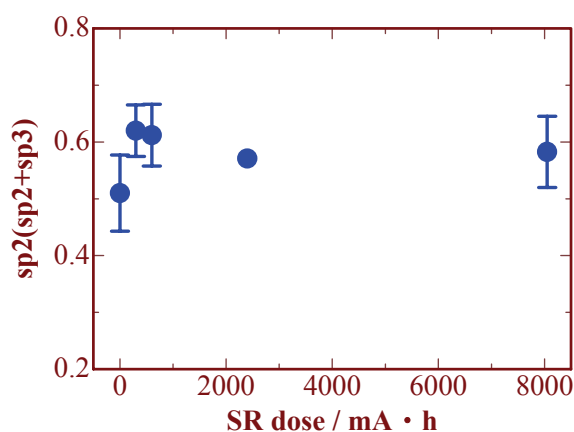
Fig. 1. Dose dependence of $sp^2/(sp^2+sp^3)$ ratio in the DLC film

[1] H. Kyuragi and T. Urisu, Appl. Phys. Lett. **50** (1987) 1254.
[2] H. Matsuura, S. Ohkubo, K. Oda and T. Ushiro, SEI Technical Review **171** (2007) 39 (Japanese).
[3] K. Kanda, K. Yokota, M. Tagawa, M. Tode, Y. Teraoka and S. Matsui, Jpn. J. Appl. Phys. to be published.
[4] K. Kanda, T. Kitagawa, Y. Shimizugawa, Y. Haruyama, S. Matsui, M. Terasawa, H. Tsubakino, I. Yamada, T. Gejo and M. Kamada, Jpn. J. Appl. Phys. **41** (2002) 4295.
[5] K. Kanda, Y. Shimizugawa, Y. Haruyama, I. Yamda, S. Matsui, T. Kitagawa, H. Tsubakino and T. Gejo, Nucl. Instrum. Methods Phys. Res. B **206** (2003) 880.

Study on the Electronic Structures of the Layered Li$_2$MO$_3$-LiMO$_2$ Materials in Li De-Intercalation Process

H. Kobayashi[1] Y. Takenaka[2] and M. Shikano[1]

[1]*Research Institute for Ubiquitous Energy Devices, AIST, Ikeda, Osaka 563-8577, Japan*
[2]*Department of Chemistry and Materials Engineering, Faculty of Chemistry, Materials and Bioengineering, Kansai University, Suita, Osaka 564-8680, Japan*

The layered Li$_2$MO$_3$-LiMO$_2$ (M =transition metal) materials are one of the promising positive electrode materials of lithium secondary battery because of their large capacity when operated above 4.6 V [1]. Especially, Li[Ni$_{0.17}$Li$_{0.2}$Co$_{0.07}$Mn$_{0.56}$]O$_2$ displays a 1st discharge capacity of c.a. 280 mAh/g in the voltage range of 2.5 to 4.8 V and keep a reversible capacity of c.a. 250 mAh/g after 50 cycles [2]. Several papers have reported on the mechanism why these materials show large reversible capacity. However, the initial charge and discharge process are still ambiguous. We have reported on the characteristic structural change during Li de-intercalation for LiNi$_{1/2}$Mn$_{1/2}$O$_2$ [3,4] using synchrotron radiation. Detailed information on the crystal and electronic structures above 4.6 V is very important in order to improve the calendar life and thermal stability of these materials and, therefore, the structural changes of Li$_{1.01}$Ni$_{0.49}$Co$_{0.21}$Mn$_{0.29}$O$_2$ (Sample A) and Li$_{1.20}$Ni$_{0.17}$Co$_{0.10}$Mn$_{0.53}$O$_2$ (Sample B) were investigated in Li de-intercalation process.

The de-lithiated samples from samples A and B were electrochemically prepared using coin-type cells with Li/1M LiPF$_6$ in EC:DMC(1:2)/samples. Electronic structures were investigated by the total electron yield mode at BL4B and BL1A in UVSOR. The data were analyzed using the program Athena.

Figure 1 shows the 1st charge curves of the samples A and B in the voltage range of 2.0 and 4.8 V. The Li/Sample A cell showed the 1st charge capacity of 282 mAh/g with the characteristic plateau region around 4.5 V. On the other hands, the Li/Sample B cell showed the 1st charge capacity of 251 mAh/g without plateau region.

Figure 2 shows the Ni L-edge XANES spectra for the de-lithiated samples from the samples A and B (BL4B). The spectrum measured contained peaks a and b, corresponding to the valence state of 2+ and 3~4+, respectively. The sample A showed that the intensity of peak b increased to y=0.8 with Li de-intercalation. On the other hand, the sample B showed that the maximum of peak b was observed at y=0.4. These results indicate that Li de-intercalation mechanism is different between these samples.

Fig. 1. 1st charge curves for the samples A and B.
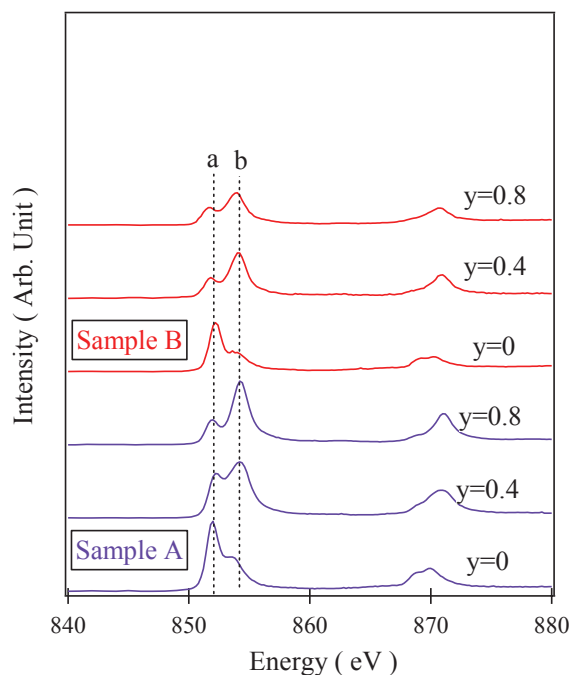
Fig. 2. Ni L-edge XANES spectra for the de-lithiated samples from the samples A and B (BL4B).

[1] A. Ito *et al.*, J. Power Sources **183** (2008) 344.
[2] A. Ito *et al.*, J. Power Sources **195** (2010) 567.
[3] Y. Arachi *et al.*, Solid State Ionics **176** (2005) 895.
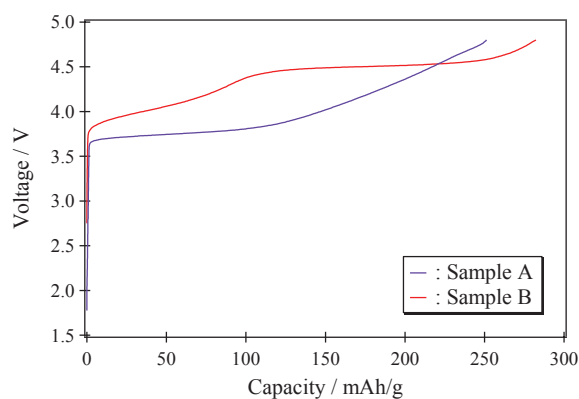[4] H. Kobayashi *et al.*, J. Power Sources **146** (2005) 640.

Ⅲ-6. APPLIED MATERIALS

Effects of Periodicity Imperfection on Mini-Bands in Semiconductor Superlattice

K. Hashimoto[1], T. Ujihara[1], Y. Maeda[1], M. Kuwahara[2], H. Miyazaki[3] and Y. Takeda[1]

[1]*Graduate School of Engineering, Nagoya University, Nagoya 464-8603, Japan*
[2]*EcoTopia Science Institute, Nagoya University, Nagoya 464-8603, Japan*
[3]*UVSOR Facility, Institute for Molecular Science, Okazaki 444-8585, Japan*

Recently, a quantum dot solar cell is proposed to achieve a high conversion efficiency that can reach over 50%, theoretically. The concept of the quantum dot solar cell is to utilize mini-bands in the periodic alignment of quantum dots as a middle band in the carrier excitation in order that the band structure is adjusted to the solar light spectrum. The theoretical calculation is based on an assumption of "the perfectly periodic potential." However, it is presently impossible to produce quantum dots of equal size and perfect periodicity. In this study, the effects of periodicity imperfection on the mini-band structure, especially hole mini-bands, were investigated. In place of aligned quantum dots, we examined a superlattice structure which consists of multiple quantum wells because the preparation method has been established.

We fabricated three specimens: a GaAs bulk sample, an AlGaAs/GaAs superlattice, and a disordered AlGaAs/GaAs superlattice. Figure 1 shows the detailed structures of each sample. The second well layer in the disordered superlattice was made thicker. Amorphous arsenic layers were deposited on the sample surfaces to suppress oxidation. The arsenic layer was thermally removed just before measurements. On the evaluation of the mini-band structure, the synchrotron-radiation photoemission measurements at BL5U of the UVSOR facility were performed.

Figure 2 shows the energy spectra in a valence band around Γ point. These mappings were processed by the second order differential with respect to the binding energy. There are mainly two bands that are symmetrical at the red arrows. The lower and higher energy bands are thought to be a heavy hole band and a light hole band, respectively. Theoretically, heavy hole band and light hole band in GaAs are doubly-degenerated at the Γ point. But, in the present result, these bands are split and its width of the GaAs sample is 180 meV corresponding to the width of band splitting at the wavenumber $k_{//} = 0.0669$ Å^{-1}. Thus, these mappings show the band structures at this wavenumber.

The bands of (a) GaAs and (b) periodic superlattice are widely dispersive, while those of (c) disordered superlattice are flatter. The width of dispersion depends on the degree of confinement effect. This flatter band is considered to be due to the quantum level in the thicker well layer.

Figure 3 shows widths of band splitting between the

heavy hole band and the light hole band as a function of wavenumber. We found that the band splitting width of superlattice is larger than that of GaAs bulk. As far as we know, this result is the first direct observation of the band splitting due to the mini-bands of the ordered superlattice. The splitting energy of the disordered superlattice is wider comparing to that of GaAs. However, the wavenumber dependence is small because the band splitting is due to the narrow quantum level in the quantum well. These results imply that a disorder of only one layer in superlattice disturbs the ideal mini-band structure.
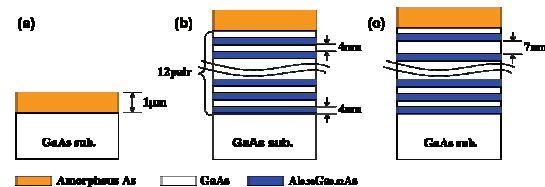

Fig. 1. Schematic images of the sample structure. (a) GaAs bulk sample, (b) periodic superlattice and (c) disordered superlattice.
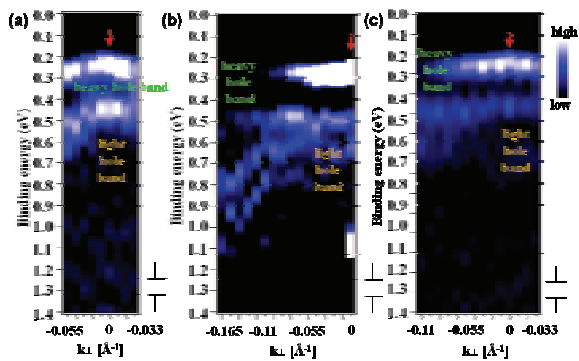

Fig. 2. Photoemmision spectra of (a) GaAs bulk sample, (b) periodic superlattice and (c) disordered superlattice.
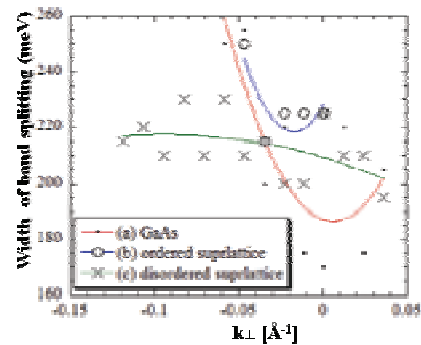

Fig. 3. Width of band splitting between heavy hole band and light hole band.

Angle-Resolved Photoemission Study on Epitaxial Graphene Grown on SiC(0001)

A. Ruammaitree, H. Hu, H. Nakahara, K. Akimoto, S. Harada, K. Soda and Y. Saito

Department of Quantum Engineering, Graduate School of Engineering, Nagoya University, Nagoya 464-8603, Japan

Graphene, which has many exotic properties such as high mobility and linear dispersion (Dirac cone) at the K-point in the Brillouin zone, can be synthesized by various methods. Annealing SiC is one of the efficient approaches for a large scale production of graphene [1], where it is important to control the layer number of grown graphene. To determine its layer number, there are several techniques such as Auger electron spectroscopy, x-ray photoelectron spectroscopy and ellipsometry. The accuracy of their techniques depends on their models. In this report, not only the electronic structure but also the estimation of layer number of graphene epitaxially grown on SiC is studied by angle-resolved photoemission spectroscopy (ARPES). The result can give us the accurate number of the epitaxial graphene layers.

The epitaxial graphene on an n-type Si-terminated 6H-SiC(0001) substrate of $12\times3\times0.25$ mm^3 (CRYSTAL BASE co. ltd.) was prepared by annealing it in an atmosphere of argon, as follows. After ultrasonic cleaning with acetone, the substrate was immediately mounted on a sample holder and put in a chamber with the base pressure of $\sim10^{-8}$ Pa. In order to remove oxides on the substrate surface, we deposited silicon around 2 monolayers on it. Si molecules deposited are expected to crash and eliminate the oxide molecules from the surface. Then the sample was transferred, without exposure to air, to an argon chamber where it was annealed by resistive heating in the atmosphere of argon. The annealing temperature was measured by an optical pyrometer. The epitaxial growth of graphene was confirmed by reflection high energy electron diffraction (RHEED). The transverse and longitudinal orientations of the substrate are [-1, 0, 1, 0] and [-1, 2, -1, 0], respectively, and the unit cell of the graphene rotates by 30 degrees to the SiC cell.

The ARPES measurement was conducted at room temperature with a hemispherical electron analyzer (MBS A-1) and a circularly polarized photon beam as an excitation source. To obtain a clear Dirac cone image at the K point, the excitation photon energy was set to 80 eV and the angle between the photon beam and the surface normal was 23 degrees. Total energy resolution including the thermal broadening was estimated to be 0.12 eV by measuring the Fermi edge of an Au film.

ARPES is one way for estimating the layer number of epitaxial graphene [2]. Figure 1 shows the electronic structure around the K point (zero wave number in the figure) for the sample prepared by annealing at 1948 K under the argon pressure of 0.03 MPa. The green dot curves represent π and π^* bands which originate from double layered graphene, while the red lines stand for a linear dispersion of a graphene monolayer. The presence of a brighter curve in the valence band and a bright area in the band gap suggests that this sample may be composed of the monolayer and bilayer graphenes. This is consistent with our x-ray diffraction observation of the averaged layer number of ~1.6, which will be reported elsewhere.
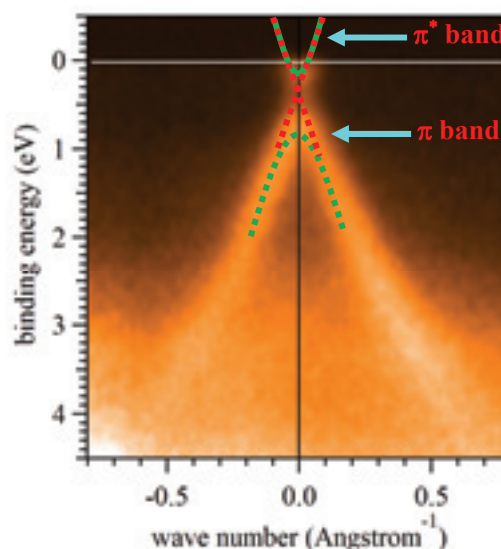

Fig. 1. Electronic band dispersion around the K point (zero wave number) of the graphene of the SiC(0001), which was synthesized by annealing at 1948 K under the argon pressure of 0.03 MPa.

[1] J. Hass *et al*., J. Phys.: Condens. Matter **20** (2008) 323202.
[2] T. Ohta *et al*., Phys. Rev. Lett. **98** (2007) 206802.

Ⅲ-6. APPLIED MATERIALS

Valence-Band Structure of Mg$_2$Si in High-Pressure Phase

K. Soda, T. Shimada, H. Kondo, S. Harada, K. Nishida and M. Hasegawa

Graduate School of Engineering, Nagoya University, Nagoya 464-8603, Japan

Valence-band electronic structure has been studied for Mg$_2$Si in a metastable hexagonal high pressure phase by photoelectron spectroscopy. Semiconducting Mg$_2$Si and its related compounds have received much attention because of its high thermoelectric properties with light constituent elements [1-3]. Mg$_2$Si in a normal pressure phase show n-type thermoelectric power, probably due to Mg-derived defects, and its related p-type compounds are desired to develop. Recently we have found high p-type thermoelectric power and large electric conductivity for the metastable high pressure phase. According to a band structure calculation [3], the fundamental band gap is expected to collapse to a pseudogap in so far reported high pressure phases, orthorhombic anti-cotunnite (> 7.5 GPa at room temperature) and hexagonal Ni$_2$In-type (> 21.3 GPa) structures. However, the electronic structure has not been clarified for the present high pressure phase yet.

Specimens of metastable hexagonal high pressure phase Mg$_2$Si were prepared under 7 GPa at 1173 K by multi-anvil cell. Mg$_2$Si in a normal pressure phase was also obtained by pressing Mg$_2$Si powder without annealing. Valence-band spectra were recorded at 10 K with a total energy resolution of 0.12 eV at the excitation photon energy $h\nu$ of 70 eV. The origin of the binding energy E_B was set to the Fermi energy E_F of a reference Au film electrically connected to the specimen. Although the specimens were *in situ* fractured or filed to clean their surfaces for the photoelectron measurement, contamination by oxide species, unfortunately, was not completely removed. However, it seems not to affect the valence-band structure near E_F so much, since the bands of the oxide species are located at $E_B > \sim 4$ eV [6, 7].

Figure 1 shows typical valence-band spectra near E_F of Mg$_2$Si in the normal and high pressure phases together with an Au spectrum and density of states (DOS) for the normal pressure phase, which was calculated by an all-electron full-potential linearized augmented plane wave (FLAPW) method with the WIEN2k code [4] at the experimental lattice constant a = 0.6354 nm of the anti-fluorite structure. Calculated indirect band gap of ~ 0.2 eV is narrower than experimentally reported (0.63 eV [3] and 0.77 eV [5]), which may be partly attributed to the well-known tendency in the density functional calculation. The spectral intensity is normalized at E_B ~ 2 eV and the origin of E_B for the calculated DOS is set to the conduction bottom because of the n-type thermoelectric properties of the normal pressure phase. For the normal pressure phase, the spectral intensity decreases towards E_F, as predicted. However,

a small but definite intensity is observed around E_F, which might be ascribed to defect states within the band gap and might even imply the conduction bottom near E_F as expected by the band structure calculation and the n-type thermoelectric power. On the other hand, the intensity at E_F is clearly increased and the valence band top moves to E_F for the high pressure phase. This is consistent with both the high electric conductivity and the p-type thermoelectric power, although it is difficult to study the unoccupied conduction band by photoelectron spectroscopy.

Further study is intended for specimens synthesized in Ar atmosphere.
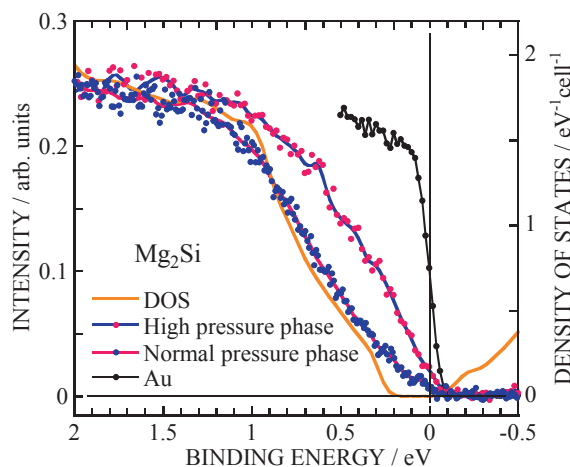
Fig. 1. Valence-band photoelectron spectra of Mg$_2$Si in normal and high pressure phases. Fermi edge of a reference Au film and calculated density of states (DOS) of normal pressure phase Mg$_2$Si are also shown for comparison.

[1] Y. Noda *et al*., J. Jpn. Inst. Mtals **53** (1989) 487.
[2] M. Akasawa *et al*., J. Appl. Phys. **104** (2008) 013703.
[3] F. Yu *et al*., Solid State Commun. **150** (2010) 620.
[4] K. Schwarz *et al*., Comp. Phys. Commun. **147** (2002) 71.
[5] U. Winler, Helv. Phys. Acta. **28** (1955) 633.
[6] M. Cardona *et al*., Phys. Stat. Sol. **58** (1973) 483.
[7] M. Brause *et al*., Surf. Sci. **398** (1998) 184.

In-situ Observations of Photoinduced Effects on Amorphous Chalcogenide Semiconductors by Synchrotron Orbital Radiation

K. Hayashi

Department of Electrical and Electronic Engineering, Gifu University, Gifu 501-1193, Japan

Introduction

It is well known that amorphous chalcogenide semiconductor materials show a variety of photoinduced effects [1-3]. Photodarkening (photoinduced optical absorption edge shift), photodegradation (photoinduced defect creation) and photoinduced volume change are representative photoinduced phenomena. These phenomena are caused by irradiation of light (bandgap (BG) light) having photon energy comparable to the optical bandgap. These phenomena can in general be either irreversible, i.e. the photoinduced changes are permanent after irradiation, or reversible, in which case the changes can be removed by annealing to the glass-transition temperature. The photoinduced changes by BG light of the x-ray diffraction and the volume have directly shown that these phenomena are due to a change of the local structure of the amorphous network. Several previous studies of photoinduced effects have reported that there is no direct correlation among photodegradation, photodarkening and photoinduced volume change. The detail is not clarified though the dynamics of those photoinduced effects certainly seems to be different.

Our recent studies have focused on the photoinduced energy structure changes in the vacuum ultraviolet (VUV) region by irradiation of BG light. To obtain a wide knowledge of the photoinduced phenomena, we have investigated photoinduced effects in the VUV region by the transmission spectra of amorphous thin films prepared onto polymer membrane substrates. In previous work, we reported the VUV transmission spectra of substrate-free evaporated amorphous thin films that removed the substrate [4]. Few studies have examined whether the photoinduced change of the chemical bonds contributes to photodarkening and photodegradation. To understand the dynamics and the correlation of photoinduced structure changes in the VUV region and the photodegradation in amorphous chalcogenide semiconductors, real time in-situ measurements are required. However, it is difficult to measure the transmission change while irradiating the BG light. Therefore, those dynamics and correlations are examined by measuring the total photoelectron yield (TPEY) that can measure the optical property in the VUV region. In this report, we will compare the transmission spectrum and the TPEY spectrum in the amorphous thin films.

Experimental

Samples used for the measurement of the transmission spectrum were substrate-free evaporated amorphous chalcogenide (a-As_2S_3 and a-As_2Se_3) semiconductor thin films. Samples used for the measurement of the TPEY spectrum were prepared onto quartz substrates which fabricated gold electrodes by conventional evaporation technique. The thickness of the amorphous films was from around 160 nm to 300 nm. The measurements were performed at room temperature at the BL5B beam line. A pinhole of 1.5 mm in a diameter was inserted between the monochromator and sample to remove stray light. The intensity of the VUV light was monitored by measuring the TPEY of a gold mesh.

Results and Discussion

Figure 1 shows the VUV transmission spectrum and the TPEY spectrum of a-As_2S_3 films at room temperature. It is necessary to note it because the intensity correction by incident light strength is not performed as for both spectra. As shown in the figure, the absorption peak corresponds very well in both spectra. The escape depth of the photoelectrons and the creation of the secondary electrons might influence the difference of both spectral line shapes. It will be necessary to discuss this point in the future.
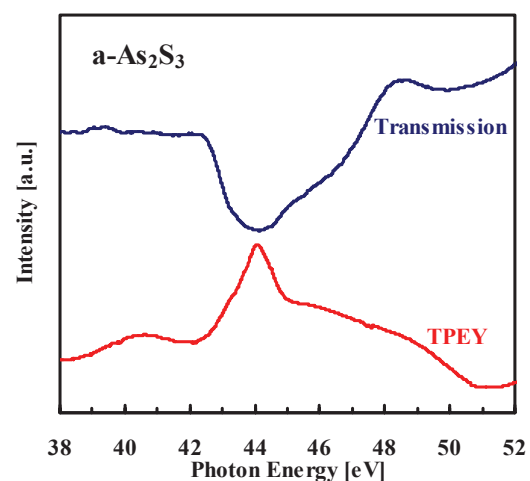

Fig. 1. VUV transmission and total photoelectron yield (TPEY) spectra of a-As_2S_3 film.

[1] Ke. Tanaka, Rev. Solid State Sci. **4** (1990) 641.
[2] D. L. Staebler and C.R. Wronski, Appl. Phys. Lett. **31** (1977) 292.
[3] S. R. Elliot, J. Non-Cryst. Sol. **81** (1986) 71.
[4] K. Hayashi, UVSOR Activity Report **34** (2006) 79.

Ⅲ-6. APPLIED MATERIALS

Characterization of 10-Bilayer TiO$_2$/ZnO Mirrors at 2.74 nm

H. Kumagai[1], Y. Tanaka[1], M. Murata[1], M. Sanjo[1], T. Shinagawa[2] and M. Chigane[2]

[1]*Graduate School of Engineering, Osaka City University, Osaka 558-8585, Japan*
[2]*Inorganic Materials Lab., Osaka Municipal Technical Research Institute,
Osaka 536-8553, Japan*

The authors have proposed the use of a novel metal oxide multilayer for soft-x-ray reflectors at water-window wavelengths [1], because an oxide multilayer can prevent the formation of an alloy at the interface without any buffer layer, and the absorption of oxygen in oxides is negligible at water-window wavelengths; moreover, the metal oxide multilayer can be fabricated by atomic layer deposition or atomic layer epitaxy (ALE). These techniques can be used to control surfaces on an atomic scale by sequentially dosing the surface with appropriate chemical precursors and then promoting surface chemical reactions that are inherently self-limiting. We have found that the self-limiting adsorption mechanism is effective in the fabrication of thin oxide films such as aluminum oxide and titanium oxide. Moreover, we reported the experimental demonstration of a high reflectivity of over 30% at a wavelength of 2.74 nm and an incident angle of 71.8° from the normal incidence using novel metal oxide multilayers consisting of titanium oxide and aluminum oxide fabricated by controlled growth by atomic layer deposition with sequential surface chemical reactions [1]. For high-power x-ray processing, crystalline multilayer mirrors might be more useful than those with amorphous layers. Therefore, the authors recently demonstrated the fabrication of novel oxide superlattice structures of crystalline TiO$_2$/ZnO on sapphire substrates for multilayer mirrors with high reflectivity at 2.74 nm [2, 3].

In the fabrication study, first of all, (001)-oriented wurtzite ZnO and (100)-oriented rutile TiO$_2$ films were grown on a (001)-oriented sapphire substrate by atomic layer epitaxy at a substrate temperature of 450 °C [4, 5]. These films were grown layer by layer owing to the self-limiting nature of surface chemical reaction. The ZnO films were grown using DEZ and H$_2$O vapors at a constant growth rate of nearly 0.26 nm/cycle. The TiO$_2$ films were deposited using TCT and H$_2$O at a constant growth rate of nearly 0.076 nm/cycle.

We fabricated a 10-bilayer TiO$_2$/ZnO multilayer mirror by atomic layer epitaxy at a substrate temperature of 450 °C [2, 3]. Figure 1 shows that the multilayer mirror achieved a high reflectivity of 29.4% at a wavelength of approximately 2.74 nm and a grazing angle of 2θ=10°. The FWHM of the experimentally obtained reflectivity at 2.74 nm was 0.041 nm, which corresponds to Δλ/λ=1.5%. The TiO$_2$/ZnO multilayer is expected to be useful for soft x-ray mirrors once further studies are conducted in terms of the growth rate, interface, surface roughness, and reactant vapors. Further reduction of the surface and interface roughness will lead to the fabrication of normal-incidence reflectors at the water-window wavelengths.
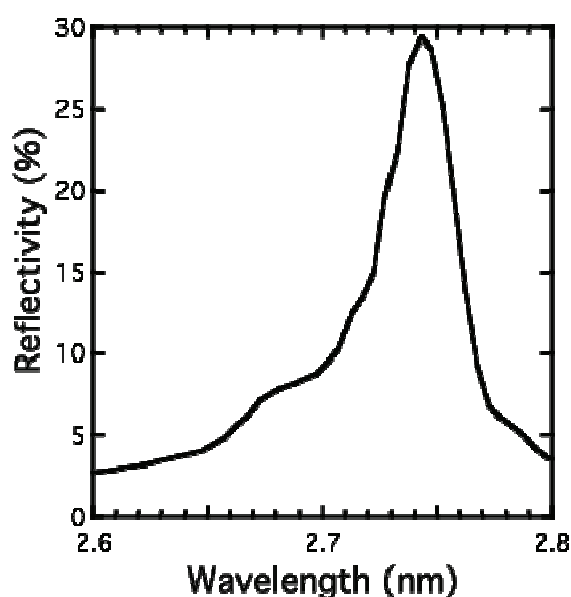
Fig. 1. Experimental reflectances of the ALE-grown 10-bilayer TiO$_2$/ZnO structure on a sapphire (0001) substrate at a wavelength of approximately 2.74 nm and a grazing angle of 2θ=10°.

[1] H. Kumagai, K. Toyoda, K. Kobayashi, M. Obara and Y. Iimura, Appl. Phys. Lett. **70** (1997) 2338.
[2] H. Kumagai, Y. Tanaka, M. Murata, Y. Masuda and T. Shinagawa, Journal of Physics: Condensed Matter **22** (2010) 474008 pp.1-7.
[3] H. Kumagai and Y. Yanagihara, Review of Laser Engineering **38** (2010) 976.
[4] H. Kumagai, Y. Masuda and T. Shinagawa, Journal of Crystal Growth **314** (2011) 146.
[5] H. Kumagai, Y. Masuda and T. Shinagawa, Materials Science and Engineering (2011) in press.

Band Alignment at CNT/SiC Interface Formed by Surface Decomposition

T. Maruyama[1], S. Sakakibara[1], H. Ito[1], H. Yamane[2], E. Shigemasa[2] and N. Kosugi[2]

[1]*Department of Materials Science and Engineering, Meijo University,*
Nagoya 468-8502, Japan
[2]*Institute for Molecular Science, Okazaki 444-8585, Japan*

Carbon nanotube (CNT) growth by surface decomposition of SiC is a synthesis method for self-organized CNT films only by heating SiC single crystal at high temperature in a vacuum [1]. By this method, high density aligned zigzag-type CNTs can be produced perpendicular to the substrate surfaces (Fig. 1). Moreover, it has been demonstrated that grown CNTs are atomically bonded to SiC substrate [2]. This is a distinguished characteristic of this material, because there are some interlayers at the interface in other CNT/semiconductor heterojunctions. In this study, to clarify the electronic structure at the CNT/SiC interface, we performed the photoemission spectroscopy (PES) experiments.

CNT films formed by surface decomposition of 6H-SiC(000-1) face were used as samples. The current-voltage (I-V) measurement for CNT (~400 nm)/SiC heterojunction showed distinct rectifying behavior with the forward direction occurring at positively biased CNTs. For PES measurement, the samples with the CNT thickness of about several nm were also prepared to investigate the CNT/SiC interface. The PES measurement was carried out in a high-resolution angle-resolved PES system at BL6U. All PES spectra were measured at normal emission with the incident photon energy of 60 and 350 eV. The overall energy resolution was below 100 meV at room temperature (~300 K).

Figure 2 (a) shows photoemission spectrum near valence band maximum (VBM) of CNTs (~400 nm) with that of Au. The Fermi edge is observed in the spectrum of CNTs, indicating that they were metallic tubes.

The value of Schottky barrier height at the interface between metallic CNTs and SiC was evaluated by the energy difference between the C 1s core levels at the CNT/SiC interface (shown in Fig. 2 (b)) and the VBM to the core level separations in the CNT(~400nm)/SiC and SiC substrate samples, as described by

$$E_{SB} = E_g^{SiC} + \left(E_{C1s}^{SiC} - E_{VBM}^{SiC}\right) + \left(E_{C1s}^{CNT(CNT/SiC)} - E_{C1s}^{SiC(CNT/SiC)}\right) - E_{C1s}^{CNT}$$
$$= 3.0 + 280.87 + 1.76 - 284.22 = 1.41 \ [eV]$$

where E_i^s denotes the energy of feature i in sample s, and the band gap of 6H-SiC, E_g^{SiC}, is 3.0 eV [3]. The obtained band alignment at the CNT/SiC interface is shown in Fig. 3. The Schottky barrier height at the CNT/SiC interface, 1.4 eV, is fairly high, compared with conventional metal/SiC Schottky barriers. Our

result indicates that the band bending occurred at the interface, which might be induced by deep level traps.
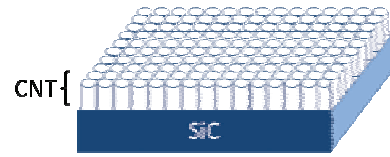
Fig. 1. Schematics of CNTs on SiC formed by surface decomposition.
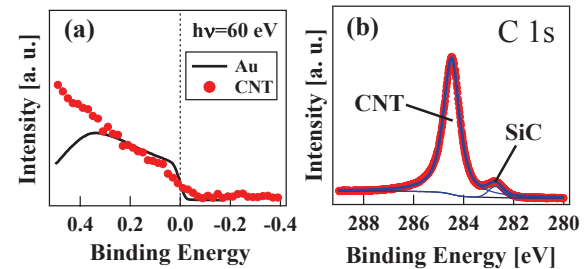
Fig. 2. Photoemission spectra of CNT (~400 nm)/SiC heterojunction: (a) valence band near the Fermi level (hν = 60 eV), (b) C 1s core level (hν = 350 eV).
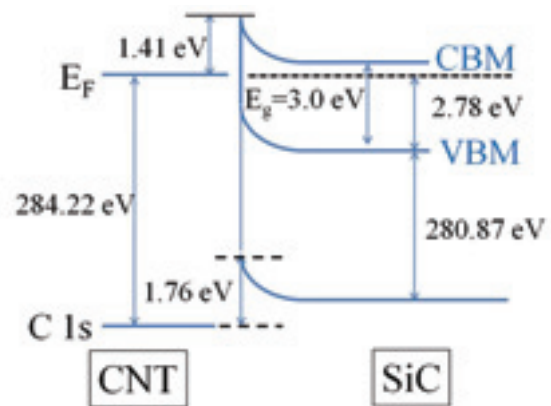
Fig. 3. Band alignment of CNT/SiC heterojunction.

[1] M. Kusunoki *et al.*, Appl. Phys. Lett. **77** (2000) 531.
[2] M. Kusunoki *et al.*, Chem. Phys. Lett. **366** (2002) 458.
[3] O. Madelung, Semiconductors: Data Handbook (Springer-Verlag) (2004) 61.

Ⅲ-6. APPLIED MATERIALS

Far-Infrared Reflective Study of Alkali Niobate Ceramics

H. Matsudo, S. Koide, T. Nishi, I. Kagomiya and K. Kakimoto
Graduate School of Engineering, Nagoya Institute of Technology Nagoya 466-8555, Japan

Introduction

Alkali niobate is one of the promising candidates of lead-free piezoelectric material. Li-doped $Na_{0.5}K_{0.5}NbO_3$ (LNKN) solid solution shows an excellent piezoelectric property of d_{33}=235 pC/N when the Li content is 6.0 mol% (L6). The phase transition of LNKN varies with Li content, and changes at room tempereature from orthorhombic to tetragonal at 5-7 mol% of Li content. However, LNKN undergoes the temperature-dependent successive structural phase transition. We have investigated such phase transition by using Raman scattering to clarify its origin and the related good piezoelectric property. Especially, the ferroelectric property recorded at room temperature was closely related to the frozen-modes of optical lattice vibration below room temperature. Therefore, the phonon behavior of L6 has been investigated more. In this study, IR reflectivity of LNKN ceramics was measured, and the effect of Li incorporation against the lattice vibration of LNKN was discussed.

Experimental Procedure

The ceramic sample was synthesized by an ordinal solid-state reaction method. The surface of $Li_{0.06}(Na_{0.5}K_{0.5})_{0.94}NbO_3$ (L6) and $Na_{0.5}K_{0.5}NbO_3$ (NKN) ceramics were polished and used for IR reflective study.

Their reflectivity far-infrared spectra were obtained at 78 and 300 K using the beamline BL6B, then the spectra were corrected by using Michelson interferometer (Bruker, IFS66v) and synchrotron radiation source.

Results and Discussion

Dielectric permittivity of L6 ceramics was calculated by Kramers-Kronig transform method. Any dielectric anomalies originated from structural phase transitions has not been detected below 273 K in the previous impedance analysis. However, an optical mode was disappeared during the heating step. Figure 1 shows the measured reflectance spectra of non-poled L6 ceramics at 110, 120, 130, 140 and 150 K. The optical mode was observed at 223 cm^{-1} at temperatures below 150 K. This mode was not detected for NKN. Figure 2 shows the real part of permittivity of L6 ceramics and the fitting result. The strong peak of the mode could not fit well to a traditional oscillator model. A strong Li-O mode in LNKN seems to be correlated with the result, and we will investigate the further mode analysis for the poled-samples and single crystal.
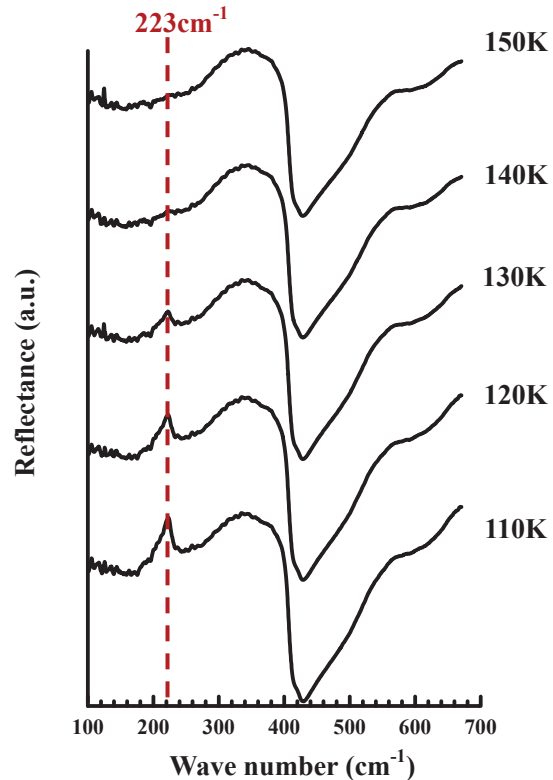

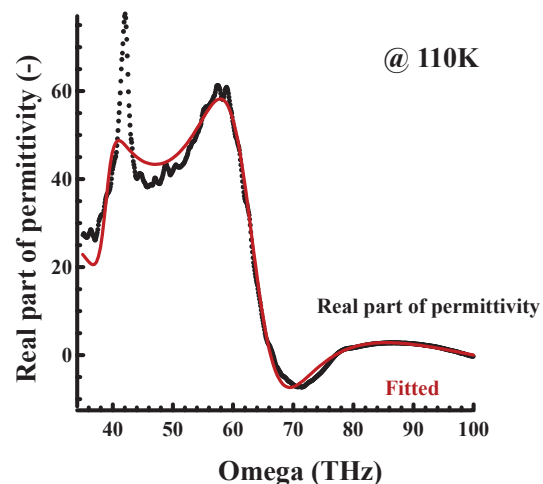Fig. 1. Far-infrared reflectance spectra of L6 ceramics at 110, 120, 130, 140 and 150 K.

Fig. 2. Real part of permittivity of L6 ceramics at 110 K and the fitting result based on traditional oscillator model at 110 K.

Effects of Temperature Dependent Chemical Potential on Seebeck Coefficient of TiS$_2$

T. Takeuchi[1,2], A. Yamamoto[2] and K. Ogawa[2]

[1]EcoTopia Science Institute, Nagoya University, Nagoya 464-8603, Japan

[2]Department of Crystalline Materials Science, Nagoya University, Nagoya 464-8603, Japan

Temperature dependence of chemical potential was measured for the n-type TiS$_2$ thermoelectric material by means of angle resolved photoemission spectroscopy (ARPES), and compared with its measured Seebeck coefficient. The ARPES measurements were performed using 22 eV photon source and the MBS A1 analyzer located at the BL7U in the UVSOR at Okazaki, Japan.

Figures 1 (a) and (b) show typical example of ARPES intensity images obtained for the present sample at 15 K and 140 K along the momentum line crossing the M point. The intensity-peak varying with momentum is observable in the ARPES images. This experimentally revealed fact indicates that the quality of samples was good enough, and also that the electronic states in this sample are described with the Bloch states **k**. The presence of Bloch states **k** is responsible for the metallic electrical conduction observed for this sample. The energy shift of ARPES spectra with varying temperature is also observable for the present sample. This energy shift in ARPES spectra must be caused by the temperature dependence of chemical potential.

The chemical potential of n-type materials generally moves toward lower energy with increasing temperature. By considering that (a) the chemical potential of apparatus is kept constant regardless of the sample temperature and (b) the chemical potential observable in the photoemission spectra is pinned at the chemical potential of the apparatus, it is naturally understood that the photoemission spectrum at given temperature shifts towards the opposite energy direction of the chemical potential shift of samples. Indeed, the ARPES spectrum of the n-type TiS$_2$, in which the chemical potential is supposed to move towards lower energy, was moved towards higher energy with increasing temperature.

In order to quantitatively extract the temperature dependence of chemical potential from the measured ARPES spectra, the ridge in ARPES intensity, that indicates the energy–momentum dispersion, was plotted in Fig. 1 (c). From the determined energy-momentum dispersion, we identified that the chemical potential shift of −6 meV took place during the temperature increase from 15 K to 140 K [1].

The contribution of chemical potential to Seebeck coefficient was calculated from the measured value of chemical potential shift. We assumed here that the contribution of chemical potential to Seebeck coefficient is linearly varying with absolute temperature as it is described in the Sommerfeld theory, and mathematically transformed the equation $S_\mu(T)$; $(\mu(T) - \varepsilon_F)/(|e|T)$ into the following formula.

$$S_\mu(T) \approx T(\mu(T) - \mu(T_1))/(|e|(T^2 - T_1^2)) \qquad (1)$$

The resulting value was $S_\mu(T) = -43$ μ V/K at 140 K, which exceeds 30 % of the measured value, S (140 K) = −135 μV/K [1].

The present analysis clearly proved that the contribution of chemical potential to Seebeck coefficient is not negligibly small but considerably large. We have confirmed that this fact is also true for the Bi$_2$Te$_3$ and Bi$_2$Se$_3$ thermoelectric materials [2]. It is confidently argued, therefore, that the proper understanding of the relation between chemical potential and Seebeck coefficient should be required to develop a practical thermoelectric material possessing a large magnitude of Seebeck coefficient.

[1] T. Takeuchi, A. Yamamoto, K. Ogawa, Mater. Res. Soc. Symp. Proc. (2011), in press.
[2] A. Yamamoto, K. Ogawa, T. Takeuchi, Materials Transactions (2011), in press.
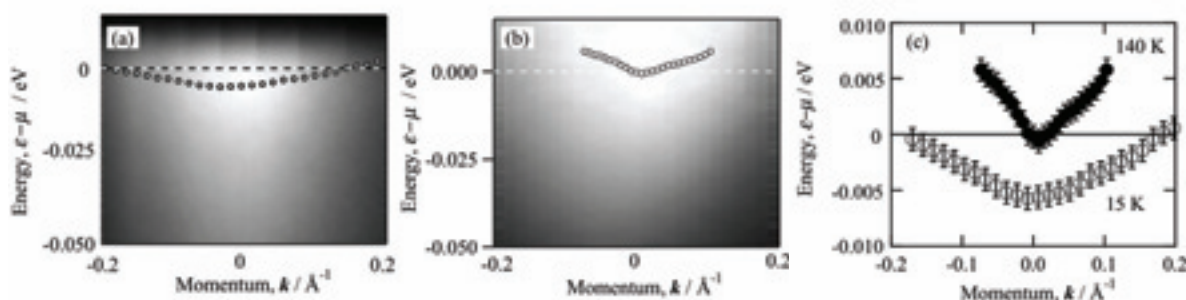
Fig. 1. ARPES intensity $I(\mathbf{k},e)$ of TiS$_2$ measured at (a) 15 K and (b) 140 K. In order to observe the states above μ, the 140 K spectrum was divided by the Fermi-Dirac distribution function. The peak energy is plotted as a function of momentum in (c). The chemical potential shift of −6 meV was caused by the temperature increase from 15 K to 140 K [1].

Ⅲ-6. APPLIED MATERIALS

Reflection Spectroscopy of 6FDA-Based Polyimide Films

H. Ito, N. Fujita, T. Yabumoto, S. Matsumoto and H. Matsumoto

School of Science & Technology, Meiji University, Kawasaki 214-8571, Japan

Introduction

Photo-alignment is attracting attention as a method of fabricating the alignment layer in liquid crystal (LC) displays. In this method, a polyimide (PI) film is irradiated by linearly polarized ultraviolet light (LPUVL). In an alignment layer produced by this method, the LC molecules are oriented by a mechanism that is not understood.

We investigated the optical properties of PI films irradiated by LPUVL in the ultraviolet (UV) and vacuum ultraviolet (VUV) regions to examine the mechanism.

We used fluorine-containing PI that is expected to find wide application.

Experimental

Materials

We investigated the optical properties of PIs based on 2,2′-bis(3,4-dicarboxyphenyl)hexafluoro propane dianhydride (6FDA). Four types of phenylene were used as the diamine: 1,3-phenylene diamine (mPD), 4-methyl-1,3-phenylene diamine (MPD), 2,4,6-trimethyl-1,3-phenylene diamine (TMPD), and 2,3,5,6-tetramethyl-1,4-phenylene (TeMPD). They were synthesized at the Nagai lab, Meiji University [1]. Figure 1 shows their chemical structures.
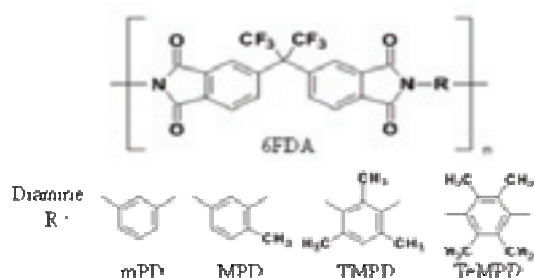

Fig. 1. Chemical structures of 6FDA-based PIs.

Sample preparation

We dissolved the PIs with *N,N*-dimethylacetamide (DMAc). The PI films were prepared by spin coating on quartz substrates. The PI-coated substrates were baked at 100°C for 1 h. The film thicknesses were controlled to about 400 nm.

These PI films were irradiated by LPUVL from a 200 W Hg–Xe lamp. Linearly polarized light was obtained by reflection from a quartz plate at Brewster's angle. The degree of polarization was 99% at 254 nm. The irradiation intensity was about 700 μW/cm^2 at 254 nm. We irradiated the films with 8 J of LPUVL.

Reflection measurements

UV and VUV reflectance spectra of the films were measured at up to 17 eV with a 3-m normal incident monochromator (grating: G2 and G3) at BL-7B of UVSOR. A silicon photodiode sensor was used to detect the reflected light.

Results and Discussion

Figure 2 shows the UV and VUV reflectance spectra of the 6FDA-based PI films from 4.5 to 17 eV. The solid line indicates the reflectance before LPUVL irradiation, and the dotted line indicates the reflectance after 8 J of LPUVL irradiation.
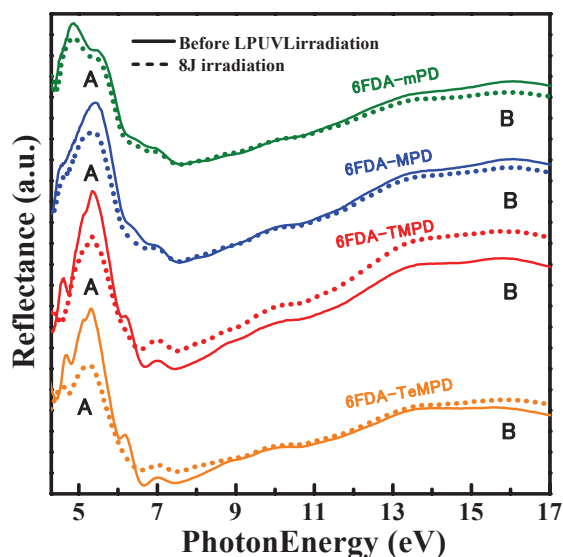
Fig. 2. Reflectance of 6FDA-based PIs.

The spectra of the PI films are fairly similar and consist of a prominent band group around 5.5 eV (the A band) and another broad band group (the B band) near 17 eV.

The appearance of the A band varied in the four spectra taken before LPUVL irradiation. The reason may be differences in the diamines.

A significant spectral change was observed after LPUVL irradiation of the 6FDA-TeMPD film. But the spectrum of the 6FDA-mPD film showed the least change after irradiation. This difference in the degree of spectral change implies that the methyl groups added to phenylene in the diamine affect the photo-alignment of PI films.

[1] S. Miyata *et al.,* J. of Appl. Polym. Sci. **107** (2008) 3933.

Auger-Free Luminescence Emitted from A_2ZnCl_4 (A = Cs, Rb) Crystals

A. Ohnishi[1], M. Saito[1], M. Kitaura[1], M. Sasaki[1], T. Kajitani[2] and M. Itoh[2]

[1]Depeartment of Physics, Yamagata University, Yamagata 990-8560, Japan

[2]Department of Electrical and Electronic Engineering, Shinshu University, Nagano 380-8553, Japan

The Auger-free luminescence (AFL) is a peculiar type of intrinsic luminescence in ionic crystals in which the valence excitation through a nonradiative Auger process is energetically forbidden. The AFL is characterized by a high quantum yield and a short lifetime of the order of ns. Therefore, it is very useful as the fast scintillator for high-energy physics, positron emission tomography and so on.

In the present work, we have investigated the luminescence of A_2ZnCl_4 (A = Cs, Rb) crystals under the outermost core excitation, in order to find the existence of AFL.

A_2ZnCl_4 (A = Cs, Rb) crystals were prepared by evaporating a stoichiometric mixture of solutions of CsCl or RbCl and $ZnCl_2$. Experiments were performed at the BL7B beamline of UVSOR. The emission spectra in this measurement were not corrected for the spectral dispersion. The excitation spectra were corrected for the spectral distribution of the light source.

When Cs_2ZnCl_4 was excited at 10 K at 21.4 eV, two luminescence bands appeared at 3.2 and 4.2 eV. The blue line of Fig. 1 shows the excitation spectrum for the 4.2 eV band. The excitation spectrum for the 3.2 eV band was practically the same as that for the 4.2 eV band. For reference, the reflection spectrum measured for the cleaved surface of Cs_2ZnCl_4 is also shown by the red line. Sharp peak at 7.3 eV is assigned to the $n = 1$ exciton absorption, which is due to the transition from the Cl $3p$ valence band to the conduction band. Sharp peaks at 13.2 and 13.9 eV may be core exciton bands due to the transitions from the outermost core band to the conduction band.

The excitation spectrum rises at around 13.5 eV as the photon energy is increased. This threshold energy corresponds almost to the transition energy between the outermost core band and the conduction band, and thus both of the 4.15 eV and 3.31 eV bands are supposed to be the AFL bands due to the radiative recombination between a valence electron and an outermost core hole. It is noteworthy that the threshold energy of the AFL is slightly higher than the lowest-energy core exciton band at 13.2 eV. This fact suggests that core excitons decay nonradiatively through Auger-electron emission.

Luminescence decay measurements were also performed using a time-correlated single-photon counting technique under the single bunch operation. It was proved that, at 10 K, the 4.15 eV and 3.31 eV bands are composed of a fast decay component with the lifetime of about 1.8 ns.

In Rb_2ZnCl_4 crystal, two AFL bands peaking at 2.8 and 4.3 eV were observed at 10 K under excitation at 21.4 eV. In Fig. 2, excitation (blue) and reflection (red) spectra of Rb_2ZnCl_4 are shown. The excitation spectra for the 2.8 and 4.3 eV bands were the same. Sharp peaks at 7.3 and 16.5 eV in the reflection spectrum is assigned to the $n = 1$ exciton and core exciton absorption bands, respectively. From the excitation spectrum, it turns out that both bands are stimulated with photons above about 14 eV. This result suggests that the 2.8 and 4.3 eV bands are the AFL bands in Rb_2ZnCl_4. However, it should be noticed that the threshold energy is located at the energy lower than the core exciton peaks. The reason for such a disagreement is under investigation now.
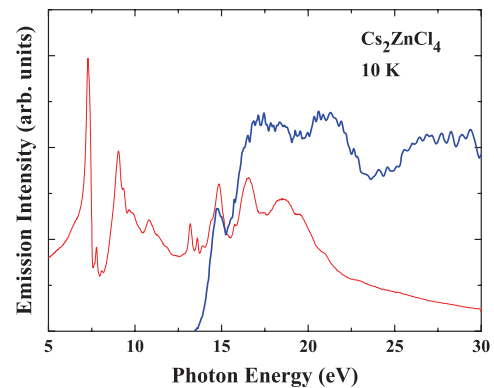

Fig. 1. Excitation spectrum at 10 K for the 4.2 eV band in Cs_2ZnCl_4 (blue line). Reflection spectrum (red line) is also shown for reference.
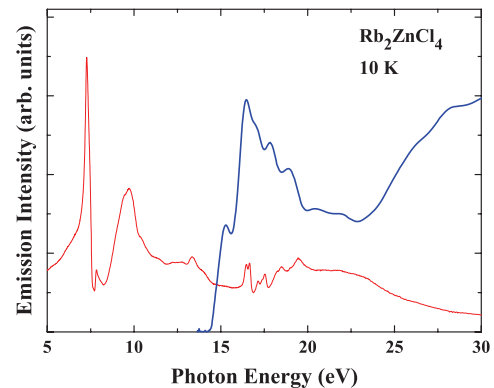

Fig. 2. Excitation spectrum at 10 K for the 4.3 eV band in Rb_2ZnCl_4 (blue line). For reference, reflection spectrum is also shown by a red line.

Ⅲ-6. APPLIED MATERIALS

Electronic Structure of Delocalized Singlet Biradical Ph$_2$-IDPL Solid Film

K. Kanai[1], Y. Noda[2], K. Kato[2], T. Kubo[3], K. Nakasuji[4] and K. Seki[2]

[1] *Department of Physics, Faculty of Science and Technology, Tokyo University of Science, Noda 278-8510, Japan*

[2] *Department of Chemistry, Graduate School of Science, Nagoya University Nagoya 464-8602, Japan*

[3] *Department of Chemistry, Graduate School of Science, Osaka University, Osaka 560-0043, Japan*

[4] *Fukui University of Technology, Fukui 910-8505, Japan*

Recently, Kubo *et al.* have successfully isolated a biradical hydrocarbon, diphenyl derivative of s-indacenodiphenalene (Ph$_2$-IDPL) which possesses a relatively small HOMO-LUMO gap E_g and strong intermolecular interactions [1]. The partial occupation of the LUMO is thought to contribute to stabilization of the intermolecular interaction, leading to intermolecular covalency. Thus, a strong intermolecular interaction is characteristic of singlet biradicals.

In this work, the electronic structure of a Ph$_2$-IDPL film has been investigated. A small E_g compared with that of typical π-conjugated small molecules was observed even for the amorphous film of Ph$_2$-IDPL. This result indicates that the small E_g is an important characteristic of the singlet biradical electronic structure. Moreover, the photon energy dependence of ultraviolet photoemission spectra shows that the stacked Ph$_2$-IDPL molecular chain in the polycrystalline film develops an energy band structure in the direction of the surface normal of the film. The intermolecular covalency therefore evolves into the quasi one-dimensional energy band along the molecular stacking direction.

The UPS measurements were performed at the BL8B of the UVSOR.

Figure 1 shows UPS and IPES spectra of Ph$_2$-IDPL amorphous film on graphite substrate. The simulated spectra for the monomer well explain the observed spectra over the entire energy range. Since strong intermolecular coupling among the molecules is expected to significantly alter its electronic structure, these results clearly show that this Ph$_2$-IDPL film on graphite is composed of the monomers. Notably, the observed E_g is rather small. From the results shown in Fig. 1, E_g is about 1.2 eV, which is smaller than those of many other typical π-conjugated molecules.

Figure 2 shows the UPS and IPES spectra of Ph$_2$-IDPL crystal and the polycrystalline film. The film spectra differ from the spectra for a monomer. In particular, the electronic structure of the film around E_F produces broader spectral features compared to the monomer spectra. The UPS spectrum of the film closely resembles that of the crystal. The E_g for the polycrystalline film was estimated to be 0.84 eV. These results well explains the previously reported ambipolar field effects of amorphous Ph$_2$-IDPL film
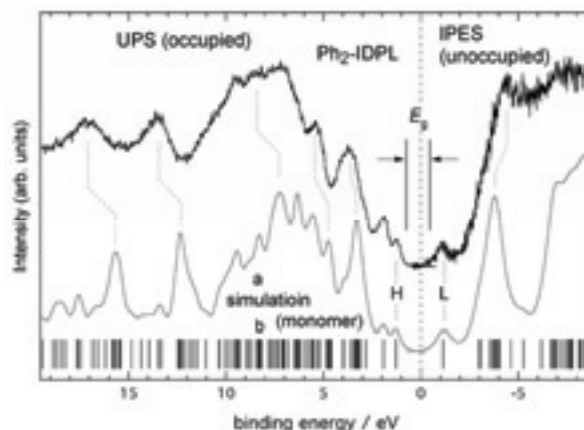
Fig. 1. UPS and IPES spectra of Ph$_2$-IDPL film on graphite. Simulated spectra labeled "a" were calculated by the DFT method for monomer.
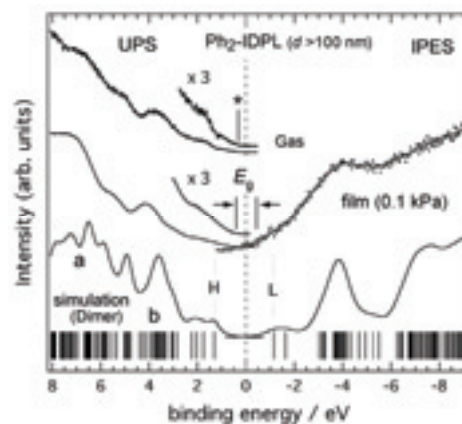
Fig. 2. UPS and IPES spectra of Ph$_2$-IDPL film on graphite and simulated spectra for the dimer.

by Chikamatsu *et al.* [2]. The small E_g would result in a small injection barrier both for electrons and holes at the electrode interface. The extremely small E_g observed in the polycrystalline Ph$_2$-IDPL film is possibly caused by strong intermolecular coupling.

[1] T. Kubo *et al.*, Angew. Chem. Int. Ed. **44** (2005) 6564.
[2] M. Chikamatsu *et al.*, Appl. Phys. Lett. **91** (2007) 043506.

Interface Electronic Structures
of a High Performance Organic Planar Hetero-junction Solar Cell

Y. Nakayama[1], J. Wagner[2], Y. Tanaka[3], S. Machida[3],
T. Nishi[1,4], A. Opitz[2], W. Brütting[2] and H. Ishii[1,3]
[1]*Center for Frontier Science, Chiba University, Chiba 263-8522, Japan*
[2]*Institute of Physics, University of Augsburg, Augsburg 86135, Germany*
[3]*Graduate School of Advanced Integration Science, Chiba University, Chiba 263-8522, Japan*
[4]*UVSOR Facility, Institute for Molecular Science, Okazaki 444-8585, Japan*

Organic photovoltaics (OPVs) are expected as next generation power conversion devices complementary to conventional Si-based solar cells. For OPVs, a bulk hetero-junction concept is generally adopted to redeem small exciton diffusion length, nevertheless this concept also has disadvantages (e.g. spoiled effective mobility μ_{eff}) that depress the power conversion efficiency. A planar hetero-junction (PHJ) OPV based on diindenoperylene (DIP) and C_{60} was recently reported to reveal high performance [1]. DIP has to be deposited on a heated hole injection layer (HIL) to achieve high efficiency. The origin(s) of the improved performance, which may be attributed to a reduced interface energy barrier and/or enhanced bulk μ_{eff} of DIP, have not been clarified yet. In this study, we determined the interface electronic structures of the DIP-C_{60} based high performance PHJ-OPV.

EDOT:PSS substrates were prepared by a method described in Ref. [1] in nitrogen atmosphere. The work function of the substrate varied in the range of 4.9 ± 0.2 eV. DIP was deposited (ca. 0.05 nm/s) onto the polymer substrates at ca. 100 °C in high vacuum. Note that heating of the polymer up to the deposition temperature significantly increased the work function [Fig. 1 (a)]. C_{60} was deposited (ca. 0.02 nm/s) onto a DIP thin film at RT. All PES spectra were taken with the photon energy of 40 eV at BL8B in UVSOR. For the organic films of 1.5 nm or thicker, sample bias of +5 V was applied in order to avoid sample charging.

Figure 1 shows the UPS secondary electron cutoff (SECO) and spectra of a PEDOT:PSS substrate and DIP overlayers. The onset of the highest occupied molecular orbital (HOMO) of DIP (Φ_h) appeared at 0.2 eV from the Fermi level (E_F). This value is apparently smaller than the literature (0.45 eV [1]) of DIP films deposited at RT. In addition, a negative vacuum level shift (Δ) is evinced by SECO, which is also strikingly in contrast to the RT deposition case.

The HOMO level offset (ΔE) at the C_{60}-DIP interface is estimated to be 1.0 eV as shown in Fig. 2. Slightly positive Δ was revealed at this interface. The energy level diagram of the topical OPV cell is shown in Fig. 2 (d). Despite aforementioned HOMO energy difference, ΔE is identical to that of the interface formed on DIP deposited at RT (1.05 eV [1]). The reduced Φ_h by high temperature DIP deposition should be a reason of improved OPV performance.
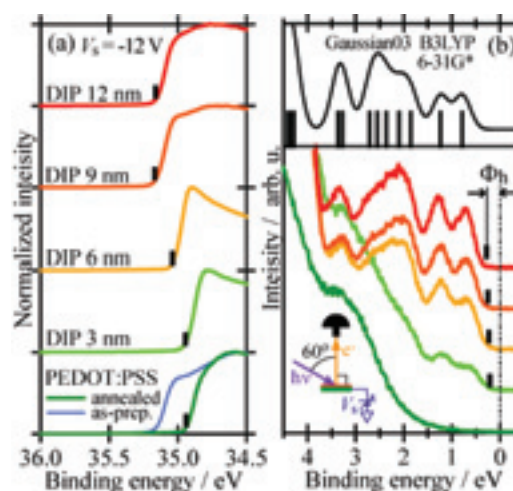
Fig. 1. (a) SECO and (b) UPS of DIP deposited on a heated PEDOT:PSS substrate. A simulated density-of-state curve of DIP is shown in the upper panel of (b).
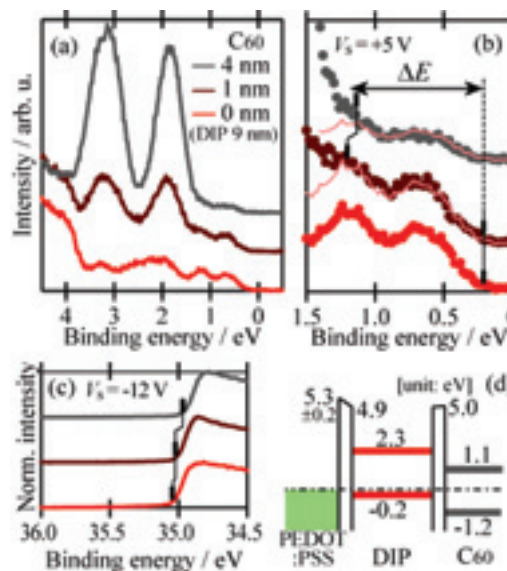
Fig. 2. (a) UPS spectra of C_{60} deposited on DIP(9 nm) /PEDOT:PSS. (b) Magnified spectra of (a). Thin red lines indicate hypothetical DIP contribution. (c) SECO spectra of C_{60} on DIP/PEDOT:PSS. (d) An energy level diagram of the hetero-interfaces in the DIP-C_{60} based high performance PHJ-OPV [1]. The numbers represent the energy with respect to E_F.

[1] J. Wagner *et al.*, Adv. Funct. Mater. **20** (2010) 4295.

Electronic Structures of Room Temperature Ionic Liquids Studied by UPS and IPES

T. Sato[1], T. Iwahashi[1,2], Y. Sakai[1], K. Kanai[3], T. Nishi[4] and Y. Ouchi[1]

[1] *Department of Chemistry, Nagoya University, Nagoya 464-8602, Japan*
[2] *Venture Business Laboratory (VBL), Nagoya University, Nagoya 464-8601, Japan*
[3] *Faculty of Science and Technology, Department of Physics, Tokyo University of Science, Chiba 278-8510, Japan*
[4] *UVSOR Facility, Institute for Molecular Science, Okazaki 444-8585, Japan*

Room temperature ionic liquids (RTILs) are salts in a liquid phase at ambient temperature and pressure, and have attracted much attention due to their unique nature of nonvolatility, high conductivity, and wide electrochemical window. Recently, RTILs are utilized as a potential gate material for organic field effect transistors as well as capacitors, fuel cells, organic photovoltaic cells, and Li-ion batteries. In such applications, electronic structure, such as HOMO and LUMO levels, of RTIL strongly affects the performance of the devices, and hence understanding of the electronic structures of RTILs should be a key issue for further development of such potential applications.

In this brief report, we examined the HOMO and LUMO levels and the energy gaps of the TFSA RTILs with cations of 1-ethyl-3-methylimidazolium ([emim]$^+$), 1-propyl-1-methyl pyrrolidinium ([P13]$^+$), 1-butyl- 1-methyl pyrrolidinium ([P14]$^+$), 1-propyl-1-methylpiperidinium ([PP14]$^+$), *N,N,N*-trimethyl propylammonium ([TMPA]$^+$), and [DEME]$^+$ cations by UPS and IPES. UPS measurements were carried out at the beamline BL8B2 of UVSOR facility at Institute for Molecular Science. IPES measurements were conducted at Nagoya University. The samples were prepared by putting one droplet of RTIL on scratched Au substrates. All measurements were performed under ultra-high vacuum condition of $2 \times 10^{-8} \sim 1 \times 10^{-7}$ Pa.

Figure 1 shows the UPS and IPES spectra of the TFSA RTILs with respect to the Fermi level of Au. The results for [DEME]BF$_4$ are also shown as a reference. As is seen in Fig. 1, the HOMO and LUMO levels of each RTIL differ from those of the isolated ions estimated from the *ab initio* calculations,[1] and these energy shifts are toward the lower and higher energies for the cation and the anion, respectively. This energy shift is understood as a contribution of Madelung energy which stabilizes and destabilizes the orbital energies of the anion and the cation, respectively. On the other hand, we found that the energy gaps of the quaternary ammonium-based RTILs are wider with shifting the HOMO and LUMO levels higher and lower binding energy side, respectively, relative to those of [emim]TFSA as shown in Fig. 1. It is noteworthy that not only the energy gap but also the HOMO and LUMO levels are almost the same for the quaternary ammonium-based

RTILs other than [DEME]TFSA even if the calculated energy gap has some differences for each cation. Considering that the calculated energy gap of the TFSA anion is much narrower than that of the quaternary ammonium-based cations except the [DEME]$^+$ cation, we can propose that both the HOMO and LUMO levels of the ammonium-based RTILs examined in this study, except [DEME]TFSA, is attributed to the TFSA anion. The observed energy gaps of the quaternary ammonium-based RTILs without methoxy group are also ~2 eV wider than the calculated gap of the TFSA anion similarly to the case of [emim]TFSA. The energy gap broadening of ~2 eV seems to be a condensed state effect for the TFSA RTILs.
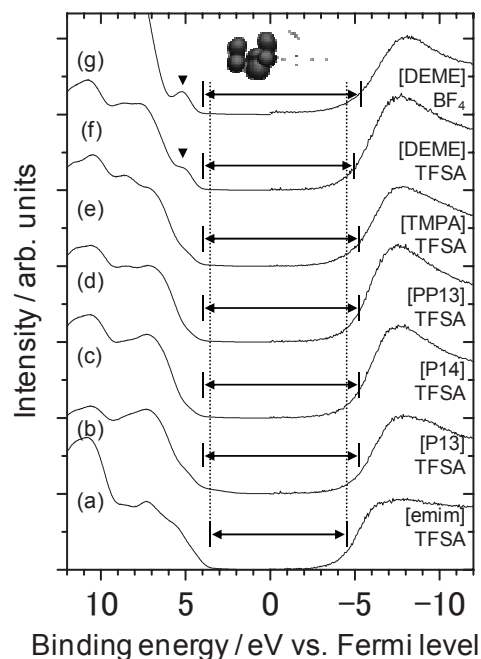
Fig. 1. UPS and IPES spectra of (a) [emim]TFSA, (b) [P13]TFSA, (c) [P14]TFSA, (c) [PP13]TFSA, (e) [TMPA]TFSA, (f) [DEME]TFSA, and (g) [DEME]BF$_4$. The abscissa is set the Fermi level of the Au substrate as zero. Inset shows the MO pattern of HOMO of [DEME]$^+$ cation. The triangles on the UPS spectra represent the peaks originating from O 2p of [DEME]$^+$ cation.

[1] K. Kanai *et al.*, J. Electron Spectrosc. Relat. Phenom. **174** (2009) 110.

Experimental Evidence of Acceptor-Like Levels in $SrGa_2S_4$:Eu^{2+} Phosphor Thin-Films

Y. Suzuki[1], M. Kitaura[1], S. Tanaka[2], H. Kominami[3], K. Hara[3], A. Ohnishi[1] and M. Sasaki[1]

[1]*Faculty of Science, Yamagata University, Yamagata 990-8560, Japan*
[2]*Interdisciplinary Faculty of Science and Engineering, Shimane University, Matsue 690-8504, Japan*
[3]*Research Institute of Electronics, Shizuoka University, Hamamatsu 432-8011, Japan*

The type of charge carrier in narrow-gap semiconductors can be artificially controlled by the addition of impurities. The exchange of carrier type between electron and holes is challenge in wide-gap semiconductors with ionic character, because the *p*-type conduction due to holes is hard to occur due to the large effective mass and strong phonon coupling. Therefore, there have been few reports that succeeded the carrier type exchange in the wide-gap semiconductors. Recently, Tanaka *et al*. have reported that the hot carrier type in inorganic electroluminescence (EL) thin-film devices is exchangeable for different rare-earth ion doping [1]. Strontium thiogallate ($SrGa_2S_4$) is also one of the host materials showing such carrier type exchange. This material has the feature of *n*-type in Ce^{3+}-doping. The carrier type is changed to *p*-type in Eu^{2+}-doping. Judging from the practical sense mentioned above, these results are to be very surprising. On the other hand, there are ambiguous points on the fundamental physic of such *p*-type conduction, *e.g*., the presence of acceptor-like levels and the contact type at the interface between phosphor and metal electrode thin-films. The elucidation of these points is our main purpose: hence, ultraviolet photoelectron spectroscopy (UPS) experiment was carried out.

Eu^{2+}-doped $SrGa_2S_4$ thin-films were deposited on quartz substrates heated at 200 $^{\circ}$C using electron beam sources. The concentration of Eu^{2+} ions was set to be 2 mol% in the preparation. The thickness was adjusted to be 100 nm using quartz oscillators. The as-deposited thin-films were annealed at 850 $^{\circ}$C in the H_2S+Ar gas mixture for 30 minutes, in order to supply with sulfur. The composition and crystalinity of $SrGa_2S_4$:Eu^{2+} thin-films were checked by X-ray diffraction measurement. In UPS experiment, the surface was cleaned in vacuum with Ar^+ ion gun. An appearance of the clean surface was judged from the peak energy and spectral shape of the Ga-3*d* peak.

Figure 1 (a) shows the typical UPS spectrum of $SrGa_2S_4$;Eu^{2+} thin-films at room temperature under excitation with photons at 18 eV. The absolute binding energy was determined by referring to the Fermi level of tantalum plates for the fixing of samples. In Fig. 1 (a), a prominent band appears around 5.0 eV. This band is ascribed to the valence band dominated by S-3*p* orbitals [2]. As shown in Fig. 1 (b), this band starts at E_{th}=0.86 eV. The fundamental absorption edge of $SrGa_2S_4$ is located at 4.0 eV,
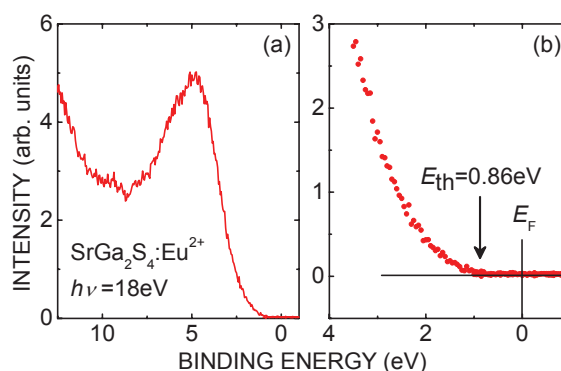

Fig. 1. UPS spectrum of $SrGa_2S_4$:Eu^{2+} thin-films at room temperature under excitation with photons at 18 eV: (a) Valence band region and (b) near-Fermi level region.

according to the absorption spectrum at room temperature [3]. We suppose that the fundamental edge is due to the band-to-band transition, because no exciton absorption peaks were found in the reflection spectrum at room temperature. In this case, the threshold energy for the valence band is expected to be 2.0 eV, higher than the value of E_{th}. This result can be explained by considering that acceptor-like levels are on the valence band. Therefore, our experimental results are adopted as one of the evidence supporting that holes are dominant charge carrier in the $SrGa_2S_4$:Eu^{2+} thin film.

UPS experiment allows us to know not only the electronic structure but also the physical constants characteristics of materials. We determined the ionization potential of $SrGa_2S_4$:Eu^{2+} to be 4.96 eV. This value is higher than the work functions of metals except gold [4]. From this fact, it is suggested that the interface between $SrGa_2S_4$:Eu^{2+} and metal electrode thin-films shows a tendency to form the Shottky-type barrier for hole conduction. The Shottky-type barrier may also involve the *p*-type conduction in the $SrGa_2S_4$:Eu^{2+} thin-film.

[1] K. Tanaka and S. Okamoto, Appl. Phys. Lett. **89** (2006) 203508.
[2] M. Kitaura *et al*., UVSOR Activity Report **37** (2010) 137.
[3] C. Chartier *et al*., Electrochem. Solid-State Lett. **9** (2006) G53.
[4] H. B. Michaelson, J. Appl. Phys. **48** (1977) 4729.

Ⅲ-6. APPLIED MATERIALS

Photoinduced Shift of the Photoelectron Spectra at the Zn-Phthalocyanine/C$_{60}$ Interface

S. Tanaka, K. Fukuzawa and I. Hiromitsu

Interdisciplinary Faculty of Science and Engineering, Shimane University, Matsue 690-8504, Japan

The electronic structure of the organic/organic and the organic/electrode interface of the organic electronics devices, such as organic light emitting diode, organic solar cell, and organic thin film transistor, has attracted much interest since it affects the performance of these devices [1]. For example, the authors have recently reported that the lithium-phthalocyanine thin film on indium-tin oxide (ITO) improves the device performance of the organic solar cell. This improvement was caused by the formation of the advantageous electronic structure for the hole extraction at the ITO/organic layer [2, 3]. It is widely accepted that the electronic structure of the organic layer in the devices can be inferred from the photoelectron spectra of the organic thin films. The photoelectron spectroscopy is a powerful tool for the estimation of the electronic structure of the samples. Thus, the photoelectron spectroscopy under the solar light irradiation can be useful to understand the electronic structure of the organic solar cells under the working condition. In the present study, we focused on the electronic structure of a donor/acceptor (DA) heterojunction of the organic solar cells. As a typical DA interface of the organic solar cell, the Zn-phthalocyanine (ZnPc)/C$_{60}$ interface was studied.

The photoelectron spectra were measured as a function of the thickness of the organic layer on an ITO substrate *in situ*. For the observation of the photoinduced effect on the electronic structure, the photoelectron spectra under the light irradiation were compared with that under dark. A solar simulator was used as the light source for the irradiation. The simulated airmass 1.5 solar illumination was exposed to the sample in a vacuum chamber through a viewport. The distance from the viewport to the sample was approximately 30 cm. All the photoelectron measurements were carried out with a photon energy of 40 eV at room temperature. The overall energy resolution was approximately 0.2 eV.

Figure 1 shows the photoelectron spectra of the C$_{60}$ (1 nm) layer on the ZnPc (15 nm) layer. The abscissa indicates the kinetic energy of photoelectron. The red dots and the black dots represent the photoelectron signals with and without the light irradiation, respectively. The peak at around 33.8 eV is the highest occupied molecular orbital (HOMO) of ZnPc. The HOMO peak position was shifted toward higher kinetic energies approximately 0.06 eV under the light irradiation compared with the HOMO peak under dark. In contrast, no significant shift was observed on the HOMO peak position of the ZnPc

film without the C$_{60}$ over layer (not shown). The photoinduced shift showed dependences both on the light intensity and on the thickness of the C$_{60}$ layer.

In general, there are several possibilities for the origin of the spectrum shift: the degradation of the molecules, the charging up of the sample, the thermal effect, and the photoinduced charge redistribution. We have considered that the shift was caused by the photoinduced charge redistribution at the ZnPc/C$_{60}$ interface from the following reasons. The degradation of the molecules should cause nonreversible changes on the photoelectron spectrum, however, the present shift was observed reversibly. The charging up is also excluded, since the charging up would cause a shift toward the lower kinetic energies and deform the spectral shape. Although the slight increase of the temperature of the substrate was observed while the light irradiation, the effect of the temperature on the photoelectron spectra is empirically negligible in the present temperature range. Hence, the shift of the HOMO peak can be attributed to the photoinduced effects on the charge redistribution at the DA interface. These preliminary results indicate that the photoelectron spectroscopy under the light irradiation is a valuable method to investigate the electronic structure of the organic solar cell system under the working conditions.
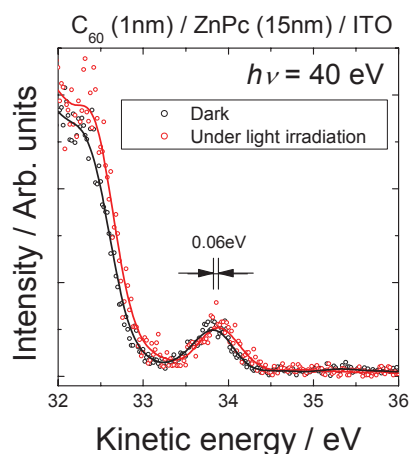

Fig. 1. Photoelectron spectra of C$_{60}$ (1 nm) / ZnPc (15 nm) on the ITO substrate with (red) and without (black) the light irradiation.

[1] H. Ishii *et al*., Adv. Mater. **11** (1999) 605.
[2] S. Tanaka *et al*., UVSOR Activity Report **37** (2009) 80.
[3] S. Tanaka *et al*., Appl. Phys. Lett. **97** (2010) 253306.

Identification of Catalytic Active and Inactive Species in Nitrogen Doped TiO$_2$ Photocatalyst by N K-edge XAFS Analysis

T. Yoshida[1], S. Muto[2] and E. Kuda[2]

[1]*EcoTopia Science Institute, Nagoya University, Nagoya 464-8603, Japan*
[2]*Department of Materials, Physics and Energy Engineering, Nagoya University, Nagoya 464-8603, Japan*

Introduction

In the field of catalytic chemistry, a specific function in a solid catalyst crucially depends on the chemical state of a specific active component (active site). In this context X-ray absorption fine structure (XAFS) is expected as one of the most powerful techniques for chemical state analysis of the active site, because it provides information on the local structure and electronic states around the specific element of interest. In the present study, a sophisticated combination of XAFS and a theoretical calculation method allows us identification of photocatalytic active and inactive species in nitrogen doped TiO$_2$ catalysts.

Experimental

The samples used in this study were TiO$_2$ (1 0 0) single crystals (5 x 5 x 0.5 mm^3), supplied by Furuuchi Kagaku, Japan. Mass analyzed 100 keV N$_2^+$ ions (50 keV/ N$^+$ ion) were injected into the samples at room temperature, perpendicular to the sample surface. The N$^+$ fluence ranged from 1 to 5 x 10^{21} m^{-2}. After the ion implantation, parts of the samples were heat-treated at 573 K for 2 hours in air.

A typical photocatalytic experiment consisted of placing the N$^+$-implanted sample in 0.5 ml of aqueous methylene-blue (MB) solution (9.8 μmol/L) and subsequent exposure to visible-light using a 15 W Xe lamp with a cut filter for λ > 430 nm.

N K-edge XANES spectra of the N$^+$-implanted TiO$_2$ samples were measured at the BL8B&4B station of UVSOR-II at the Institute for Molecular Science, Okazaki, Japan. Data were recorded at room temperature in total electron yield mode, and the X-ray energy dependence of the N Auger electron yield was monitored.

Results and Discussion

The photocatalytic activity reached its maximum at a fluence of 3 x 10^{21} m^{-2} and then decreased with the fluence. The sample implanted at a fluence of 5 x 10^{21} m^{-2} followed by heat-treatment at 573 K was almost photocatalytically-inactive under visible-light irradiation.

Figure 1 shows N K-edge XANES spectra of the N$^+$-implanted TiO$_2$ samples, a TiN powder and theoretical spectra of several structure models.

Common XANES features in Fig. 1 (a) and (c) suggest that N in the sample implanted by 3 x 10^{21} m^{-2} (highest active photocatalyst: H-cat) is in a chemical environment similar to that in TiN. More thorough observation suggested that double-peak around 400 eV in Fig. 1 (c) shifted to the lower energy side compared with that of TiN, which was well reproduced by the theoretical prediction using FEFF code when N occupies one of the O sites of TiO$_2$ [Fig. 1 (d)]. On the other hand, the XANES spectrum of the sample implanted with the N$^+$ fluence of 5 x 10^{21} m^{-2} followed by heat-treatment (almost inactive to visible-light : I-cat) shows a distinct single peak around 401 eV [Fig. 1 (e)]. This feature of the XANES spectrum was succesffuly reproduced by theoretical simulations based on the model where an O atom in TiO$_2$ was replaced by NO$_2$ [Fig. 1 (f)].
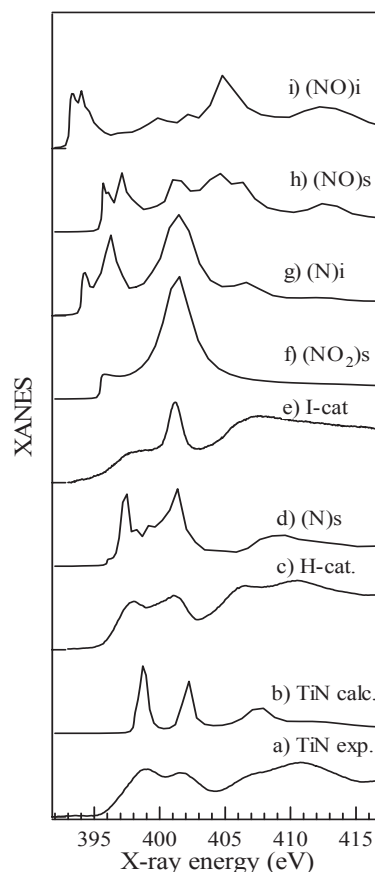
Fig. 1. N K-edge XANES spectra of (a) TiN crystal, (c) the sample N$^+$-implanted with 3 x 10^{21} m^{-2}, (e) that with 5 x 10^{21} m^{-2} followed by heating at 573 K for 2 h, and theoretical spectra of structure models for (b) TiN, (d) substitutional N-doping, (e) substitutional NO$_2$-doping, (g) interstitial N-doping, (h) substitutional NO-doping and (i) interstitial NO-doping.

List of Publications

J. Fujioka, Y. Ida, Y. Takahashi, N. Kida, R. Shimano and Y. Tokura, **"Optical Investigation of the Collective Dynamics of Charge-Orbital Density Waves in Layered Manganites"**, Phys. Rev. B **82** (2010) 140409.

M. Fujita and M. Itoh, **"Polarization Dependence of the Fundamental Absorption Edge and Urbach Rule in PbMoO$_4$ Crystals"**, Phys. Status Solidi B **247** (2010) 2240.

R. Guillemin, M. Simon and E. Shigemasa, **"Doppler Effect in Fragment Autoionization Following Core-to-Valence Excitation in O$_2$"**, Phys. Rev. A **82** (2010) 051401.

A. Hara, T. Awano, Y. Ohno and I. Yonenaga, **"Structural Elements of Ultrashallow Thermal Donors Formed in Silicon Crystals"**, Jpn. J. Appl. Phys. **49** (2010) 050203.

A. Herzog, M. Marutzky, J. Sichelschmidt, F. Steglich, S. Kimura, S. Johnsen and B. B. Iversen, **"Strong Electron Correlations in FeSb$_2$: An Optical Investigation and Comparison with RuSb$_2$"**, Phys. Rev. B **82** (2010) 245205.

T. Hirahara, Y. Sakamoto, Y. Saisyu, H. Miyazaki, S. Kimura, T. Okuda, I. Matsuda, S. Murakami and S. Hasegawa, **" Topological Metal at the Surface of an Ultrathin Bi$_{1-x}$Sb$_x$ Alloy Film"**, Phys. Rev. B **81** (2010) 165422.

T. Hirahara, Y. Sakamoto, Y. Takeichi, H. Miyazaki, S. Kimura, I. Matsuda, A. Kakizaki and S. Hasegawa, **"Anomalous Transport in an *n*-type Topological Insulator Ultrathin Bi$_2$Se$_3$ Film"**, Phys. Rev. B **82** (2010) 155309.

E. Hirata, K. Tamagawa and Y. Ohki, **"Cr^{3+} Impurities and Photoluminescence in LaAlO$_3$"**, Jpn. J. Appl. Phys. **49** (2010) 091102.

W. Hua, H. Yamane, B. Gao, J. Jiang, S. Li, H. S. Kato, M. Kawai, T. Hatsui, Y. Luo, N. Kosugi and H. Ågren, **"Systematic Study of Soft-X-Ray Spectra of Poly(Dg)•Poly(Dc) and Poly(Da)•Poly(Dt) DNA Duplexes"**, J. Phys. Chem. B **114** (2010) 7016.

T. Iizuka, S. Kimura, A. Herzog, J. Sichelschmidt, C. Krellner, C. Geibel and F. Steglich, **"Temperature- and Magnetic-Field-Dependent Optical Properties of Heavy Quasiparticles in YbIr$_2$Si$_2$"**, J. Phys. Soc. Jpn. **79** (2010) 123703.

M. Itoh and T. Katagiri, **"Intrinsic Luminescence from Self-Trapped Excitons in Bi$_4$Ge$_3$O$_{12}$ and Bi$_{12}$GeO$_{20}$: Decay Kinetics and Multiplication of Electronic Excitations"**, J. Phys. Soc. Jpn. **79** (2010) 074717.

K. Kanai, Y. Noda, K. Kato, T. Kubo, K. Iketaki, A. Shimizu, Y. Ouchi, K. Nakasuji and K. Seki, **"Electronic Structure of Delocalized Singlet Biradical Ph$_2$-IDPL Solid Film"**, Phys. Chem. Chem. Phys. **12** (2010) 12570.

H. Katayanagi and K. Mitsuke, **"Communication: Mass-Analyzed Velocity Map Imaging of Thermal Photofragments from C$_{60}$"**, J. Chem. Phys. **133** (2010) 081101.

M. Kimura, H. Fujiwara, A. Sekiyama, J. Yamaguchi, K. Kishimoto, H. Sugiyama, G. Funabashi, S. Imada, S. Iguchi, Y. Tokura, A. Higashiya, M. Yabashi, K. Tamasaku, T. Ishikawa, T. Ito, S. Kimura and S. Suga, **"Polaronic Behavior of Photoelectron Spectra of Fe$_3$O$_4$ Revealed by Both Hard X-ray and Extremely Low Energy Photons"**, J. Phys. Soc. Jpn. **79** (2010) 064710.

S. Kimura, T. Iizuka, H. Miyazaki, A. Irizawa, Y. Muro and T. Takabatake, **"Electronic-Structure-Driven Magnetic Ordering in a Kondo Semiconductor CeOs$_2$Al$_{10}$"**, Phys. Rev. Lett. **106** (2011) 056404.

S. Kimura, T. Ito, M. Sakai, E. Nakamura, N. Kondo, T. Horigome, K. Hayashi, M. Hosaka, M. Katoh, T. Goto, T. Ejima and K. Soda, **"SAMRAI: A Novel Variably Polarized Angle-Resolved Photoemission Beamline in the VUV Region at UVSOR-II"**, Rev. Sci. Instrum. **81** (2010) 053104.

S. Kimura, Y. Muro and T. Takabatake, **"Anisotropic Electronic Structure of the Kondo Semiconductor CeFe$_2$Al$_{10}$ Studied by Optical Conductivity"**, J. Phys. Soc. Jpn. **80** (2011) 033702.

S. Kimura, E. Nakamura, M. Hosaka, T. Takahashi, and M. Katoh, **"Design of Terahertz Pump – Photoemission Probe Spectroscopy Beamline at UVSOR-II"**, AIP Conf. Proc. **1234** (2010) 63.

M. Kitaura, A. Ohnishi, M. Sasaki, C. Hidaka and T. Takizawa, **"Excitation Processes of Trivalent Cerium Ions in Calcium Thiogallate Crystals by Hot Photocarriers"**, IOP Conf. Ser.: Mater. Sci. Eng. **15** (2010) 012090.

H. Kumagai, Y. Tanaka, M. Murata, Y. Masuda and T. Shinagawa, **"Novel TiO$_2$/ZnO Multilayer Mirrors at 'Water-Window' Wavelengths Fabricated by Atomic Layer Epitaxy"**, J. Phys.: Condens. Matter **22** (2010) 474008.

H. Matsuhashi, K. Nagashima, N. Naijo and H. Aritani, **"Surface Base Sites of MgO Covered with Al$_2$O$_3$: XANES Analysis of Al and Mg *K*-edges"**, Top. Catal. **53** (2010) 659.

H. Miyazaki, H. J. Im, K. Terashima, S. Yagi, M. Kato, K. Soda, T. Ito and S. Kimura, **"La-Doped EuO: A Rare Earth Ferromagnetic Semiconductor with the Highest Curie Temperature"**, Appl. Phys. Lett. **96** (2010) 232503.

T. Miyazaki, R. Sumii, H. Umemoto, H. Okimoto, Y. Ito, T. Sugai, H. Shinohara and S. Hino, **"Ultraviolet Photoelectron Spectra of Mono-metal Endohedral Fullerene Er@C$_{82}$ (I)"**, Chem. Phys. **378** (2010) 11.

M. Nagasaka, T. Hatsui, H. Setoyama, E. Rühl and N. Kosugi, **"Inner-shell Spectroscopy and Exchange Interaction of Rydberg Electrons Bound by Singly and Doubly Charged Kr and Xe Atoms in Small Clusters"**, J. Electron Spectrosc. Relat. Phenom. **183** (2011) 29.

A. Ohno and N. Ohno, **"Relaxed Exciton Luminescence of KCl Crystals Heavily Doped with KI"**, Phys. Status Solidi C **8** (2011) 112.

S. R. Park, W. S. Jung, G. R. Han, Y. K. Kim, C. Kim, D. J. Song, Y. Y. Koh, S. Kimura, K. D. Lee, N. Hur, J. Y. Kim, B. K. Cho, J. H. Kim, Y. S. Kwon, J. H. Han and C. Kim, **"Intrinsic Quasi-Particle Dynamics of Topological Metallic States"**, New J. Phys. **13** (2011) 013008.

J. Palaudoux, P. Lablanquie, L. Andric, K. Ito, E. Shigemasa, J. H. D. Eland, V. Jonauskas, S. Kucas, R. Karazija and F. Penent, **"Multielectron Spectroscopy: Auger Decays of the Krypton 3*d* Hole"**, Phys. Rev. A **82** (2010) 043419.

Y. Sakamoto, T. Hirahara, H. Miyazaki, S. Kimura and S. Hasegawa, **"Spectroscopic Evidence of a Topological Quantum Phase Transition in Ultrathin Bi$_2$Se$_3$ Films"**, Phys. Rev. B **81** (2010) 165432.

R. Sato, T. Kawai and K. Kifune, **"Optical Properties of Sol-Gel Processed TiO$_2$ Thin Films up to the Vacuum Ultraviolet Energy Region"**, J. Non-Crys. Solids **356** (2010) 1300.

S. Sheinerman, P. Lablanquie, F. Penent, Y. Hikosaka, T. Kaneyasu, E. Shigemasa and K. Ito, **"PCI Effects in Argon 2p Double Auger Decay Probed by Multielectron Coincidence Methods"**, J. Phys. B: At. Mol. Opt. Phys. **43** (2010) 115001.

Y. Taira, M. Adachi, H. Zen, T. Tanikawa, N. Yamamoto, M. Hosaka, Y. Takashima, K. Soda and M. Katoh, **"Generation of Energy-Tunable and Ultra-Short-Pulse Gamma Rays Via Inverse Compton Scattering in an Electron Storage Ring"**, Nucl. Instrum. Methods Phys. Res. A (2011) *(in press)*.

S. Tanaka, T. Hanada, K. Ono, K. Watanabe, K. Yoshino and I. Hiromitsu, **"Improvement of Power Conversion Efficiency of Phthalocyanine/C$_{60}$ Heterojunction Solar Cells by Inserting a Lithium Phthalocyanine Layer at the Indium-Tin Oxide/Phthalocyanine Interface"**, Appl. Phys. Lett. **97** (2010) 253306.

T. Tanikawa, M. Adachi, H. Zen, M. Hosaka, N. Yamamoto, Y. Taira and M. Katoh, **"Observation of Saturation Effect on Vacuum Ultraviolet Coherent Harmonic Generation at UVSOR-II"**, Appl. Phys. Express **3** (2010) 122702.

M. Watanabe, T. Hatano, K. Saito, W. Hu, T. Ejima, T. Tsuru, M. Takahashi, H. Kimura, T. Hirono, Z. Wang, M. Cui, M. Yamamoto and M. Yanagihara, **"Multilayer Polarization Elements and Their Applications to Polarimetric Studies in Vacuum Ultraviolet and Soft X-Ray Regions"**, Nuc. Sci. Techniq. **19** (2008) 193.

S. Watanabe, K. Ogasawara, M. Yoshino and T. Nagasaki, **"First-Principles and Experimental Analysis of f^n-$f^{n-1}d^1$ Absorption Spectra and Multiplet Energy Levels of Pr^{3+}, Nd^{3+}, and U^{3+} in LiYF$_4$"**, Phys. Rev. B **81** (2010) 125128.

I. Yamamoto, T. Nakagawa, Y. Takagi and T. Yokoyama, **"Spin Reorientation Transitions of Ni/Pd(111) Films Induced by Fe Deposition"**, Phys. Rev. B **81** (2010) 214442.

N. Yamamoto, M. Shimada, M. Adachi, H. Zen, T. Tanikawa, Y. Taira, S. Kimura, M. Hosaka, Y. Takashima, T. Takahashi and M. Katoh, **"Ultra-Short Coherent Terahertz Radiation from Ultra-Short Dips in Electron Bunches Circulating in a Storage Ring"**, Nucl. Instrum. Methods in Phys. Res. A (2011) *(in press)*.

H. Yamane, A. Gerlach, S. Duhm, Y. Tanaka, T. Hosokai, Y. Y. Mi, J. Zegenhagen, N. Koch, K. Seki and F. Schreiber, **"Site-Specific Geometric and Electronic Relaxations at Organic-Metal Interfaces"**, Phys. Rev. Lett. **105** (2010) 046103.

Y. Zhang, L. X. Yang, M. Xu, Z. R. Ye, F. Chen, C. He, H. C. Xu, J. Jiang, B. P. Xie, J. J. Ying, X. F. Wang, X. H. Chen, J. P. Hu, M. Matsunami, S. Kimura and D. L. Feng, **"Nodeless Superconducting Gap in $A_xFe_2Se_2$ (A = K, Cs) Revealed by Angle-resolved Photoemission Spectroscopy"**, Nat. Mater. **10** (2011) 273.

IMS Workshop on Generation and Applications of Intense THz Radiation

Date: January 13-14, 2011
Place: Seminar Room (#201) of main building,
Institute for Molecular Science, Okazaki, Japan

Program

January 13th (Thursday)

13:00-13:30   Registration

Chair: Masahiro Adachi (UVSOR)
13:30-13:40   **Shin-ichi Kimura**（UVSOR）
                   Introduction
13:40-14:20   **G. L. Carr**   (BNL)
                   Coherent THz Pulses from the NSLS SDL Photo-injected Linac
                   and Applications in Ultra-fast Material Dynamics
14:20-14:40   **Miho Shimada**   (KEK)
                   Terahertz light source expected at the Compact Energy Recovery Linac (cERL)
14:40-15:05   **Masahito Katoh**   (UVSOR)
                   THz Radiation from Electron Storage Ring
15:05-15:30   **Masaaki Ashida**   (Osaka Univ.)
                   Electric Field Detection of Terahertz Coherent synchrotron radiation
                   and Its Application

15:30-15:50   Coffee break

Chair: Shin-ichi Kimura (UVSOR)
15:50-16:15   **Koichi Tsukiyama**   (Tokyo Univ. Sci.)
                   Present status of Free Electron Laser at
                   Tokyo University of Science (FEL-TUS)
16:15-16:40   **Shuji Sakabe** (Kyoto University)
                   Intense laser plasma radiations and THz generations
16:40-17:05   **Toshiaki Hattori** (Univ. Tsukuba)
                   Nonlinear Time-Domain Two-Dimensional Terahertz Spectroscopy:
                   Proposal of Experiments and a Theoretical Model
17:05-17:30   **Masayoshi Tonouchi**   (Osaka Univ.)
                   Terahertz Spectroscopy of Advanced Electronic Materials
17:30-18:00   **Koichiro Tanaka** (Kyoto Univ.)
                   Terahertz Nonlinear Spectroscopy in Solids

18:30-20:30   Banquet (UVSOR Seminar room)

January 14th (Friday)

Chair: Heishun Zen (UVSOR)
09:00-09:25   **Ryunosuke Kuroda** (National Institute of Advanced Industrial Science and Technology)
Development of a high-power THz source using an S-band compact electron linac and its applications
09:25-09:50   **Goro Isoyama**   (Osaka Univ.)
Development of THz FEL
09:50-10:10   **Toshiharu Takahashi**   (Kyoto Univ.)
Development of Near-field sub-THz Microscopy
using Coherent Transition Radiation
10:10-10:35   **Hiroyuki Hama**   (Tohoku Univ.)
t-ACTS (test Accelerator as Coherent THz Source) project

10:35-10:55   Coffee break

Chair: Tatsuya Mori (UVSOR)
10:55-11:20   **Masanori Hangyo**   (Osaka Univ.)
Terahertz waves and metamaterials
11:20-11:50   **Kodo Kawase**   (Nagoya Univ.)
Novel terahertz wave source and imaging applications
11:50-12:15   **Masahiko Tani**   (Univ. Fukui)
THz imaging using pulsed THz radiation

12:15-13:30   Lunch

Chair: Shin-ichi Kimura (UVSOR)
13:30-14:00   **Nobuhiko Sarukura**   (Osaka Univ.)
Parametric amplication of THz waves, Possibility of CPA
14:00-14:25   **Ryo Shimano**   (Univ. Tokyo)
Intense terehertz pulse induced phenomena in low dimensional electron systems:
carbon nanotubes and organic conductors
14:25-14:50   **Tatsuya Mori**   (UVSOR)
Terahertz time-domain spectroscopy of off-center rattling phonons
in clathrate compounds

14:50-15:00   Closing remarks

UVSOR Lunch Seminar

FY2010

Apr. 21   Dr. Hiroshi IWAYAMA, UVSOR Facility, Institute for Molecular Science
Coulomb explosion of rare gas clusters irradiated by extreme-ultraviolet free electron laser pulses

May 12   Dr. Masaharu MATSUNAMI, UVSOR Facility, Institute for Molecular Science
Combination of Photoemission and Optical Spectroscopies for the Study of Strongly Correlated Electronic Structure

May 26   Dr. Tatsuya MORI, UVSOR Facility, Institute for Molecular Science
Terahertz time-domain spectroscopy of rattling phonons in type-I clathrates

Oct. 27   Mr. Yoshitaka TAIRA, Graduate School of Engineering, Nagoya University
Generation of ultra-short gamma ray pulses via laser Compton scattering and development of pulse width measurement technique

Dec. 8   Dr. Naoto YAMAMOTO, Graduate School of Engineering, Nagoya University
Development of high brightness spin polarized electron source

Mar. 30   Dr. Hidetoshi MIYAZAKI, UVSOR Facility, Institute for Molecular Science
Electronic structure of the ferromagnetic semiconductor EuO: A three-dimensional angle-resolved photoemission spectroscopic study